Ali Kadir, BSc (Hons), MIMechE, CIMA

HIGH-TEMPERATURE CORROSION PROTECTION OF GAS TURBINE BLADES WITH MICRO-COATINGS AND NANO-COATINGS: *SIMULATION AND EXPERIMENTS*

Ali Kadir, BSc (Hons), MIMechE, CIMA

Senior Lecturer (Mechanical Engineering)

Multi-physical Engineering Sciences Group (MPESG)

Aeronautical and Mechanical Engineering Department

School of Science, Engineering and Environment (SEE)

University of Salford, Manchester, UK.

Submitted in Partial fulfilment of the Requirements for the Degree of

Doctor of Philosophy, March 2021

ABSTRACT

Material degradation at high temperature is a serious problem in gas turbines in aircraft. In these systems, the expansion blades experience high temperatures ranging from 850 Celsius to in excess of 1000 Celsius. High temperature corrosion is very significant therefore in such systems and either limits their use or reduces their life, considerably affecting the efficiency and the performance of the devices. One of the main methods for protecting blades from corrosion damage is coating. Oxidation is the most important *high-temperature* corrosion reaction. In this PhD therefore, the focus has been to explore both experimentally and numerically the performance of *micro-coatings and nano-coatings* for high temperature corrosion protection of gas turbine blade specimens. Titanium and silicon carbide (ceramic) materials were used for the micro-coating (double layer coating). An aluminium oxide and titanium oxide mix was deployed for the nano-coating (single layer coating). TGA (thermo-gravimetric analysis) and SEM (scanning electron microscopy) tests of both flame-sprayed micro- and nano-coated specimens have been conducted. Corrosion rates (linked to oxidation) were obtained with the parabolic model for both types of coatings tested in TGA. Morphology was studied using SEM. Numerical simulations have been conducted (thermal stress finite element and also CFD simulations) for micro-coatings and stress analysis and thermal stress analysis simulations have been performed for nano-coatings. ANSYS mechanical software was used for all stress simulations with the ANSYS FLUENT discrete phase solver employed for CFD modelling of high temperature gas effects and erosion on the micro-coating coating models. For the micro-coatings both single (titanium) and double (titanium and silicon carbide) systems were studied whereas for the nano-coatings, a single layer was found to be sufficient. While the micro-coatings did offer good protection, double layers (titanium and silicon carbide) were needed and still some high stress zones were observed in the core section of the specimen face, although better performance was achieved than with a single titanium coating layer. Erosion was also more effectively reduced with the *double layer* micro-coating on the specimen. Overall, the nano-coatings were found to achieve significantly superior performance to micro-coatings both in the experiments and simulations. Greater than 99% reduction in corrosion rate was achieved in the experiments for the micro-coatings compared with the uncoated bare steel (AISI304) sample, and 45.4% reduction in corrosion rate was

achieved in the experiments for the nano-coatings compared with the micro-coated sample. For the nano-coating, a *single layer* of aluminium oxide (60%)-titanium oxide (40%) significantly reduced high stress zones, minimized cracking, and suppressed surface degradation under high temperature conditions, thereby producing the best protection of all coatings studied.

The present PhD has made important novel contributions to modern practical high temperature gas turbine protection, and has shown, in particular, that a significant decrease in corrosion rate and much lower thermal stresses and lower surface damage are produced with nano-coatings compared with micro-coatings. A number of publications have also been produced, which appear in the Appendix.

Ali Kadir

ACKNOWLEDGEMENTS

DECLARATION

I, Ali Kadir, declare that this thesis is my original work, and no portion of the work referred to in this report has been submitted in support of an application for another degree or qualification of this or any other university, or other institution of learning.
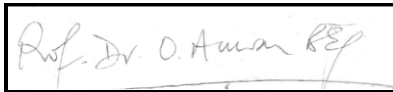
……………………….   …………………………..
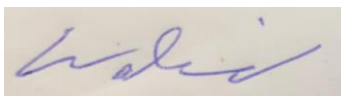**Signature**   **Date**

Mr. Ali Kadir

……………………….   …………………………..
Approved by   **Date**
Prof. Dr. Anwar Bég (Supervisor)

……………………….   …………………………..
Approved by   **Date**
Dr. Walid S. Jouri (Co-Supervisor)

NOMENCLATURE

List of Abbreviations

A	Area (cm^2)
ABAQUS	Finite Element Computer Code
ADINA	Automatic Dynamic Incremental Analysis
AHYPER	Anisotropic Hyper elasticity
AISI 304	Stainless Steel
Aliphatic	Compound any chemical compound
ANSYS	Analysis System
AVPRIN	Average Principle
AZ 31 alloy	Mixture with magnesium alloy with other metals
BC	Bond coat.
BSE	Back Scattered Electrons
C	Species
CFD	Computational Fluid Dynamics.
CHALPHAD	Computer coupling of phase diagram and thermochemistry
CMAS	Calcium-Magnesium-Alumina-Silicate
CNT	Carbon nanotube
CNTRC	Carbon nanotube reinforced composite
COMSOL	Computer Solution (software)
CVD	Chemical vapour Deposition
d	interplanar spacing (pm, nm, Angstrom)
DC	Direct current
DCL	Double-ceramic-layer
DEM	Discrete Element Method
DEMs	Discrete Element Methods
DLC	Diamond Like Carbon
DPM	Discrete Phase model.
EB-VPD	Electron-Beam Physical Vapour Deposition

EDS	Energy Dispersive Spectrometer
EDXA	Energy Dispersive X-ray Analysis
EFFNU	Effective Poisson Ratio
EIS	Electrochemical Impedance Spectroscopy
EPCR	Components (x, y, z, xy, yz, xz) creep strain.
EPEL	Equivalent Elastic strain
EPPL	Component (x, y, z, xy, yz, xz) of plastic strain.
EPTH	Components (x, y, z, xy, yz, xz) of thermal Strain
FC	Failure Criteria.
FEM	Finite Element Method
FOD	Foreign Object Damage.
GP	Genetic Programming
GTE	Gas Turbine Engine
HVOF	High Velocity Oxyfuel
HVOFGF	High velocity oxyfuel gas fuelled
HVOFLF	High velocity oxyfuel liquid fuelled
Incoloy 800	Nickel-iron-chromium alloy
Inconel 625	Nickel-Chromium alloy for high strength
JML-1	Platinum-Aluminide coating system
KeV	Kilo energy Volt
K-omega	Turbulence Energy-Turbulence Dissipation rate
LDE	Liquid Droplet Erosion
LPE	Liquid Particle Erosion
LES	Large eddy simulation
LLP	Low Pressure Plasma Spraying
M	Material
MA7S4	Nickel chromium super alloy
MATLAB	Mathematical laboratory (symbolic software)
MCS	Monte Carlo Simulation
MD	Molecular Dynamics

MP	Material property.
MUSCL	Monotonic Upstream-centred Scheme for Conservation Laws
$\frac{mg}{cm^2}$	$\frac{milli\ gramme}{(Centimetre)^2}$
n	Constant which represents the order of the diffraction.
NASTRAM	NASA Structural Analysis
NURBS	Non-uniform rational B-splines
OPENFOAM	Open source Field Operation and Manipulation
P-B ratio	Pilling-Bedworth ratio
PVD	Physical Vapour Deposition
PVM	Parallel virtual machine
RNG	Renormalizable group (turbulence model)
RSM	Reynolds stress models
SE	Secondary Electrons
SEM	Scanning Electron Microscope
SEM	Scanning Electro-Microscope
SEQV	Von Mises equivalent stress output
SINT	Stress intensity output
SOU	Second order up-winding
SPE	Solid Particle Erosion
TB	Triangular Elements
TBC	Thermal Barrier coatings
TC	Topcoat
TES	Thermal equivalent strain
TF	Thermal fatigue.
TGA	Thermal Graphic Analysis
TGO	Thermally Grown Oxide
TSI	Thermal Strain Intensity
UDF	User-defined function.
VPD	Physical Vapour Deposition
VPS	Vacuum plasma Spraying

W/W	Weight by weight
XRD	X-Ray Diffraction
YSZ	Yttria Stabilised zirconia

List of Chemical symbols

Al_2O_3	Alumina (Aluminium Oxide)
Ar	Argon
CaO	Calcium Oxide.
$CaO\text{-}SiO_2\text{-}ZrO_2$	Calcium Oxide-Silicon Oxide-Zirconium Oxide
CM247LC	Nickel base superalloy powder with low carbon content
CM247LC	Microstructure of Nickel based super alloy with low carbon content.
CMAS	Calcium Magnesium Alumina Silicate
Co	Cobalt
Cr	Chrome
Cr_2O_3	Chromium Oxide
Fe	Iron
Fe	Iron
FLiNaK	Molten salt
FLiNaK	Molten salt, alkaline metal fluoride salt mixture LiF-NaF-KF
$Gd_2Zr_2O_7$	Gadolinium Zirconate Oxide
$Gd_2Zr_2O_7$	Gadolinium Zirconium heptoxide
H_2	Hydrogen
He	Helium
IN-738LC	Nickel base superalloy with low carbon content
IN-738LC	Nickel based super alloy with low carbon content.
IN939	Nickel based super alloy.
KF	Potassium fluoride
$LaPO_4$	Lanthanum Phosphate compounds
$LaPO_4$	Lanthanum Phosphorous Oxozon (tetraoxygen)
LiF	Lithium fluoride

Monel-400 alloy	Nickel copper alloy
N_2	Nitrogen
NaCl	Sodium Chloride
NaF	Sodium fluoride
Ni	Nickel
NiCr	Nickel chrome.
NiCrAlY	Nickel chrome Aluminium Yttrium
NiCrBSi	Nickel Chrome Boron Silicium
Ni-P	Nickel Phosphorous
Ni-P	Nickel Phosphorous
Ni-P	Nickel phosphorus
$Ni-P-Al_2O_3$	Electroless Nickel Aluminium
$Ni-P-Al_2O_3$	Nickel Phosphorous Alumina
O_2	Oxygen
Pd	Palladium.
Pt_2Al_3	Platinum-Aluminium (Diffusion Barrier)
S	Sulphur
Si	Silicon
SiO_2	Silicon Dioxide
SiO_2	Silicon Oxide.
SO_2	Sulphur Oxide
Ti	Titanium
(TiCrAl)N	Titanium Chrome Aluminium Multi-layer Nano Coating
Ti_3SiC_2	Titanium Silicon carbide
TiN	Titanium Nitride
TiN	Titanium Nitride
TiO_2	Titanium Oxide
TiSiCN	Titanium Silicon Carbonitride
TiSiCN	Titanium Silicon Carbonitride
V_2O_5	Vanadium Oxide

V$_2$O$_5$	Vanadium Oxide
V$_2$O$_5$	Vanadium Oxide.
Y$_2$O$_3$	Yttrium Oxide
Y$_2$O$_3$	Yttrium oxide.
YSZ	Yttrium Silicon Zirconia
YSZ	Zirconia
ZrO$_2$	Ziconium Oxide.
(ZrCrNbAl)N	Zirconium Chrome Niobium Aluminium Multi-layer coating
$\boldsymbol{\beta}$-NiAl	Oxidation product of NiAl

List of Greek Notations

$\alpha_{inst}(T)$	Instantaneous coefficient of thermal expansion in 1/Kelvin or 1/^{0}C.
$\bar{\alpha}(T)$	Mean value of coefficient of thermal expansion in 1/Kelvin or 1/^{0}C.
$\alpha_x, \alpha_y, \alpha_z$	Thermal expansion coefficients in x, y,z directions in 1/Kelvin or 1/^{0}C.
β	Coefficient of thermal volumetric expansion in 1/Kelvin or 1/^{0}C.
δT	Temperature increment in Kelvin or ^{0}C.
ε_o	Principal Strain
ε_x	Strain in x direction
ε_y	Strain in y direction
ε_z	Strain in z direction
ε_{xy}	Strain in xy direction
ε_{xz}	Strain in xz direction
ε_{yz}	Strain in yz direction
ε_e	Von Mises or Equivalent Strain
$\varepsilon_1, \varepsilon_2, \varepsilon_3$	Output Principal Strain values 1, 2 and 3
ε_I	Strain Intensity.
$\varepsilon_{xt}, \varepsilon_{yt}, \varepsilon_{zt}$	Strains in layers x, y and z-directions in tension.
$\varepsilon_{xc}, \varepsilon_{yc}, \varepsilon_{zc}$	Strains in layers x, y and z-directions in compression.
$\varepsilon_{xt}^f, \varepsilon_{yt}^f, \varepsilon_{zt}^f$	Failure strains in layers x, y and z -directions in tension.

$\varepsilon_{xc}^{f}, \varepsilon_{yc}^{f}, \varepsilon_{zc}^{f}$	Failure strains in layers x, y and z -directions in compression.
ε^{el}	Elastic strain vector.
ε	Total strain vector.
ε^{th}	Thermal strain vector.
$\in$	Dissipation Rate
θ	reflection angle in degrees
k	Turbulence energy
λ	Second coefficient of viscosity in kg/ms
λ_1	wavelength (pm, nm, Angstrom)
μ	dynamic viscosity in kg/ms.
μ_e	Effective viscosity in kg/ms.
μ_t	Turbulence viscosity in kg/ms.
v'	Effective Poisson ratio.
v_{xy}, v_{yz}, v_{xz}	Minor Poisson ratio in xy, yz and xz plane.
$\bar{v}_{xy}, \bar{v}_{yz}, \bar{v}_{xz}$	Major Poisson ratio in xy, yz and xz plane.
ξ_1^f	Value of maximum strain failure criterion.
ξ_3	Value of Tsai-Wu failure criterion.
ρ	Density in kg/m³.
ρ_m	Mixture density in kg/m³.
σ_o	Principal Stress (N/m²).
$\sigma_1, \sigma_2,$ and σ_3	Three Principal stresses (N/m²).
σ_I	Output Stress Intensity (N/m²).
σ_e (SEQV)	Equivalent stress (N/mm²).
σ_1^f	Maximum stress failure (N/m²)
$\sigma_{xt}, \sigma_{yt}, \sigma_{zt}$	Tensile stresses in layers x, y and z directions in N/m².
$\sigma_{xc}, \sigma_{yc}, \sigma_{zc}$	Compressive stresses in layers x, y and z directions in N/m².
$\sigma_x, \sigma_y,$ and σ_z	Stresses in layers x, y and z-directions in N/m².
$\sigma_{xt}^f, \sigma_{yt}^f,$ and σ_{xt}^f	Failure stresses in layers x, y and z -directions in tension in N/m².

$\sigma_{xc}^f, \sigma_{yc}^f, and\ \sigma_{zc}^f$	Failure stresses in layers x, y and z -directions in compression in N/m^2.
σ_t^f	Input failure tensile stress limit in N/m^2.
σ_c^f	Input failure compression stress limit in N/m^2.
σ_e	Equivalent Stress in N/m^2.
σ_1, σ_3	Principal stresses in N/m^2.
σ	Stress vector in N/m^2.
$\sigma_x^R, \sigma_y^R, \sigma_z^R$	Reynolds stress components in x,y and z directions in N/m^2.
τ_{MAX}	Maximum Shear stress in N/m^2.
φ	Cell centred value.
φ_f	Face Value.
$\nabla\varphi$	Gradient.

List of Roman Symbols

A	Cross-sectional area normal to the direction of heat flow in m^2
A_{face}	Area of the cell face at the wall in m^2
B	Brinell hardness
$b(v)$	Relative particle velocity in m/s
c	Specific heat in J/kg K
$C(d_p)$	Function of particle diameter in m
C, f, and b	Boundary conditions
C_μ	Constant.
$C_{1\epsilon}, C_{2\epsilon}$, and $C_{3\epsilon}$	Constants.
C_p	Specific heat capacity at constanat pressure (J/kgK).
d_e	Nodal displacement vector in m
dT/dx	Temperature gradient in K/m
E_c	Young's Modulus of the composite in GPa
E_x, E_y, E_z	Young's Modulus in x, y and z directions in GPa

$f(\alpha)$	Function of impact angle in degrees
F_s	Particle shape-coefficient user defined function
G_b	Mean velocity gradient.
g_x, g_y, g_z	Components of acceleration due to gravity in m/s^2
G_{xy}, G_{yz}, G_{xz}	Shear modulus in the *x, y* and z plane in N/m^2
$G_{k,m}$	Turbulence kinetic energy in Joules.
h_f	Film coefficient in W/m^2. K.
H_p	Particle hardness.
K	Thermal conductivity in W/(m.K)
K_{xx}, K_{yy}, K_{zz}	Conductivity in the element x, y, and z directions in W/(m.K)
L	Volume coordinates for nodes in m^3
$\dot{m}_p$	Mass flow of the particle in kg/s.
N	Node
n	Velocity exponent
p	Pressure (Pa)
Q	Heat flow rate by conduction in Watts
Q_V	Volumetric heat source (J/m^3)
q	Heat flux vector in W/m^2
q^*	Specified heat flow in W/m^2
$\ddot{q}$	Heat generation rate per unit volume in Watts
R	Gas constant in J/kgK
R_x, R_y, R_z	Distributed resisitance in N/m^3
$R_{accretion}$	Accretion rate
$R_{erosion}$ or ER	Erosion rate.
R_x, R_y, R_z	Distributed resisitance in N/m^3
S_k and $S_\in$	User-defined source terms.
S1, S2, and S3	Output Quantities Principal stresses (N/m^2)
t	Time in Seconds

T	Current temperature at the point in Kelvin or ^{0}C
T_0	Total (or stagnation) temperature (K).
T_{ij}	Stress tensor in Pa
T_x, T_y, T_z	Viscoss loss terms in N/m^3.
T^*	Specified Temperature in Kelvin or ^{0}C
T_B	Bulk temperature of the adjacent fluid in Kelvin or ^{0}C
T_{REF}	Reference (strain – free) temperature in Kelvin or ^{0}C.
T_S	Temperature at the surface of the model in Kelvin or ^{0}C
$U^h(x, y, z)$	Displacement vector in x, y and z direction in m
u_i	Orthogonal velocities $(u_1 = V_x, u_2 = V_y, u_3 = V_z)$ in m/s
u, v, w	Displacement at each node in m
$\vec{v}_m$	Mixture velocity in m/s.
v_x, v_y, v_z	Velocity vector in x, y and z directions in m/s
V_x, V_y, V_z	Components of velocity vector in the x,y, z directions in m/s
Vol	Volume of the element in m^3
v	Velocity vector in m/s
v_c	Poisson's ratio of the composite
V_p	Volume coordinates at a point in m^3
W^V	Viscous work term (J/m^3)
x, y, z	Global Cartesian coordinates
Y_M	Fluctuating dilatation to overall dissipation rate
ρ_c	Density of the composite in kg/m^3

TABLE OF CONTENTS

**CHAPTER 3 THEORY FOR MATHEMATICAL METHODOLOGY AND
NUMERICAL SIMULATIONS (ANSYS WORKBENCH)**

CHAPTER 4 EXPERIMENTAL METHODOLOGIES FOR HIGH TEMPERATURE CORROSION PROTECTION WITH MICRO-/NANO-COATINGS.

CHAPTER 5 EXPERIMENTAL STUDY OF HIGH TEMPERATURE OXIDATION BEHAVIOUR OF AISI 304 STAINLESS STEEL COATED WITH MICRO-COATING AND NANO-COATING.

CHAPTER 6 COMPUTATIONAL SIMULATIONS OF MICRO-COATED AND NANO-COATED GAS TURBINE BLADE SPECIMENS

CHAPTER 7 CONCLUSIONS AND FUTURE PATHWAYS

List of Figures

List of Tables

List of Publications (see Appendix for extracts)

1] **Ali Kadir** and O. Anwar Bég, Thermal stress and computational fluid dynamics (CFD) analysis of coatings for high-temperature corrosion, *ICHTFM 2018: 20th International Conference on Heat Transfer and Fluid Mechanics, WASET, Istanbul, Turkey, August 16 – 17 (2018).*

2] **Ali Kadir**, O. Anwar Bég, Tasveer A. Bég and Walid S. Jouri, Finite element thermal stress simulation of (flame-spray) nano-powder- coated gas turbine blades under high temperature, *IIER 767TH International Conference on Recent Innovations in Engineering and Technoogy (ICRIET), Doha, Qatar, December 10-11 (2019).*

3] **Ali Kadir**, O. Anwar Bég, M. E. El Gendy, Tasveer A. Bég and M. Shamshuddin, Computational fluid dynamic and thermal stress analysis of coatings for high-temperature corrosion protection of aerospace gas turbine blades, *Heat Transfer (2019).* doi: 10.1002/htj.21493 (*25 pages*)

4] **Ali Kadir**, O. Anwar Bég and W.S. Jouri, Finite element analysis of nanocoated composite gas turbine blades using metallic oxide nanopowders, *Proc. IMechE-Part N: J Nanoengineering, Nanomaterials and Nano-systems (2020).* **In press**

5] **Ali Kadir**, O. Anwar Bég and W.S. Jouri, Progress in numerical modelling of nano-coated gas turbine blade samples with TGA/XRD/SEM experimental corroboration, *Nanoscience & Technology- An International Journal (2021)*. **Submitted**

6] **Ali Kadir**, O. Anwar Bég, M. El Gendy and Walid S. Jouri, Thermal conduction and elastostatic stress FEA of gas turbine blade specimens coated with nanomaterials and tested with XRD/SEM, *I8TH BUU Conf., Burapha University, Thailand, September 14-16, (2021).* **To be presented**

CHAPTER 1   INTRODUCTION

1.1   Introduction

In this introductory chapter, an overview of the motivation for this PhD has been provided including aims and objectives. Key aspects of high temperature corrosion science (e.g. oxidation) in aero- gas turbine engines and coating materials used for gas turbine blades have also been outlined in addition to the structure of the PhD.

In subsequent chapters, full details of the adopted experimental and computational methodologies are described which have been applied to the *novel coating systems* studied i. e. micro-coating (titanium-silicon carbide) and nano-coating (aluminium oxide-titanium oxide) on a representative specimen of the gas turbine blade.

1.2   Motivation

Material degradation at high temperatures and under corrosive environments is a serious problem in several traditional and high-technological industries. Gas turbines in aircraft, fossil fuelled power plants, refineries and petrochemical industries, ceramic and electronic glass manufacturing, and heating elements for high temperature furnaces are some examples where corrosion either limits their use or reduces their life, considerably affecting the efficiency. It also has an important role in material selection for construction of industrial equipment [1,2]. In real gas turbine operations, important considerations are:

- intense centrifugal stresses act on the blade due to high angular speeds and,

- thermal stresses arise due to temperature gradient within the blade material

- Oxidation associated with chemical reaction (corrosion)).

Temperature is the principal concern for corrosion effects. The analysis of a gas turbine blade mainly consists of the following three parts: *structural, thermal and gas flow analysis*. The

analysis can be carried out under *steady state or transient conditions* using finite element or finite volume software e.g. ANSYS.

Many different substrates are used for the alloys blade material e.g. superalloy, Monel-400, Hastealloy X & Inconel 625. Since the gas turbine is a device designed to convert the heat energy of fuel into useful work such as mechanical shaft power via turbine blades, the blades are most important components in a gas turbine power plant. A blade can be defined as the medium of transfer of energy from the gases to the turbine rotor. Both static and temperature loads have a significant effect on the blades. Therefore, the coupled (static and thermal) analysis of turbine blades is explored in this PhD. Severe hot corrosion attack of turbine blades after long term operation, results from a combination of temperature and corrosive gases. This leads to significant damage and degradation of the blade structure which adversely affects performance and requires significant monitoring, repair and replacement, thereby increasing risks and also costs. There are a number of solutions to this problem including:

- Improve the filtration system and use high quality, low contaminant fuels

- Air cooling channels within the turbine blade

- Develop more corrosion resistant blade alloys [1, 2]

- Develop improved coating systems [3].

The last of these solutions (improved coating systems) provides the best strategy and is the focus of this PhD. Currently gas turbine blades tend to deploy a variety of different coatings e.g. platinum aluminide, ceramics etc. In this PhD two coatings types are studied to establish their comparative performance in high temperature corrosion protection of gas turbine blades (both prepared via flame spraying deposition):

- micron sized coatings

- nanoscale coatings

A small specimen is studied which can be tested both experimentally and also simulated in finite element software to examine the different protective capabilities of micro-coatings (titanium and silicon carbide ceramic) and nano-coatings (aluminium oxide and titanium oxide nano-powder mix).

1.3 Aims

The main aim of the present PhD is to compare the performance of micro-coatings (titanium and silicon carbide) and nano-coatings (aluminium oxide and titanium oxide) for the high temperature corrosion protection of gas turbine blade specimens using both experimental (thermogravimetric analysis i.e. TGA and scanning electronic microscopy i.e. SEM) and computational (finite element thermal stress and CFD) simulation. TGA is to be used to quantify corrosion rates on the coatings under high temperature conditions and SEM is deployed to examine the morphology and chemical contents.

ANSYS finite element software will be employed to compute Von Mises (equivalent elastic stress), Von Mises strain (equivalent elastic strain) and total deformation to provide insight into material response characteristics of the uncoated and coated specimens (both micro-coating and nano-coating) under high thermal loading. CFD will be deployed to compute the turbulent gas flow on micro-coatings with a discrete phase solver (DPS) for erosion analysis.

1.4 Objectives

The following are the main objectives of this thesis:

1] To *design and test gas turbine blade specimens* for high temperature loading conditions and explore the relative performance of *micro-coatings* (comprising ceramic and titanium layers) of *nano-coatings* (alumina and titania nano-powder mix) synthesized with flame spray

techniques using TGA (thermogravimetric analysis) for *corrosion rate estimation* and SEM (scanning electron microscopy) for *structural morphology of chemical constituent elements*.

2] To simulate the *mechanical and thermo-mechanical behaviour* of single (titanium) and double-layered (titanium and silicon carbide ceramic) micro-coated gas turbine blade samples with ANSYS software and achieve a deeper understanding of actual coating performance.

3] To simulate the high temperature *erosion characteristics* of double-layered titanium and silicon carbide ceramic) micro-coated gas turbine blades with the ANSYS FLUENT computational fluid dynamics code discrete phase model (DPM) and a turbulence model, in order to provide an insight into the high temperature erosion behaviour.

4] To simulate the *mechanical and thermo-mechanical* behaviour of *nano-coated* gas turbine blade samples with ANSYS for different alumina/titania mix nano-powder percentages.

5] To compare the relative high temperature corrosion protection performance of both micro- and nano-coatings *via corrosion rates and thermal stresses* and make recommendations thereof for the gas turbine industry.

1.5 The Modern Aero-Gas Turbine Engine

The gas turbine [3] obtains its power by utilizing the energy of burnt gases and the air which is at high temperature and pressure by expanding through the several rings of fixed and moving blades, to get a high pressure of order of 4 to 10 bar (atmospheres) of working fluid which is essential for expansion a compressor is required. The quantity of working fluid and speed required are more, so generally a centrifugal or axial compressor is required. The turbine drives the compressor, so it is coupled to the turbine shaft. If after compression the working fluid were to be expanded in a turbine, then assuming that there were no losses in either component, the power developed by the turbine can be increased by increasing the volume of working fluid at constant pressure or alternatively increasing the pressure at constant volume. Either of these

may be done by adding heat so that the temperature of the working fluid is increased after compression. To get a higher temperature of the working fluid a combustion chamber is required where combustion of air and fuel takes place giving temperature rise to the working fluid. The turbine escapes energy from the exhaust gas. Like the compressor, a turbine can be centrifugal or axial [3]. **Figure 1.1** shows the temperature and pressure distribution in a modern aero gas turbine engine.
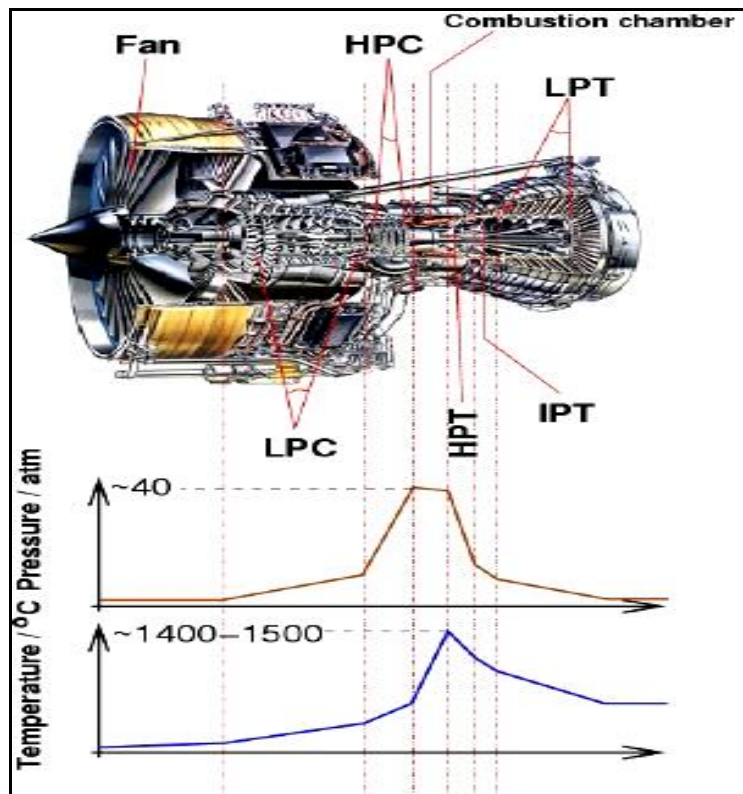
(LPC) Low Pressure Compressor
(HPC) High Pressure Compressor
(HPT) High Pressure Turbine
(IPT) Intermediate Pressure Turbine
(LPT) Low Pressure Turbine

Figure 1.1: Rolls-Royce Trent 800 Jet Engine showing the different stages and pressure/temperature profiles along the engine.

In each type of jet engine, the fast-moving exhaust gas is used to spin the turbine, since the turbine is attached to the same shaft as the compressor at the front of the engine, and the

compressor will turn together, the turbine may extract just enough energy to turn the compressor. The rest of the exhaust gas is left to exit the rear of the engine to provide *thrust* as in a pure jet engine. Or extra turbine stages may be used to turn other shafts to power other machinery such as the rotor of a helicopter, the propellers of a ship or electrical generators in power stations. The key focus of this PhD is the gas turbine blade coating performance under high temperature. Some examples of commercial blades are shown in **Figure 1.2** with corrosion damage due to hot gas effects.
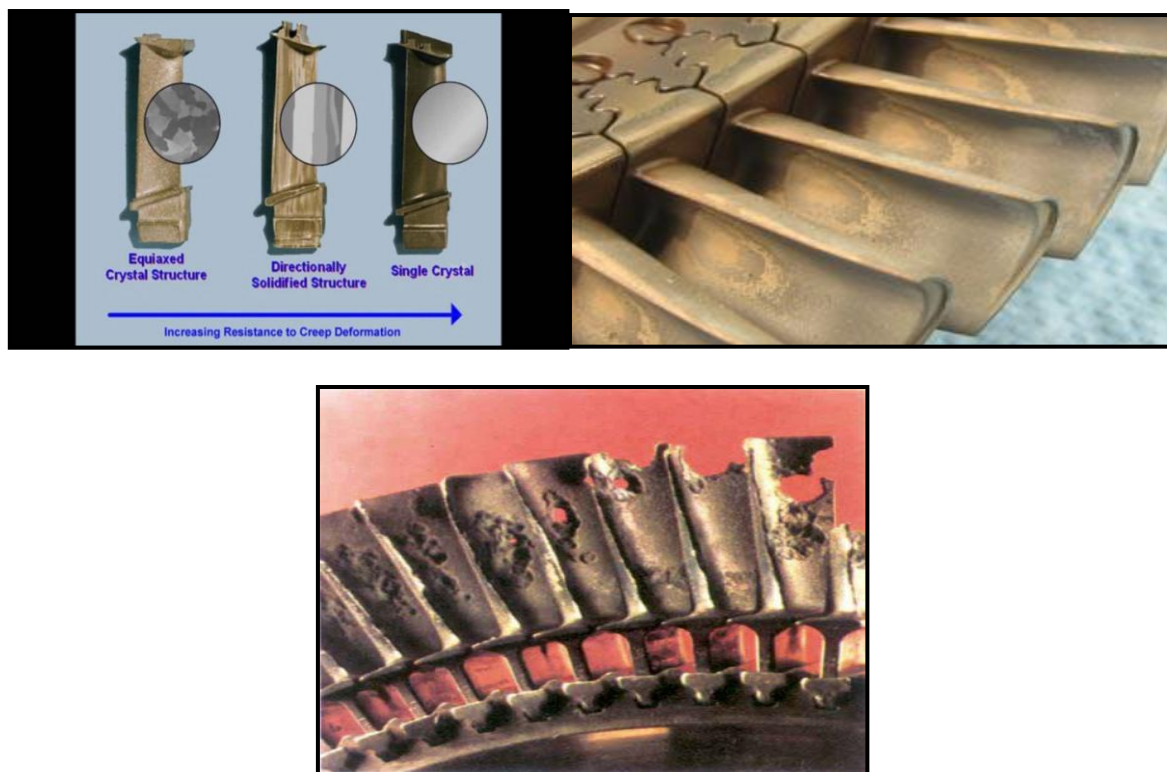
Figure 1.2: Top left- gas turbine blade types, top right surfacial damage, below centre- sulphidation on gas turbine blades – [all images courtesy of Boeing Aerospace, USA and Rolls Royce, UK].

1.6   High Temperature Corrosion

The term *high-temperature corrosion* refers to material degradation at temperatures higher than ambient temperatures when the material (e.g. for a gas turbine blade) is exposed to corrosive environments. Two issues must be considered in high-temperature corrosion:

- The first is the *high temperature* itself which creates thermal stresses (a *thermo-mechanical effect*) which can lead to cracking, delamination of coatings, structural failure etc [3].

- The second is *high-temperature corrosion*, which is a *thermo-chemical* effect, and which if not mitigated, can lead to premature surface damage, flaking, degradation etc, leading to high economic losses.

In industrial atmospheres most gas mixtures contain several components which could react with the material to form other corrosive products besides oxides [4] such as sulphide and Chlorine.

1.7   Materials and Coatings for High-Temperature Corrosion

With the increasing demand for energy, it is important to make the operating systems highly efficient. For example, in gas turbines, there is a trend to continuously increase the gas inlet temperature to make them run more efficiently. With temperature increments, the material specification becomes quite stringent. The requirement not only involves strong corrosion resistance at these temperatures, but also it must have stable and excellent *high-temperature mechanical properties*, such as resistance to creep [5,6]. Simultaneous achievement of both these corrosion and mechanical requirements cannot in many cases be obtained by alloy development independently. Although the development of more corrosion resistant blade alloys would appear to be an attractive alternative, the trend in recent years has been towards increased temperature capability but alloys designed for this purpose are inherently *less corrosion-resistant* than their predecessors. A number of important observations can be made regarding the diffusion of elements such as tungsten, molybdenum, titanium, cobalt, nickel, and chromium within the total coating structure after complete processing. Titanium has greater diffusivity through platinum-aluminium inter-metallics than the refractory elements such as

tungsten and molybdenum. A similar behaviour is also apparent for cobalt. Although nickel can effectively diffuse throughout the β-NiAl structures, the inter-metallic Pt_2Al_3 behaves as an effective diffusion barrier restricting the movement of nickel to the surface, thereby allowing unrestricted growth of protective Al_2O_3. The results of long-term high temperature stability tests on alloy blades would suggest that the latter situation is maintained, indicating that the stoichiometric inter-metallics of platinum and aluminium are effective diffusion barrier materials when operating under hot corrosive gas conditions. The ability of titanium to establish a relatively high composition profile throughout the coating structure is undoubtedly beneficial to coating performance. Refractory elements such as tungsten and molybdenum, although essential solid solution strengtheners have an adverse effect upon resistance to hot corrosion and it is thought that the ability to restrict these refractory element mobilities gives rise to the improved performance over conventional aluminides. The relatively high level of chromium throughout the platinum aluminide structure is considered an additional important benefit for the system and is different to that of some commercial platinum aluminide coatings [7, 8]. Within the platinum-aluminium binary system there are a number of inter-metallic compounds. Due to the kinetics of the aluminising process, only the inter-metallics $PtAl_2$, Pt_2Al_3 and $PtAl$ are generally found in aluminised structures. Only the molecular volume of Pt_2Al_3 shows any resemblance to the 'ideal' volume predicted by linear correlation between volume and composition. Aluminium-rich inter-metallics form with considerable *expansion*; the platinum-rich with a *contraction*. Coating systems based upon the platinum-aluminium binary and which specifically generate $PtAl_2$ at the surface constituting a significant portion of the platinum aluminide layer, may undergo as much as 19 per cent surface volume contraction during service as a result of degeneration from $PtAl_2$ to $PtAl$. It is unlikely that such a volume change within an inherently brittle matrix could be accommodated without void formation or cracking [9]. Platinum aluminide systems in general may well have the potential for application

in both hot corrosion and oxidation environments making them suitable as protective coatings for high strength alloys in industrial, marine, and aero gas turbines. Similarly, their resistance to sulphidation at high temperatures may well be a property that can be exploited in other industrial process environments normally considered corrosive to the best cast or wrought nickel-based alloys. The JML−1 platinum aluminide coating system has undergone exhaustive assessment in Rolls-Royce and in other independent burner rig trials, one of which was carried out at the Johnson Matthey Group Research Centre. The results from these trials have shown the JML−1 system to considerably outperform the conventional aluminide coatings [1, 2]. The key to the performance of platinum aluminides is, however, very much dependent upon achieving the optimum coating composition and structure through controlled processing. Therefore, in this PhD *both micro-coating (titanium-silicon carbide ceramic) and nano-coatings (aluminium oxide-titanium oxide)* are investigated as *novel designs* for enhancing thermal protection of gas turbine blades in corrosive environments.

In super-alloy development, high mechanical strength is achieved by an alloy with a high percentage of *Al* and relatively low *Cr* content, and thus the cost of corrosion resistance which requires high chromium content. It is necessary to use an alternative approach to meet the severe requirement of strength and corrosion resistance. The other option is a composite system in which mechanical strength is achieved by alloy development and corrosion resistance by surface coating or surface modification. This strategy has proved to be quite successful in many industrial applications [1-3]. In gas turbines, there are more than fifty different components which require an efficient coating to resist the corrosive-erosive environment. Similarly, additional protection is needed on materials when cheaper fuels are used with high impurity content such as sulphur [1, 5].

Surface modification in the wider sense includes all types of coatings and surface treatments that result in a change of the surface microstructure and composition. There are several ways

in which coatings can be classified; the simplest is in terms of the *mechanism of the coating process*. High-temperature materials commonly operate in environments involving various combinations of oxidation, corrosion, erosion, and wear. Satisfactory performance requires the component to have resistance to these environments. In some applications, the inherent resistance of the base material must be supplemented by a coating to ensure the required component life [2,6]. Use of coatings in industrial gas turbines began in the 1960s with chromium coatings on blades. Around the same time, corrosion problems on aero gas turbine blades required the application of aluminide coats; the operating temperatures being too high for chromium coatings [6,7]. The use of coatings has progressed from the early 'problem solving' type of application to the situation in which surface coatings of various types are an integral part of the component design process [2,6]. An essential requirement for the application of a metallic material at high temperature is its resistance to high-temperature oxidation or corrosion. This is achieved if it forms a *protective oxide scale* on its surface. Oxide scales can arise in operation by reaction of elements in the material with oxygen in the environment or they can be produced by deliberate pre-oxidation in atmospheres containing oxygen at suitable temperatures. The protection action of these oxide scales depends on their property in reducing the rate of the corrosion reaction by acting as a diffusion barrier between the metallic and the corrosive environment. Oxide scales, therefore, are key functions in the application of materials in high-temperature technology. The behaviour of the *protective oxide scales* is an essential part for the material to respond to thermochemical-mechanical conditions. The diffusion barrier, which prevents severe chemical attack, can be damaged by mechanical loadings. For a reliable assessment with reference to material behaviour, it is important to have as much quantitative information as possible on the condition of the scale within these surroundings.

To promote the development of suitable protective oxide scales on the material surface, the

relevant alloying elements are added during the production process. The most important alloying elements in this situation are *Cr* and *Al*. In some cases, *Si* is also used [8]. Other elements in the alloy are the base component which incorporated is the surface scale in addition to these elements. Ceramics include silicon carbide and zirconium which offer enhanced protection against high temperature and also excellent abrasion resistance, although they can be susceptible to cracking.

1.8   Thermal barrier coatings

A *thermal barrier coating* is a ceramic coating that is applied to the turbine blade once the manufacturing process has been completed. Ceramics e.g. Zirconia, Silicon Carbide etc, are used to coat the turbine blades as they generally have higher melting temperature points than metal and some with low thermal conductivity. This enables the gas turbine to run at higher burn temperatures as the ceramic coating does not conduct the heat of the gas and therefore the temperature of the blade alloy will not increase. This makes the engine more powerful and efficient. Ceramics themselves cannot be used to make the whole blade as they are not resilient enough. The best ceramic to use in the turbine engine is a ceramic with very low thermal conductivity, a maximum service temperature above the gas burn temperature and good strength. Zirconia is the most common ceramic used for this application as it covers all these properties [9]. Some schematic and actual thermal barrier coated gas turbine blades are shown in **Figure 1.3** below.
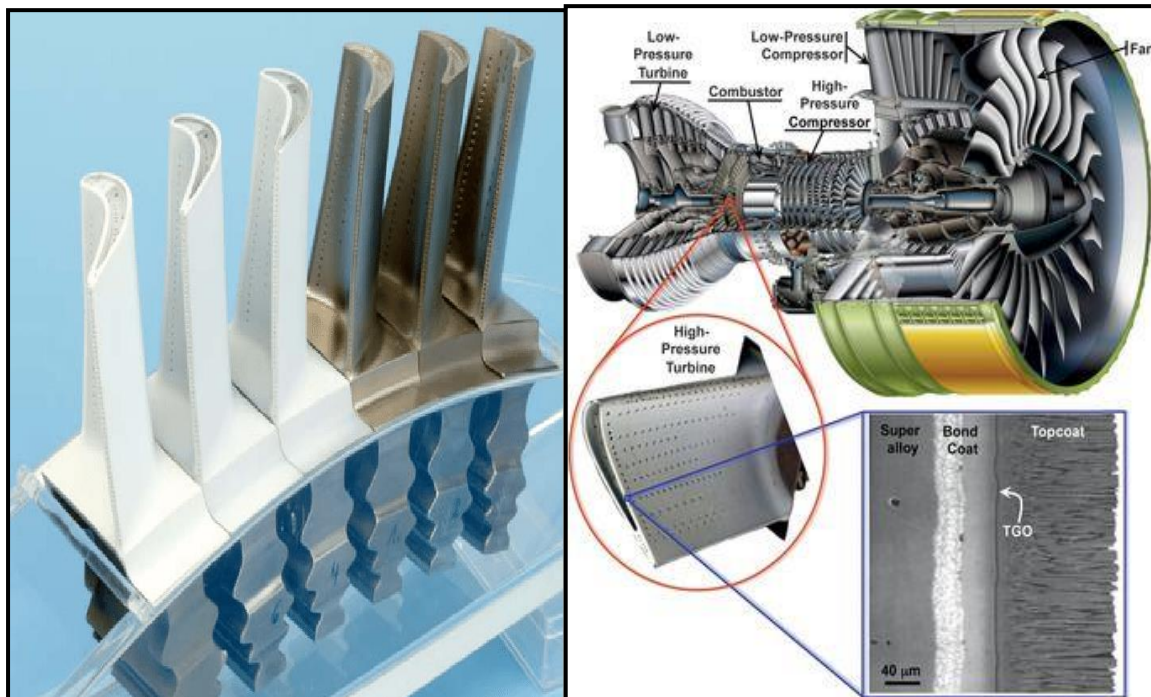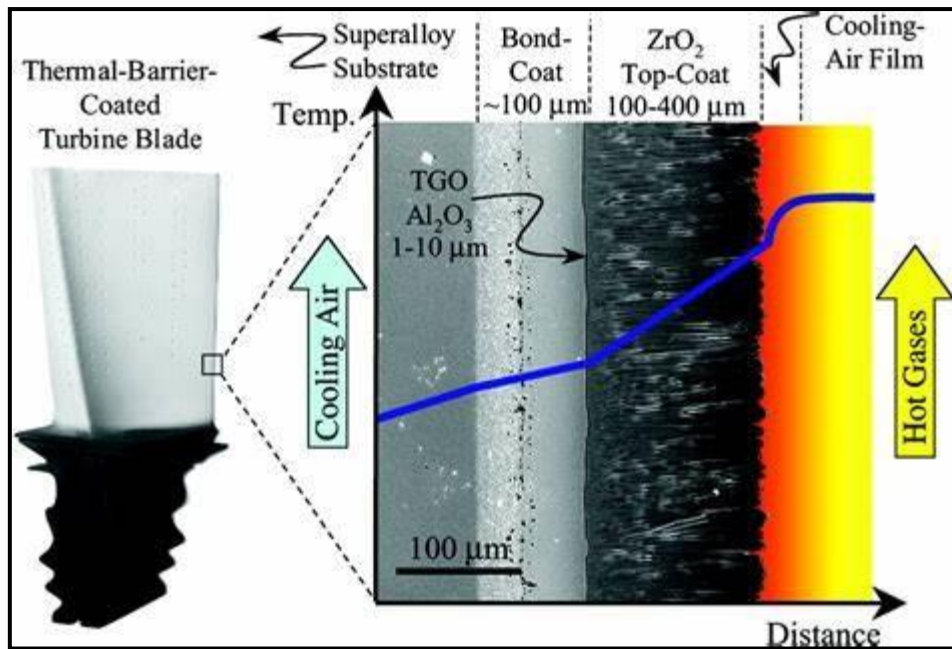
Figure 1.3: Thermal barrier coating structure and implementation in modern gas turbine

blades- [courtesy Boeing Aerospace, Washington, USA].

In this PhD **two different thermal protection coating systems** will be studied both experimentally using TGA and SEM and computationally using thermal stress finite element analysis (and computational fluid dynamics for erosion). These are:

(i) titanium-Silicon carbide micro-coatings

(ii) aluminium oxide-titanium oxide nano-powder nano-coatings

A temperature range of 850-1000 Celsius is considered to represent actual high temperatures encountered in real gas turbine blade environments. These two different novel coatings are shown to offer improved thermal protection and offer an alternative to conventional systems in use such as platinum coated or purely ceramic zirconia coated blades. However, the nano-coating will be shown to be considerably more effective in reducing corrosion rate, and also in suppressing thermal stresses.

1.9   Structure of PhD

As expressed in the Aims and Objectives earlier, this PhD focuses on *static and thermo-mechanical behaviour assessment of micro/nano coated gas turbine blade specimens for high temperature corrosion protection* using experimental (TGA, SEM) and numerical (ANSYS finite element/ FLUENT CFD) software. The entire PhD structure is summarized below in **Figure 1.4**.
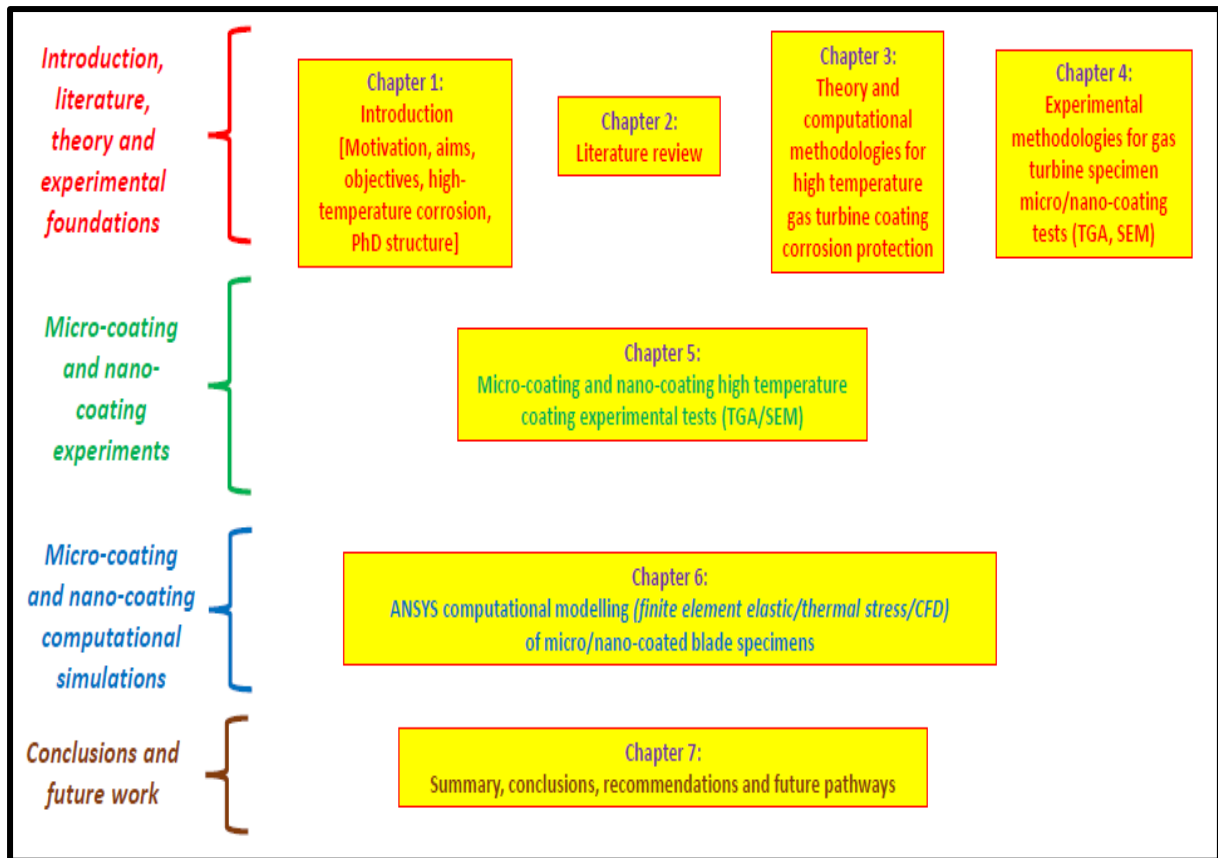
Figure 1.4: Overview of PhD Thesis with connected themes.

- In *Chapter 2,* a detailed literature review spanning key research works in high temperature corrosion protection with metallic/ceramic micro-coatings and nano-coatings, both from an experimental and simulation viewpoint is presented.

- *Chapter 3* provides full details of the theoretical methodology including finite element analysis (FEA) and computational fluid dynamics (CFD).

- In *Chapter 4* full details of experimental methods and techniques deployed (flame spraying coating preparation, TGA, SEM etc) for both micro-coatings and nano-coatings are given, with a comparison of oxidation corrosion rates obtained with the parabolic (nonlinear) model via TGA and also different morphologies obtained with SEM.

- *Chapters 5 and 6 constitute the novel research conducted in this PhD.* Chapter 5

describes the TGA and SEM experimental testing of micro-coatings (titanium and silicon carbide ceramic) and nano-coatings (aluminium oxide and titanium oxide nano-powder mix) and compares the performance of these coatings. *Chapter 6* describes detailed finite element stress and thermal stress analysis conducted on micro-coatings and nano-coatings and additionally CFD simulations of erosion on micro-coatings, with a comparison of high temperature corrosion protection via thermal stress behaviour.

- *Chapter 7* summarizes the main findings and recommendations and outlines possible future research themes in high temperature gas turbine corrosion studies.

Chapter 2: Literature Review

2.1　Introduction

Modern gas turbine blades experience significant thermal loading during expected life cycles. Temperatures can attain in excess of 1000 Celsius and it is therefore necessary to coat the blades with thermal barrier coatings (TBCs) which also provide protection from oxidation, corrosion, debris impact and thereby mitigate possible failures [1-4]. Additionally, there are *high centrifugal stresses and shock loadings* present. Many excellent studies have been conducted on the performance of TBCs in real systems. Temperature decay across TBCs is a *function of material and geometrical properties of the coating*, in particular the thickness of the layer and thermal conductivity [5].

Thermal barrier coatings (TBCs) as noted earlier in chapter 1, are advanced ceramic coatings applied to metallic surfaces like gas turbine blades and other aerospace engines. The function of the TBCs is to provide thermal insulation from the hot gas that flows through the turbine blades. TBCs consist of a *two-layer coating system* which comprises of an oxidation and *corrosion resistant layer* called the *bond coat* and an *insulating ceramic top layer* called the *topcoat*.

Ceramics have emerged as the most resilient to high temperature conditions, although cracking may occur, and other discontinuities may appear under long duration exposure to corrosive gases. Once coatings are compromised these may lead to thermal fracture, yield behavior and even creep failures. A critical aspect of sustaining good thermal protection is the interfacial bonding between layers and in particular the bonding integrity between the blade and the first layer of coating.

Control of oxidation is also a very significant aspect of mitigating high temperature corrosion damage. In this chapter the available scientific literature for all *high temperature corrosion, coating manufacture, coating spraying methods and numerical modelling* aspects of this PhD are reviewed and *in particular it is identified that there are gaps in the work which has been communicated in the literature with respect to both corrosion TGA and SEM testing and finite element thermal stress analysis of both micro-coatings and nano-coatings.*

The literature review conducted in this chapter has revealed that while many high temperature corrosion studies have been communicated in the literature for micro-coatings and nano-coatings (for many different coating materials), and limited work has been done on purely numerical simulations of gas turbine blade thermal stresses, *no research papers* have included *simultaneously* both experimental (TGA, SEM) *and advanced thermal stress finite element* (and/or CFD) simulations to corroborate the tests for *combined titanium-silicon carbide micro-coatings and aluminium oxide-titanium oxide nano-coatings.*

This has therefore provided the novelty of the present PhD and these aspects are described in detail for combined titanium-silicon carbide micro-coatings and aluminium oxide-titanium oxide nano-coatings, in chapter 5 (experimental) and chapter 6, with comparisons given in both chapters and then summarized later in chapter 7 (conclusions section).

2.2 High temperature corrosion coating materials and manufacturing

High temperature corrosion in gas turbine blades can exceed 1000 Celsius. For technological materials, the scales frequently consist of several phases with component layers of various compositions. The distribution of these component layers after long periods of time is determined by their suitability and the gradient of the oxygen partial pressure over the whole scale. The coatings involve using protective oxides, Cr_2O_3 and Al_2O_3, for the base alloys, and

they could contain a higher percentage of aluminium or chromium than the base alloys because their compositions are not limited by their mechanical properties. The protective effect of Cr_2O_3 is limited to around 1000^oC due to the formation of volatile CrO_3, while Al_2O_3 is effective to higher temperatures [6,7]. Often *AISI304, AISI326*, and *AISI310*, stainless steels are used as the substrate. A conventional *micro-coated gas turbine blade* is shown in **Figure 2.1**.
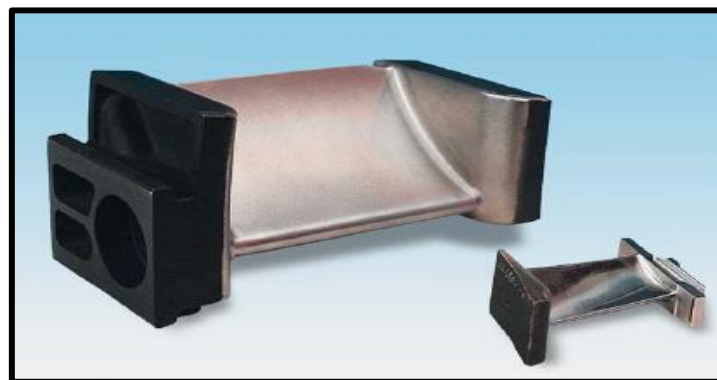
Figure 2.1: Coated gas turbine vanes [courtesy-Boeing Aerospace, Washington, USA].

It is important to note that when the micro-coating is performed in commercial organizations e.g. Sulzer, the apparatus available is much larger and more advanced and all the coating are deposited by automation and robotics devices (**Figure 2.2**). Additionally, the health and safety standards are much higher compared with manual spraying in laboratories in educational establishments. **Figure 2.3** shows a modern high-volume production system developed for the coating process of larger components.
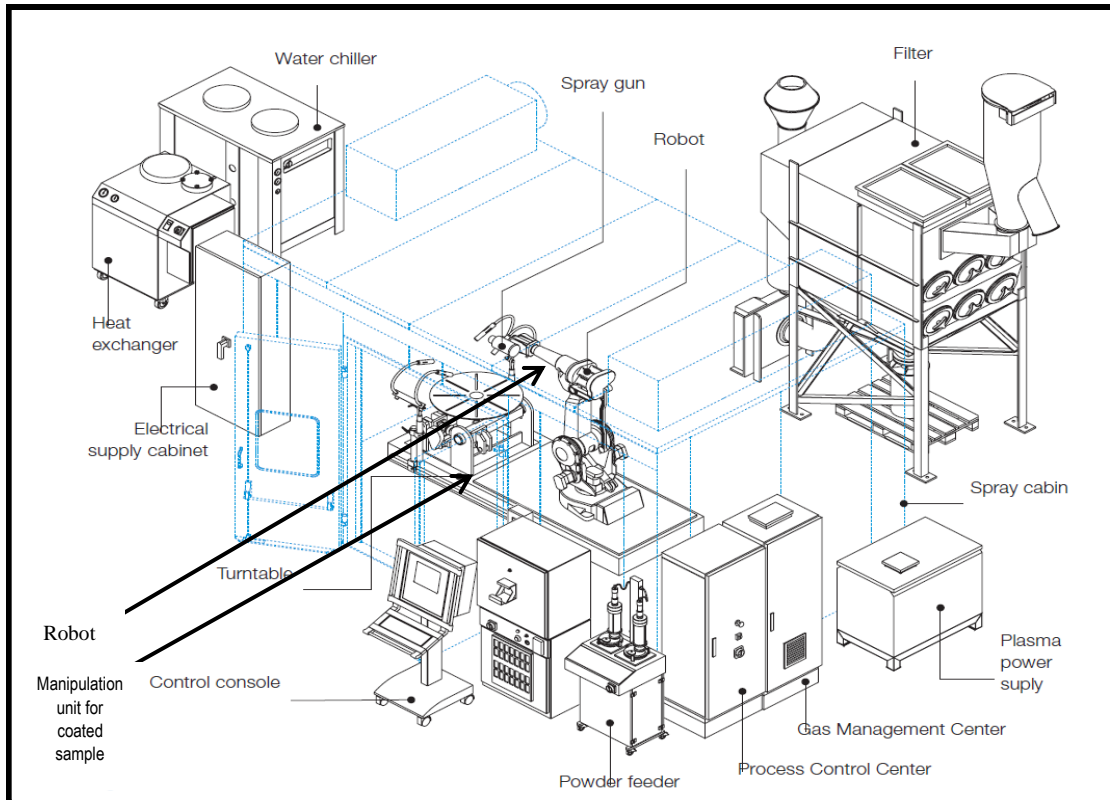
Figure 2.2: Coating facility used in Industry (Source: Sulzer Metzo Switzerland).

Figure 2.3: A modern high-volume production system for coating gas turbine blades-(Source: Sulzer).

In **Figures 2.4**, various completed coatings on an entire gas turbine aero jet engine is shown.
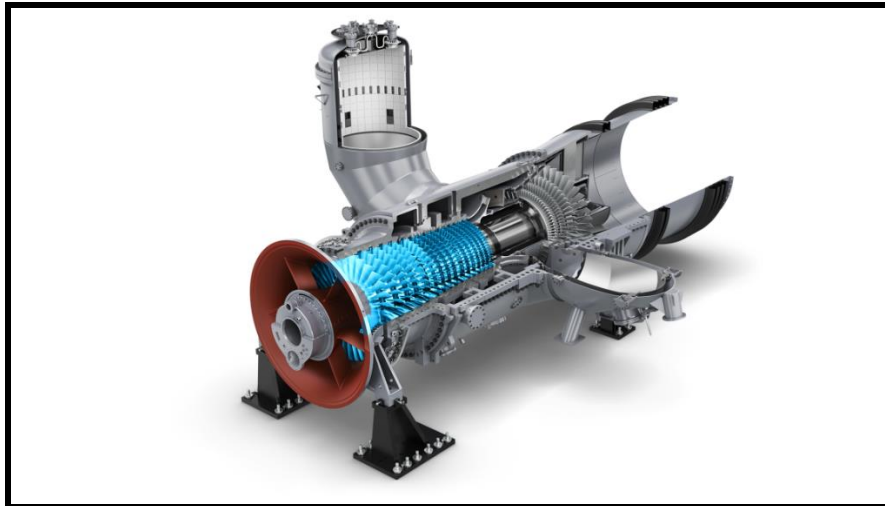
Figure 2.4: Completed jet engine turbine with hundreds of coated vanes (blades) [courtesy General Dynamics, USA].
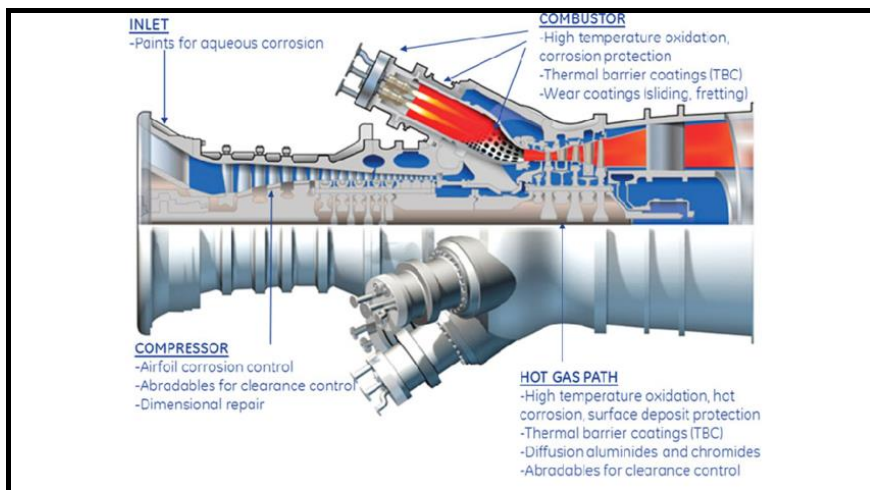
Figure 2.5: Corrosion-sensitive zones in jet engine system- [courtesy Lockheed Martin, Virginia, USA].

Figure 2.5 shows the "sensitivity zones" in modern thermal HVOF micro-coated jet engine components- clearly the corrosion effect is multi-faceted and is experienced throughout the jet propulsion process. However *high temperature corrosion* arises mainly in the combustor and hot gas flow path where the blades are used. The porosity of a thermal spray coating is *process-dependant*, and exhibits an anisotropic, layered structure. These basic characteristics can be modified within a wide range to suit the specific application. With certain thermal spray coating such as Arc wire spray coating, shows porosity and not melted parts of the coating whereas,

with HVOF there is no porosity shown. Under severe conditions, a combination of 50% *Cr*/50% *Ni* over Incoloy 800 has been demonstrated cost benefits to the user. Although 50% *Cr*/50% *Ni* has excellent corrosion resistance, at the same time it has low ductility, plus fabrication problems can arise in the manufacturing process [8]. Reducing the chromium content will minimise the potential to 12% chromium phase formation and this can be an advantage [9-11]. Aluminised coatings are the most common type of diffusion coatings used extensively to protect a wide range of aero, marine, and industrial gas turbine components. The thickness of the coating on the exterior surface of gas turbine blades is 25-75 *μm* and the aluminium content can be varied from 25-40%, depending on the process temperature and heat treatment [11].

In the past eight decades, considerable modifications have been made in materials used for micro-coatings for gas turbine blades and also the blade alloy materials as shown in **Figure 2.6**.
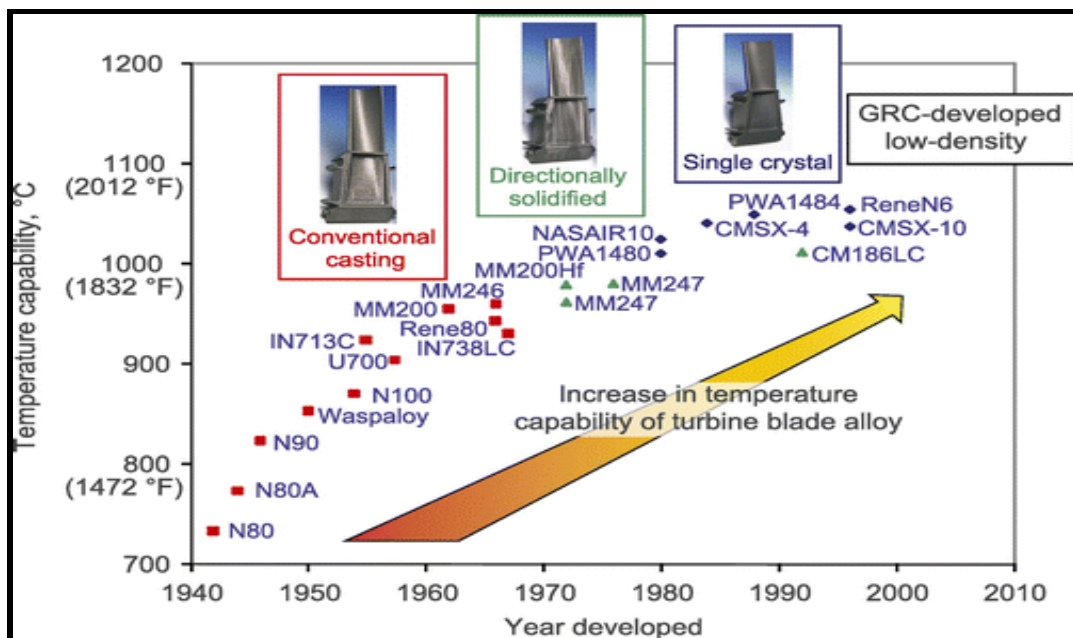
Figure 2.6: Micro-coating evolution [8].

Since coatings are formed by interdiffusion between the depositing aluminium and the base material, the coating composition will be influenced significantly by the base materials [11,12].

In the early 1970s, the *MCrAlY* (*M = Co*, *Ni*, or both *Co* and *Ni*) overlay coatings were developed, their advantages were:

➢ wider selection of chemical compositions was possible.

➢ superior oxidation or corrosion resistance.

➢ superior ductility.

➢ Improved scale adherence in thermal cycling conditions because of yttrium addition.

Superalloys offer a unique combination of high-temperature strength and oxidation-corrosion resistance. They were developed initially for aero-gas turbines and *MA7S4* (*Ni*-20%, *Cr* containing 0.5% Y_2O_3) was used in turbine stator blades [13,14]. In service, coating degradation occurs by:

➢ progressive loss of *Cr*, *Al* and other protective elements from the surface by oxidation and corrosion processes.

➢ coating/substrate interdiffusion in general results in diffusion of *Al* from the coating into the substrate.

2.3 High temperature corrosion protection of alloy blades with metal and ceramic micro-coatings -*Experimental Studies*

Many interesting studies of thermal protection employing micro-coatings have been communicated in the past few decades. Current technology in thermal barrier coating systems used in gas turbine blade applications relies on the use of a micro-metallic bond coat which as mentioned has two purposes. Firstly, it develops a thin layer of aluminium oxide enhancing the adhesion of the ceramic topcoat. Secondly it furnishes an additional resistance to oxidation. Among the available protective coatings materials, Ni-based alloys deposited by thermal spray are coatings which are widely deployed in industry to increase component resistance against wear, oxidation, and corrosion.

Alternatively, the role of platinum in bond coats of the diffusion-type deposited on a nickel-based superalloy for gas turbines have also been considered. However, many studies have revealed that the actual degradation of gas turbine blades results from *de-bonding* i.e. loss of adhesion of the coatings from the substrate metallic blade at high temperatures.

Echsler *et al.* [15] investigated bond coat oxidation in gas turbine thermal coatings between 950 and 1100 ° C using scanning electron microscopy (SEM), determining maximum crack lengths under long duration. Patnaik *et al.* [16] studied experimentally the oxidation, thermal fatigue (TF) and inter-diffusion in a directionally solidified nickel-based superalloy with a diffusion aluminide coating, noting the propagation of extensive cracks in the coating associated with internal cooling passages along the blade. Many excellent works up to 1989 were reviewed lucidly by Mévrel [17]. Yoshiba [18] reported on high temperature corrosive thermal creep rupture tests for many nickel-base superalloys and several plasma spray coating systems. He considered cases where a ceramic topcoat is present and absent showing significant corrosion-induced creep rupture strength degradation associated with coating bonding defects. Yoshiba *et al.* [19] performed high temperature oxidation and hot corrosion tests at 800 to 1100 °C under isothermal and thermal-cycle conditions for Y_2O_3-stabiIized zirconia (YSZ) and CaO-SiO_2-ZrO_2 (C_2S-CZ) ceramic topped coatings with a focus of failure. They observed that spalling arises more freely in the YSZ-TBC system owing to localized oxidation along the ceramic topcoat/metallic (NiCrAlY) bond coat interface. They also identified important hot corrosion mechanisms and the synthesis of a new phase layer composed of with more corrosive species (oxygen) at the inner region of the ceramic topcoat. Bai *et al.* [20] reported on detailed tests on the resistance of various coatings on superalloy IN-738LC to high temperature oxidation and corrosion. They showed that at temperatures exceeding 850 °C, aluminized–chromized coating layers *are most easily compromised* against oxidation and that this is attributable to the spalling or cracking of the oxide scales. However,

the aluminized coatings were found to produce better protection under hot corrosion conditions compared with siliconized coatings which exhibit excessive brittle fracture caused by thermal shock and are inadequate for superalloy IN-738-LC. Koo *et al.* [21] also investigated coating behaviour during high temperature oxidation and hot corrosion of superalloy IN-738LC with three aluminized coatings (simple aluminized, Rh-electroplated aluminized and Pd-electroplated aluminized coatings) also conducting Vickers hardness tests (for micro-hardness). They found that Rh-plated aluminized performs the best followed by simple aluminized, Pd-plated aluminized, and uncoated superalloy IN-738LC samples. Sumner *et al.* [22], conducted careful experiments to study the influence of fly ash, gas moisture and high gas temperatures on the alkali sulphate induced hot corrosion of CM247LC, Haynes 230, IN939 and IN728LC gas turbine super alloys. They identified Type I (sulphidation and internal damage), type II (pitting) and mixed mode hot corrosion under different thermal loadings and furthermore that hot corrosion damage is decreased with the presence of fly ash. Higher chromium content alloys were observed to achieve better resilience compared with high Aluminum content CM247LC super alloys and showed better oxidation resistance. Oska *et al.* [23] investigated the performance of thermal spray NiCr (51Ni-46Cr-2Si-1Fe) and FeCr (Fe-19Cr-9W-7Nb-4Mo-5B-2C-2Si-1Mn) powders on gas turbine blades using HVOFGF (gas-fuelled) and HVOFLF (liquid-fueled) systems under high temperature corrosion conditions. Khan *et al.* [24] described corrosion kinetics, surface morphology and X-ray analysis of Inconel 617 super alloy under high temperatures. They observed that V_2O_5 component in the salt mixture exerts a significant role in corrosion degradation of the super alloy and accelerates hot corrosion effects and that better protection is achieved with lower concentrations.

The above studies generally confirmed that *chemical constitution* of the super alloy and thermal insulation capability of the micro-coatings both have a critical role in the impact of hot corrosion on long-term gas turbine blade performance. Ceramics tend to perform quite well;

however, they are prone to *fracture and delamination*. Thermal mismatch stress within the coatings can be elevated if bonding is not sustained. There is evidently a balance between the thermal insulation capability and thermal stress level and a crucial engineering task is to accurately determine the optimum thermal coating thickness. This presents an on-going challenge for corrosion engineers which can be greatly assisted with numerical simulation. Computational mechanics provides a safe, easily controlled, relatively inexpensive methodology for mimicking realistic high temperature corrosion conditions and evaluating the thermal barrier coating (TBC) protection performance of an unlimited number of *micro-coating* materials for super alloys. This can therefore allow protective layers to be optimized in the design process and therefore improve the efficiency of gas turbine blade systems. Although the conventional TBC system is composed of a load carrying substrate, a ceramic topcoat (TC), a metallic bond-coat (BC), and the thermally grown oxide (TGO) that forms between TC and BC, modifications to these structures can be easily attained with computational simulation. Of course, data must be extracted from actual tests and material properties must be representative of high thermal conditions. A dilemma faces modern gas turbine designers. Sustaining coating integrity for a TBC is more problematic than pure metallic coatings due to the considerable transition in properties from the metallic substrate to the ceramic coating. This issue is further amplified since TBCs attain the greatest efficiency benefit at the highest operating temperatures, where TBC failure is most likely to cause unacceptable component damage. Thus, while coatings with even lower conductivity may be possible the high variability of TBC thermal cycle life implies that the implementation of these coatings to their full potential will depend on their susceptibility to failure.

In the studies reviewed above, experimental testing has been demonstrated to be a critical technique for establishing the quality and efficacy of coatings for high temperature applications.

However, the literature review conducted in this PhD has clearly shown that the specific coating material combination of a titanium layer with a superposed ceramic (Silicon carbide) layer i.e. double-layer micro-coating, has not been addressed anywhere previously. This novel metal-ceramic coating combination has therefore been identified as an alternative thermal barrier coating material design and is addressed experimentally in chapter 5 and computationally in chapter 6.

2.4 High temperature corrosion protection with nano-coatings - *experimental studies*

Nanomaterials have emerged as a major development in 21st century engineering. They include many different types of nanostructures, which are engineered at the nanoscale (1-100nm) i.e. one thousandth of the scale of micro-materials. Representative examples are carbon nanotubes, metallic nanoparticles, nanowires, nano-shells and many other configurations which may be embedded within existing materials (metals, ceramics) or deposited as external coatings. Examples of nanomaterials in aerospace are shown in **Figure 2.7**. Nanomaterials are engineered from a variety of products, such as carbon or metals (copper, silver, zinc etc) but nanomaterials, by definition, must have at least one dimension that is less than approximately 100 nanometers. Most nanoscale materials are too small to be seen with the naked eye and even with conventional lab microscopes.
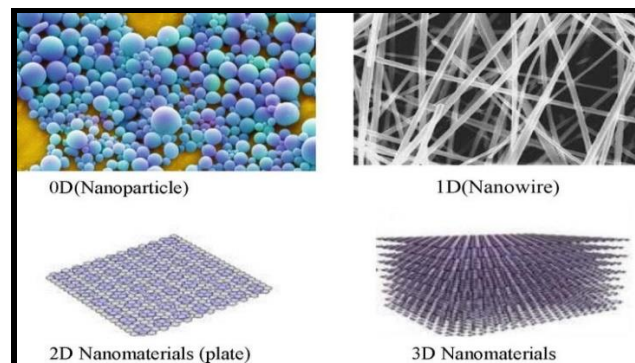
Figure 2.7: Nanomaterials used in coatings [courtesy UCLA Nanoscience Institute, USA].

Nano-engineered structures possess superior properties including enhanced thermal and electrical conductivity, superior tensile strength, enhanced resistance to corrosion and wear, self-sensing, self-healing properties, as well as high strength to weight ratios [25]. Nanomaterials are increasingly being deployed in numerous engineering applications owing to their unique mechanical properties, including high strength-to-weight ratio, excellent electrical and thermal conductivity and high aspect ratios. Both carbon-based and metallic nanoparticles have been explored extensively. They provide enhanced protection in extreme loading situations including high temperature propulsion (gas turbines), roller coaster shock absorbers, marine chassis structures, aircraft wings, rail tracks etc. Nano-powders comprising various metallic oxides or silicates can be successfully deposited surfacially on structures using thermal spray technologies. This enables *complete surface coating* of structural elements.

With the tremendous potential of nano-structured materials, nano-coatings comprising mixtures of nanoparticles (carbon and/or metallic) bonded more carefully to the substrate may achieve enhanced protection.

Since nanomaterials are engineered at the nanoscale and cracks generally propagate at the *micro-scale*, the use of nano-coatings may achieve better protection preventing hot corrosive gases from penetrating coatings and damaging the steel substrate which constitutes the blade. In recent years therefore a number of studies have emerged which focus on nano-coating performance under various temperature regimes spanning a range of technological applications, including high temperature corrosion.

Several studies of the improved mechanical performance of coated structures with nanomaterials have been communicated in recent years. Islam *et al.* [26] used electrochemical impedance spectroscopy (EIS) to investigate the contribution of SiO_2 nanoparticles on hardness and corrosion resistance of electroless Ni–P coatings. They showed that although pure medium-

and high-P coatings achieve a satisfactory corrosion protection, their performance attributes are greatly elevated through incorporation of silica (SiO_2) nanoparticles. Overall, the SiO_2 nanoparticles improve the deposit morphology via grain structure modification, decrease in the surface roughness and minimization of surface porosity in the nanocomposite coatings which produce greater micro hardness and wear resistance. Ghazali *et al.* [27] studied the corrosion inhibition behaviour of super-amphiphobic coating using functionalized aluminium oxide nanoparticles. Arihwar *et al.* [28] have explored the reduction of degradation in biomaterial coating with titanium and zinc oxide nano-powders. Sana *et al.* [29] used a sol–gel method to investigate the effect of TiO_2-containing nano-coatings on the color protection of heat-treated materials. Dastmalchian [30] deployed electrochemical impedance spectroscopy to evaluate the corrosion performances of nano-coatings (featuring nano-silica i.e., hydrophilic Aerosol3 200 and hydrophobic aerosol R805) applied onto mild steel substrates that were immersed in 3.5% (w/w) NaCl solutions. It was observed that coatings which contained nano-silica *increased the barrier properties* of the binder, as well as the coatings' electrochemical resistance compared with pure polyurethane coatings. Vereschaka *et al.* [31] examined the influence of thickness of multi-layered nano-structured coatings Ti-TiN-(TiCrAl)N and Zr-ZrN-(ZrCrNbAl)N on wear and thermal degradation of metal cutting tools at various cutting speeds. Wang *et al.* [32] investigated the improvement in oxidation of Ti_3SiC_2 coating surface to improve its wear resistance by producing oxide layers and healing microcracks that initiated from the thermal sprayed process. They observed that the thickness of the oxide layer and the average content of oxygen on the surface were gradually increased with increasing temperature with a significant improvement in crack-healing features at higher temperatures (in excess of 400 °C). They further noted that delamination and abrasive wear are the principal features controlling the tribological behaviour of thermal oxidation treated Ti_3SiC_2 coatings. Zhu *et al.* [33] employed a laser cladding technique to investigate high temperature corrosion protection

of Hastelloy-N alloy in LiF-NaF-KF (ternary eutectic alkaline metal fluoride salt mixture, commonly referred to as FLiNaK) molten salt using an amalgamation of pure Ni and Co coatings using the immersion experiments with samples was performed in molten FLiNaK salt at 900 °C for 100 hours showed that the *corrosion rates* of the pure Ni-coated specimen and the pure Co-coated specimen were approximately 40% and 36% of that of Hastelloy-N alloy, respectively. Significant intergranular corrosion was observed due to a selective dissolution of the elemental Cr occurred on the surface of bare Hastelloy-N alloy. Furthermore, dense pure metal (Ni or Co) coatings showed lesser corrosion and achieved improved protection of the Hastelloy-N substrate. Swaminathan *et al.* [34] studied the performance of hard erosion resistant nano-coatings in mitigating solid particle erosion (SPE) and liquid droplet erosion (LDE) on gas turbine. They employed plasma enhanced magnetron sputtering method to apply different nano-material coatings (up to 30μm thickness) on various substrates and showed that the best protection is achieved with coatings comprising nanostructured titanium silicon carbonitride (TiSiCN), titanium nitride (TiN), and multi-layered nano-coatings. They also showed that these nano-coatings produce a significant elevation in erosion resistance by a factor of 20 over the bare substrate and also enhance markedly the high-cycle fatigue strength at zero and high mean stresses. Sudagar *et al*. [35] investigated the performance of nano-coatings for electroless nickel alloy, composite and described the benefits of nano plating, bath techniques, preparation, characterization and new depositing mechanisms for high temperature corrosion protection. Karthikeyan and Ramamoorthy [36] studied experimentally using X-ray diffraction the formation and characteristics of electroless nickel phosphorous (Ni–P) nano-coatings and electroless nickel phosphorous alumina (Ni–P–Al_2O_3) coating with varying reducing agent concentration, showing that corrosion deposition rate and surface roughness of both coatings are greatly modified by reducing agent (sodium hypophosphite). They also found that a composite coating is produced as a result of the embedding of nano

alumina in the Ni–P coating and this enhances the coating hardness and mitigates high temperature corrosive penetration. Guo *et al*. [37] conducted detailed tests on the high-temperature corrosion behaviour of plasma sprayed nanostructured $Gd_2Zr_2O_7$-$LaPO_4$ thermal barrier coatings for gas turbine applications. They considered a 900 Celsius temperature for four-hour periods and observed that the coatings exhibited exceptional hot corrosion resistance and achieved better performance in V_2O_5 salt which was attributed to the generation of a reaction layer and the nanostructure produced with nano-particles which mitigates crack formation and subsequent hot corrosive gas penetration through the thermal barrier coatings. Li *et al.* [38] using air plasma spraying to fabricate nanostructured 30 mol% $LaPO_4$ doped $Gd_2Zr_2O_7$ ($Gd_2Zr_2O_7$-$LaPO_4$) thermal barrier coatings (TBCs). The coatings consist of $Gd_2Zr_2O_7$ and $LaPO_4$ phases, with desirable chemical composition and *nano-material* zones embedded in the coating microstructure. Calcium-magnesium-alumina-silicate (CMAS) corrosion tests were carried out at 1250 °C for up to 8 hours to examine corrosion resistance and it was shown that *nanostructured* $Gd_2Zr_2O_7$-$LaPO_4$ coatings attain very impressive high resistance to corrosive penetration. Lima and Marple [39] investigated the performance of nanostructured YSZ (zirconia–8 wt% yttria) thermal barrier coatings engineered to counteract sintering effects in the hot sections of gas turbines. They showed that sintering could significantly increase the thermal diffusivity/conductivity and elastic modulus values of these types of coatings in high temperature environments. Both nanostructured and conventional YSZ coatings were heat-treated at 1400 °C for 1, 5 and 20 hrs. It was found that the nanostructured coatings counteract sintering effects, due to the presence of a bimodal microstructure exhibiting regions with different sintering rates: (i) matrix (low rate) and (ii) nano zones (high rate). The thermal diffusivity and elastic modulus values of the nanostructured YSZ coatings were also shown to be substantially decreased compared to conventional YSZ coatings, even after an exposure to a temperature of 1400 °C for 20 hrs.

Overall the nanostructured YSZ coatings were found to achieve improved performance in high temperature environments when compared to those of conventional YSZ coatings. Zhou and Yu [40] also studied the response of thermal spray zirconia–8 wt% yttria (YSZ) deposits employed as thermal barrier coatings (TBCs) in the hot sections of gas turbines, showing that the nanostructured TBC exhibits promising thermal cyclic oxidation resistance. Dahotre and Nayak [41] considered many aspects of nano-coatings engineered for high temperature applications including amenability for honing, surface roughness and topography, residual stress, adherence, damage tolerance and resistance, tribological properties, lubrication, coefficient of friction and hot hardness. They noted that nano-grains of a crystalline phase can overcome many of the problems associated with conventional coatings produced with standard techniques e.g. chemical-vapor-deposited diamond-like carbon (DLC) coating, plasma sprayed metal matrix composite coating, tribologically functional ceramic coatings, etc. Gell [42] described major improvements and increase in strength and hardness combined with toughness and ductility, enhanced diffusivity and reduced thermal conductivity achieved with nano-structured materials for gas turbine thermal barrier coatings. These studies have generally shown that for nano-coatings to be useful in gas turbine engine applications, a coating thickness of at least 1 mil (25 microns) is required and preferably at least 3 mils (75 microns) is required. Therefore, while the *nanoscale particles are much smaller than microscale particles, the thickness of the nanocoating must be approximately the same as the micro-coating*. Promising nano-structured ceramic materials for gas turbine thermal protection include alumina (Al_2O_3) and titanium oxide (TiO_2). Such nano-structured materials share the common attribute in that they all have a relatively high co-efficient of thermal expansion which makes them more suitable for application to metallic substrates than other ceramic materials which have lower coefficients of thermal expansion. Additionally, titanium oxide as the other component of the

nano-structured coating has the advantage of an exceptionally high melting point and thermal resistance.

The literature review conducted above has shown that while considerable work has been reported on many different metal oxide nano-materials and also stabilized zirconia (e.g. yttria stabilized zirconia (ZrO_2 plus Y_2O_3)) and ceria (CeO_2) nanoparticles for nano-coatings, *relatively sparse work has been reported for combined flame sprayed mixes of alumina*

($Al_2 O_3$)60% and titanium oxide (TiO_2)40% nano-powder coatings.

This has motivated the consideration of combined alumina ($Al_2 O_3$) and titanium oxide (TiO_2) nano-powder mix nano-coatings, for the first time, which is also addressed in chapter 5 (experimental) and chapter 6 (numerical) where different percentage mixes of this composite nano-coating are considered.

2.5 Mathematical/Computer Modelling Approaches for High Temperature Corrosion

Over the past two decades numerous approaches have been developed for simulating various aspects of high-temperature corrosion. These include continuum-based (mechanics) methods (FEM, DEM), molecular methods (Molecular Dynamics MD) and chemical analysis tools (e. g. NOVA, CALPHAD). The quality of results achieved is strongly linked to the quality of data available and the numerical algorithm capability as well as hardware specifications.
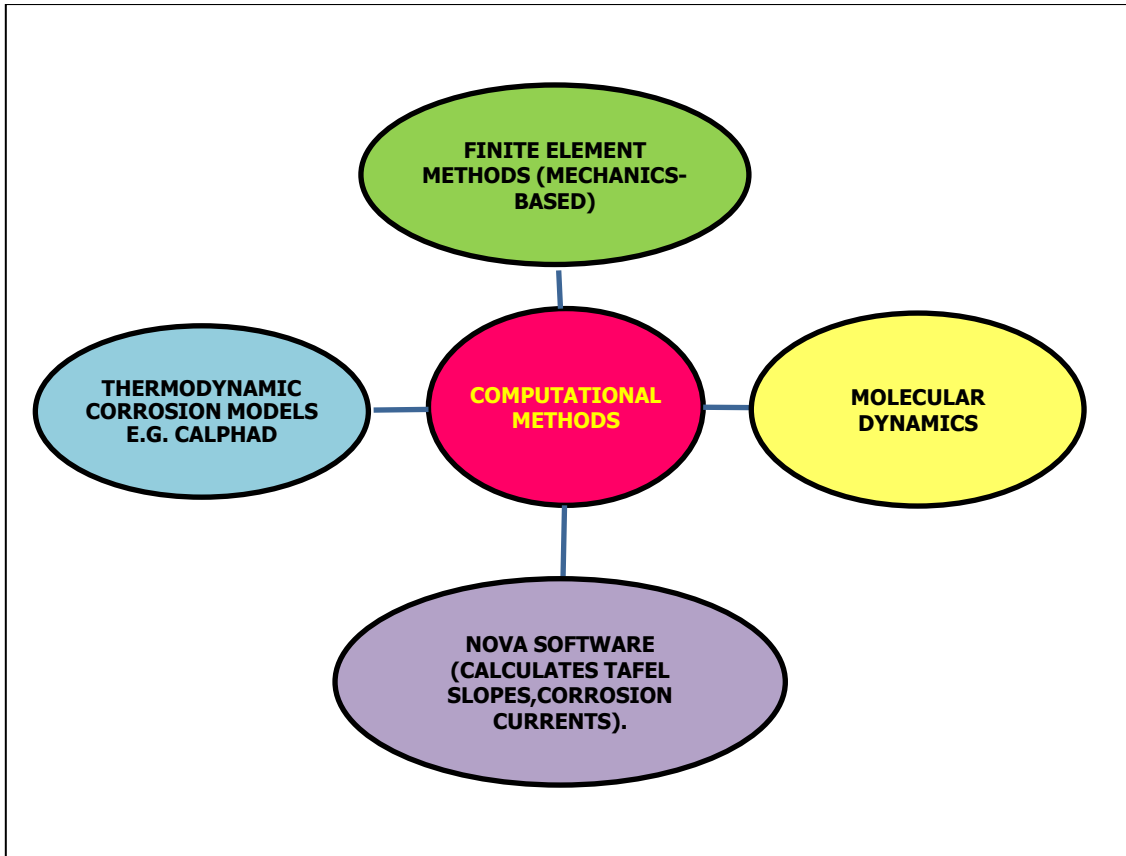
Figure 2.8: Key numerical approaches for high temperature corrosion (HTC) analysis.

Figure 2.8 summarizes some of the different *computational simulation methodologies* available for corrosion analysis.

2.5-1 Thermodynamic Corrosion Models

The corrosion of materials is often a life limiting process that affects almost all materials. It is expensive, both in terms of the potential tremendous economic costs that can arise from unexpected failures, environmental damage and so forth, but also the high cost of maintenance and repair associated with the life extension of plant equipment and service. Material scientists and engineers often have to conduct many expensive and time-consuming corrosion experiments to fully qualify a material or design more corrosion resistant ones. Corrosion is a kinetic process that is driven by the underlying thermodynamics of a system that is a material in a given environment. Thermodynamic investigation of corrosion under various

environments is extremely important for efficient design and production of high-quality materials, for advanced processing of corrosion-resistant coatings, for optimal performance of commercial materials in industrial, environmental, medical and military applications and for environmental protections and safety assessments. A number of thermodynamic simulation tools have been developed for corrosion analysis among which probably the Swedish software, **CALPHAD** (Computer Coupling of Phase Diagrams and Thermochemistry) [43] is the best. It was founded in 1969 at the Royal Institute of Technology in Stockholm, Sweden. In the CALPHAD method, the corrosion engineer collects and assesses all available experimental and theoretical information available on phase equilibria and thermochemical properties in a system. The thermodynamic properties of each phase are then described through the Gibbs free energy, applying a mathematical model containing adjustable parameters. These parameters are evaluated by optimizing the fit of the model to all the assessed information, also involving coexisting phases. Following this it is possible to recalculate the phase diagram, as well as the thermodynamic properties of all the phases and the system as a whole. The philosophy of the CALPHAD method is to obtain a consistent description of the phase diagram and the thermodynamic properties so as to reliably predict the set of stable phases and their thermodynamic properties in regions without experimental information and for metastable states during simulations of phase transformations. This approach is also part of the future pathways described in **Chapter 7.**

2.5-2   Numerical Mass Diffusion Models

Generally, the driving force of high-temperature corrosion processes can be separated into (*i*) transport mechanisms, *i.e.*, solid-state diffusion, and (*ii*) thermodynamics of chemical reactions. The commonly used, phenomenological way to treat diffusion processes is the application of a second-order partial differential equation (Fick's 2nd law) formulating a

relationship between the derivative of the concentration of a species c after the time t and its gradient by means of the location- and temperature-dependent mass diffusion coefficient D. The use of analytical solutions for the corrosion diffusion equation to describe the corrosion phenomena in complex situations is widely limited. Therefore, numerical techniques, e.g. the *finite-difference method* are required, which have the advantage that the concentrations of the species can be calculated in discrete steps of time and location. This approach can also incorporate computational thermodynamics in each of the discrete steps. The basic idea of the finite-difference method to solve partial differential equations is to replace spatial and time derivatives by suitable approximations and then to numerically solve the resulting difference equations. The basic idea of the finite-difference method to solve partial differential equations is to replace *spatial and time derivatives* by suitable approximations and then to numerically solve the resulting difference equations. For separation of diffusion along grain boundaries from that in the bulk, a two-dimensional calculation is required. In this case, the diffusion coefficient D is treated as a matrix containing the diffusion coefficients of the diffusing species as a function of the position x and y. This allows to change the diffusion coefficient locally, e.g., along grain boundaries. The *non-Fickian* differential equation is solved for all species participating in the corrosion process and stepwise for the complete reaction time using the commercial simulation environment MATLAB (simplified for one-dimensional diffusion). To account for possible chemical reactions of the ongoing corrosion process, the calculated concentrations at c must be corrected according to the local thermodynamic equilibrium. This becomes possible by transferring the concentration c into the thermodynamic subroutine ChemApp. ChemApp [44] is a thermochemical software based on a numerical Gibbs' energy minimization routine in combination with tailor-made data bases. The excessive computation time has to be greatly reduced and this can be easily achieved with a parallel computing system PVM (parallel virtual machine). Using this computation methodology, the thermodynamic

equilibrium calculations are distributed to individual "thermodynamic workers ". On the surface of the low-Cr ferritic steels a thick oxide scale was formed following the *parabolic rate law kinetics* (also adopted in Chapter 5 for experimental TGA analysis of both micro-coatings and nano-coatings), which is strongly dependent on the microstructure (grain size) of the alloy. A number of studies [10, 13] have shown that this oxide scale is composed of two layers - an outer layer of magnetite (Fe_3O_4) and hematite (Fe_2O_3), which grows by outwards diffusion of iron and an inner layer of spinel ($Fe-Fe_{2-x}Cr_xO_4$) with stoichiometry varying from x=0 (pure magnetite – Fe_3O_4) up to x=2 (normal spinel – $FeCr_2O_4$). The growth of the inner layer is determined by fast diffusion of oxygen along alloy grain boundaries resulting in an intergranular oxidation mechanism. The application of the developed simulation tool to the oxidation of low-Cr steels is demonstrated by ChemApp calculations of the inner oxide scale growth. To account for the inter-crystalline oxidation mechanism, the diffusion of oxygen and chromium along alloy grain boundaries can be separated from that in the bulk [44].

2.5-3   Finite Element Mechanics Codes

So far, thermodynamic and non-Fickian mass diffusion corrosion software have been reviewed. These approaches yield important information on the corrosion aspects; however, they do not provide information on the *structural degradation* of the coatings or super alloys under high temperature in gas turbine blade applications. In order to gain an insight into this commercial *finite element codes* are required. From the viewpoint of super-alloy coatings, without doubt the most practicable approach is *finite element analysis (FEA)*. This technique is therefore adopted in this PhD (chapter 6) as it permits actual *thermo mechanical behaviour* prediction as opposed to simpler methods which only address corrosion chemistry or chemical effects in isolation from the structural mechanics. FEA allows full control of specifying geometries, material properties, loading conditions and provides a seamless facility for interfacing thermal

and structural deformation and full theoretical details are given in Chapter 3. However, FEA cannot currently also accommodate the thermo-fluid-structural interaction simultaneously with corroding surfaces via chemical reaction models. Many commercial FEM codes have been developed which are applicable to various aspects of HTC stress analysis and these are summarized in **Figure 2.9**.
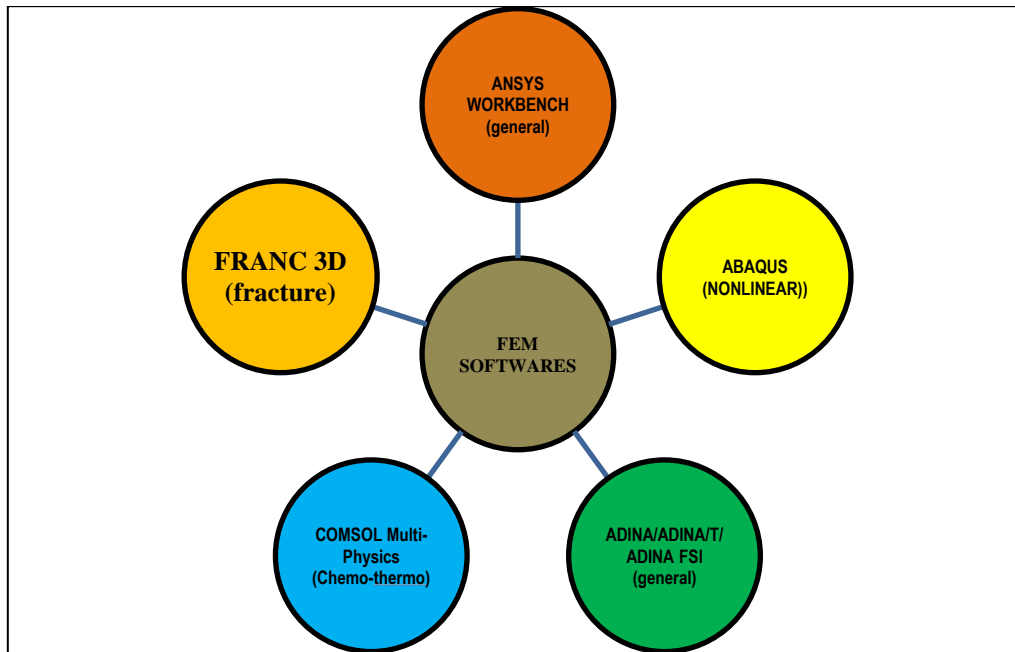
Figure 2.9: Computational finite element commercial software for high temperature

Corrosion.

FEA solvers permit complex geometrical models to be constructed and furthermore also allow the simultaneous analysis of thermal, stress and flow fields. Significant work has been conducted in for example Magnesium alloy high temperature corrosion thermal stress analysis with these FEM packages. Grogan *et al.* [45] developed a physical corrosion model based on finite element (FE) technique for predicting mechanical strength of corroded metal stents. The developed model was able to capture the change in surface due to corroding environment. Duddu *et al.* [46] developed an extended FE model for modeling galvanic corrosion in magnesium alloys showing that this approach can be used to model crevice geometry without

remeshing. Shang *et al.* [47] deployed molecular dynamic simulations to study the adsorption behavior of composite coatings on Mg alloys.

2.5-4 Molecular, Neural and Other Computational Approaches

Generally, all the computational approaches described earlier considered have been deterministic i.e. they have not used statistical or adaptive methods simulation techniques. Modern developments in high performance computing have enabled particle methods to become realistic alternatives to traditional methods. These include molecular dynamics (MD), Monte Carlo simulation (MCS), discrete element methods (DEMs), neural network (genetic) models and so on. Molecular dynamics has been recently deployed to investigate high temperature corrosion of metals in gas turbine systems by Haris *et al.* [48]. Particle-based computer methods are in fact the future of high temperature corrosion simulation and in particular can simulate comfortably multi-functional surfaces (intelligent thermal barrier coatings, adaptive protection systems, smart coatings, nano-coatings etc.). However, they require massive computational hardware resources and are therefore not explored in this PhD.

It is apparent, therefore, from the above literature that the current state-of-the-art in scientific modeling of corrosion is directed at two fronts, viz. *mechanical and chemical models*. These models are capable of generating accurate solutions in predicting either thermal stress/deformation corrosion characteristics *or* thermo-chemical corrosion rates. However, the computational approach adopted in this PhD is finite element thermal stress (and CFD) modelling as it has the advantages of good accuracy, simultaneous consideration of thermal and stress and flow effects and the ability to accommodate complex geometries and does not require high performance computing facilities. Having selected finite element analysis (ANSYS mechanical and ANSYS FLUENT) as the primary modelling tool for this PhD, here

relevant works where this approach has been applied are now reviewed. In the next sub-section, *micro-coating* finite element simulation studies are reviewed first. Following this, *nano-coating finite element and CFD flow simulations* are reviewed.

2.6 Finite element and CFD numerical studies of high temperature corrosion protection with ceramic *micro-coatings*

Bäker [49] presented detailed two-dimensional finite element simulations of crack initiation and propagation at the interface between the TGO and the TBC in thermal barrier micro-coatings. He showed that cracks in the peak position propagate in mode II for cases where even with TGO thickness is small and achieve lower stress relaxation than valley cracks. Chen [50] examined the influence of Foreign Object Damage (FOD) and mechanical erosion in failure analysis of thermal barrier coatings, using a novel impact scaling analysis and a moving finite element method. He studied in detail the effects of particle size, velocity, temperature, and TBC composition and showed that *transient stresses* mobilize the propagation of cracks whereas residual stresses dictate the delamination of the coating. Yang *et al.* [51] investigated with finite element analysis the cyclic high thermal loading effects on ceramic coated turbine blades, identifying critical zones using the maximum principal stress criterion and showing that with sustained excessive thermal stresses there is significant reduction in thermal fatigue life. Mohamed [52] employed ABAQUS finite element software to simulate thermal coating performance with four approaches, namely TGO thickness computation, elasticity and creep effect analysis, a coupled oxidation constitutive approach and fracture mechanics. He evaluated the local von Mises stress distribution on each of the three layers of the coating, validating against previous experimental results. Fan *et al.* [53] examined the double-ceramic-layer (DCL) thermal coating system using a virtual crack closure interfacial element method, computing energy release rates for interfacial delamination. They conducted a parametric investigation of geometrical and material parameter influence and showed that it is possible to

determine an optimal thickness ratio of outer to inner ceramic layers. They further showed that local separation between two ceramic layers facilitates the onset of delamination and assists in it spreading at the inner coating and lower layer interface. Xu *et al.* [54] presented detailed simulations aimed at establishing the contribution of mixed oxides on structural integrity and interfacial failure mechanisms in a thermal barrier coating system, observing that large mixed oxide growth rates encourage the synthesis and subsequent propagation of interface cracks leading to ceramic coating de-bonding. Gupta *et al.* [55] described both experimental (laser flash tests) and finite element computations focused on elucidating the performance of zirconia coatings in thermal protection of gas turbine components. They found that low thermal conductivity coatings achieve greater resistance when large globular pores and connected cracks within the coating microstructure are present. Busso *et al.* [56] considered the effect of the oxidation induced degradation of a plasma-sprayed thermal barrier coating (PS-TBC) system on the local ceramic–metal interfacial stresses using a parametric unit cell finite element code. They noted that local morphology of the oxidized interface, sintering of the ceramic coating, stress relaxation effects due to creep and the thickness of the thermally grown oxide (of the order of micrometers) all contribute substantially to the local stresses responsible for mesoscopic crack nucleation and growth. These studies were confined to thermo-mechanical stress analysis and did not consider the corrosive gas environment. To simulate the total thermo-structural and fluid dynamics problem, a CFD approach is generally required. The temperature field generated by computational flow simulation provides a more accurate thermal loading input for the coatings. Zhu *et al*. [57] were among the first researchers to employ a coupled thermal stress and thermofluid simulation in high temperature gas turbine corrosion analysis. They employed a three-dimensional finite element model of multi-layered coated turbine blade with a conjugate heat transfer analysis and decoupled thermal-stress computation procedure. They computed the thermal flow field impinging on the coating with

three turbulence models (RNG k-ε, realizable k-ε and SST k-ω model), obtaining the best correlation with experimental high temperature data for temperature and pressure distribution with the realizable k-ε turbulence model. Their simulations succinctly demonstrated that improved thermal protection (insulation performance) is achieved at the blade leading and trailing edges, that specific danger zones susceptible to failure exist and that greater stress levels are induced in the ceramic layer relative to the bond coating (leading to possible spalling). Tang *et al.* [58] performed a similar analysis to [57] although they considered a non-uniform temperature distribution along the blade surface and evaluated a leading-edge (where the gas flow first hits the blade curved surface and the boundary layer growth starts) temperature reaching 1030 °Celsius. They further computed a peak stress of 3.75 GPa located at the centre of the blade suction face for thermally grown oxide (TGO) and a maximum compressive stress of −3.5 GPa at the leading edge in the cooling stage (a cause of potential failure). Sadowski and Golewski [59] conducted coupled CFD and transient thermal stress analysis in unprotected and thermal barrier coated alloy Inconel 713 up to 1000 °Celsius with 0.5mm deep coatings. They used ANSYS Fluent code to compute the pressure and thermal fields induced by the combustion gas and ABAQUS to simulate the resulting thermo-structural behaviour in the coated blade. It is noteworthy however that *none of these studies have considered finite element thermal stress behaviour of titanium- silicon carbide micro-coatings nor erosion CFD analysis*. This has identified very strong novelty therefore for the simulations which are described in Chapter 6.

2.7 Finite element studies of high temperature corrosion protection with *nano-coatings*

Nano-coatings, which have been shown to achieve exceptional improvement in resistance to deformation and surfacial damage [34]. While a number of researchers have investigated nanomaterial reinforced structures, *very little work has been communicated on high temperature nano-coating* (using *metallic nano-powder mix*) finite element simulations.

Carbon nanotube (CNT)-reinforced plate structures (as a model of e.g. a blade substrate) have been studied however by several investigators. Zhu *et al.* [60] simulated the bending and vibration of thin-to-moderately thick composite plates reinforced by single-walled carbon nanotubes using ANSYS software. They employed first order shear deformation plate theory and explored a variety of distributions of the uniaxially aligned reinforcement material. Malekzadeh and Shojaee [61] deployed a mapping-differential quadrature technique to model the elastic stability of quadrilateral laminated thin-to-moderately thick plates composed of perfectly bonded carbon nanotube reinforced composite (CNTRC) layers. They explored in detail the the influence of volume fraction of carbon nanotubes (CNTs), geometrical shape parameters, thickness-to-length ratio, different kinds of CNTs distribution along the layers thickness and boundary conditions. Lei *et al.* [62] utilized an element-free kp-Ritz method to investigate the bending stresses in laminated CNT reinforced functionally graded plates. They determined the effective material properties of the laminated nanocomposite plates using an extended rule of mixtures. Other finite element investigations of carbon nanotube reinforced structures under high temperature have been presented by Alibeigloo and Liew [63] and Shen and Xiang [64]. However, none of the above studies considered *nano-powder deposited coatings* on plate structures (gas turbine specimens). Very sparse work has been communicated on 3-dimensional static stress analysis of nano-coated plate structures using nano-powder sprayed materials. Nano-structured thermal barrier coatings (TBCs) using *metallic oxide nano-powder mixes* are intended to operate as an improved temperature-resistance material (superior to micro-coating) since they also possess thermal conductivity which reduces the transfer of heat to the substrate but provide better integrity under high temperature combatting the penetration of hot gases and cracks due to corrosive effects. Several investigators have recently investigated metallic/ceramic nano-coatings for corrosion protection with finite element analysis. Ashok *et al.* [65] studied using ANSYS software the thermal behaviour of Yttrium

stabilised Zirconia nano-coatings for fatigue and corrosion protection in gas turbine blades. They showed that the nano-coating material has a higher efficiency in insulating the temperature, at high temperature working conditions and strongly reduces thermal stresses compared with conventional micro-coatings or thermally grown oxides (TGO). They also showed that a 5μm top coat which is ceramic coating made up of nanoscale Yttrium stabilised Zirconia insulates the major temperature from entering to the substrate and this is the main reason for the protection of the substrate from degrading at a faster rate. Abbas *et al.* [66] used ANSYS software to also investigate nanostructured yttria stabilized zirconia (YSZ) thermal barrier coating systems (TBCs), also considering varying thickness of the thermally grown oxide (TGO). They computed radial, axial and shear stresses and also elastic strain energy for TGO failure assessment from calculated stresses within the TGO for varying thickness. Radial stresses at TGO/bond coat interface and maximum axial stresses in nanostructured zirconia coatings were shown to be lower than in traditional YSZ up to a critical TGO thickness of 6 – 7μm, after which stresses in nanostructured zirconia coatings increased considerably. However, radial compressive stresses in nanostructured TBCs were significantly lower in all TGO thickness cases and shear stresses were slightly higher in particular for high oxide thickness. Clearly therefore no research has been conducted on *metallic nano-coated gas turbine blades in high temperature* and in particular *alumina/titania mix nano-powder coatings* have never been studied computationally anywhere in the literature. This confirms the novelty of the approach used in this PhD in chapter 6 where, for the first time, *both elastostatic and thermal stress finite element models are described for alumina/titania nano-coatings*, to simulate the actual experiments conducted in Chapter 5 on nano-coated blade specimens.

2.8 Thermal Spray Techniques

Thermal spray coating is a technique used for applying a protective surface layer via special equipment or systems in which the melted material or molten spray material, either in powder or wire form, is propelled at high speed on to a cleaned and prepared substrate surface. **Figures 2.10-2.12** show examples of thermal spray methods, coating materials and thickness characteristics of thermal spray respectively.
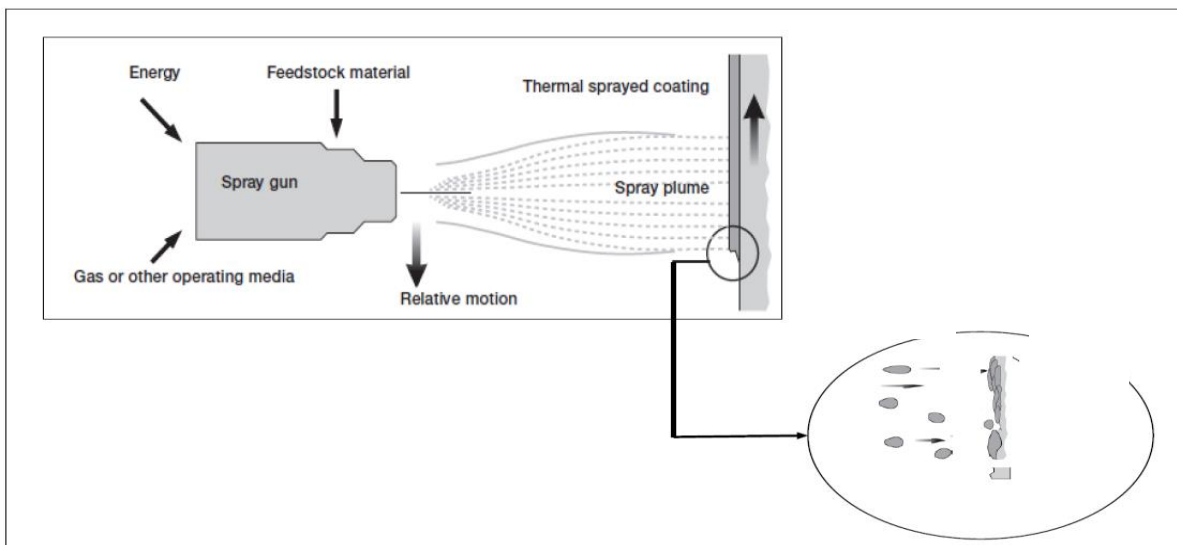
Figure 2.10: Thermal Spraying Method (Source: Sulzer).
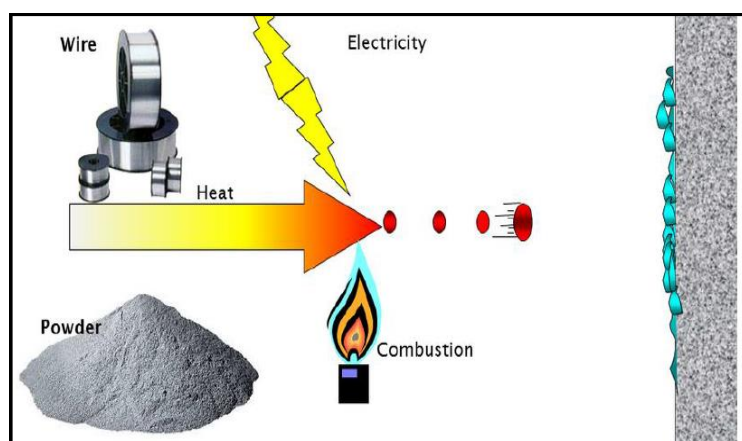
Figure 2.11: Thermal Spray diagram (Source NASA)
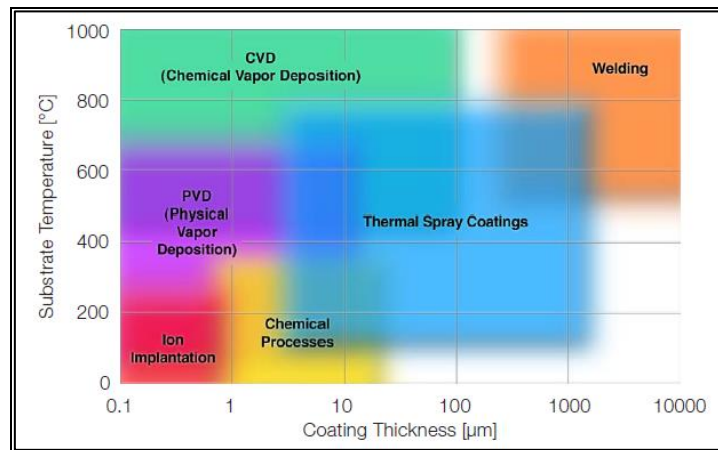
Figure 2.12: Coating materials, coating thickness and characteristics of Thermal Spray (Source: Sulzer).

The methods and apparatus used for thermal spraying are:

      (a) Flame spraying which is divided into

            (i) Wire Flame spraying

            (ii) Powder flame spraying

      (b) Plasma Arc spray

      (c) High Velocity oxy-fuel spray (HVOF)

      (d) Thermal Spraying Gun with selected work condition

The substrate materials before spraying must be grit blasted to roughen its surface and cleaned with ultrasound machine to have the mechanical bonding with the coated material.

(a)   **Flame Spraying**

(i) Wire Flame Spraying

The primary function of the flame is to melt the inserted material(wire). A stream of air then atomizes the molten material and directs towards the specimen. The spray rate for the material such as steel is 0.5-9kg/hr at a temperature of 4000^0C. The process of the spraying is shown in **Figure 2.13**.
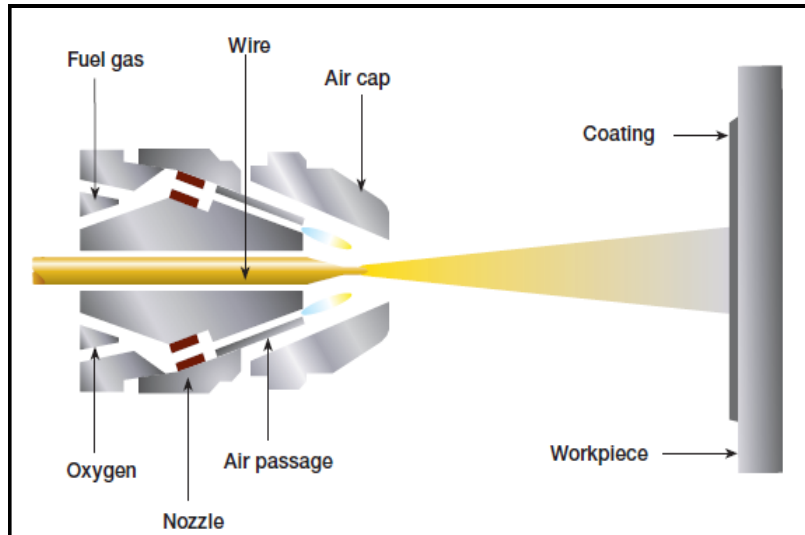
Figure 2.13: Schematic diagram of the wire flame process (Source: Sulzer).

(ii) Powder Flame Spraying

The coating technique is identical in principles to the wire flame spraying except that the coating material used is in powder form. Use of powder is more popular than wire, because combined materials can be mixed in different percentages. Porosity can be and adhesion is generally lower. Spray rate is 0.5-9 kg/hr at a temperature of 3000 ^{0}C. The process powder flame is shown in **Figure 2.14**.
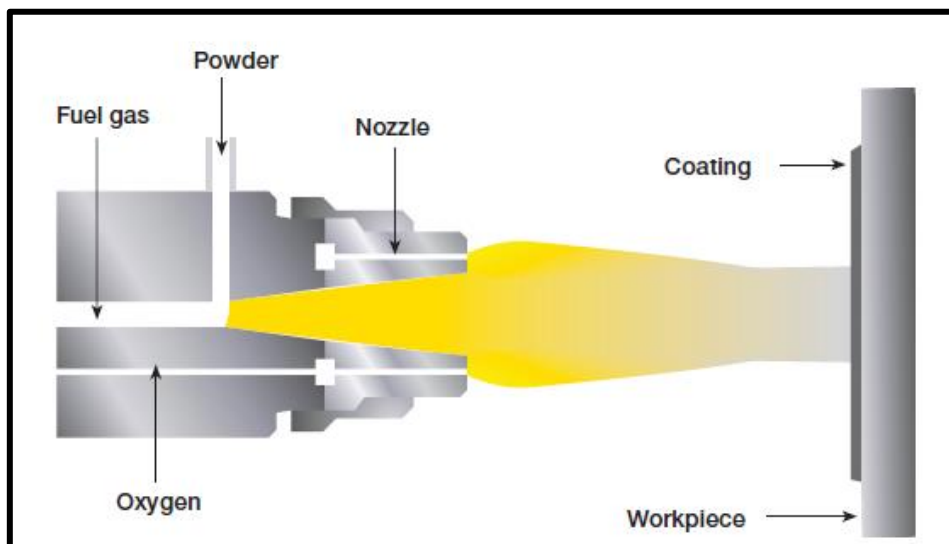
Figure 2.14: Schematic diagram of the powder flame spray process (Source: Sulzer)

(b) **Plasma Spray**

This method is also known as air or atmosphere (APS). The temperature of the plasma in the powder heating region is in the range of 12000-16000 ^{0}C which is above of the melting point of any material.

Figure 2.15 shows, the gas flowing between the electrodes (Ar, He, H_2, N_2 or mixtures) are superheated by a DC arc, produces a *plasma plume* several centimetres in length [67, 68]. The spray material is injected in powder form outside the gun nozzle into the plasma which melts the material and accelerates by the gas on to the workpiece [69].
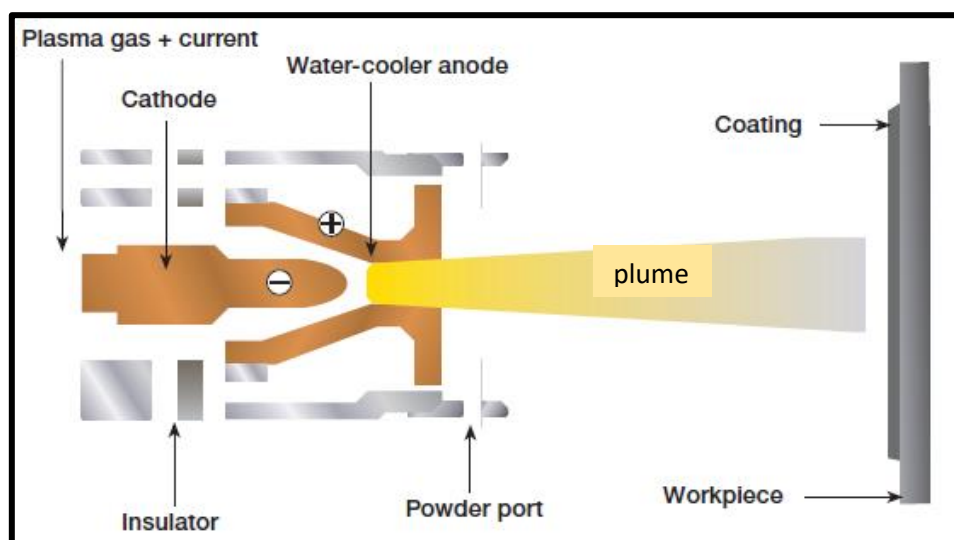
Figure 2.15: Schematic diagram of the plasma spray process (Source: Sulzer).

(c)   High velocity Oxy-fuel spray (HVOF)

Figure 2.16 shows the schematic diagram for HVOF. It is the newest method of thermal spray (HVOF) to the family of thermal spray processes. The fuel gases used in the process are propane, propylene, hydrogen, acetylene, and natural gas. The burning gas mixture is accelerated through the nozzle design of the supersonic jet at speed of Mach 4 (4900 km/h i.e. 1320m/s) at a temperature in the range 2600-3000 ^{0}C, which produces an impact on the substrate leads in an improved coating characteristic. The (HVOF) method has the capability

of depositing ceramics as well as metals, in addition it can be used to apply wear resistance coating for many applications such as turbines and jet engine plus corrosion protection.
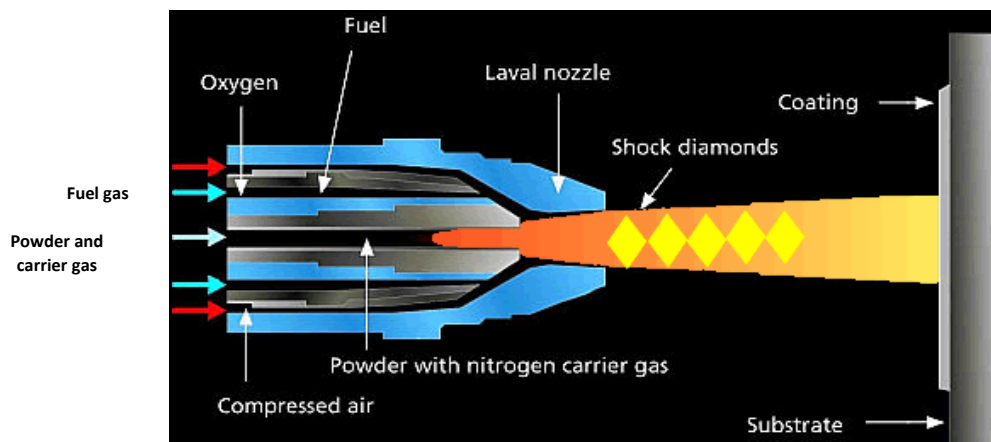
Figure 2.16: Schematic diagram of the (HVOF) process (Source: Sulzer).

The microstructure of coatings depends on the coating components, manufacturing method used, and process applied. Generally, *MCrAlY* coatings can be produced by thermal spraying: vacuum plasma spraying (*VPS*), high velocity oxygen fuel spray (*HVOF*), sputtering or evaporation (physical vapour deposition, *VPD*), electron-beam physical vapour deposition (*EB-VPD*). In industrial applications, thermal sprays coatings are preferred. Although all these thermal spray techniques are equally efficient, in this PhD, an alternative *thermal flame spray gun method* has been used. This is a flame heating thermal spray gun (oxyfuel), with a commercial name, *CastoDyn DS*8000 oxy-acetylene thermal spray, and this device is easy and economical to use; its production costs are lower in comparison with *VPS* and *HVOF*. This technique works equally well for *both the titanium-silicon carbide ceramic micro-coatings and the aluminium oxide-titanium oxide nano-coatings* and is therefore described in detail in the experiments in Chapter 4.

2.9 Conclusions

The detailed literature reviews described earlier have identified *several significant gap areas in high temperature corrosion protection of gas turbine blades,* which have therefore constituted the focus for novel contributions in this PhD. These gaps are summarized below:

1) *There is a lack of experimental studies* for high temperature corrosion behaviour of titanium-silicon carbide *double layer micro-coatings* either with TGA or SEM techniques.

2) *No previous studies* have examined the performance of aluminium oxide-titanium oxide nano-coatings in high temperature corrosive conditions either with TGA or SEM approaches.

3) *No previous computational studies* have examined the thermal stress finite element analysis of either of titanium-silicon carbide double layer micro-coatings or aluminium oxide-titanium oxide nano-coatings in high temperature conditions.

4) *No previous studies* have been communicated in the literature regarding erosion computational fluid dynamics simulation of titanium-silicon carbide double layer micro-coatings or aluminium oxide-titanium oxide nano-coatings in high temperature conditions.

Therefore, these four aspects are addressed for the first time in this PhD as follows:

- In **chapter 5**, aspects 1 and 2 are considered using **experimental methods** (TGA/SEM).
- In **chapter 6**, aspects 3 and 4 are considered using **computational** finite element thermal stress and CFD erosion methods.

The above methodology provides a comprehensive platform for comparing experimentally and computationally the novel micro-coating and nano-coating performance in high temperature protection of gas turbine blades. These are the key novelties addressed and provide the motivation and justification in this PhD thesis.

CHAPTER 3: THEORY FOR MATHEMATICAL METHODOLOGY AND NUMERICAL SIMULATIONS

3.1 Introduction

In reproducing conditions for high temperature gas turbine corrosion, the most powerful methodology after experimental testing is *computational simulation*. This has become the modus operandi for 21st century engineering. It has evolved to a new level of sophistication and furthermore is much more economical and controllable than experiments. There are many commercial softwares which are used in modern engineering simulation including ADINA, COMSOL, OPENFOAM, NASTRAN, ABAQUS etc. These softwares generally feature numerical "solver" formulations based on the most versatile numerical method known as the *finite element method* (FEM). These codes can simulate structural, thermal and fluid dynamic phenomena. To properly interpret the output of these software i.e. contour plots of deformation, equivalent stress/strain, temperature, velocity, pressure, vorticity etc, it is essential to appreciate the mathematical methodology underlying the codes. Therefore, all relevant aspects of this are covered in this chapter - i.e. *finite element structural static analysis, thermoelastic stress analysis and computational fluid dynamics*, (including turbulence models and discrete phase modelling erosion, the SIMPLE algorithm). The software deployed for all simulations of micro-coatings or nano-coatings on gas turbine blades, whether stress analysis, thermal stress analysis or CFD is **ANSYS workbench** (v16.1, 17.1 and 19.1). The coating stress analysis is simulated with a "composites" approach i.e. different layers of coating superposed on the substrate.

3.2 Finite Element Structural Approach

ANSYS Workbench uses advanced finite element formulations for stress analysis. These are generally linear. Here aspects of the formulations and finite element types employed are reviewed. These approaches are utilized in Chapter 5 for 3-dimensional simulations since no

other finite element code is available at Salford University. All information has been adapted from the ANSYS Theory Manual [1].

3.3 Combined Stresses and Strains

When a model has only one functional direction of strains and stress (e.g., LINK8), comparison with an allowable value is straightforward. However, when there is more than one component, the components are normally combined into one number to allow a comparison with an allowable.

3.4 Combined Strains

The principal strains are calculated from the strain components by the 3-D matrix equation:

$$
\begin{vmatrix}
\varepsilon_x - \varepsilon_o & \frac{1}{2}\varepsilon_{xy} & \frac{1}{2}\varepsilon_{xz} \\
\frac{1}{2}\varepsilon_{xy} & \varepsilon_y - \varepsilon_o & \frac{1}{2}\varepsilon_{yz} \\
\frac{1}{2}\varepsilon_{xz} & \frac{1}{2}\varepsilon_{yz} & \varepsilon_z - \varepsilon_o
\end{vmatrix} = 0
\tag{3.1}
$$

Where ε_o= principal strain (3 values). The **three principal strains** are labelled ε_1 , ε_2, and ε_3 (output as 1, 2, and 3 with strain items such as EPEL). The **principal strains** are ordered so that ε_1 is the most positive and ε_3 is the most negative. The strain intensity ε_1 (output as INT with strain items such as EPEL) is the largest of the absolute values of $\varepsilon_1 - \varepsilon_2$, $\varepsilon_2 - \varepsilon_3$, or $\varepsilon_3 - \varepsilon_1$. That is:

$$
\varepsilon_I = MAX(|\varepsilon_1 - \varepsilon_2|, |\varepsilon_2 - \varepsilon_3|, |\varepsilon_3 - \varepsilon_1|)
\tag{3.2}
$$

The **von Mises** or *equivalent strain* ε_e (output as EQV with strain items such as EPEL) is computed as:

$$
\varepsilon_e = \frac{1}{1+v'}\left(\frac{1}{2}[(\varepsilon_1 - \varepsilon_2)^2 + (\varepsilon_2 - \varepsilon_3)^2 + (\varepsilon_3 - \varepsilon_1)^2]\right)^{\frac{1}{2}}
\tag{3.3}
$$

Here ANSYS employs the following logic:

v'= **effective Poisson's ratio =** **User Input value (EFFNU on AVPRIN command**

<table>
<tr><td rowspan="3"></td><td>default</td><td>**Poisson's ratio (as defined on the MP commands)**
For EPEL and EPTH
0.5 for EPPL and EPCR
0.5 if referenced material is hyper-elastic and
User-mat (accessed with TB, HYPER, TB,
AHYPER, and/or T, USER)

0.0 for line elements (includes beam, link, and
pipe elements, as well as discrete elements),
cyclic symmetry analysis, and load
case operations (LOPER)</td></tr>
</table>

Figure 3.1: ANSYS Poisson ratio specification.

3.5   Combined Stresses

The principal stresses (σ_1, σ_2, σ_3) are calculated from the stress components by the cubic equation:

$$\begin{vmatrix} \sigma_x - \sigma_o & \sigma_{xy} & \sigma_{xz} \\ \sigma_{xy} & \sigma_y - \sigma_o & \sigma_{yz} \\ \sigma_{xz} & \sigma_{yz} & \sigma_z - \sigma_o \end{vmatrix} = 0 \tag{3.4}$$

Here σ_o = Principal stress (3 values). The three principal stresses are labelled σ_1, σ_2, and σ_3 (output quantities S1, S2, and S3). The principal stresses are ordered so that σ_1 is the most positive (tensile) and σ_3 is the most negative (compressive).

The stress intensity σ_I (output as SINT) is the largest of the absolute values of (σ_1- σ_2), (σ_2- σ_3), or (σ_3 - σ_1). That is:

$$\sigma_I = \text{MAX}(|\sigma_1 - \sigma_2||\sigma_2 - \sigma_3||\sigma_3 - \sigma_1|) \tag{3.5}$$

The von Mises or equivalent stress σ_e (output as SEQV) is computed as:

$$\sigma_e = \sqrt{\left[\frac{1}{2}\left[(\sigma_1 - \sigma_2)^2 + (\sigma_2 - \sigma_3)^2 + (\sigma_3 - \sigma_1)^2\right]\right]} \tag{3.6}$$

or

$$\sigma_e = \left(\frac{1}{2}\left[(\sigma_x - \sigma_y)^2 + (\sigma_y - \sigma_z)^2 + (\sigma_z - \sigma_x)^2 + 6(\sigma_{xy}^2 + \sigma_{yz}^2 + \sigma_{xz}^2)\right]\right)^{\frac{1}{2}} \tag{3.7}$$

When $v' = v$ (input as PRXY or NUXY on MP command), the equivalent stress is related to the equivalent strain through

$$\sigma_e = E\varepsilon_e \tag{3.8}$$

Where: E= Young's modulus in N/m^2 (input as EX on MP command)

3.6 Failure Criteria

ANSYS employs failure criteria to assess the *possibility of failure* of a material. Doing so allows the consideration of orthotropic materials, which might be much weaker in one direction than another. Failure criteria are available in POST1 for all plane, shell, and solid structural elements (using the FC family of commands). Possible failure of a material can be evaluated by up to six different criteria, of which three are pre-defined. They are evaluated at the top and bottom (or middle) of each layer at each of the in-plane integration points.

The failure criteria are outlined briefly below:

Maximum Strain Failure Criteria

$$\xi_1^f = \text{maximum of} \begin{cases} \frac{\varepsilon_{xt}}{\varepsilon_{xt}^f} \text{ or } \frac{\varepsilon_{xc}}{\varepsilon_{xc}^f} & \text{whichever is applicable} \\ \frac{\varepsilon_{yt}}{\varepsilon_{yt}^f} \text{ or } \frac{\varepsilon_{yc}}{\varepsilon_{yc}^f} & \text{whichever is applicable} \\ \frac{\varepsilon_{zt}}{\varepsilon_{zt}^f} \text{ or } \frac{\varepsilon_{zc}}{\varepsilon_{zc}^f} & \text{whichever is applicable} \\ \frac{|\varepsilon_{xy}|}{\varepsilon_{xy}^f} \\ \frac{|\varepsilon_{yx}|}{\varepsilon_{yz}^f} \\ \frac{|\varepsilon_{xz}|}{\varepsilon_{xz}^f} \end{cases} \tag{3.9}$$

Where:

ξ_1^f = value of maximum strain failure criterion

$$\varepsilon_{xt} = \begin{cases} 0 \\ \varepsilon_x \end{cases} \text{ whichever is greater}$$

ε_x = strain in layer x-direction

$$\varepsilon_{xc} = \begin{cases} \varepsilon_x \\ 0 \end{cases} \text{ whichever is lesser}$$

ε_{xt}^f = failure strain in layer x-direction in tension.

Maximum Stress Failure Criteria

$$\sigma_1^f = \text{maximum of} \begin{cases} \dfrac{\sigma_{xt}}{\sigma_{xt}^f} \text{ or } \dfrac{\sigma_{xc}}{\sigma_{xc}^f} \quad \text{whichever is applicable} \\[2ex] \dfrac{\sigma_{yt}}{\sigma_{yt}^f} \text{ or } \dfrac{\sigma_{yc}}{\sigma_{yc}^f} \quad \text{whichever is applicable} \\[2ex] \dfrac{\sigma_{zt}}{\sigma_{zt}^f} \text{ or } \dfrac{\sigma_{zc}}{\sigma_{zc}^f} \quad \text{whichever is applicable} \\[2ex] \dfrac{|\sigma_{xy}|}{\sigma_{xy}^f} \\[2ex] \dfrac{|\sigma_{yx}|}{\sigma_{yz}^f} \\[2ex] \dfrac{|\sigma_{xz}|}{\sigma_{xz}^f} \end{cases} \tag{3.10}$$

Where:
σ_1^f = value of maximum stress failure criterion.

$$\sigma_{xt} = \begin{cases} 0 \\ \sigma_x \end{cases} \text{ whichever is greater}$$

σ_x = Stress in layer x-direction

$$\sigma_{xc} = \begin{cases} \sigma_x \\ 0 \end{cases} \text{ whichever is lesser}$$

σ_{xt}^f = failure stress in layer x-direction in tension.

3.7   Tsai-Wu Failure Criteria

This is applicable in general stress analysis and popular in gas turbine structural analysis and

design if the criterion used is the "strength index":

$\xi_3 = $ A+B $\qquad$ (3.11)

and if the criterion used is the inverse of the "strength ratio":

$$\xi_3 = \cfrac{1}{\left[-\cfrac{B}{2A}+\sqrt{\left(\cfrac{B}{2A}\right)^2+\cfrac{1}{A}}\right]} \qquad (3.12)$$

Where:

ξ_3= value of Tsai-Wu failure criterion

$$A = -\frac{(\sigma_x)^2}{\sigma_{xt}^f \sigma_{xc}^f} - \frac{(\sigma_y)^2}{\sigma_{yt}^f \sigma_{yc}^f} - \frac{(\sigma_z)^2}{\sigma_{zt}^f \sigma_{zc}^f} + \frac{(\sigma_{xy})^2}{(\sigma_{xy}^f)^2} + \frac{(\sigma_{yz})^2}{(\sigma_{yz}^f)^2} + \frac{(\sigma_{xz})^2}{(\sigma_{xz}^f)^2}$$

$$+ \frac{C_{xy}\sigma_x\sigma_y}{\sqrt{\sigma_{xt}^f \sigma_{xc}^f \sigma_{yt}^f \sigma_{tc}^f}} + \frac{C_{yz}\sigma_y\sigma_z}{\sqrt{\sigma_{yt}^f \sigma_{yc}^f \sigma_{zt}^f \sigma_{zc}^f}} + \frac{C_{xz}\sigma_x\sigma_z}{\sqrt{\sigma_{xt}^f \sigma_{xc}^f \sigma_{zt}^f \sigma_{zc}^f}}$$

$\qquad$ (3.13)

$$B = \left(\frac{1}{\sigma_{xt}^f} + \frac{1}{\sigma_{xc}^f}\right)\sigma_x + \left(\frac{1}{\sigma_{yt}^f} + \frac{1}{\sigma_{yc}^f}\right)\sigma_y + \left(\frac{1}{\sigma_{zt}^f} + \frac{1}{\sigma_{zc}^f}\right)\sigma_z \qquad (3.14)$$

$C_{xy}, C_{yz}, C_{xz} = x - y, y - z, x - z,$ respectively denote the coupling coefficients for Tsai-Wu

theory.

3.8 Safety Tools in the ANSYS Workbench Product

The ANSYS Workbench product uses safety tools that are based on *four different stress quantities*:

1. **Equivalent stress** (σ_e).

2. **Maximum tensile stress** (σ_1).

3. **Maximum shear stress** (τ_{MAX})

This uses Mohr's circle:

$$\tau_{MAX} = \frac{\sigma_1 - \sigma_3}{2} \qquad (3.15)$$

Where: σ_1 and σ_3 = principal stresses.

4. **Mohr-Coulomb stress**

This theory uses a stress limit based on

$$\frac{\sigma_1}{\sigma_t^f} + \frac{\sigma_3}{\sigma_c^f} \hspace{5cm} (316)$$

Where:

σ_t^f = input tensile stress limit

σ_c^f = input compression stress limit

3.9   3-D ANSYS finite elements

For 3-D stress analysis, 3-D finite elements must be used. A three-dimensional (3D) solid element can be considered to be the most general of all solid finite elements since all the field variables are dependent on all three Cartesian coordinates, *x, y and z*. This type of element is critical to dynamic stress modelling of landing gear. An example of a 3D solid structure under loading is shown in **Figure 3.2.** As can be seen, the force vectors here can be in any arbitrary direction in space. A 3D solid can also have any arbitrary shape, material properties and boundary conditions in space. As such, there are altogether six possible stress components, three normal and three shear stresses, that need to be taken into consideration. Typically, a 3D solid element can be a tetrahedron or hexahedron in shape with either flat or curved surfaces. Each node of the element will have three translational degrees of freedom. The element can thus deform in all three directions in space. Since the 3D element is said to be the most general solid element, the truss, beam, plate, 2D solid and shell elements can all be considered to be special cases of the 3D element. The formulation of 3D solids elements is straightforward, since it is basically an extension of 2D solids elements. All the techniques used in 2D solids can be utilized, except that all the variables are now functions of x, y and z. The basic concepts, procedures and formulations for 3D solid elements can also be found in e.g. Bathe [2].
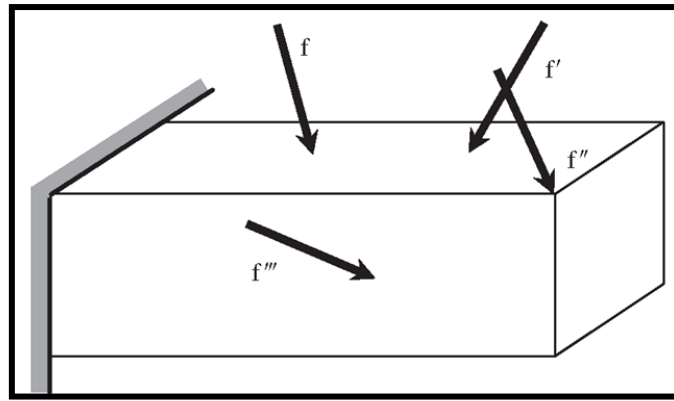
Figure 3.2: Example of a 3D solid under loadings.

Tetrahedron Element - Strain Matrix

Consider the same 3D solid structure as **Figure 3.2**, whose domain is divided in a proper manner into a number of tetrahedron (pyramid) elements (**Figure 3.3**) with four nodes and four surfaces, as shown in **Figure 3.4**. A tetrahedron element has four nodes, each having three DOFs (u, v and w), making the total DOFs in a tetrahedron element equal to twelve.
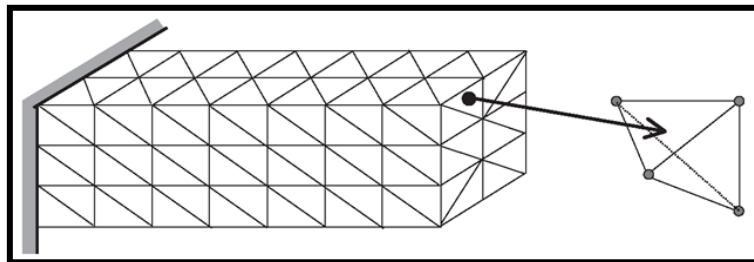
Figure 3.3: Solid block e.g. gas turbine blade specimen, divided into four-node tetrahedron elements.
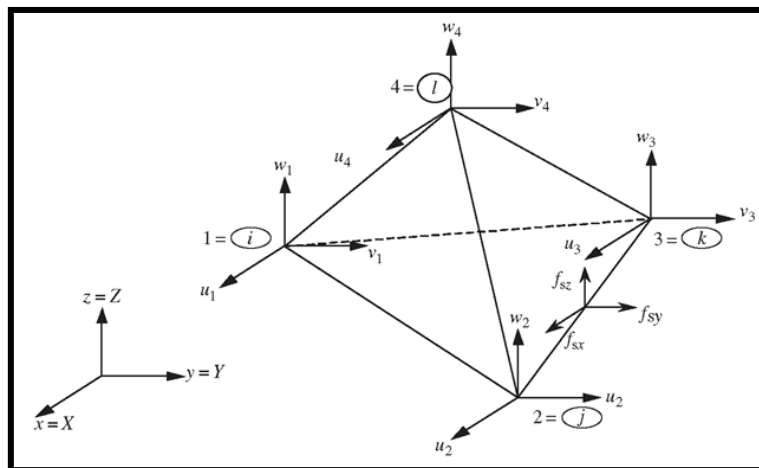
Figure 3.4: A tetrahedron element.

The nodes are numbered 1, 2, 3 and 4 by the right-hand rule. The local Cartesian coordinate system for a tetrahedron element can usually be the same as the global coordinate system, as there are no advantages in having a separate local Cartesian coordinate system. In an element, the displacement vector U is a function of the *coordinates x, y and z*, and is interpolated by shape functions in the following form, which should by now be shown to be part and parcel of the finite element method:

$$U^h(x, y, z) = N(x, y, z)d_e \tag{3.17}$$

Here the nodal displacement vector, d_e, is given as:

$$d_e = \begin{bmatrix} u_1 \\ v_1 \\ w_1 \\ u_2 \\ v_2 \\ w_2 \\ u_3 \\ v_3 \\ w_3 \\ u_4 \\ v_4 \\ w_4 \end{bmatrix} \begin{matrix} \left. \vphantom{\begin{matrix} u_1 \\ v_1 \\ w_1 \end{matrix}} \right\} \text{displacement at node 1} \\ \left. \vphantom{\begin{matrix} u_2 \\ v_2 \\ w_2 \end{matrix}} \right\} \text{displacement at node 2} \\ \left. \vphantom{\begin{matrix} u_3 \\ v_3 \\ w_3 \end{matrix}} \right\} \text{displacement at node 3} \\ \left. \vphantom{\begin{matrix} u_4 \\ v_4 \\ w_4 \end{matrix}} \right\} \text{displacement at node 4} \end{matrix} \tag{3.18}$$

The matrix of *shape functions* has the following form:

$$\begin{array}{cccc} \text{Node 1} & \text{Node 2} & \text{Node 3} & \text{Node 4} \end{array}$$

$$\begin{bmatrix} N_1 & 0 & 0 & N_2 & 0 & 0 & N_3 & 0 & 0 & N_4 & 0 & 0 \\ 0 & N_1 & 0 & 0 & N_2 & 0 & 0 & N_3 & 0 & 0 & N_4 & 0 \\ 0 & 0 & N_1 & 0 & 0 & N_2 & 0 & 0 & N_3 & 0 & 0 & N_4 \end{bmatrix} \tag{3.19}$$

To develop the *shape functions*, we make use of what are designated *volume coordinates*, which is a natural extension from the area coordinates for 2D solids. The use of the volume

coordinates makes it more convenient for shape function construction and element matrix integration. The volume coordinates for *node 1* is defined as:

$$L_1 = \frac{V_{p234}}{V_{1234}} \qquad (3.20)$$

Here V_{P234} and V_{1234} denote, respectively, the volumes of the tetrahedrons P234 and 1234, as shown in **Figure 3.5**. The volume coordinate for node 2-4 can also be defined in the same manner:
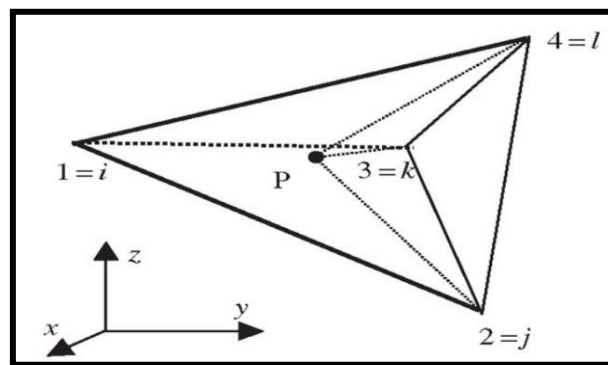
Figure 3.5: Volume coordinates for tetrahedron elements.

All structural meshes are built using 3-D tetrahedron elements ("tets").

3.10 Stress and strain relationships for linear *thermo*-elasticity

Detailed thermal stress simulations are described in Chapter 6 for both micro-coating and nano-coatings and the relevant theory is therefore now elaborated. Thermo-elasticity involves the coupling of *thermal conduction heat transfer* with *elasticity*. Thermal conduction is based on the classical Fourier law of heat conduction. In one-dimension this equation takes the form: *Q = -kA(dT/dx)*. Here 'Q' is the heat flow rate by conduction (W), 'k' is the thermal conductivity of body material ($W \cdot m^{-1} \cdot K^{-1}$), 'A' is the cross-sectional area normal to direction of heat flow (m^2) and 'dT/dx' is the temperature gradient ($K \cdot m^{-1}$). A fully 3-D version is considered. It is noteworthy that a negative sign in Fourier's equation indicates that the heat flow is in the direction of negative gradient temperature and that serves to make heat flow positive. Thermal conductivity 'k' is one of the transport properties. Others are the viscosity associated with the

transport of momentum and species diffusion coefficient associated with the transport of mass. Thermal conductivity 'k' provides an indication of the rate at which heat energy is transferred through a medium by conduction process. The law of heat conduction, also known as Fourier's law [3], states that the *rate of heat transfer through a material is proportional to the negative gradient in the temperature and to the area, at right angles to that gradient, through which the heat flows*. This law may be stated in two equivalent forms: the *integral form*, in which the amount of energy flowing into or out of a body as a whole is considered, and the *differential form*, in which the local flow rates or fluxes of energy are considered. Newton's law of cooling is a discrete analogue of Fourier's law, while Ohm's law is the electrical analogue of Fourier's law. The thermal conductivity, *k* is often treated as a constant, though this is not always true. While the thermal conductivity of a material generally varies with temperature, the variation can be small over a significant range of temperatures for some common materials. In anisotropic materials, the thermal conductivity typically varies with orientation; in this case *k* is represented by a second-order tensor. In non-uniform materials, *k* varies with spatial location. However, in the current PhD study, isotropic thermal conductivity has been assumed for both the gas turbine substrate and coatings. The full conductivity tensor for general materials is given in due course. Inherent to Fourier's equation is the assumption that steady state heat conduction takes place, bounding surfaces are *isothermal* in character i.e. constant and uniform temperatures are maintained at the two faces and there is no internal heat generation. Next the elasticity formulation in thermal stress analysis is considered. This requires relationships for linear materials. The stress is related to the strains by:

$$\{\sigma\} = [D]\{\varepsilon^{el}\} \tag{3.21}$$

Where:

$\{\sigma\}$ = Stress vector

$[D]$ = Elastic or elastic stiffness matrix

$\{\varepsilon^{el}\}$ = Elastic vector

$\{\varepsilon\}$ = Total strain vector

$\{\varepsilon^{th}\}$ = Thermal strain vector

The stress vectors are shown in **Figure 3.6**. The ANSYS program uses the sign convention that tension is positive, and compression is negative for direct stresses and strains.

Equation 3.21 can be inverted to:

$$\{\varepsilon\} = \{\varepsilon^{th}\} + [D]^{-1}\{\sigma\} \tag{3.22}$$

For the three-dimensional model, the thermal strain vector is:

$$\{\varepsilon^{th}\} = \Delta T \lfloor \alpha_x \quad \alpha_y \quad \alpha_z \quad 0 \quad 0 \quad 0 \rfloor^T \tag{3.23}$$

Where:

α_x = The thermal coefficient of expansion in the x direction

ΔT = $T - T_{REF}$

T = Current temperature at the point in question

T_{REF} = Reference (strain – free) temperature
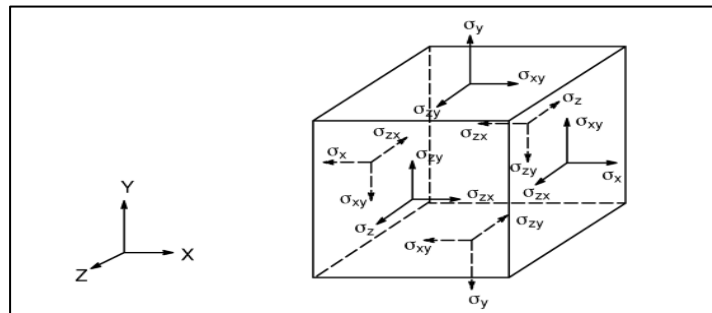
Figure 3.6: Stress Vectors.

The flexibility or compliance matrix, $[D]^{-1}$, in a columnized normal format is shown as:

$$[D]^{-1} = \begin{bmatrix} \dfrac{1}{E_x} & -\dfrac{v_{xy}}{E_y} & \dfrac{-v_{xz}}{E_z} & 0 & 0 & 0 \\[2mm] -\dfrac{v_{yx}}{E_x} & \dfrac{1}{E_y} & \dfrac{-v_{yz}}{E_z} & 0 & 0 & 0 \\[2mm] -\dfrac{v_{zx}}{E_x} & -\dfrac{v_{zy}}{E_y} & \dfrac{1}{E_z} & 0 & 0 & 0 \\[2mm] 0 & 0 & 0 & \dfrac{1}{G_{xy}} & 0 & 0 \\[2mm] 0 & 0 & 0 & 0 & \dfrac{1}{G_{yz}} & 0 \\[2mm] 0 & 0 & 0 & 0 & 0 & \dfrac{1}{G_{xz}} \end{bmatrix} \tag{3.24}$$

Or in a row normalised format the matrix can be shown as:

$$[D]^{-1} = \begin{bmatrix} \dfrac{1}{E_x} & -\dfrac{\bar{v}_{xy}}{E_y} & \dfrac{-\bar{v}_{xz}}{E_z} & 0 & 0 & 0 \\[2mm] -\dfrac{\bar{v}_{yx}}{E_x} & \dfrac{1}{E_y} & \dfrac{-\bar{v}_{yz}}{E_z} & 0 & 0 & 0 \\[2mm] -\dfrac{\bar{v}_{zx}}{E_x} & -\dfrac{\bar{v}_{zy}}{E_y} & \dfrac{1}{E_z} & 0 & 0 & 0 \\[2mm] 0 & 0 & 0 & \dfrac{1}{G_{xy}} & 0 & 0 \\[2mm] 0 & 0 & 0 & 0 & \dfrac{1}{G_{yz}} & 0 \\[2mm] 0 & 0 & 0 & 0 & 0 & \dfrac{1}{G_{xz}} \end{bmatrix} \tag{3.25}$$

Where:

E_x = Young's modulus in the x direction

v_{xy} = Minor Poisson ratio

$\bar{v}_{xy}$ = Major Poisson ratio

G_{xy} = Shear modulus in the *x, y* plane

The $[D]^{-1}$ matrix *must be positive* and assumed to be *symmetric*. The expansion of the equations (3.22) with equations (3.23), (3.24) and the triangular matrix sections and writing them explicitly will result in the following equations:

$$\varepsilon_x = \alpha_x \Delta T + \frac{\sigma_x}{E_x} - \frac{v_{xy}\,\sigma_y}{E_y} - \frac{v_{xz}\,\sigma_z}{E_z} \tag{3.26}$$

$$\varepsilon_y = \alpha_y \Delta T + \frac{\sigma_y}{E_y} - \frac{v_{xy}\,\sigma_x}{E_y} - \frac{v_{yz}\,\sigma_z}{E_z} \tag{3.27}$$

$$\varepsilon_z = \alpha_x \Delta T + \frac{\sigma_z}{E_z} - \frac{v_{xz}\,\sigma_x}{E_z} - \frac{v_{yz}\,\sigma_z}{E_z} \tag{3.28}$$

Where:

$$\varepsilon_{xy} = \frac{\sigma_{xy}}{G_{xy}}$$

$$\varepsilon_{yz} = \frac{\sigma_{yz}}{G_{yz}}$$

$$\varepsilon_{xz} = \frac{\sigma_{xz}}{G_{xz}}$$

Alternatively, the equations can be represented as:

$$\sigma_x = \frac{E_x}{h}\left[1 - (v_{yz})^2 \frac{E_y}{E_z}\right](\varepsilon_x - \alpha_x \Delta T) + \frac{E_x}{h}\left(v_{xy} + v_{xz}v_{yz}\frac{E_y}{E_z}\right)(\varepsilon_y - \alpha_y \Delta T)$$
$$+ \frac{E_x}{h}(v_{xz} + v_{yz}v_{xy})(\varepsilon_z - \alpha_z \Delta T) \tag{3.29}$$

$$\sigma_y = \frac{E_y}{h}\left[1 - (v_{xz})^2 \frac{E_x}{E_z}\right](\varepsilon_y - \alpha_y \Delta T) + \frac{E_x}{h}\left(v_{xy} + v_{xz}v_{yz}\frac{E_y}{E_z}\right)(\varepsilon_x - \alpha_x \Delta T)$$
$$+ \frac{E_y}{h}(v_{yz} + v_{xz}v_{xy})(\varepsilon_z - \alpha_z \Delta T) \tag{3.30}$$

$$\sigma_z = \frac{E_z}{h}\left[1 - (v_{xy})^2 \frac{E_x}{E_y}\right](\varepsilon_z - \alpha_z \Delta T) + \frac{E_x}{h}\left(v_{xz} + v_{yz}v_{yz}\frac{E_y}{E_z}\right)(\varepsilon_x - \alpha_x \Delta T)$$
$$+ \frac{E_y}{h}(v_{yz} + v_{xz}v_{xy})(\varepsilon_y - \alpha_y \Delta T) \tag{3.31}$$

Where:

$$\sigma_{xy} = G_{xy}\varepsilon_{xy}$$
$$\sigma_{yz} = G_{yz}\varepsilon_{yz}$$
$$\sigma_{xz} = G_{xz}\varepsilon_{xz}$$
$$h = 1 - (v_{xy})^2 \frac{E_x}{E_y} - (v_{yz})^2 \frac{E_y}{E_z} - (v_{xz})^2 \frac{E_x}{E_z} - 2\, v_{xy}v_{yz}v_{xy}\frac{E_x}{E_y}$$
$$G_{xy} = G_{yz} = G_{xz} = \frac{E_x}{2(1 + v_{xy})}$$

3.11 Temperature – Dependent coefficient of thermal expansion

For a typical component, the thermal strain from equation (3.22) is:

$$\epsilon^{th} = \alpha(T - T_{ref}) \tag{3.32}$$

The above equation assumes that α itself is not a function of temperature. If α is a function of temperature, the equation (3.32) becomes:

$$\epsilon^{th} = \int_{T_{ref}}^{T} \alpha_{inst}(T)dT \tag{3.33}$$

63

Where, $\alpha_{inst}(T)$ = instantaneous coefficient of thermal expansion However, the program uses a weighted- average value for α:

$$\epsilon^{th} = \bar{\alpha}(T)\left(T - T_{ref}\right)$$ (3.34)

Where,

$$\bar{\alpha}(T) = \frac{\int_{T_{ref}}^{T} \alpha_{inst}\, dT}{T - T_{ref}} = \text{Mean value of coefficient of thermal expansion}$$

The data is usually supplied as a *mean value* and this data is correctly used by ANSYS, even if T_{REF} is not only the definition temperature about which the data is supplied but also the reference temperature at which zero strains exist.

3.12   Structural strain and stress evaluations

The element integration point strains and stresses are computed by combining the following two equations:

$$\{\varepsilon^{el}\} = [B]\{u\} - \{\varepsilon^{th}\}$$ (3.35)

$$\{\sigma\} = [D]\{\varepsilon^{el}\}$$ (3.36)

Where,

$\{\varepsilon^{el}\}$ = Elastic vector

$[B]$ =Strains-displacement matrix evaluated at integration point

$\{u\}$ = Nodal displacement vector

$\{\varepsilon^{th}\}$ =Thermal strain vector

$\{\sigma\}$ = Stress vector

$[D]$ = Elastic or elastic stiffness matrix

3.13   Heat flow fundamentals

The first law of thermodynamics states that energy is conserved. Considering this as a differential control volume:

$$\rho c \left(\frac{\partial T}{\partial t} + \{v\}^T \{L\} T\right) + \{L\}^T \{q\} = \ddot{q}$$ (3.37)

Where,

ρ = Density (kg/m³)

64

C   = Specific heat (J/kgK)

T   = Temperature (K)

t   = Time (s)

$$\{L\} = \begin{Bmatrix} \frac{\partial}{\partial x} \\ \frac{\partial}{\partial y} \\ \frac{\partial}{\partial z} \end{Bmatrix} = \text{Vector operator}$$

$$\{v\} = \begin{Bmatrix} v_x \\ v_y \\ v_z \end{Bmatrix} = \text{Velocity vector for mass transport of heat}$$

$\{q\}$ = Heat flux vector

$\ddot{q}$ = Heat generation rate per unit volume

Fourier's law is also used to relate the heat flux vector to thermal gradients:

$$\{q\} = -[D]\{L\}T \tag{3.38}$$

Where,

$$[D] = \begin{bmatrix} K_{xx} & 0 & 0 \\ 0 & K_{yy} & 0 \\ 0 & 0 & K_{zz} \end{bmatrix} = \text{Conductivity matrix}$$

K_{xx}, K_{yy}, K_{zz}= conductivity in the element *x, y, and z* directions, respectively. Combining equations (3.37) and (3.38):

$$c \left(\frac{\partial T}{\partial t} + \{v\}^T \{L\}T \right) = \{L\}^T [D]\{L\}T + \ddot{q} \tag{3.39}$$

Expanding the equation to a more familiar form:

$$\rho c \left(\frac{\partial T}{\partial t} + v_x \frac{\partial T}{\partial x} + v_y \frac{\partial T}{\partial y} + v_z \frac{\partial T}{\partial z} \right) =$$
$$\ddot{q} + \frac{\partial}{\partial x}\left(K_x \frac{\partial T}{\partial x} \right) + \frac{\partial}{\partial y}\left(K_y \frac{\partial T}{\partial y} \right) + \frac{\partial}{\partial z}\left(K_z \frac{\partial T}{\partial z} \right) \tag{3.40}$$

It is assumed that all the effects are in the global Cartesian system. Three types of boundary conditions are considered.

1. Specified temperatures acting over surface S₁:

$$T = T^*$$

Where,

      T* is the specified temperature.

2. Specified heat flows acting over surface S_2:

$$\{q\}^T\{\eta\} = -q^* \tag{3.41}$$

Where,

      $\{\eta\}$ = unit outward normal vector
      q^* = specified heat flow

3. Specified convection surfaces acting over surface S_3 (Newtons law of cooling)

$$\{q\}^T\{\eta\} = h_f(T_S - T_B) \tag{3.42}$$

Where:

      h_f = film coefficient
      T_B = bulk temperature of the adjacent fluid (K)
      Ts   = temperature at the surface of the model (K)

Combining Eqn. (3.41) with Eqn. (3.42):

$$\{n\}^T[D]\{L\}T = q^* \tag{3.43}$$

$$\{n\}^T[D]\{L\}T = h_f(T_B - T) \tag{3.44}$$

Pre-multiplying equation by a virtual temperature, integrating over the volume of the element and combing with some manipulation yields:

$$\int_{vol} \left(\rho c \, \delta T \left(\frac{\partial T}{\partial t} + \{v\}^T\{L\}T \right) + \{L\}^T(\delta T)[D]\{L\}T \right) d(vol) =$$
$$\int_{s_2} \delta T q^* d(s2) + \int_{s_3} \delta T h_f(T_B - T) d(S_3) + \int_{vol} \delta T \ddot{q} \, d(vol) \tag{3.45}$$

Where:

vol   = volume of the element

δT = an allowable virtual temperature.

3.14   Fluid flow Fundamentals

The fluid flow problem is defined by the laws of conservation of mass, momentum, and energy.

These laws are expressed in terms of partial differential equations which for *laminar* flow are

the famous *Navier-Stokes equations*. In the present PhD, attention is confined to *Newtonian*

flow which approximates reasonably well the hot air in gas turbine environments associated with jet engines.

3.14-1 Continuity Equation

From the law of conservation of mass, D'Alembert's continuity equation is generated:

$$\frac{\partial \rho}{\partial t} + \frac{\partial(\rho V_x)}{\partial x} + \frac{\partial(\rho V_y)}{\partial y} + \frac{\partial(\rho V_z)}{\partial z} = 0 \tag{3.46}$$

Where:

V_x, V_y, V_z = components of the velocity vector in the x, y *and* z direction respectively (m/s);

ρ = density (kg/m^3)

x, y, z = global Cartesian coordinates (m)

t = time (s)

The rate of change of density can be replaced by the rate of change of pressure and the rate at which the density changes with pressure:

$$\frac{\partial \rho}{\partial t} = \frac{\partial \rho}{\partial p} \frac{\partial p}{\partial t} \tag{3.47}$$

Where p = pressure (Pascals). The evaluation of the derivative of density with repect to pressure is derived from the equation of the state. For compressible ideal gas flow:

$$\rho = \frac{p}{RT} \quad \rightarrow \quad \frac{\partial \rho}{\partial p} = \frac{1}{RT} \tag{3.48}$$

Where: R = gas constant (J/kgK)

T = Temperature (K)

If the incompressible solution algorithm is used, the specific value can be cotrolled with:

$$\frac{\partial \rho}{\partial p} = \frac{1}{\beta} \tag{3.49}$$

Here β is the coefficient of thermal volumetric expansion.

3.14-2 Momentum Equations (Navier-Stokes)

In a Newtonian fluid, the relationship between the stress and the rate of deformation of the fluid (in indicial notation) is:

$$T_{ij} = -p\,\delta_{ij} + \mu\left(\frac{\partial u_i}{\partial x_j} + \frac{\partial u_j}{\partial x_i}\right) + \delta_{ij}\,\lambda\frac{\partial u_i}{\partial x_j} \tag{3.50}$$

Where:

T_{ij} = Stress tensor (Pa)

u_{ij} = orthogonal velocities $\left(u_1 = V_x, u_2 = V_y, u_3 = V_z\right)$ (m/s)

μ = dynamic viscosity (kg/(ms))

λ = second coefficient of viscosity (kg/(ms))

δ_{ij} = Deformation in the *x,y and z* directions (m).

The final term in Equation (3.50) i.e. the *product of the second coefficient of viscosity and the divergence of the velocity*, is zero for a constant density fluid and is considered small enough to be neglected in a compressible fluid. Equation (3.50) transforms the momentum equation to the *Navier-Stokes* equations; however, these will still be referred to as the momentum equations elsewhere in this chapter.

The momentum equations, without further assumptions regarding the properties, are as follows:

$$\frac{\partial \rho V_x}{\partial t} + \frac{\partial\left(\rho V_x{}^2\right)}{\partial x} + \frac{\partial\left(\rho V_y V_x\right)}{\partial y} + \frac{\partial\left(\rho V_z V_x\right)}{\partial z} = \rho g_x - \frac{\partial p}{\partial x} \left.\vphantom{\frac{\partial}{\partial}}\right\} \tag{3.51}$$

$$+R_x + \frac{\partial}{\partial x}\left(\mu_e \frac{\partial V_x}{\partial x}\right) + \frac{\partial}{\partial y}\left(\mu_e \frac{\partial V_x}{\partial y}\right) + \frac{\partial}{\partial z}\left(\mu_e \frac{\partial V_x}{\partial z}\right) + T_x$$

$$\frac{\partial \rho V_y}{\partial t} + \frac{\partial\left(\rho V_x V_y\right)}{\partial x} + \frac{\partial\left(\rho\, V_y{}^2\right)}{\partial y} + \frac{\partial\left(\rho V_z V_y\right)}{\partial z} = \rho g_y - \frac{\partial p}{\partial y} \left.\vphantom{\frac{\partial}{\partial}}\right] \tag{3.52}$$

$$R_y + \frac{\partial}{\partial x}\left(\mu_e \frac{\partial V_y}{\partial x}\right) + \frac{\partial}{\partial y}\left(\mu_e \frac{\partial V_y}{\partial y}\right) + \frac{\partial}{\partial z}\left(\mu_e \frac{\partial V_y}{\partial z}\right) + T_y$$

$$\frac{\partial \rho V_z}{\partial t} + \frac{\partial(\rho V_x V_z)}{\partial x} + \frac{\partial(\rho V_y V_z)}{\partial y} + \frac{\partial(\rho V_z{}^2)}{\partial z} = \rho g_z - \frac{\partial p}{\partial z}$$

$$R_z + \frac{\partial}{\partial x}\left(\mu_e \frac{\partial V_z}{\partial x}\right) + \frac{\partial}{\partial y}\left(\mu_e \frac{\partial V_z}{\partial y}\right) + \frac{\partial}{\partial z}\left(\mu_e \frac{\partial V_z}{\partial z}\right) + T_z$$

(3.53)

Where: g_x, g_y, g_z = components of acceleration due to gravity (m/s^2)

ρ = density (kg/m^3)

μ_e = effective viscosity (kg/(ms))

R_x, R_y, R_z = distributed resisitance (N/m^3)

T_x, T_y, T_z = viscoss loss terms (N/m^3)

For laminar flow, the effective viscosity is simply the dynamic viscosity. The terms R_x, R_y, R_z are the distributed resistance used to model the effect of some geometric feature without explicitly modelling the precise geometry such as flow through screens and porous media. The terms T_x, T_y, T_z are *viscous loss terms* which are eliminated in the constant property case. The order of the differentiation is reversed in each term, reducing the term to a derivative of the continuity equation, which is zero.

$$T_x = \frac{\partial}{\partial x}\left(\mu \frac{\partial V_x}{\partial x}\right) + \frac{\partial}{\partial y}\left(\mu \frac{\partial V_y}{\partial x}\right) + \frac{\partial}{\partial z}\left(\mu \frac{\partial V_z}{\partial x}\right)$$

(3.54)

$$T_y = \frac{\partial}{\partial x}\left(\mu \frac{\partial V_x}{\partial y}\right) + \frac{\partial}{\partial y}\left(\mu \frac{\partial V_y}{\partial y}\right) + \frac{\partial}{\partial z}\left(\mu \frac{\partial V_z}{\partial y}\right)$$

(3.55)

$$T_z = \frac{\partial}{\partial x}\left(\mu \frac{\partial V_x}{\partial z}\right) + \frac{\partial}{\partial y}\left(\mu \frac{\partial V_y}{\partial z}\right) + \frac{\partial}{\partial z}\left(\mu \frac{\partial V_z}{\partial z}\right)$$

(3.56)

The conservation of energy can be expressed in terms of the stagnation (total) temperature, often useful in highly compressible flows, or the static temperature, appropriate for low speed incompressible analysis.

3.14-3 Compressible Energy Equation

The complete energy equation is solved in the compressible case with heat transfer since hot air at high supersonic speed is studied in gas turbine jet engine environments. In terms of the total (or *stagnation*) temperature, the energy equation, as described by White [4], is:

$$\frac{\partial}{\partial t}\left(\rho C_p T_0\right) + \frac{\partial}{\partial x}\left(\rho V_x C_p T_0\right) + \frac{\partial}{\partial y}\left(\rho V_y C_p T_0\right) + \frac{\partial}{\partial z}\left(\rho V_z C_p T_0\right) =$$

$$\frac{\partial}{\partial x}\left(K\frac{\partial T_0}{\partial x}\right) + \frac{\partial}{\partial y}\left(K\frac{\partial T_0}{\partial y}\right) + \frac{\partial}{\partial z}\left(K\frac{\partial T_0}{\partial z}\right) + W^V + E^K + Q_V + \Phi + \frac{\partial P}{\partial t}$$

(3.57)

Transient heat gradient term

Nonlinear convective heat transfer

Fourier heat conduction terms

Transient pressure gradient

Where: C_p = Specific heat capacity at constanat pressure (J/kgK)

T_0 = Total (or stagnation) temperature (K)

K = Thermal conductivity (W/mK)

W^V = Viscous work term (J/m^3)

Q_V = Volumetric heat source (J/m^3)

Φ = Viscous heat generation term (J/m^3)

E^K = Kinetic energy (J/m^3)

The static temperature is calculated from the total temperature difference with the kinetic

$$T = T_0 - \frac{V^2}{2C_p}$$

(3.58)

Where V= magnitude of the fluid velocity vector (m/s). The static and total temperature for the non-fluid nodes will be the same. The *viscous work term* (internal friction in the viscous fluid) is represented by:

$$W^V = V_x\mu\left[\frac{\partial^2 V_x}{\partial x^2} + \frac{\partial^2 V_x}{\partial y^2} + \frac{\partial^2 V_x}{\partial z^2} + \frac{\partial}{\partial x}\left(\frac{\partial V_x}{\partial x} + \frac{\partial V_y}{\partial y} + \frac{\partial V_z}{\partial z}\right)\right]$$

$$+ V_y\mu\left[\frac{\partial^2 V_y}{\partial x^2} + \frac{\partial^2 V_y}{\partial y^2} + \frac{\partial^2 V_y}{\partial z^2} + \frac{\partial}{\partial y}\left(\frac{\partial V_x}{\partial x} + \frac{\partial V_y}{\partial y} + \frac{\partial V_z}{\partial z}\right)\right] \tag{3.59}$$

$$+ V_z\mu\left[\frac{\partial^2 V_z}{\partial x^2} + \frac{\partial^2 V_z}{\partial y^2} + \frac{\partial^2 V_z}{\partial z^2} + \frac{\partial}{\partial z}\left(\frac{\partial V_x}{\partial x} + \frac{\partial V_y}{\partial y} + \frac{\partial V_z}{\partial z}\right)\right]$$

The above equation can be summarised as:

$$W^V = U_j\mu\left[\frac{\partial}{\partial x_i} \cdot \frac{\partial U_j}{\partial x_i} + \frac{\partial}{\partial x_k}\left(\frac{\partial U_k}{\partial x_j}\right)\right] \tag{3.60}$$

Where the repetition of a subscript implies a summation over the the three orthogonal direction.

The kinetic energy term represented by:

$$E^K = -\frac{\partial}{\partial x}\left[\frac{K}{C_p}\frac{\partial}{\partial x}\left(\frac{1}{2}|V^2|\right)\right] - \frac{\partial}{\partial y}\left[\frac{K}{C_p}\frac{\partial}{\partial y}\left(\frac{1}{2}|V^2|\right)\right] - \frac{\partial}{\partial z}\left[\frac{K}{C_p}\frac{\partial}{\partial z}\left(\frac{1}{2}|V^2|\right)\right] \tag{3.61}$$

Finally, the *viscous dissipation* represented by:

$$\Phi = 2\mu\left[\left(\frac{\partial V_x}{\partial x}\right)^2 + \left(\frac{\partial V_y}{\partial y}\right)^2 + \left(\frac{\partial V_z}{\partial z}\right)^2\right] +$$

$$\mu\left[\left(\frac{\partial V_y}{\partial x} + \frac{\partial V_x}{\partial y}\right)^2 + \left(\frac{\partial V_z}{\partial y} + \frac{\partial V_y}{\partial z}\right)^2 + \left(\frac{\partial V_x}{\partial z} + \frac{\partial V_z}{\partial x}\right)^2\right]$$

$$\tag{3.62}$$

Or in tensor notation:

$$\Phi = \mu\left(\frac{\partial U_i}{\partial x_k} + \frac{\partial U_k}{\partial x_i}\right)\frac{\partial U_i}{\partial x_k} \tag{3.63}$$

3.15 Turbulence

If the inertia effects are strong enough with respect to viscous effects, the flow may be turbulent. In this case "turbulence modelling" is used which means that the instantaneous velocity is fluctuating at every point in the flow field as described by Chandrasekhar [5]. Therefore the velocity is expressed in terms of a *mean value* and a *fluctuating component*:

$$V_x = \overline{V}_x + V_x' \tag{3.64}$$

Where: $\overline{V}_x$ = mean component of velocity in x-direction (m/s)

V_x' = fluctuating component of velocity in x-direction (m/s)

If an expression such as this is used for the instantaneous velocity in the Navier-Stokes equations, the equation may then be *time-averaged*, noting that the time average of the fluctuating component is zero, and the time average of the instantaneous value is the average value. The time interval for the integration is arbitrarily chosen as long as it is enough for this to be true and short enough so that the "real time" transient effects do not affect this integration.

$$\frac{1}{\delta_t} \int_0^{\delta_t} V_x' \, dt \quad ; \quad \frac{1}{\delta_t} \int_0^{\delta_t} V_x \, dt = \overline{V}_x \tag{3.65}$$

After the substitution of equation (3.64) into the momentum equations (as introduced by Reynolds) the *time averaging* leads to additional terms. The velocities in the momentum equations are the averaged ones, and droping the bar in the subsequent expression of the momentum equations, so that the absence of a bar represents the mean value. The extra terms are:

$$\sigma_x{}^R = -\frac{\partial}{\partial x}\left(\overline{\rho V_x' V_x'}\right) - \frac{\partial}{\partial y}\left(\overline{\rho V_x' V_y'}\right) - \frac{\partial}{\partial z}\left(\overline{\rho V_x' V_z'}\right) \tag{3.66}$$

$$\sigma_y{}^R = -\frac{\partial}{\partial x}\left(\overline{\rho V_y' V_x'}\right) - \frac{\partial}{\partial y}\left(\overline{\rho V_y' V_y'}\right) - \frac{\partial}{\partial z}\left(\overline{\rho V_y' V_z'}\right) \tag{3.67}$$

$$\sigma_z{}^R = -\frac{\partial}{\partial x}\left(\overline{\rho V_z' V_x'}\right) - \frac{\partial}{\partial y}\left(\overline{\rho V_z' V_y'}\right) - \frac{\partial}{\partial z}\left(\overline{\rho V_z' V_z'}\right) \tag{3.68}$$

Where σ^R = Reynolds stress component. In the eddy viscosity approach to turbulence modelling, these terms are inputted in the form of a viscous stress term with an unknown coefficient via the turbulent viscosity. An example of this statement is:

$$-\overline{\rho V_x' V_y'} = \mu_t \frac{\partial V_x}{\partial y} \tag{3.69}$$

The main advantage of this strategy comes from the observation that the representation of σ^R is of exactly the same form as that of the diffusion terms in the original equations.

The two terms can be combined if an effective viscosity is defined as the sum of the *laminar* viscosity and the *turbulent* viscosity.

$$\mu_e = \mu + \mu_t$$

<div align="right">(3.70)</div>

The solution to the turbulence problem resolves around the solution of the turbulent viscosity. In this case neither the Reynolds stress nor the turbulent heat flux terms have a fluctuating density. This is the result of the application of *Favre averaging* to the relevant equations too. This technique weights each term by the mean density to create a Favre averaged value variable, value for variable Φ which does not contain a fluctuating density:

$$\overline{\Phi} \equiv \frac{\overline{\rho\Phi}}{\overline{\rho}}$$

<div align="right">(3.71)</div>

3.16   CFD and SIMPLE Algorithm

CFD i.e. *computational fluid dynamics* is the science of using numerical methods and computers to simulate fluid dynamics [6-10]. CFD is applied in chapter 6 to simulate the hot gas flow on the micro-coated specimen model to compute erosion characteristics. With regards to the CFD analysis it is important to mention that the FLUENT simulation is conducted with the **SIMPLE** algorithm. The **SIMPLE** (Semi-implicit pressure linked equation) is a very efficient numerical algorithm which computes the discretized momentum equations to generate an interim velocity. The face mass flux is then computed using the momentum interpolation method. The discretized continuity equation is solved to generate the pressure correction. Next the cell-central pressure and velocity are corrected, and once convergence is attained the simulations are terminated. The turbulence calculations are linked to this procedure and further details are given in [11] in which gas turbine film cooling heat transfer has been analysed. Similarly, the temperature values are computed by solving the energy balance equation and updated with corrections.
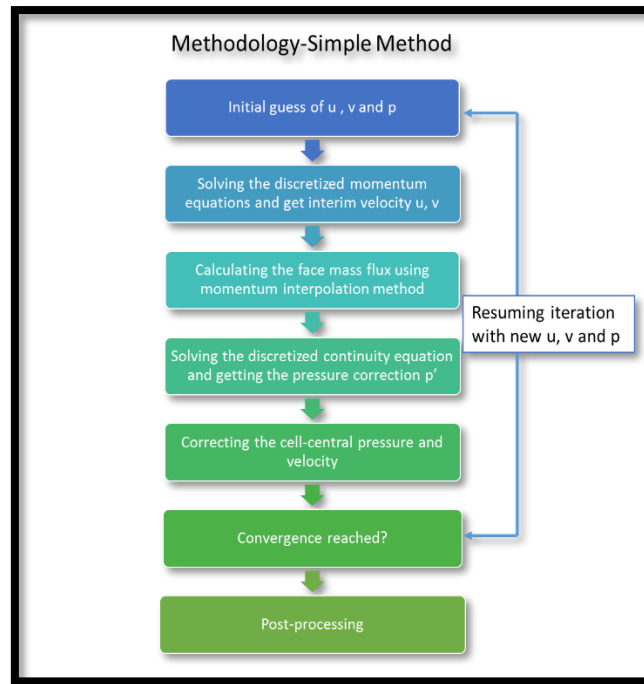
Figure 3.7: ANSYS FLUENT SIMPLE procedure

SIMPLE also employs a *second order upwind* numerical method which is necessary for turbulence to achieve a high degree of accuracy. SIMPLE computes the pressure and velocity. To employ second-order accuracy, the quantities at the cell faces are computed using a multidimensional Barth-Jespersen linear reconstruction approach [12]. Therefore, the accuracy is achieved at cell faces through a Taylor series expansion of the cell-centred solution about the cell centroid. Hence, the second order up-winding is selected, where the face value 'φ_f' is computed using the following expression:

$$\emptyset_f, SOU = \emptyset + \nabla\emptyset . \vec{r} \tag{3.72}$$

Here, 'φ' and '$\nabla\varphi$' are the cell-centred value and its gradient in the upstream cell, respectively. The parameter $\vec{r}$ is the displacement vector from the upstream cell centroid to the face centroid. This formulation requires the determination of the gradient '$\nabla\varphi$' in each cell. The gradient '$\nabla\varphi$' eventually reaches a limit so that no new maxima or minima are introduced. Second-order

upwind is available in the pressure-based and density-based solvers [13]. Convergence can be hindered by a number of factors. Large numbers of computational cells, overly conservative under-relaxation factors and complex flow physics are often the main causes. Sometimes it is difficult to know whether a converged solution has been attained. Other than mesh convergence study, numerical controls and modelling techniques can be exercised to enhance convergence and maintain stability. There are no universal metrics for judging convergence. Residual definitions that are useful for one class of problems are sometimes misleading for other classes of problems.

3.17   Discrete Particle Model (DPM) in ANSYS FLUENT

In addition to solving transport equations for the continuous phase, **FLUENT** [14] allows engineers to simulate a *discrete second phase* in a Lagrangian frame of reference. This second phase consists of spherical particles (which may be taken to represent droplets, bubbles, swarfing i.e. erosion of particles e.g. from a gas turbine blade surface) dispersed in the continuous phase. **FLUENT** computes the trajectories of these discrete phase entities, as well as heat and mass transfer to/from them. The coupling between the phases and its impact on both the discrete phase trajectories and the continuous phase flow can be included. **FLUENT** provides the following discrete phase modelling options:

- calculation of the discrete phase trajectory using a Lagrangian formulation that includes the discrete phase inertia, hydrodynamic drag, and the force of gravity, for both steady and unsteady flows
- prediction of the effects of turbulence on the dispersion of particles due to turbulent eddies present in the continuous phase
- heating/cooling of the discrete phase
- vaporization and boiling of liquid droplets

- combusting particles, including volatile evolution and char combustion to simulate coal combustion

- optional coupling of the continuous phase flow field prediction to the discrete phase calculations

- droplet breakup and coalescence

These modelling capabilities allow **FLUENT** to simulate a wide range of discrete phase problems including particle separation and classification, spray drying, aerosol dispersion, bubble stirring of liquids, rocket spray fuel injection, liquid fuel combustion, and coal combustion. The physical equations used for these discrete phase calculations are described next and thereafter instructions for setup, solution, and postprocessing are provided.

3.17-1 Particle Erosion and Accretion Theory

Particle erosion and accretion rates can be monitored *at wall boundaries*. The *erosion ra*te is defined as

$$R_{erosion} = \sum_{p=1}^{N_{particles}} \frac{\dot{m}_p C(d_p) f(\alpha) v^{b(v)}}{A_{face}} \tag{3.73}$$

Where $C(d_p)$ is a function of particle diameter, α is the impact angle of the particle path with the wall face (degrees), $f(\alpha)$ is a function of impact angle, v is the relative particle velocity (m/s), $b(v)$ is a function of relative particle velocity (m/s), and A_{face} is the area of the cell face at the wall (m²). Default values are $C = 1.8 \times 10^{-9}$, $f = 1$, and $b = 0$. Since C, f, and b are defined as boundary conditions at a wall, rather than properties of a material, the default values are not updated to reflect the material being used. One has to specify appropriate values at all walls. Values of these functions for abrasive materials eroding both carbon steel and aluminium

are given by Gupta *et al*. [15]. The erosion rate as calculated above is displayed in units of removed material/(area-time), i.e., mass flux, and can therefore be changed accordingly to the defined units in **FLUENT**. The functions C and f, have to be specified in consistent units to build a dimensionless group with the relative particle velocity and its exponent. To compute an erosion rate in terms of length/time (mm/year, for example) one may either define a custom field function to divide the erosion rate by the density of the wall material or include this division in the units for C and/or f. Note that the units given by **FLUENT** when displaying the erosion rate are no longer valid in the latter case. A variety of erosion models [16-20] containing model constants [21-22] and angle functions can be easily implemented into **FLUENT**. The equations describing some of the erosion models can be modified to appear in the form of the general equation describing the erosion rate. For example, the Tulsa angle dependent model [23] is described by Equation (3.74):

$$ER = 1559B^{-0.59}F_s \, v^{1.73} \, f(\alpha) \tag{3.74}$$

This can be rewritten with the following substitutions:

$$v^{1.73} \ = \ v^{b(v)}$$

$$1559 \, B^{-0.59}F_s \ = C\big(d_p\big) \tag{3.75}$$

Here ER is the erosion rate, B is the Brinell hardness and F_s is the particle shape coefficient. User-defined functions can be used to describe erosion models of any form. For more complex models, such as those models with varying function angles, $f(\alpha)$, the default "**Erosion Model"** in the wall "**Boundary Conditions"** panel cannot be used. Hence, a user-defined function should be used instead. For information on how to apply user-defined functions for DPM erosion models, one can refer to the **DEFINE_DPM_EROSION** macro in a separate UDF (user-defined function) module. Note that the particle erosion and accretion rates can be displayed only when *coupled calculations* are enabled. The accretion rate is defined as:

$$R_{accretion} = \sum_{p=1}^{N_{particles}} \frac{\dot{m}_p}{A_{face}} \qquad (3.76)$$

3.17-2 Discrete Phase Model (DPM) and Boundary Conditions

When a particle strikes a boundary face, one of several contingencies may arise:

- The particle may be reflected via an elastic or inelastic collision.

- The particle may escape through the boundary. The particle is lost from the calculation at the point where it impacts the boundary.

- The particle may be trapped at the wall. Non-volatile material is lost from the calculation at the point of impact with the boundary; volatile material present in the particle or droplet is released to the vapour phase at this point.

- The particle may pass through an internal boundary zone, such as a porous blade.

- The particle may slide along the wall, depending on particle properties and impact angle.

- Engineers can implement a user-defined function to model the particle behaviour when hitting the boundary. These boundary condition options are now described.

Figure 3.8: Erosion caused by corrosion in a jet engine gas turbine – [courtesy *Boeing, USA*]

ANSYS Fluent features advanced erosion fluid dynamics modelling by including three industry-standard models to the previous default model. Erosion wear is the loss of material due to repeated impact of solid particles on a surface and causes major economic losses across diverse industries such as oil and gas, hydraulic transportation, and chemical processes. Engineers need to quickly evaluate the erosion on dozens of design variations to find ways of stretching the parts lifespan in order to reduce costs and maximize process up-time. ANSYS aids greatly in achieving this. Although ANSYS formulations have been described above, it is judicious to briefly review the *physics of erosion*. Erosion is a mechanical process that happens due to the repeated impact of solid particles on a metal surface [24]. If the surface material is ductile, repeated particle impacts will result in the formation of craters and platelets; craters will grow with subsequent particle impact and eventually platelets are easily removed into the flow, **Figure 3.9-a**. Brittle material on the other hand, will grow lateral and radial cracks under sand particle impact, which will grow and eventually form small pieces that are removed by continuous solid particle impingement, **Figure 3.9-b**. Erosion is a complex phenomenon that depends on many parameters. Particle parameters can include the following:

- **Particle shape or angularity**

    Angular particles cause more erosion than spherical particles

- **Particle size**

$$\text{Erosion rate } (ER) \propto \left(d_p\right)^n \text{ with } 0.3 \leq n \leq 2$$

- **Erodent particle hardness**

$$ER \propto H_p \text{ with } H_p < 700HV$$

Flow parameters, on the other hand, have a stronger effect on erosion as it determines particle concentration, particle impact angle, and impact velocity. Other parameters affecting erosion are the properties of the target surface, i.e. surface hardness and multiphase effects [25].
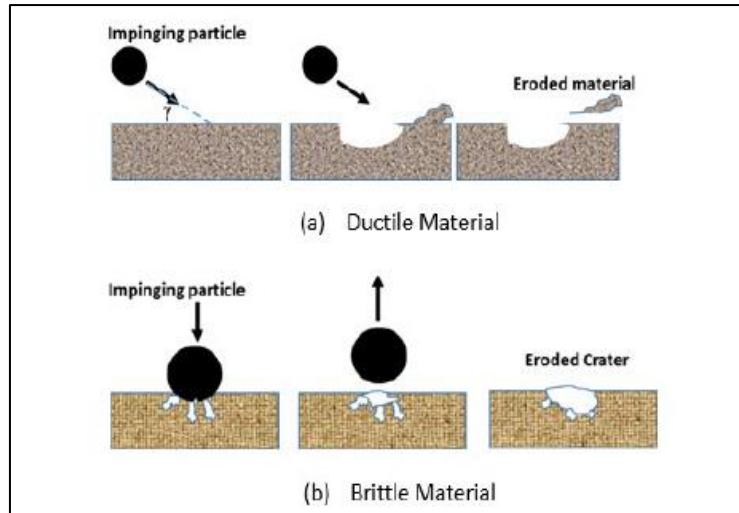
Figure 3.9: Erosion Mechanism (a) Ductile material (b) Brittle Material [25]

Progress in understanding the erosion due to solid particles has been achieved by the use of computational fluid dynamics (CFD). CFD allows the accurate modelling of fluid flow and particle trajectory in many applications including pipelines, bends, gas turbines etc. Once the impact velocity and angle of the particles colliding against the surface are calculated, empirical correlations to quantify the erosion rate can be implemented. Many empirical erosion correlations have been published in the literature. All include the impingement angle, impact velocity, particle diameter, particle mass, and collision frequency. A typical erosion model has the following general form as with the default erosion fluid dynamics model in ANSYS Fluent:

$$ER = \sum_{p=1}^{N_{trajt}} \frac{\dot{m}_p C(d_p) f(\alpha) v_p^n}{A_{face}} \tag{3.77}$$

Where,

- $\dot{m}_p$ is the mass flow rate of the particles (kg/s)

- $C(d_p)$ is particle diameter function (m)

- $f(\alpha)$ is the impact angle function (α) (degrees)

- v_p is the particle impact velocity (m/s)

- n is the velocity exponent (no units)
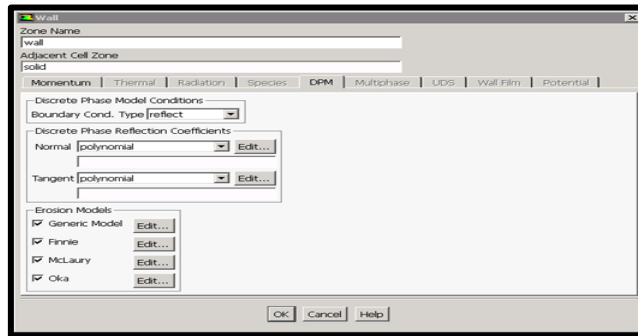
Figure 3.10: Erosion Models Available in ANSYS Fluent

As with turbulence modelling, there is no one size that fits all erosion models. Each erosion model has been empirically calibrated for a certain flow scenario, so one should consider the relevant flow conditions for each model before using any erosion model. Erosion rate is usually calculated *after the flow field* has been established in the domain. This can be thought of as a *post-processing step* for CFD analysis. Therefore, erosion can be predicted in low particle loading scenarios, particle volume loading <10%. Engineers must solve and converge the CFD model, save the case and data. Then the user selects and enables "Discrete Particle Model" from the model tree (**Figure 3.10**) and activates the Erosion/Accretion model from the "Physical Models" tab, as shown in **Figure 3.11.**
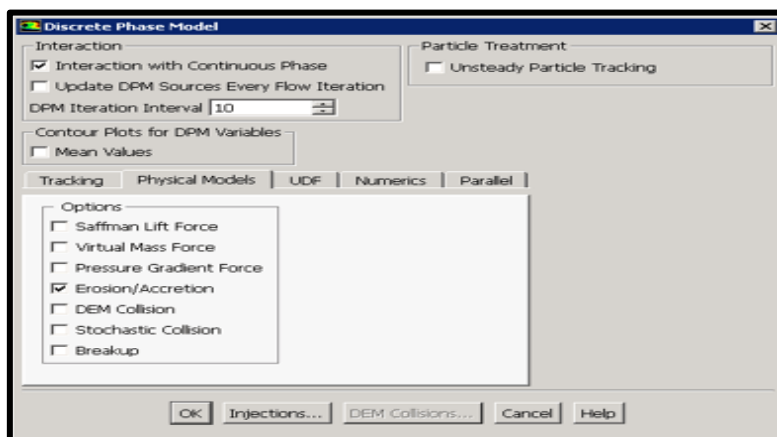
Figure 3.11: Discrete Particulate Model (DPM) Panel in ANSYS Fluent

Particle injections in the model are defined. Finally, the particle diameter, injection speed and flow rate with the particle normal and tangential reflection coefficients in the wall B.C. (Boundary Conditions) panel for the walls of interest are specified. In *chapter 6* it will be shown how the DPM option is also mobilized to simulate *hot gas injection as a continuous stream of high temperature uniform air particles representing corrosive gas impingement* on the blade sample onto the model. This provides a facility for computing the corrosion damage induced by hot gas turbine environments. The particles are set at a speed of 5 m/s with a temperature of 1273.15 Kelvins. Boundary conditions are left unaltered with the exception of the inlet with a similar velocity condition to that of the injected particles. A simple scheme with *second order upwind pressure and momentum* is selected and the solution converges after 427 iterations within a time frame of 180 minutes. All simulations with ANSYS FLUENT in chapter 6 have been executed using a Lenovo Y510p laptop machine with 8 GB of RAM and an Intel® Core i7-4700MQ CPU @ 2.4 GHz processor running on a Windows 10 platform.

3.18   Turbulence Models

In the CFD simulations reported later in this PhD (chapter 6), turbulent flow is considered as this is required for realistic gas turbine behaviour. A turbulence model is therefore implemented in ANSYS FLUENT. A turbulence model is a computational procedure used to close the system of mean flow equations i.e. *Reynolds averaged Navier Stokes (RANS) equations* [26]. For most engineering applications it is unnecessary to resolve the details of the turbulent fluctuations. Turbulence models allow the calculation of the mean flow without first calculating the full time-dependent flow field. The engineer only needs to know how turbulence affects the mean flow. In particular, to conduct simulations, expressions for the *turbulent Reynolds stresses* are required. For a turbulence model to be useful, it must have wide applicability, be accurate, simple, and economical to run (mesh densities should not be excessive). To describe the effects of turbulent fluctuations of velocities and scalar quantities in a single phase,

FLUENT uses various types of closure models. In comparison to single-phase flows, the number of terms to be modelled in the momentum equations in multiphase flows is large, and this makes the modelling of turbulence in multiphase simulations extremely complex. However, in the gas turbine CFD simulations in *Chapter 6,* only 2 phases are considered so mesh densities do not become insurmountable. **FLUENT** provides three methods for modelling turbulence (e.g. in multiphase flows) within the context of the k-$\in$ models. In addition, **FLUENT** provides two turbulence options within the context of the Reynolds stress models (RSM). The k-ε turbulence model options are:

- mixture turbulence model (the default)
- dispersed turbulence model
- turbulence model for each phase

Note that the descriptions of each method below are presented based on the standard k-ε model. The multiphase modifications to the RNG and realizable k-ε models are similar and are therefore not presented explicitly. The RSM turbulence model options are:

- mixture turbulence model (the default)
- dispersed turbulence model
- For either category, the choice of model depends on the importance of the secondary-phase turbulence in the application. In Chapter 6, the *k-epsilon standard turbulence model* has been adopted (for turbulent CFD hot gas flow on the micro-coated blade specimen model) and is described briefly below.

3.18-1 *k-* $\in$ **Turbulence Models**

FLUENT provides three turbulence model options in the context of the k - $\in$ models: the *mixture turbulence* model (the default), the *dispersed turbulence* model, or a *per-phase turbulence* model.

3.18-1.1 k - $\in$ Mixture Turbulence Model

The mixture turbulence model is the *default multiphase turbulence model*. It represents the first extension of the single-phase k-$\in$ model, and it is applicable when phases separate, for stratified (or nearly stratified) multiphase flows, and when the density-ratio between phases is close to 1. In these cases, using mixture properties and mixture velocities is sufficient to capture important features of the turbulent flow. The k and $\in$ equations describing this model are as follows:

$$\frac{\partial}{\partial t}(\rho_m k) + \nabla.(\rho_m \vec{v}_m k) = \nabla.\left(\frac{\mu_{t,m}}{\sigma_k}\nabla k\right) + G_{k,m} - \rho_m \epsilon \tag{3.78}$$

$$\frac{\partial}{\partial t}(\rho_m \epsilon) + \nabla.(\rho_m \vec{v}_m \epsilon) = \nabla.\left(\frac{\mu_{t,m}}{\sigma_\epsilon}\nabla \epsilon\right) + \frac{\epsilon}{k}\left(C_{1\epsilon}G_{k,m} - C_{2\epsilon}\rho_m \epsilon\right) \tag{3.79}$$

Here the mixture density and velocity, ρ_m and $\vec{v}_m$, are computed from:

$$\rho_m = \sum_{i=1}^{N}\alpha_i \rho_i \tag{3.80}$$

and

$$\vec{v}_m = \frac{\sum_{i=1}^{N}\alpha_i \rho_i \vec{v}_i}{\sum_{i=1}^{N}\alpha_i \rho_i} \tag{3.81}$$

The turbulent viscosity, $\mu_{t,m}$, is computed from:

$$\mu_{t,m} = \rho_m C_\mu \frac{k^2}{\epsilon} \tag{3.82}$$

The production of turbulence kinetic energy, $G_{k,m}$, is computed from:

$$G_{k,m} = \mu_{t,m}(\nabla\vec{v}_m + (\nabla\vec{v}_m)^T) : \nabla\vec{v}_m \tag{3.83}$$

The constants in these equations are the same as those for the single-phase k - $\in$ model.

3.18-1.2 Standard k-$\in$ Model

The simplest "complete models" of turbulence are *two-equation models* in which the solution of two separate transport equations allows the turbulent velocity and length scales to be independently determined. The standard k-ϵ model in **FLUENT** falls within this class of turbulence model and has become the workhorse of practical engineering flow calculations since the 1970s when it was proposed by Spalding and co-workers [27]. Robustness, economy, and reasonable accuracy for a wide range of turbulent flows explain its popularity in industrial flow and heat transfer simulations. It is a *semi-empirical* model, and the derivation of the model equations relies on phenomenological considerations and empiricism. As the strengths and weaknesses of the standard $k-\in$ model have become known, improvements have been made to the model to improve its performance. The standard $k-\in$ model [28] is a semi-empirical model based on model transport equations for the turbulence kinetic energy (k) and its dissipation rate ($\in$). The model transport equation for k is derived from the exact equation, while the model transport equation for $\in$ is obtained using physical reasoning and bears little resemblance to its mathematically exact counterpart. In the derivation of the $k-\in$ model, the assumption is that the flow is fully turbulent, and the effects of molecular viscosity are negligible. The standard $k-\in$ model is therefore valid only for fully turbulent flows. The transport equations for the Standard $k-\in$ Model feature the turbulence kinetic energy, k, and its rate of dissipation,$\in$:

$$\frac{\partial}{\partial t}(\rho k) + \frac{\partial}{\partial x_i}(\rho k u_i) = \frac{\partial}{\partial x_j}\left[\left(\mu + \frac{\mu_t}{\sigma_k}\right)\frac{\partial k}{\partial x_j}\right] + G_k + G_b - \rho\epsilon - Y_M + S_k \qquad (3.84)$$

and

$$\frac{\partial}{\partial t}(\rho\epsilon) + \frac{\partial}{\partial x_i}(\rho\epsilon u_i) = \frac{\partial}{\partial x_j}\left[\left(\mu + \frac{\mu_t}{\sigma_\epsilon}\right)\frac{\partial\epsilon}{\partial x_j}\right] + C_{1\epsilon}\frac{\epsilon}{k}(G_k + C_{3\epsilon}G_b) - C_{2\epsilon}\rho\frac{\epsilon^2}{k} + S \qquad (3.85)$$

In these equations, G_k represents the *generation of turbulence kinetic energy* due to the mean velocity gradients. G_b is the generation of turbulence kinetic energy due to buoyancy, Y_M represents the contribution of the fluctuating dilatation in compressible turbulence to the overall dissipation rate. $C_{1\epsilon}$, $C_{2\epsilon}$, and $C_{3\epsilon}$ are constants. σ_k and σ_ϵ are the turbulent Prandtl numbers for k and $\in$, respectively. S_k and $S_\in$ are user-defined source terms. The turbulent viscosity or eddy viscosity, μ_t, is computed by combining k and $\in$ as follows:

$$\mu_t = \rho C_\mu \frac{k^2}{\in} \tag{3.86}$$

Here C_μ is a constant. The model constants $C_{1\in}$, $C_{2\in}, C_\mu, \sigma_k$, and σ_ϵ have the following default values : $C_{1\in} = 1.44, C_{2\epsilon} = 1.92, C_\mu = 0.09, \sigma_k = 1.0, \sigma_\epsilon = 1.3$. These default values have been determined from experiments with air and water for fundamental turbulent shear flows including homogeneous shear flows and decaying isotropic grid turbulence. They are appropriate for gas turbine simulations. In *Chapter 6*, the standard *K-epsilon* turbulence model is used in micro-coating hot gas flow erosion simulations to provide enough refinement in the velocity field and simultaneously avoid excessive compilation times required with alternate turbulence models (e.g. RNG). Other models such as *k-omega* and Large Eddy Simulation (LES) are also applicable for this type of simulation but are not discussed here. As a first approximation the *K-epsilon* turbulence model is known to provide satisfactory results [29]. Since air is considered, the model constants in the "material physics" option in ANSYS FLUENT are left unaltered. *Viscous heating* i.e. kinetic energy dissipated as thermal energy via internal friction, is however *switched on* to achieve more elegant simulation of the interfacial heat transfer between the layers of the micro-coating CFD model described in chapter 6 (i.e. at the steel core-Titanium coating and Titanium coating-Silicon Carbide ceramic interfaces). The energy equation is activated to allow a 3-dimensional heat transfer analysis to be included, based on the classical Fourier law (i.e. thermal relaxation effects are neglected).

As described earlier, the **SIMPLE** (Semi-implicit pressure linked equation) algorithm is used in the ANSYS FLUENT CFD analysis in chapter 6. This is a very efficient numerical algorithm which computes the discretized momentum equations to generate an interim velocity. The face mass flux is then computed using the momentum interpolation method. The discretized continuity equation is solved to generate the pressure correction. Next the cell-central pressure and velocity are corrected, and once convergence is attained the simulations are terminated. The turbulence calculations are linked to this procedure and further details are given in Kadir *et al.* [30] and [31]-[34]. Similarly, the temperature values are computed by solving the energy balance equation and updated. The multi-stage process inherent to CFD simulation with ANSYS FLUENT is summarized in **Figure 3.13** as described in Kadir [35].
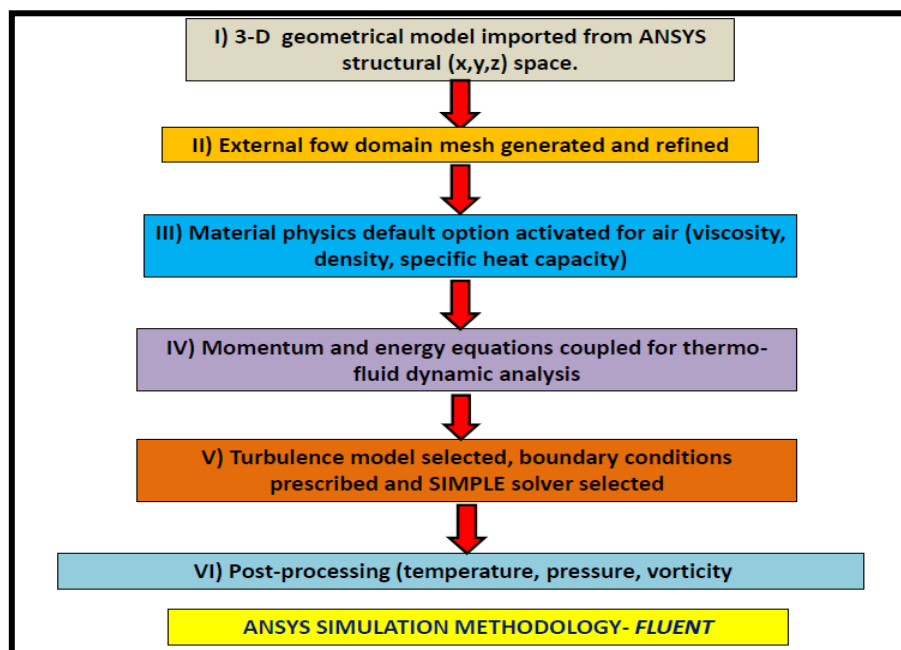
Figure 3.12: ANSYS FLUENT computational fluid dynamics procedure

3.19   Mesh Type

ANSYS FLUENT can use meshes comprising triangular or quadrilateral cells (or a combination of the two) in 2D, and tetrahedral, hexahedral, polyhedral, pyramid, or wedge

cells (or a combination of these) in 3D. The choice of which mesh type to use will depend on the application. When choosing mesh type, one must consider the following issues:

- setup time

- computational expense

- numerical diffusion

3.19-1 Setup Time

Many flow problems solved in engineering practice involve complex geometries. The creation of structured or *block-structured* meshes (consisting of quadrilateral or hexahedral elements) for such problems can be extremely time-consuming if not impossible. Therefore, setup time for complex geometries is the major motivation for using unstructured meshes employing triangular or tetrahedral cells. However, if the geometry is relatively simple, there may be no saving in setup time with either approach. Other risks of using structured or block-structured meshes with complicated geometries include the oversimplification of the geometry, mesh quality issues, and a less efficient mesh distribution (e.g., fine resolution in areas of less importance) that results in a high cell count.

3.19-2 Computational Expense

When geometries are complex or the range of length scales of the flow is large, a triangular/tetrahedral mesh can be created with far fewer cells than the equivalent mesh consisting of quadrilateral/hexahedral elements. This is due to the fact that a triangular or tetrahedral mesh allows *clustering of cells* in selected regions of the flow domain. Structured quadrilateral/hexahedral meshes will generally force cells to be placed in regions where they are not needed. Unstructured quadrilateral/hexahedral meshes offer many of the advantages of triangular/tetrahedral meshes for moderately complex geometries. A characteristic of

quadrilateral/hexahedral elements that might make them more economical in some situations is that they permit a much larger aspect ratio than triangular/tetrahedral cells. A large *aspect ratio* in a triangular/tetrahedral cell will invariably affect the skewness of the cell, which is undesirable as it may impede accuracy and convergence. Therefore, if one has a relatively simple geometry in which the flow conforms well to the shape of the geometry, such as a long thin duct, use a mesh of high-aspect-ratio quadrilateral/hexahedral cells. The mesh is likely to have far fewer cells than with triangular/tetrahedral cells. Converting the entire domain of the (tetrahedral) mesh to a polyhedral mesh will result in a lower cell count than the original mesh. Although the result is a *coarser mesh*, convergence will generally be faster, possibly saving some computational expense. In summary, the following practices are generally recommended and have been adopted in subsequent chapters of this PhD Thesis:

- For simple geometries, use quadrilateral/hexahedral meshes.

- For moderately complex geometries, use unstructured quadrilateral/hexahedral meshes.

- For relatively complex geometries, use triangular/tetrahedral meshes with prism layers.

- For extremely complex geometries, use pure triangular/tetrahedral meshes.

Excellent further details are given for finite volumes and mesh types in Rao [36].

3.19-3 Numerical Diffusion

A dominant source of error in multidimensional situations is numerical diffusion (false diffusion). The term *false diffusion* is used because the diffusion is not a real phenomenon, yet its effect on a flow calculation is analogous to that of increasing the real diffusion coefficient.

The following comments can be made about numerical diffusion:

- Numerical diffusion is most noticeable when the real diffusion is small, that is, when the situation is convection-dominated.

- All practical numerical schemes for solving fluid flow contain a finite amount of numerical diffusion. This is because numerical diffusion arises from truncation errors that are a consequence of representing the fluid flow equations in discrete form.

- The second order and the **MUSCL** (Monotonic Upstream-centred Scheme for Conservation Laws) as elaborated in Bég [37] is a discretization scheme used in **ANSYS FLUENT** which can help reduce the effects of numerical diffusion on the solution.

- The amount of numerical diffusion is inversely related to the resolution of the mesh. Therefore, one way of dealing with numerical diffusion is to refine the mesh.

- Numerical diffusion is minimized when the flow is aligned with the mesh.

This is the most relevant to the choice of the mesh. If one adopts a triangular/tetrahedral mesh, the flow can *never* be aligned with the mesh. If one uses a quadrilateral/hexahedral mesh, this situation might occur, but *not for complex flows*. It is only in a *simple* flow, such as the flow through a long duct, in which one can rely on a quadrilateral/hexahedral mesh to minimize numerical diffusion. In such situations, it is advantageous to use a quadrilateral/hexahedral mesh, since one will be able to get a better solution with fewer cells than if one were using a triangular/tetrahedral mesh. As an unstructured solver, **ANSYS FLUENT** uses internal data structures to assign an order to the cells, faces, and grid points in a mesh and to maintain contact between adjacent cells. Therefore, it does not require *i, j, k* indexing to locate neighbouring cells. This gives the flexibility to use the best mesh topology for a problem, as the solver does not force an overall structure or topology on the mesh. For 2D meshes, quadrilateral and triangular cells are accepted, and for 3D meshes, hexahedral, tetrahedral, pyramid, wedge, and polyhedral cells can be used. **Figure 3.13** depicts a variety of these finite volumes or cell types. Both single-block and multi-block structured meshes, as well as hybrid meshes containing

quadrilateral and triangular cells or hexahedral, tetrahedral, pyramid, and wedge cells are acceptable.
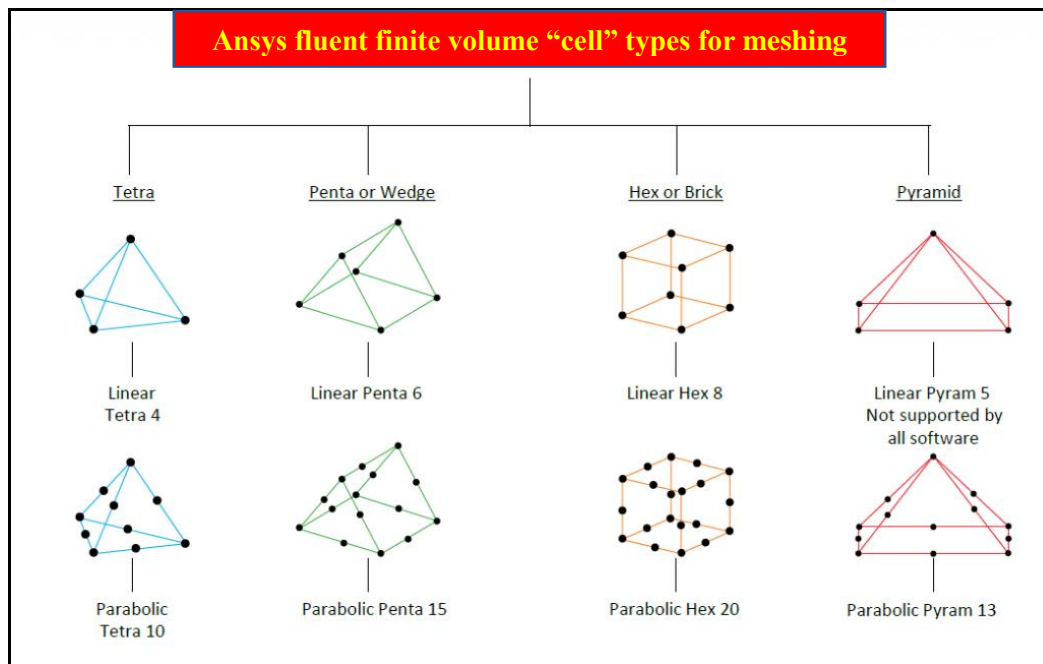
Figure 3.13: ANSYS FLUENT finite volume (cell) types used in 3-D simulations – Rao [36]

ANSYS FLUENT also accepts meshes with hanging nodes (i.e., nodes on edges and faces that are not vertices of all the cells sharing those edges or faces). Meshes with non-conformal boundaries (i.e., meshes with multiple subdomains in which the mesh node locations at the internal subdomain boundaries are not identical) are also acceptable. Some examples of meshes that are valid for **ANSYS FLUENT** are presented below. Further elaboration on cell shapes and their face-node connectivity are explained in the ANSYS FLUENT Theory Manual [13]. O-type meshes, meshes with zero-thickness walls, C-type meshes, conformal block-structured meshes, multiblock structured meshes, non-conformal meshes, and unstructured triangular, tetrahedral, quadrilateral, hexahedral, and polyhedral meshes are all acceptable in FLUENT CFD simulations.

3.20 Conclusions

In this chapter all theoretical and numerical aspects relevant to the advanced 3-D CFD/thermal elastic stress analysis presented in Chapter 6 for micro-coated and nano-coated blade specimen models, have been reviewed. More precise details of data specification, mesh design, boundary conditions, material physics and other aspects are elucidated later in chapter 6.

The FEA/CFD simulations allow a good platform for comparison with the experimental micro-/nano-coating thermal tests described in Chapter 5.

The relevant experimental apparatus (TGA and SEM) and procedures are reviewed in the next chapter (chapter 4) for the entire PhD and apply specifically to the experimental results generated and described in *Chapter 5* for both micro-/nano-coated blade substrates.

CHAPTER 4: EXPERIMENTAL METHODOLOGIES FOR HIGH TEMPERATURE CORROSION PROTECTION WITH MICRO-/NANO-COATINGS.

4.1 Introduction

In this chapter the experimental apparatus and laboratory procedures employed for high temperature corrosion protection testing of micro-coating (titanium and silicon carbide) and nano-coating (aluminium oxide and titanium oxide) are described. The flame heating thermal spraying gun is employed in the coating of the tested specimens and is one of the best techniques used to protect the components from abrasive wear, adhesive wear, erosive wear, fatigue and *high temperature corrosion*, the latter being the focus of this PhD Thesis. **TGA** (Thermographic Analysis) and **SEM** (Scanning Electro-Microscope) with energy dispersive x-ray (EDS) testing of the flame spray coated specimens relating to the performance of alloy-coated specimens under high temperature are described. Devices for securing and preparing coating mixtures i.e. the sample holder, grit blasting machines and ultrasonic mixer are also reviewed. Data processing for oxidation mass is shown and based on this procedure the appropriate calculations are described in chapter 5 for micro-coating and nano-coating samples, enabling a comparison of corrosion rates. Extensive visuals of all apparatus deployed is included.

4.2 Sample (material/manufacture/dimensions)

AISI 304 stainless steel is selected for the blade specimen since it has good mechanical properties due to good machining characteristics. The AISI 304 steel specimens were cut and machined in the workshop at Salford University. 10 bare rectangular steel test samples were produced in preparation for coating. Each sample had the following dimensions, 20mm x 10 mm x 1.5mm. The geometry is shown in **Figure 4.1**. A small hole was drilled at the top end of each sample for placement inside the TGA (not shown in **Figure 4.1**).
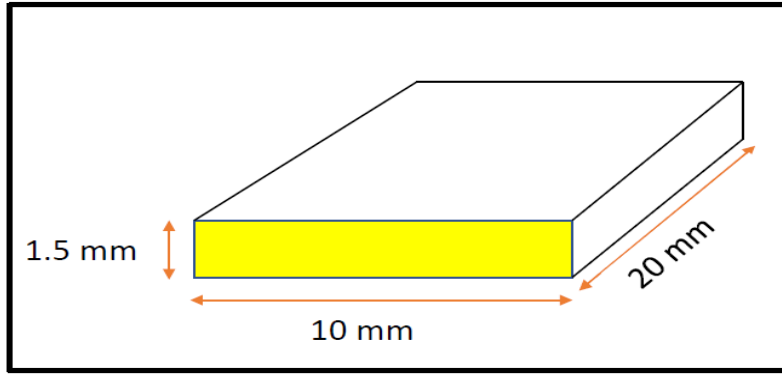
Figure 4.1: Dimensions of the substrate (uncoated) sample.

Table 4.1 below shows the chemical composition of the AISI 304 steel:

Cr	Ni	Mn	Cu	Co	Mo	Si	C	P	S	N	V	Nb	Ti
18.31	8.31	1.51	0.30	0.12	0.21	0.42	0.08	0.032	0.002	0.0389	0.083	0.009	0.003

Table 4.1: Constituent chemicals in AISI 304 Austenitic steel substrate (wt %) [1].

The uncoated sample is shown below in Figure 4.2.

Figure 4. 2 Uncoated sample.

4.3 Apparatus for sample preparation

4.3-1   Grit Blasting machine

Grit blasting is the standard equipment used for surface roughening. **Figure 4.3** shows a typical

Grit blaster (MEGA 4).

Figure 4.3: Grit Blasting Machine (Mega 4, Abraclean, GmbH 42327 Wuppertal, Germany).

Grit Material Used	Ceramic Grit, Silica
Grit Feed	Suction
Blasting Atmosphere	Cabinet Blasting
Distance between Nozzle and work Piece	10-15 cm
Gas	Synthetic air

Table 4.2: Principal details for grit blasting

The grain size of the grit blaster depends on the size of the sample which will be sprayed; for a thin piece, a finer grit size is required which will result in a finer and smooth surface after spraying applied.

4.3-2 Grinding and Polishing

Grinding is used to obtain the correct and the accurate dimension and polishing to achieve the required surface roughness. The grinder device used in the process was a Metaserv 2000.

The description and characteristics of the device are:

- Abrasive Format: Silicon-Carbide paper
- Silicon-carbide(sand) grinding paper
- Abrasive size; P200, P600, P800 and P1200
- Cooling System- water
- Platen Head(rev/min); 150 rev/min.

Each abrasive size is applied for period of 5 minutes, starting at P200 and ending at P1200.

Figure 4.4: Metaserv 2000 Grinding Machine.

Polishing will eliminate the deformation generated during the grinding procedure and all the smears from the surface of the substrate. Two steps are involved in the polishing- diamond and oxide polishing. Diamond polishing is more useful and effective. The most popular diamond particle dimensions are 6, 3, 1 micron and each abrasive size is applied for 5 minutes in turn, starting at 6 μm up to 1 μm. The polisher used in this process is Buehler Metaserv.

Figure 4.5: Polishing machine (Buehler Metaserv).

4.3-3   Ultrasonic Degreasing

The sample is sand-blasted and ultrasonically degreased in acetone for 15 minutes and finally cleaned with ethanol prior to coating. Ultrasonic cleaning is the most efficient and economical method for removing oil and grease from the surface of the specimen before the coating is applied [2].
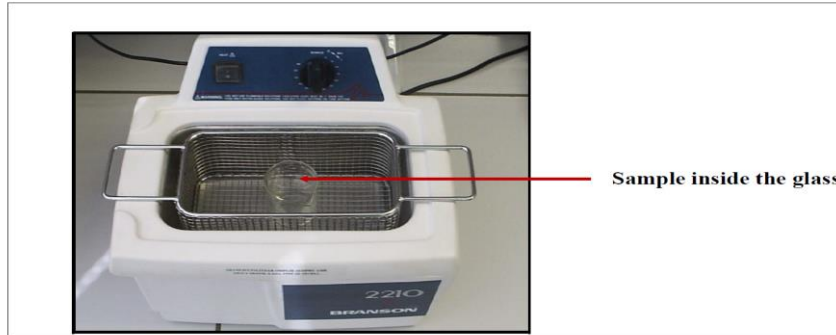
Figure 4.6: Ultrasonic degreasing machine (Branson 2210, Merck KGaA, Darmstadt, Germany).

4.4 Apparatus for coating

4.4-1 Sample Holder

The sample holder used made the spraying easier to apply since the sample was fixed and easy to rotate it at an angle around the two axes and all the edges and corners as shown in the schematic in **Figure 4.7**. The sample holder was designed and manufactured at the Department of Industrial Engineering, University of Juame I, Spain.
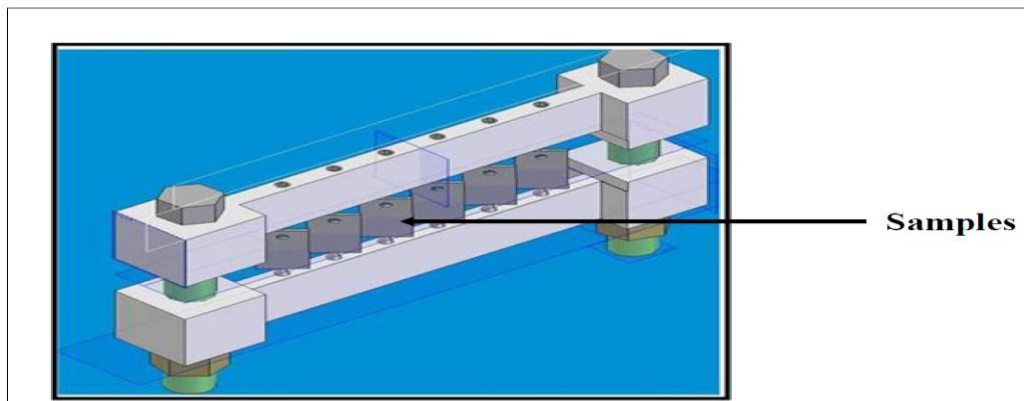
Figure 4.7: Schematic of sample holder (University of Juame I, Spain).

4.4-2 Flame heating thermal spray gun for coating

An industrial thermal spraying method [3] was used for depositing the micro- and nano-coatings on the gas turbine specimens. This was done for both the bonding material (NiCrAlY) and also for the (titanium + silicon carbide ceramic) double layer micro-coatings and the 60:40

(Al_2O_3: TiO_2) nano-coating materials. The procedure was carried out by using a flame heating thermal spray gun (Oxyfuel) known commercially as CastoDyn DS8000 oxy-acetylene thermal spray, as shown in **Figure 4.8**; the device is designed to be easy to use and safe. The device is a modular design and allows easy deposition of (powder form) coating spray to most alloys [4, 5].
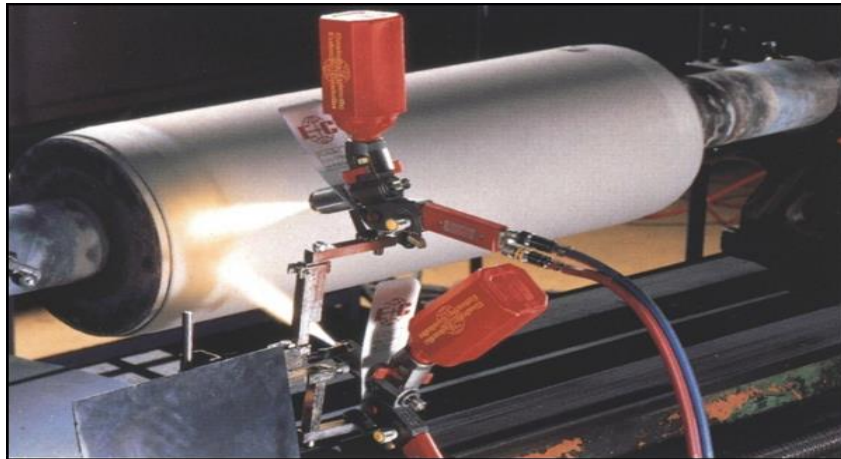
Figure 4.8: Flame Heating Thermal spray gun (Oxyfuel)- [Courtesy- Castolin GmbH, Germany].

The heat source is an Oxy-acetylene flame towards the centre in which the powder transferred by means of non-combustible carrier gas such as oxygen, neutral gas or dry compressed air.
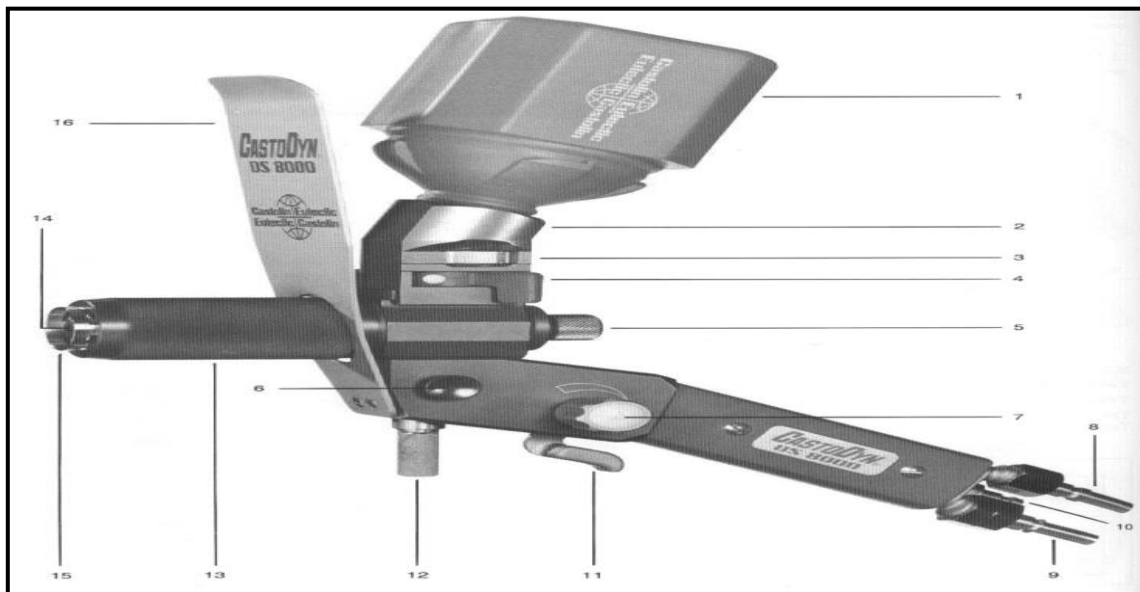
Figure 4.9: The assembled torch with components [Courtesy- Castolin GmbH, Germany].

Figure 4.9 shows the assembled torch with its components such as alloy powder, mounting powder container, powder injection, spray unit, flame zone, rapid shut-off lever, and compressed air nozzle. The numbered components are as follows:

1. Standard powder container

2. Powder containing mounting

3. Powder flow control diaphragm with 6 settings

4. Oburator. Allows the powder container mounting to be put on or taken off

5. Powder injector. Determines the flow rate of the powder carrier gas

6. Compressed air valve

7. Acetylene valve. Allows flow of acetylene to be adjusted to obtain the required flame (neutral, oxidizing or carburising)

8. Connector for oxygen

9. Connector for acetylene

10. Connector of the compressed air

11. Rapid shut-off lever for oxygen and acetylene

12. Mounting spigot

13. Knurled nozzle cover

14. Flame nozzle. Serves to introduce the powder into the flame

15. Compressed air focusing nozzle

16. Heat shield

Figure 4.10 shows internal components of the rapid shut-off lever whereas **Figure 4.11 (a), (b)** shows the acetylene control valve which signals when the lever is turned into 'on' position allowing the oxy-acetylene mixture to flow. The acetylene valve produces a neutral flame. Turning the knob on the valve makes the flame more oxidising or carburising [5].
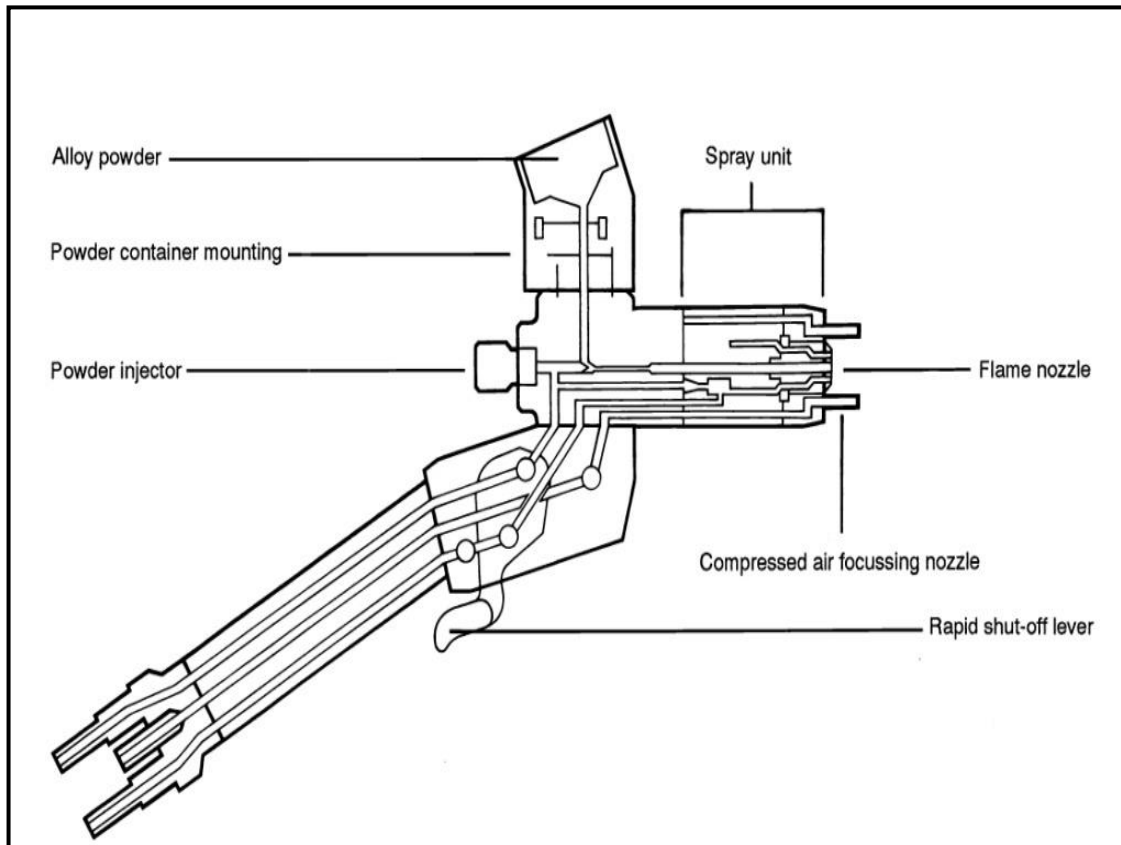
Figure 4.10: Schematic diagram for rapid Shut-off lever [Courtesy- Castolin GmbH, Germany].
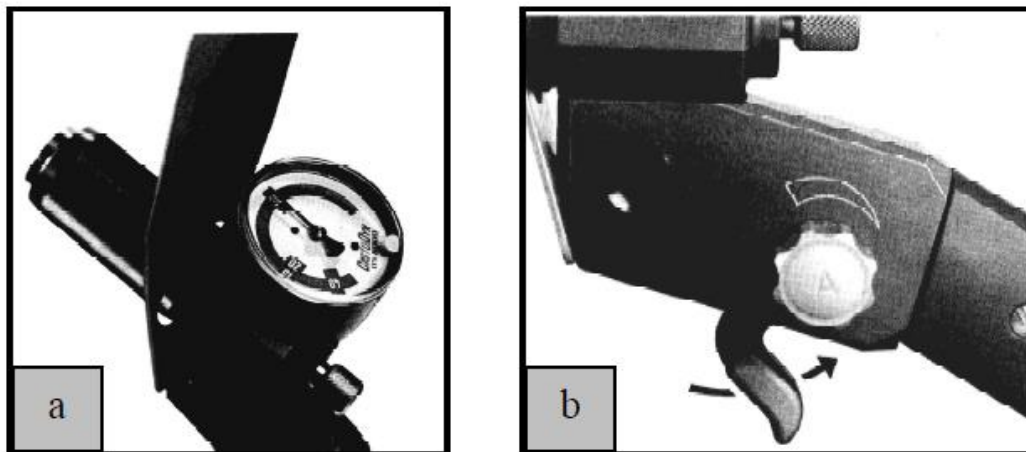
Figure 4.11: a) acetylene control valve (b) rapid shut-off lever [Courtesy- Castolin GmbH, Germany].

The microstructure of the coating relies on the coating components [6]. The *bonding material is* MCrAlY metallic powder (both Yttrium and Aluminium have high affinity for Oxygen and

Oxide during thermal spraying and the sprayed coating will therefore have fine sparse Aluminium and Yttrium-rich oxide distribution [7]. When the coating is completed on the specimen, the oxides are uniformly distributed in the material. In general, for protective coatings with high temperature corrosion resistance, thermally insulating coatings, clearance control coatings and the repair of superalloy components, the Flame Heating Thermal spray gun (Oxyfuel) is efficient and easy to handle, was therefore adopted in the present PhD.

4.5 Apparatus for Thermal testing and data analysis

The TGA apparatus used for conducting thermal tests and producing data for oxidation and corrosion rates as a function of time for the *non-coated* and *coated* gas turbine blade substrate samples is now described.

4.5-1 Thermogravimetric Analysis (TGA)

Thermogravimetric analysis (TGA) is a device which applies heat in a controlled environment (oven) and measures changes in mass or weight in response to increases in temperature or time, as shown in **Figure 4.12**.
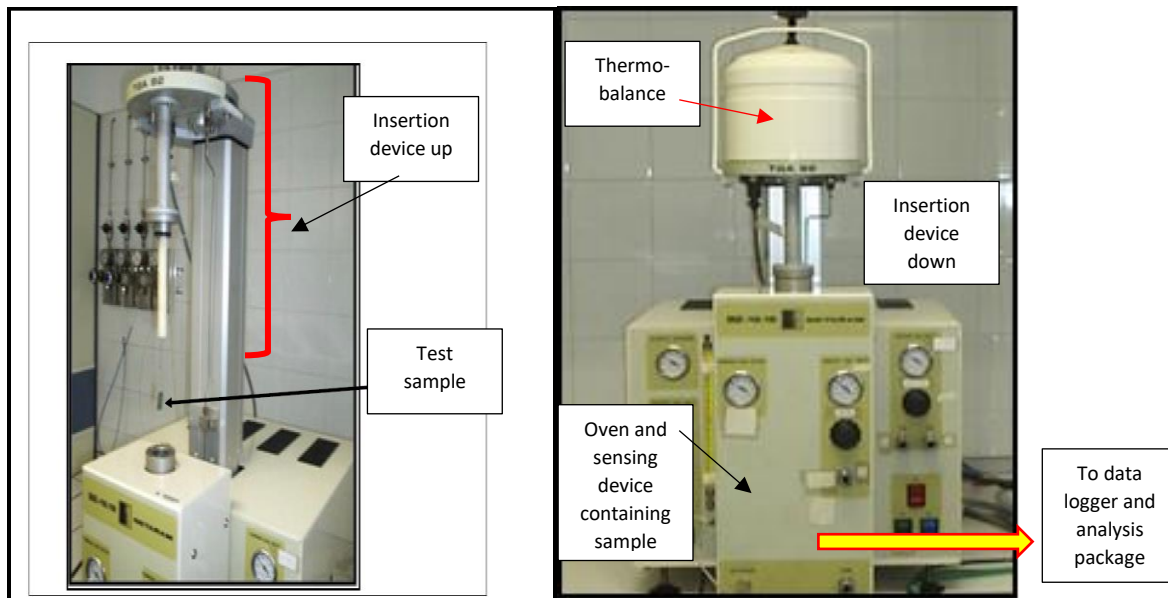
Figure 4.12: TGA Device [92-16 Setaram].

These kinds of measurements can give valuable information about a material response to oxidation, composition, decomposition kinetics, moisture content etc.

TGA [8] is one of the most important devices used to measure *oxidation kinetics*. The principle of the gravimetric technique is to measure the change in weight due to oxidation as a function of *time*.

Thermogravimetry is a sub-section of thermal analysis which will measure the physical quantity as a function of temperature. In thermogravimetry the mass change is measured. In isothermal oxidation, the specimen is exposed to temperature in a furnace at a fixed temperature and the measurement of the weight change taken as a function of time, and many values of the temperature are generated to determine the activation energy of the oxidation reaction.

The biggest advantage of a thermogravimetric apparatus with an automatic recording balance (*thermo-balance*) shown in Figure 4.13 is the *continuity of recording* the kinetics reaction. After completion of the coating process, the resulting sample is cleaned in acetone and then secured inside a Thermo-balance within the TGA device in synthetic air (1 bar pressure). Commencing from room temperature (20 Celsius) the sample is heated up to approximately 1000 Celsius at a rate of 40 Kelvins/minute. During this heating process, the coated sample is exposed to significant oxidation in the thermo-balance, for a period of 50 hours. Subsequently it is cooled again at a rate of 40 Kelvins/minute.
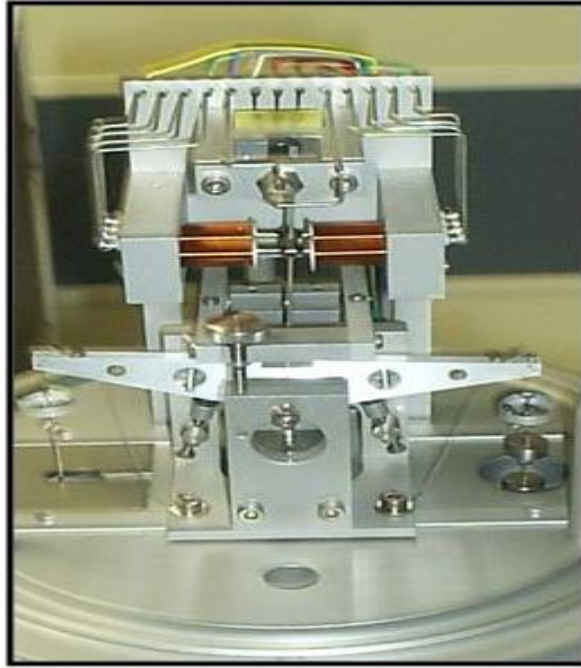
Figure 4.13: Thermo-balance [92-16 Setaram, Themys-h2, USA].

TGA is a useful method for studying the dynamics and mechanisms inherent to high temperature corrosion effects as elaborated by Wagner [8]. However, a disadvantage is *that only one very small sample can be tested each time* which makes the procedure very time-consuming and restricts testing to very small specimens, not entire coated gas turbine blades. In this regard *computational mechanics simulation*, which is described in chapter 6, provides a better and quicker method which can accelerate the generation of results in "real time". Simulation in this sense is like a "time machine". One can predict future behaviour and refine the load/thermal conditions on a gas turbine substrate model with the comfort of not having to re-set experiments which take many days if not weeks. Simulation therefore offers the advantage of "time compression technology" since multiple simulations can be run in parallel. This cannot be done with a single apparatus in the laboratory!

The kinetic data for material oxidation gives useful information enabling a good estimation of the life of the component at high temperature. The rate of oxidation is a key factor influencing corrosion in high temperature gas turbine engine environments. Oxidation rate provides an

approximation of the design life of the metal which will be used as a component in a specific temperature and environment. In addition, it produces data and information regarding how fast the oxidation happens and the life expectancy of the material employed under certain atmospheric and thermal conditions.

4.5-2 Oven

The oven was used to heat the uncoated AISI 304 substrate sample and is shown in **Figure 4.14,** for 24 hours of 900 ^{0}C.
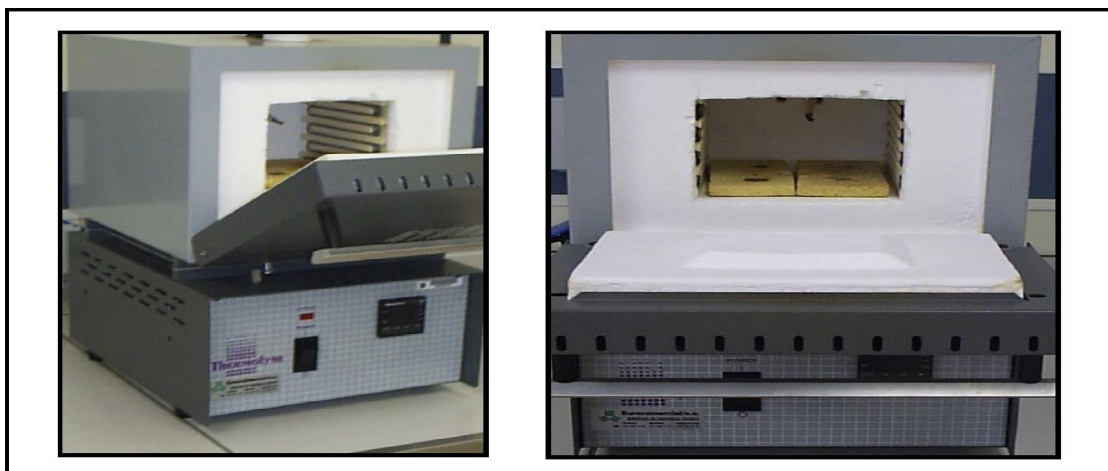
Figure 4.14: Heat Treatment furnace [Thermolyne 47900 Bench Muffle Furnace, manufacturer Thermo Scientist, USA].

4.6 Apparatus for coating morphology and elemental composition analysis

To investigate the morphology of the TGA tested specimens, SEM is used. Thereafter elemental composition of the coatings is studied with EDS. These two techniques were combined in the apparatus shown in **Figure 4.15**. Both SEM and EDS are now described.

Figure 4.15: Scanning Electron Microscope and all other components [Quanta FEG 250, Germany].

4.6-1 Scanning Electron Microscopy (SEM)

The generation of any image depends on the wavelength of light source used. Standard light has a wavelength in the range of 400-700 nm (nano meters) = 4×10^{-7} to 7×10^{-7} m. All electron-based systems have a high resolution and will produce grain boundaries and other parameters such as nodules, surface contents and many other phases which will have a variety of shapes and surface roughness. In SEM the *electrical current* will control the spot size, current size i_p i. e. probe current is usually 22 pA and the probe diameter d_p = 2 nm which is the best option for obtaining better contrast and resolution and the recommended voltage is 15Kv. Further details are given in Reimer [9].

(a)   Secondary Electrons (SE)

These are low energy electrons (< 50 eV) with low current of recommended value of 1-200 pA usually ejected from the specimen atoms by the primary beam. These electrons will generate high resolution images due to the low current value. They are produced by an electron beam or any scattered electrons which pass closer to the surface. They are emitted after a few collisions with atoms and lose most of their energy before emerging from the surface. Secondary electrons are therefore generated by *inelastic collisions* when the incident electron beam hits a specimen, and escape from a *shallow* depth. They originate from the *surface regions* and can show *topography of the sample* studied. The recommended current for SE is 1-200 pA [9].

(b)   Back Scattered Electrons (BSE)

These electrons are primary beam electrons scattered back out at the specimen; they have a range of energies up to the primary energy level. The electrons are reflected back with minimal collision with the atoms surface. They are the result of *elastic collisions of electrons with atoms*, which result in a change in the electron trajectories. Larger atoms are much stronger scatterers of electrons and therefore produce a higher signal. BSEs produced will have different energies, which will depend on the type of atom with which they impact. BSEs originate from *deeper regions* of the sample, whereas SEs originate from *surface regions*. Thus, the two carry different types of information. BSE images show high sensitivity to differences in atomic number; the higher the atomic number, the *brighter* the material appears in the image (SE imaging can provide more detailed *surface* information). The number of the BSEs reaching the detector is proportional to their atomic number. This dependence of the number of BSEs on the atomic number helps differentiate between different phases, providing imaging that carries information on the *sample composition*. BSEs reveal information about the *internal features of a specimen and elemental composition related to atomic number, as well as topographical information*. Both SEs and BSE can therefore be used in analysing coating topography. Typical example of BSE micrographs are given in the next chapter (Figures 5.12, 5.22).

The phase disparity will show in SEM micrographs, which is mostly due to the difference in the quantity of the atoms with which the electrons collide. The recommended current in BSE is 50 pA-2 nA [9].
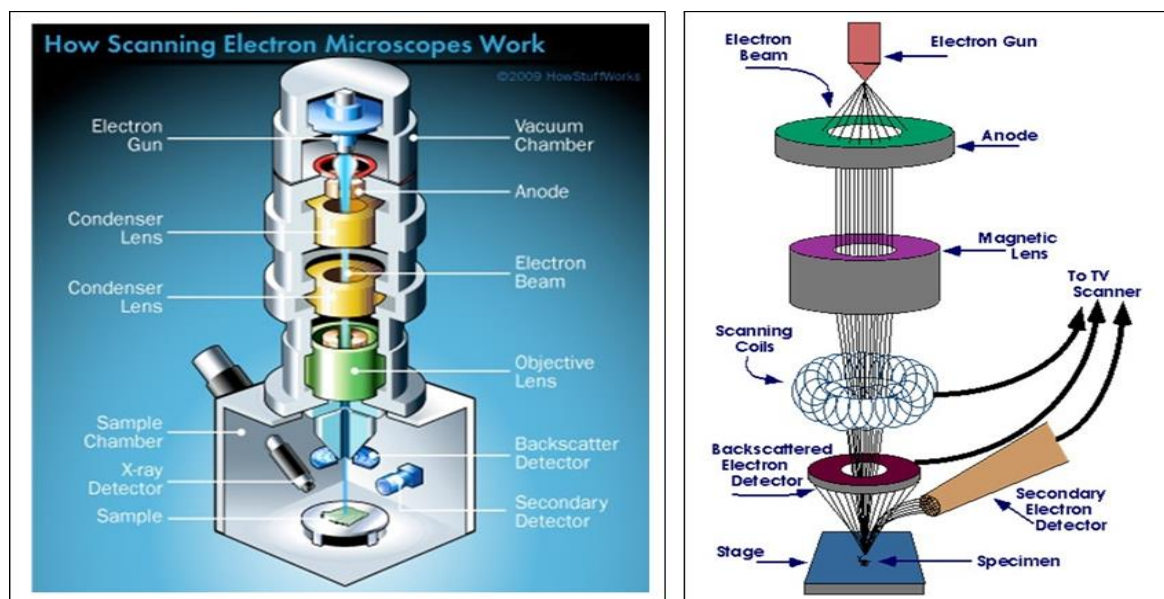
Figure 4.16: Scanning Electron Microscope (SEM) operation
(https://science.howstuffworks.com/scanning-electron-microscope2.htm).

The advantage of SEM is the impressively high magnification range. **Figure 4.16** shows how SEM operates. It can obtain 1-4nm imaging resolution depending on the instrument. Oxide samples can be tested on SEM directly providing they are coated with thin graphite on the surface to make it conductive since oxides in general are non-conductive and the charge accumulation on them can make the image unclear.

The accelerating voltage on Sem is 1-40 KeV, the magnification is usually up to 200,000x, and these values do vary in different SEM's. In the SEM shown in **Figure 4.16**, a source of electrons is concentrated in a vacuum into a fine probe which is passed over the surface of a sample. The electrons are generated by an electron gun, the point on the electrons are magnified by a series of lenses. When the electrons penetrate the surface, several interactions occur which will result in the emission of the electrons or photons from the surface. The emitted electrons are received by the detector and used to adjust the brightness of cathode ray tube. At every point the electrons hit the surface of the sample this is transferred to the corresponding point on the screen. The accumulated points produce a sample image displayed on the monitor.

4.6-2 Energy Dispersive Spectrometer (EDS)

Energy dispersive spectrometer or energy dispersive X-ray is a device attached to the SEM for compositional analysis but is independent of the mode of detection i. e. whether SE or BSEs are used. BSEs however give more detailed surface morphology based on contrast variation. EDS *or* EDXA [9] is a quantitative or semi-quantitative technique. The signal generates all the elements present on the surface of the specimen such as metal, oxide and other materials. The resolution of the EDS is between 150eV-200eV and the recommended current is 100 pA-10 nA. The EDS analysis results allow only the determination of the *elemental composition* in the tested samples (e. g. metallic elements) but do not provide details on the *mineralogy of the oxidation products*. However further studies with XRD (X ray diffraction) would enable the mineralogy of the oxidation to be determined providing deeper insight into the coating performance.

4.7 Experimental procedure

4.7-1 General procedure

In this section, all stages of the experimental procedure are explained as shown in **Figure 4.17**.
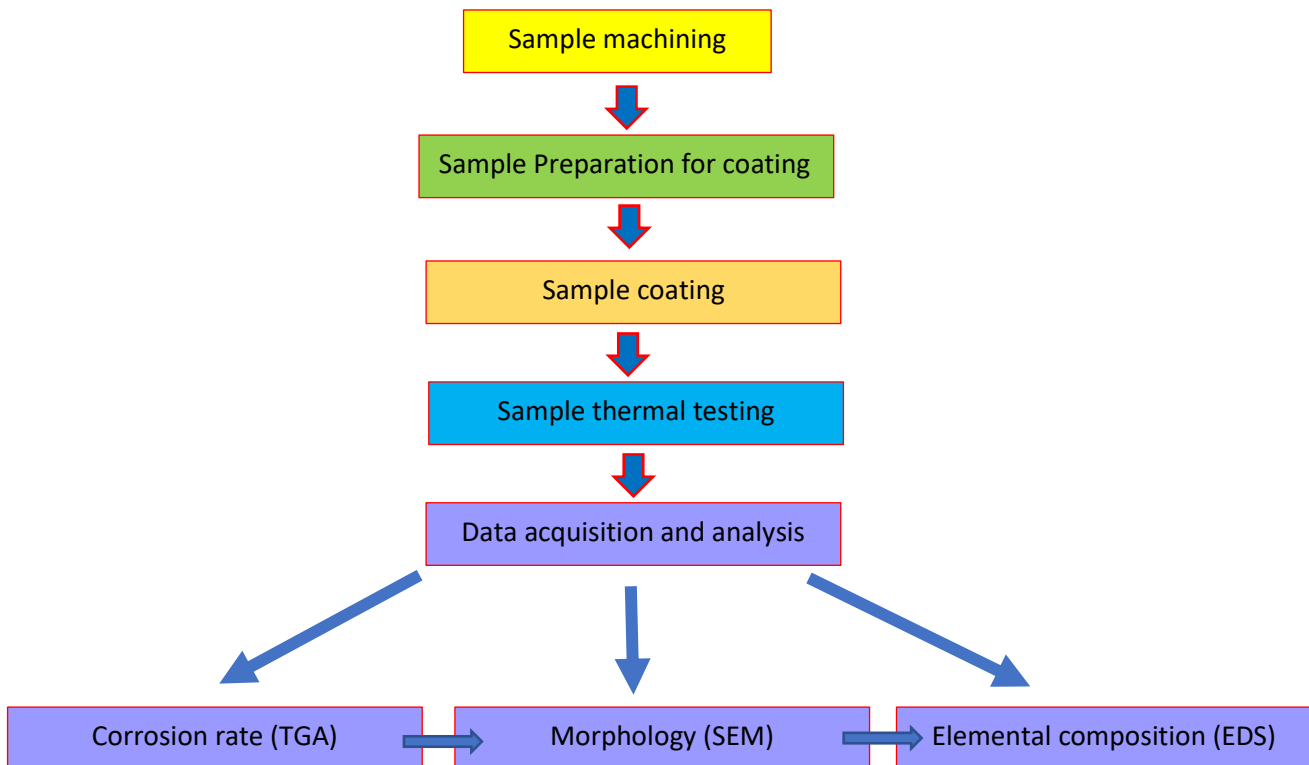
Figure 4.17: Overall experimental procedure for coated specimens.

4.7-2 Sample Machining

The machining of the samples and dimensions have already been described in section 4.2**.**

4.7-3 Sample preparation prior to coating

After machining, the sample was prepared for the coating process. The following steps were

followed.

1) The sample was sand-blasted using the grit-blasting machine (section 4.3-1).
2) The sample was then ground and polished using the grinding and polishing machines (section 4.3-2).
3) The sample was then finally cleaned (in order to ensure effective bonding and minimization of surface defects) with the ultrasonically degreasing machine (section 4.3-3) in acetone for 15 minutes and finally cleaned with ethanol prior to coating.

4.7-4 Sample coating

Prior to coating, each sample was attached to the sample holder (section 4.4.1). The sample was then either *micro-coated* or *nano-coated* using the flame heating thermal spraying gun (section 4.4-2). An example of the *nano-coated* sample is shown in **Figure 4.18** before thermal testing.

Figure 4.18: Nano-coated sample.

It should be noted that the micro-coating uses *two protective layers*, a separate titanium layer on the substrate with a superimposed upper silicon carbide ceramic layer. The resulting system is therefore considered as a *3-layered system* i.e. the substrate plus the two micro-coating layers, as shown in **Figure 4.19 a**. However, the nano-coating comprises a *single layer* of alumina (aluminium oxide) and titania (titanium oxide) nano-powder mix and the resulting system is therefore considered as a *2-layer system* i.e. substrate plus the single nano-coating layer, as shown in **Figure 4.19b**.
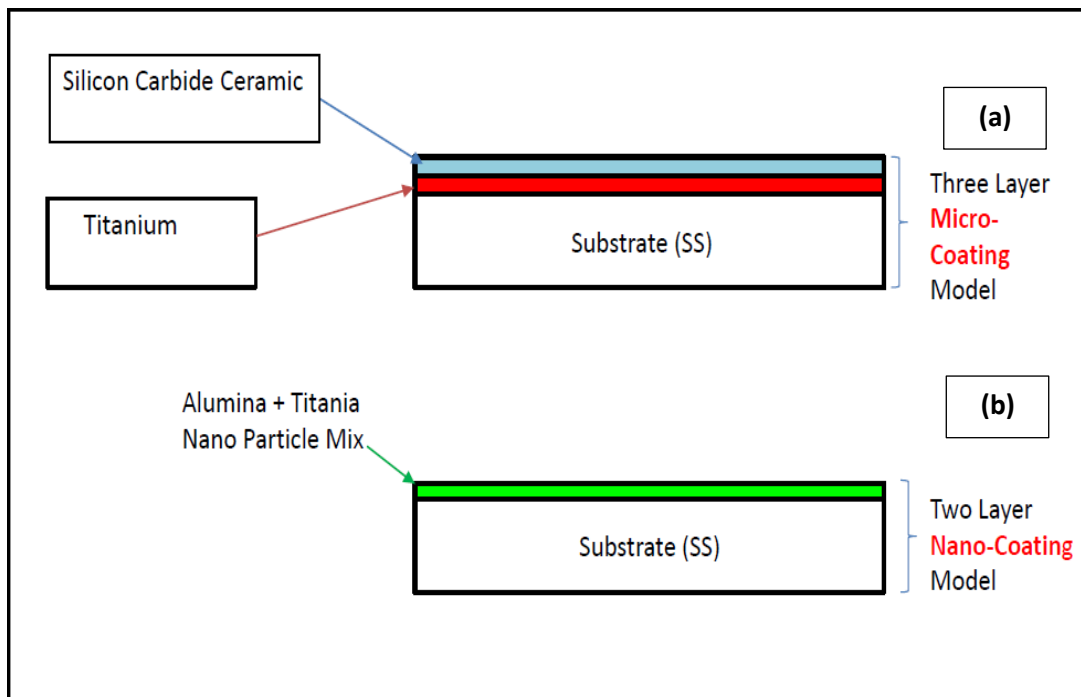
Figure 4.19 a) 3-layer micro-coating design and **b)** 2-layer nano-coating design.

4.7-5   Sample TGA thermal testing

Each *micro-coated sample* was inserted into the oven of the TGA device for a total period of

50 hours to reach a maximum temperature of just over 1000 Celsius and just under 1100 Celsius

(section 4.5-1).

Each *nano-coated sample* was inserted into the oven of the TGA device for a total period of 50

hours but in this case a maximum temperature of 850 Celsius could only be achieved since the

machine became inoperative above this temperature (section 4.5-1).

4.7-6   Data acquisition and analysis

The corrosion rate was measured with the TGA sensors inside the oven and the data was

recorded via a data logging system on a desk top workstation connected to the TGA (section

4.5-1).

The morphology of the tested samples was captured using SEM (section 4.6-1).

The elemental composition of the tested samples was finally determined with EDS (section

4.6-2).

CHAPTER 5 EXPERIMENTAL STUDY OF HIGH TEMPERATURE OXIDATION BEHAVIOUR OF AISI 304 STAINLESS STEEL COATED WITH MICRO-COATING AND NANO-COATING

5.1   Introduction

In chapter 2, several gaps in the scientific literature on experimental studies of *titanium/silicon carbide ceramic micro-coatings*, and *metallic oxide i.e. 60: 40 aluminium oxide-titanium oxide nano-coatings* were identified. In this chapter, therefore, detailed experiments relating to the performance of these two novel micro-coating and nano-coating systems for gas turbine blade specimens under high temperature are described, compared, and interpreted at length. The coated specimens have been tested first in the TGA device in order to evaluate oxidation mass and estimate the corrosion rates. The parabolic growth curve obtained is shown to agree with a benchmark reference test on high temperature behaviour of an uncoated AISI 304 bare steel sample. The corrosion rates measured are compared between the micro-coating and nano-coating performance. Following the TGA analysis, SEM and EDS have then been employed to analyse morphology and the elemental composition, respectively. It is important to note that these procedures only permit the determination of the elemental composition and cannot provide information on the mineralogy of the oxidation products, for which XRD (X ray diffraction) is required. The structure of this chapter is therefore as follows:

1) TGA results for:

- uncoated AISI 304 bare steel sample (based on the benchmark in Damra [1]) at 900 Celsius

- *titanium-silicon carbide ceramic* micro-coating (three-layer system) in excess of 1000 Celsius

- *60: 40 aluminium oxide-titanium oxide* nano-coating (two-layer system) at 850 ^{0}C.

These results included the parabolic growth rate model comparison for high temperature corrosion.

2) SEM/EDS results for:

- *titanium-silicon carbide ceramic micro-coating*

- *60: 40 aluminium oxide-titanium oxide* nano-coating

- *uncoated AISI 304 substrate which was tested only in an oven (not TGA) for 24 hours at 900 Celsius.*

These include comparison on morphology (SEM) and elemental composition (EDS).

3) Summary of overall findings.

Generally, nano-coating will be shown to achieve a much lower corrosion rate and provides significantly better protection from high temperature corrosion effects, although very good protection is also achieved with the micro-coating.

5.2 Thermogravimetric analysis (TGA) and results

The rate of oxidation is a key factor influencing corrosion in high temperature gas turbine engine environments [2]. Oxidation rate provides an approximation of the design life of the metal which will be used as a component in a specific temperature and environment. In addition, it produces data and information regarding how fast the oxidation happens and the life expectancy of the material employed under certain atmospheric and thermal conditions. The bonding material (super alloy NiCrAlY) is applied on the specimen (all six surfaces) using a thermal spray gun device at 3400 ^{0}C and constituted the bond coat. Here first the TGA results for the *titanium-silicon carbide micro-coating* is described with a comparison to the unprotected steel specimen benchmark. Next the TGA results for the *60: 40 aluminium oxide-titanium oxide* nano-coating results are presented.

5.2-1 TGA parabolic corrosion rate theory

It is known from corrosion theory [2] that after an initial linear distribution, the corrosion rate then follows the *parabolic law* of oxidation which can be described by the relationship:

$$\left(\frac{\Delta W}{A}\right)^2 \propto t \tag{5.1}$$

Here t is the time (s) and ΔW = mass gain (g), A = total surface area of sample (cm^2)

$$\left(\frac{\Delta W}{A}\right)^2 = K_p\, t \tag{5.2}$$

Transposition gives:

$$K_p = \frac{\left(\frac{\Delta W}{A}\right)^2}{t} \tag{5.3}$$

where K_p = parabolic oxidation rate constant (g^2/cm^4.s)

Equation (5.3) is therefore employed to compute the *corrosion rate* for all three test specimens i.e. the benchmark [1], micro-coated and nano-coated specimens.

5.2-2 Benchmark - uncoated AISI 304 substrate results

Figure 5.1 shows the benchmark results for the bare AISI 304 steel sample at 750-900 Celsius over a 50-hour duration based on the results of Damra [1].
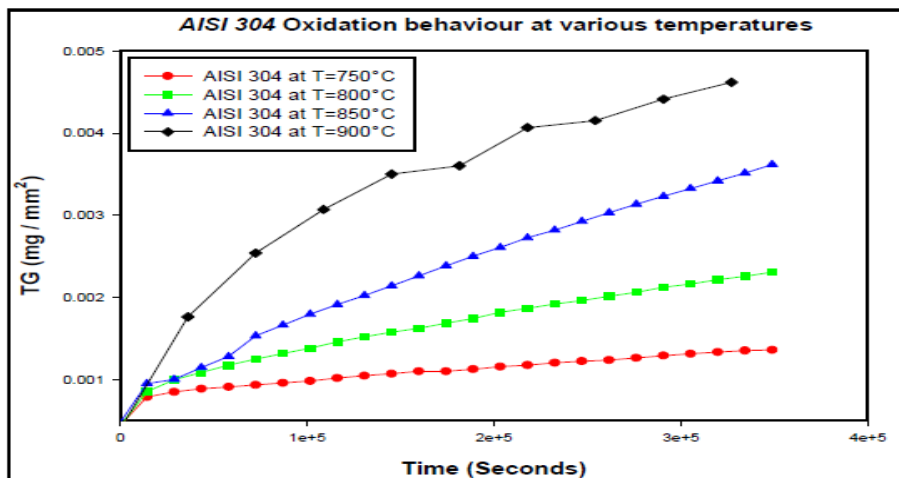
Figure 5.1: TGA oxidation behaviour of AISI 304 base metal (uncoated specimen) at various temperatures during 50 hours in the TGA – from Damra [1].

Evidently for the *unprotected sample* these results demonstrate a *parabolic behaviour* for the majority of the oxidation process. Equation (5.3) was used in [1] to determine the values of K_P which clearly increases when the temperature values are increased. This indicates that the constant rate of oxidation, K_P is a sign of the *rate of oxidation* as shown in **Table (5.1)**.

Material	Temperature (^{0}C)	$\dfrac{\Delta W}{A}\left(\dfrac{mg}{mm^2}\right)$	$K_P\left(\dfrac{g^2}{cm^4 s}\right)$
AISI 304	750	9.69×10^{-4}	2.577×10^{-8}
AISI 304	800	1.96×10^{-3}	4.041×10^{-8}
AISI 304	850	3.25×10^{-3}	5.884×10^{-8}
AISI 304	900	4.33×10^{-3}	8.437×10^{-8}

Table 5.1: Thermogravimetric results for the base metal AISI 304 (unprotected sample) at different temperatures – from Damra [1].
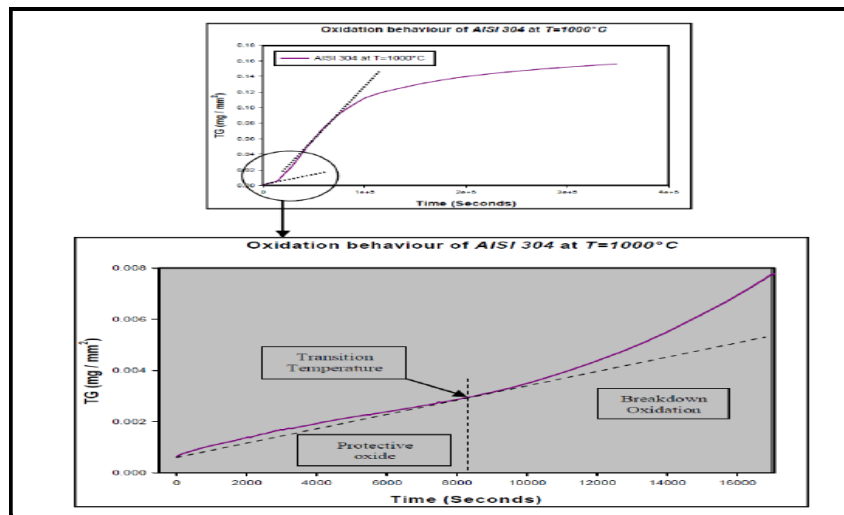
Figure 5.2: The scale breakdown for AlSI 304 (uncoated) at 1000 Celsius- from Damara [1].

Figure 5.2 shows the oxidation behaviour of the uncoated sample of AISI 3O4 [1] in synthetic air at 1000 Celsius, both before and after breakdown. At time $t = 8000\,s$, (2 hours) the transition state is initiated and the curve morphs from parabolic to linear. It should be noted that the resistance of AISI 304 steel to oxidation is related to the formation of chromic oxide Cr_2O_3. This scale is repaired under mild oxidation conditions and results in an eventual parabolic growth. Under high oxidation conditions, the chromic oxide growth at the initial stages will

follow a linear distribution. At a critical point, a sudden increase in the growth rate can arise which is known as "breakthrough" and its occurrence and profile is dependent on the alloy composition, environmental conditions and time of exposure [2]. This breakthrough leads the generation of two-part scale, which consists of an inner layer of spinel oxide (glassy mineral) shown occurring as octahedral crystals of variable colour and consists of magnesium and aluminium oxide) and an outer layer of ferric oxide (F_2O_3) [3, 4]. The sample reaches the "breakdown" state after 2 hours of oxidation. The oxidation rate increases beyond the breakdown limit and the oxidation behaviour changes from *linear to parabolic* after 2 hours. High resistance of the stainless steel is in general associated with the *formation of chromic oxide*, Cr_2O_3. This protective scale remains under lightly oxidising conditions with its development kinetics which follows a parabolic relationship. As the temperature is elevated the linearity of the graph (**Figure 5.2**) morphs to a parabolic distribution. The bare steel substrate AISI 304 cannot withstand the increase in temperature and at any time it will fracture. This further indicates that enhancement in temperature is problematic for the substrate or any other component synthesized from AISI 304 super alloy.

5.2-3 Titanium-Silicon Carbide micro-coating TGA results

After completion of the coating process, the resulting sample is cleaned in acetone and then secured inside a Thermobalance (TGA 92-16 Setaram) in synthetic air (1 bar pressure) commencing from room temperature (20 Celsius) and heating up to in excess of 1000 Celsius (1273 K) at a rate of 40 Kelvins/minute. During this heating process the micro-coated sample is exposed to significant oxidation in the Thermobalance, for a period of 50 hours. Following this it is cooled again at a rate of 40 Kelvins/minute. The experimental results are shown in due course in this section.

Figure 5.3 shows the dimensions of the micro-coated sample before TGA testing. The original specimen (uncoated) had dimensions of 20mm x 10 mm x 1.5mm (chapter 4). With the flame

thermal spray gun coating, it is not possible, as seen, to produce exactly the same coating thicknesses on all faces. The following coating thicknesses are achieved on the 6 surfaces of the substrate:

- (20.76-20) mm/2 = 0.76mm/2 = *0.38mm each* is achieved on two long edges (front and back)

- (10.98-10) mm/2 = 0.98mm/2 = *0.49mm each* on the left and right edges

- (1.86-1.5) mm/2 = 0.36mm/2= *0.18mm each* on the top and base faces.

The thicknesses were measured at half a dozen locations with a Vernier calliper and averaged.
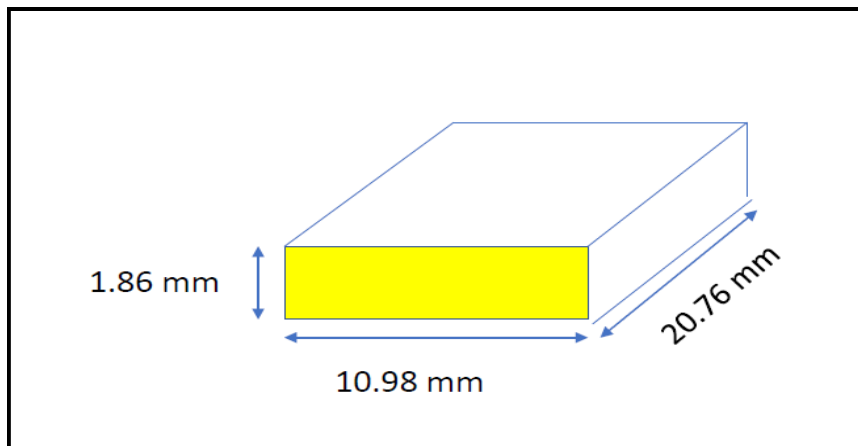
Figure 5.3 Final dimensions of flame spray micro-coated sample *before TGA testing.*

For the *original sample (uncoated):*

Total surface area = 2 x {(20 x 1.5) + (1.5 x10) +(20 x 10)} = 480mm²

For the *micro-coated sample*:

Thickness = 1.86 mm, Width   = 10.298 mm, Length   = 20.76 mm

Total surface area = 2 {(20.76 x 10.98) + (20.76 x 1.86) + (10.98 x 1.86) } = 2 {286.9812}

$$= 573.9624 \, mm^2 = 573.9624 \times 10^{-2} \, cm^2$$

The experimental results for the TGA testing on the micro-coated sample are shown in **Figure 5.4** below.
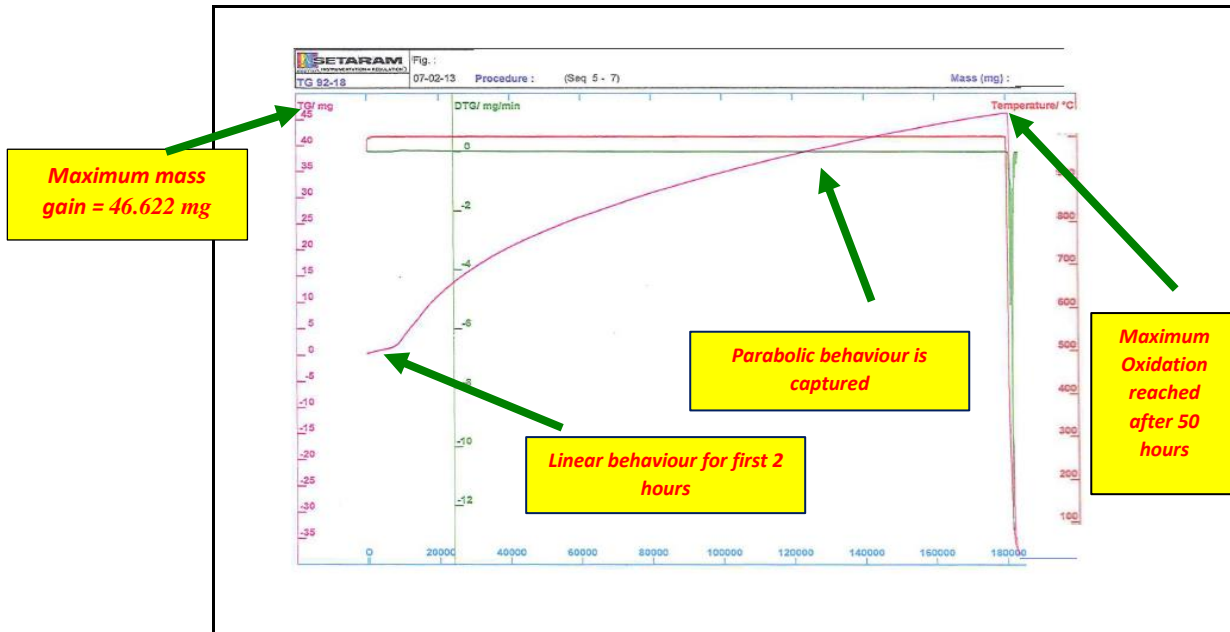
Figure 5.4: TGA oxidation behaviour of titanium-silicon carbide micro-coated AISI 304 sample over 50 hours in excess of 1000 ^{0}C.

From this graph the *mass characteristics* of the *micro-coated* sample after the TGA process can be extracted which quantify how much mass gain is produced due to oxidation:

*Mass gain from TGA result (see Fig. 5.4) = 46.622mg = **0.046622g***

Hence the corrosion mass deposited per unit area can be calculated:

$\Delta W/A$ = 0.046622g /573.962 x 10^{-2} cm^2 = 8.1228 x 10^{-3} g/cm^2 i.e. 8.1228 mg/cm^2

Since the *micro-coated* sample is subjected to 50 hours thermal loading in the TGA oven, therefore for t = 50 hours i.e. 50 x 3600s = 180,000s, one obtains from Equation (5.3):

$$K_p = \frac{\left(\frac{\Delta W}{A}\right)^2}{t} = \frac{\left(8.1228 \times 10^{-3}\right)^2}{180000} = 3.6655 \times 10^{-10} \left(\frac{g^2}{cm^4.s}\right) = 0.036655 \times 10^{-8} \left(\frac{g^2}{cm^4.s}\right)$$

117

Comparing with the Kp value of 8.437 x 10^{-8} $\left(\frac{g^2}{cm^4 s}\right)$ at the highest temperature recorded i.e. 900 Celsius (worse-case scenario) for the base metal (unprotected sample) as per **Table 5.1**, the micro-coating achieves a reduced Kp value of 0.036655 x 10^{-8} $\left(\frac{g^2}{cm^4 s}\right)$ at 1000 Celsius confirming that the titanium silicon carbide two-layer micro-coating does reduce very substantially the corrosion rate when compared with the base metal (unprotected substrate [1]).

Hence, the *percentage reduction* in Kp value is given by:

% *decrease in corrosion rate* (Kp) =

$\{[\ 8.437 \text{ x } 10^{-8} \ \left(\frac{g^2}{cm^4 s}\right) - 0.036655 \text{ x } 10^{-8} \left(\frac{g^2}{cm^4 s}\right)]/ 8.437 \text{ x } 10^{-8} \ \left(\frac{g^2}{cm^4 s}\right) \}\text{x } 100\%$

= **99.57%**

Clearly very significant protection is therefore achieved with the titanium-silicon carbide micro-coating compared with the unprotected AISI 304 base steel sample [1].

Figure 5.4 (as with the benchmark for uncoated AISI 304 substrate i.e. **Figure 5.1** [1]) shows that oxidation clearly increases with an increase in temperature. The graphical result shows a *linear plot* for the first 2 hours followed by a *parabolic profile* which is maintained for the duration of the TGA thermal test i.e. 48 hours. *This confirms the validity of using the parabolic growth model for high-temperature corrosion effects* as described in Equations (5.1) - (5.3) and elaborated in Khanna [2]. Breakdown of the coating is usually attributable to stress generation on the oxide scale during the development or growth process when the *weight increases* due to the oxidation process. However, at certain locations on the *micro-coated* specimen, the scale layer cannot withstand high stress concentrations, and this results in *cracking* in the scale or thermal creep in the substrate as evident in from the experimental results shown in **Figure 5.5**.

In addition, **Figure 5.6** shows patches and the disappearance of the coating material i.e. *swarfing and flaking,* as elaborated in Khanna [2]. **Figure 5.7** shows the sample before and after the oxidation process. There is clear indication of spallation on the sample after oxidation at high temperature.
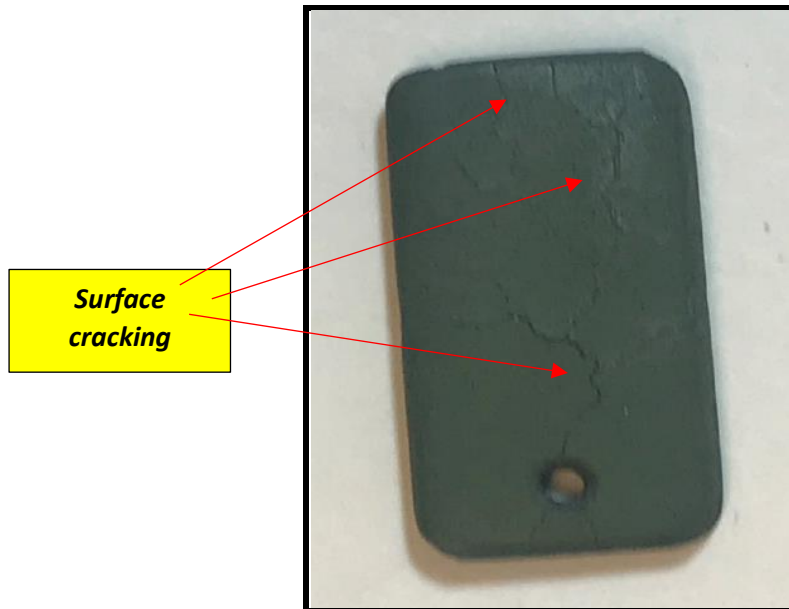
Figure 5.5: Micro-coating test sample with cracking and thermal creep.
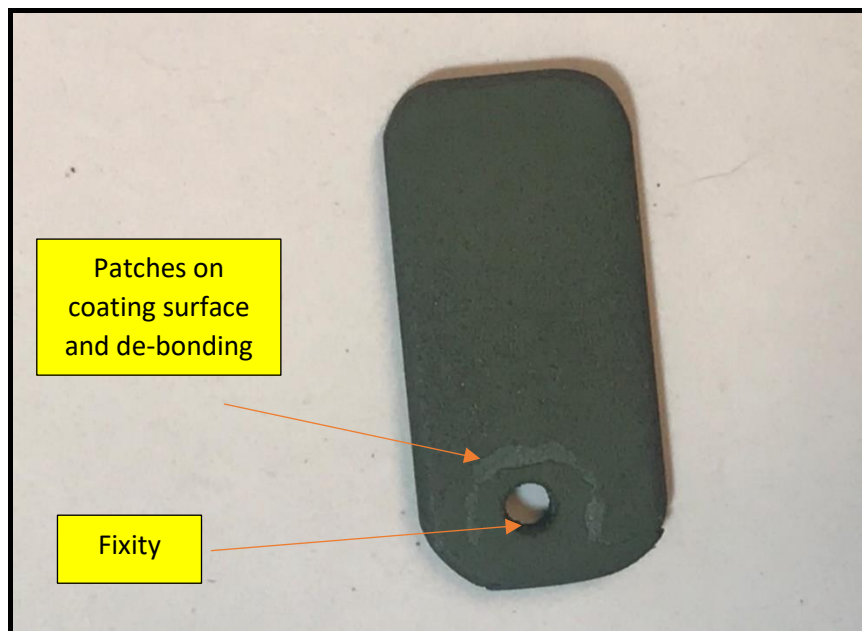
Figure 5.6: Patches appearing on the top surface of the micro-coated sample and disappearance of the coating material.
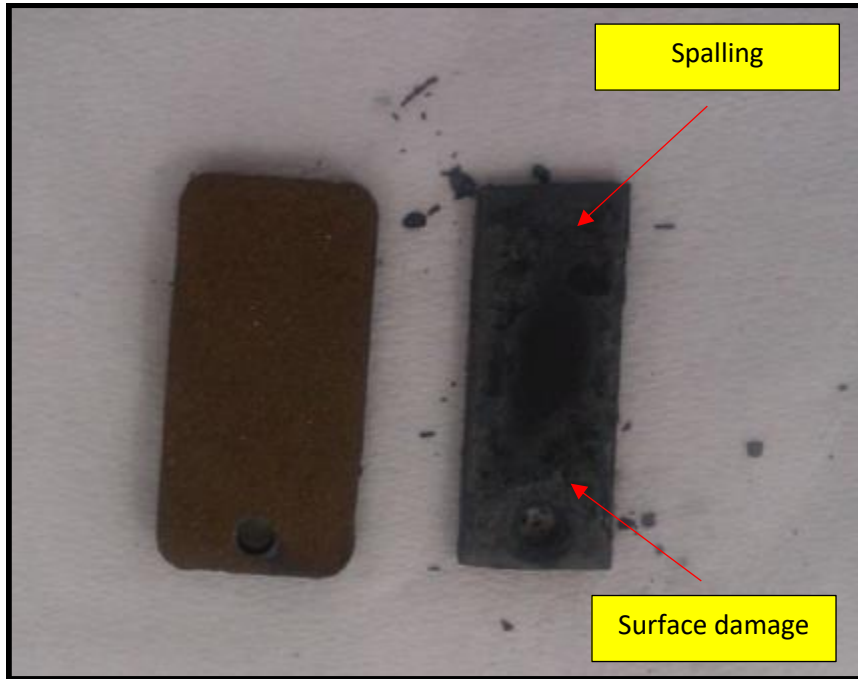
Figure 5.7: Micro-coated sample before and after oxidation.

There is normally generation and growth of a *protective oxide scale* on the surface of the coating material. The scale is initially smooth; however with continuous high temperature corrosion, it begins to degrade and there is surfacial degradation of the micro-coating accompanied with cracking, as observed in **figures 5.6-5.7,** but this is limited to localized zones on the surface of the sample. This concurs with the findings of Khanna [2].

5.2-4 60: 40 Aluminium oxide-titanium oxide nano-coating TGA results

As with the micro-coating, the same procedure was followed. After completion of the coating process, (which again used a bonding material of SA (super alloy NiCrAlY) applied on the specimen (all six surfaces) using a thermal spray gun device at 3400 ^{0}C) and constituted the bond coat, the resulting sample was cleaned in acetone and then secured inside the Thermoblance (TGA 92-16 Setaram) in synthetic air (1 bar pressure) commencing from room temperature (20 Celsius). However, in this case, *heating could only be achieved up to 850 Celsius (1123K) owing to limitations with the apparatus at that time*. The parabolic oxidation

model is used again and will be shown later in this section. The same heating rate however was applied i.e. 40 Kelvins/minute. During this heating process the coated sample was (as with the micro-coating) exposed to significant oxidation in the Thermobalance for a period of 50 hours. Following this it was cooled again at a rate of 40 Kelvins/minute, as with the micro-coating.
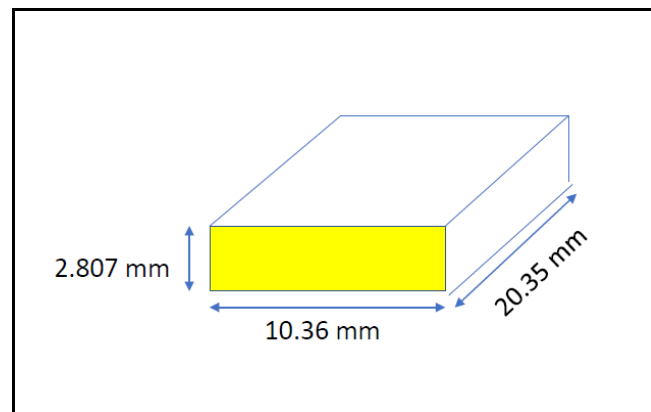
Figure 5.8: Final dimensions of 60: 40 aluminium oxide-titanium oxide nano-coated sample before TGA testing.

Figure 5.8 shows the dimensions of the nano-coated sample before TGA testing. The original specimen (uncoated) had exactly the dimensions of 20mm x 10 mm x 1.5mm (chapter 4). In this case, the following coating thicknesses are achieved:

- (20.35-20)/ 2 = 0.35mm/2 = *0.175mm each* is achieved on two edges (front and back)

- (10.36-10)/2 = 0.36mm/2 = *0.18mm each* on the left and right edges

- (2.807-1.5)/2 = 1.307mm/2 = *0.6535 mm each* on the top and base faces.

Therefore, the upper and lower faces of the sample have a thicker single nano-coating compared with the micro-coating which had *0.18mm upper and lower face coating thickness* comprising the two titanium and silicon carbide layers. As with the micro-coating, the coating thicknesses were measured at half a dozen locations with a Vernier calliper and averaged. (Al_2O_3 60% - TiO_2 40%) nano-powder mix was used for the nano-coating single layer. The same analysis is now conducted as with the micro-coating.

121

Thickness = 2.807 mm, Width = 10.36 mm, Length = 20.35 mm

Surface Area = 2{(10.36x20.35) + (10.36x2.807) + (20.35x2.807)} = 594.05794 mm²

The graph of the *weight gain against time* for 50 hrs at 850 ^{0}C is shown in **Figure 5.9** which shows once again (as with the micro-coating and also unprotected substrate results) for the corrosion rate (oxidation) the initial *linear behaviour* is captured, and the ensuing parabolic behaviour is observed with temperature increase. The parabolic law can therefore be used again.
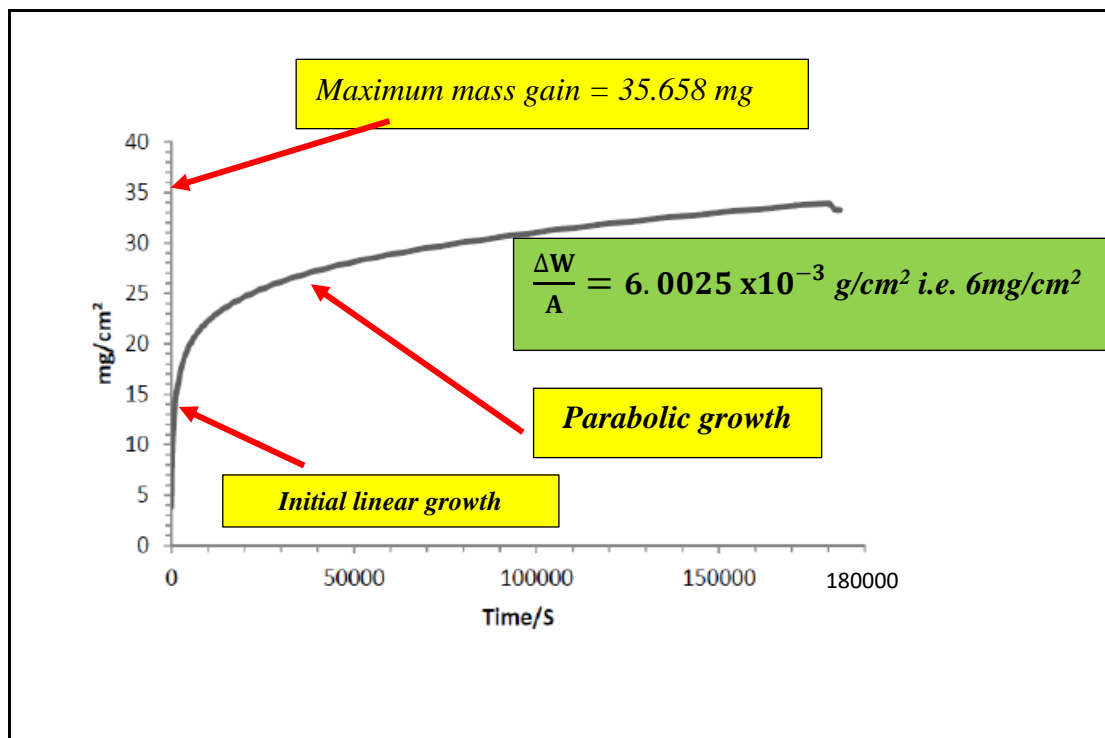
Figure 5.9: Al₂O₃-TiO₂(60%-40%) nano-coating TGA results during air oxidation for 50 hours at 850 ^{0}C.

Mass gain from TGA result =ΔW= 35.658 mg = 0.035658 g

ΔW/A = 0.035658g /594.05794x10⁻² cm² = 6.0025 x 10⁻³ g/cm²

Again applying the parabolic corrosion rate formula i.e. Equation (5.3), for K_p :

$$K_p = \frac{\left(\frac{\Delta W}{A}\right)^2}{t}$$

122

Where,

$$\frac{\Delta W}{A} = 6.0025 \ x10^{-3} \ g/cm^2 \ i.e. \ 6.0025 \ mg/cm^2$$

$$K_p = \frac{\left(\frac{\Delta W}{A}\right)^2}{t} = \frac{\left(6.0025 \ x10^{-3}\right)^2}{180000}$$

$$K_p = 2.001 x 10^{-10} \left(\frac{g^2}{cm^4.s}\right) = 0.02001 x 10^{-8} \left(\frac{g^2}{cm^4.s}\right)$$

The corrosion rate with several layers of nano-coating K_p is $0.02001 x 10^{-8} \left(\frac{g^2}{cm^4.s}\right)$ whereas in the micro-coating the K_p value is $0.036655 x \ 10^{-8} \left(\frac{g}{cm^4.s}\right)$ which indicates that the *nano-coating has produced an even lower corrosion rate than the micro-coating*. Now comparing the % reduction in *Kp* value between the *nano-coating compared with the micro-coating*, gives:

% decrease in *Kp* value =

$$\{[\ 0.03665 \ x \ 10^{-8} \ \left(\frac{g^2}{cm^4 s}\right) - 0.02001 \ x \ 10^{-8} \left(\frac{g^2}{cm^4 s}\right) \ ] / \ 0.03665 \ x \ 10^{-8} \ \left(\frac{g^2}{cm^4 s}\right) \}x \ 100\%$$

= 45.4%

Clearly a considerable improvement is achieved with the nano-coating relative to the micro-coating. The nano-coating is therefore confirmed to achieve the lowest *Kp* (corrosion rate) in both sets of TGA tests. The 60: 40 nano-coated sample before and after TGA are shown in **Figs. 5.10 and 5.11**.

Figure 5.10: Nano-coated sample *before* TGA testing.
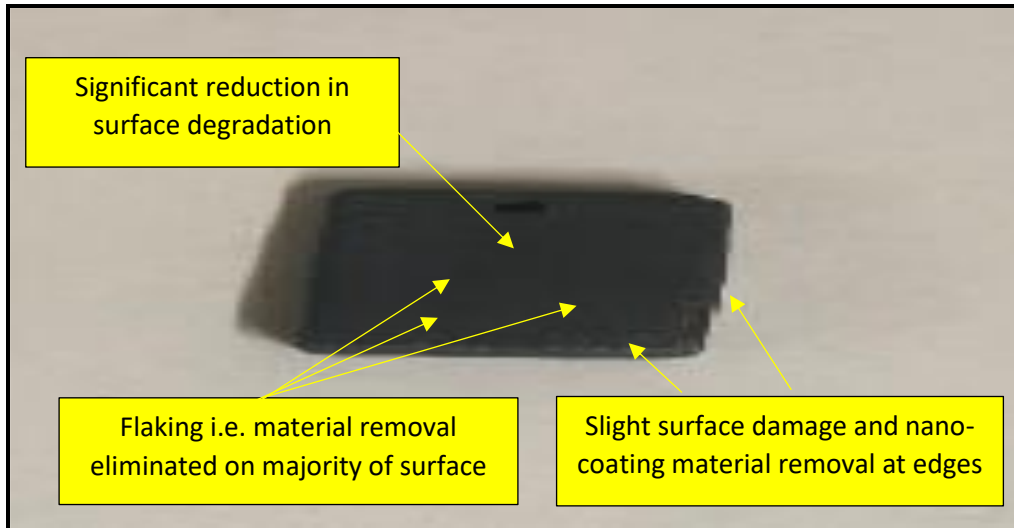
Figure 5.11: Nano-coated sample *after* oxidation by TGA testing.

As can be seen in **Figure 5.11**, significant reduction in surface degradation is achieved with the nano-coating and surface material removal is completely removed.

Finally, the three corrosion rates are documented for the unprotected substrate [1], the micro-coated sample and the nano-coated sample in **Table 5.2.**

Samples	Corrosion rate, $K_P \left(\dfrac{g^2}{cm^4 s} \right)$
Unprotected substrate AISI 304 [1]	8.437×10^{-8}
Titanium-silicon carbide micro-coated sample	0.036655×10^{-8}
60: 40 Aluminium oxide-titanium oxide nano-coated sample	0.02001×10^{-8}

Table 5.2: Corrosion rates obtained from TGA for the samples.

5.3 SEM and EDS results

In this section, both sets of results for the SEM and EDS are described for the titanium-silicon carbide micro-coated, the aluminium oxide-titanium oxide nano-coated specimens extracted from the TGA device (after 50 hours oxidation in excess of $1000\,^{0}$C for the micro-coating and 50 hours oxidation up to 850 Celsius for the nano-coating, as explained earlier in section 5.1) *and the uncoated AISI 304 (base substrate) sample*. The *morphology of the surface corrosion*

behaviour was studied using SEM. SEM micrographs for each magnification factor were obtained. *Element contents (composition)* with reference to the weight percentage (Wt%) and Atomic percentage (At%) for each magnification factor (2 sets were conducted at 5000x and 10,000 x magnification) were then determined with EDS (also known as EDXA).

5.3-1 Titanium-Silicon Carbide micro-coating results from SEM and EDS

Two sets of results were produced in the SEM and EDS for different magnification factors of 5000 and 10000. Set 1 was for magnification 5000 and set 2 for magnification 10000.

5.3-1.1 *Set 1* SEM and EDS (EDXA) results

In **set 1** the SEM magnification factor is 5000x (as shown in **Figure 5.12**) from which the 4 points are selected (*A, B, C, D*) for the EDS spectra elemental composition analysis.
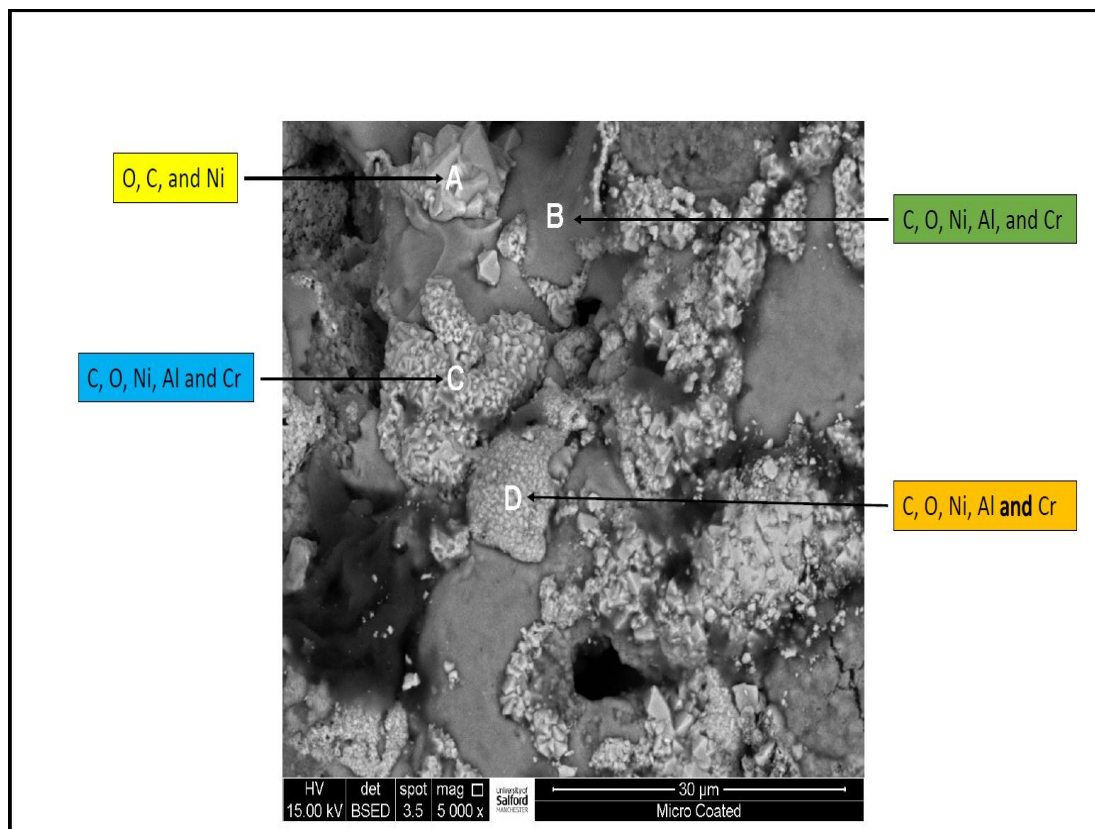
Figure 5.12: SEM micrograph of the micro-coated sample cross section with magnification factor 5000x (BSE).
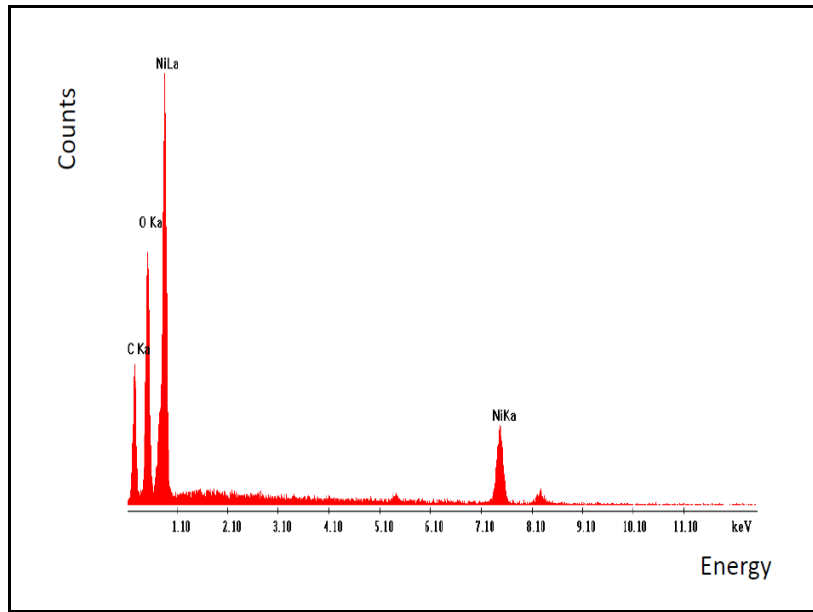
Elements	Wt %	At %
C	28.81	49.82
O	26.45	34.35
Ni	44.74	15.83
Total	100	100

Figure 5.13: EDXA Spectra at point A.

Figure 5.13 shows that the main components obtained from the EDS (EDXA) spectra resulting from oxidation in the micro-coating at *point A* are Carbon (28.81Wt% and high At% of 49.82), then Oxygen (26.45 Wt% and lower At% of 34.35) and Nickel (Higher Wt% of 44.74 and lower At% of 15.83).

Similarly, the Wt% and At% values at points *B, C and D* are obtained via EDS (EDXA) and shown in **Figures 5.14, 5.15, 5.16.**
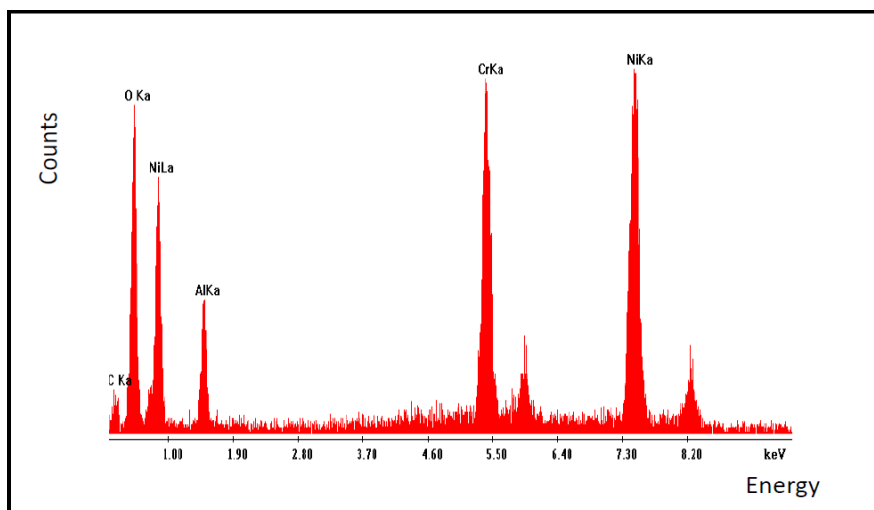
Element	Wt%	At%
C	3.19	11.11
O	7.83	20.47
Al	3.64	5.56
Cr	21.71	17.46
Ni	63.62	45.31
Total	100	100

Figure 5.14: EDXA Spectra at point B.
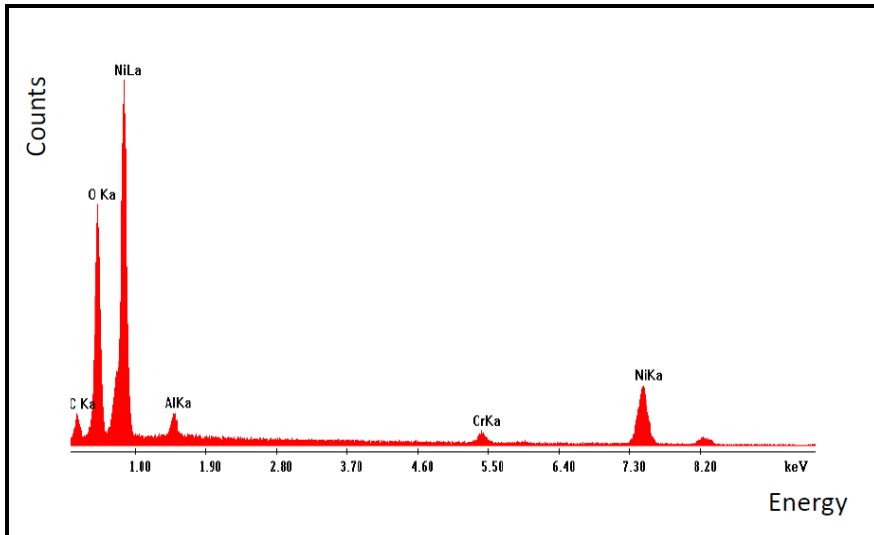
Element	Wt%	At%
C	10.98	23.66
O	30.04	48.58
Al	3.04	2.92
Cr	3.38	1.68
Ni	52.56	23.17
Total	100	100

Figure 5.15: EDXA Spectra at point C.
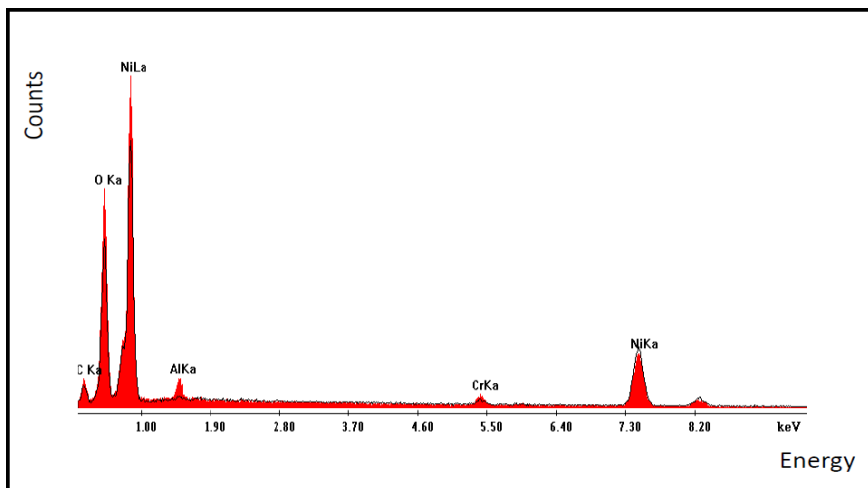
Element	Wt%	At%
C	9.82	23.19
O	25.43	45.1
Al	0.57	0.6
Cr	1.68	0.92
Ni	62.5	30.2
Total	100	100

Figure 5.16: EDXA Spectra at point D.

5.3-1.2 *Set 2* SEM and EDS (EDXA) results

In **Set 2** the SEM magnification factor is 10,000x as shown in **Figure 5.17.** The values for the Wt% and At% are obtained in similar fashion as with **Set 1**, as shown in **Figures 5.18-5.21.**
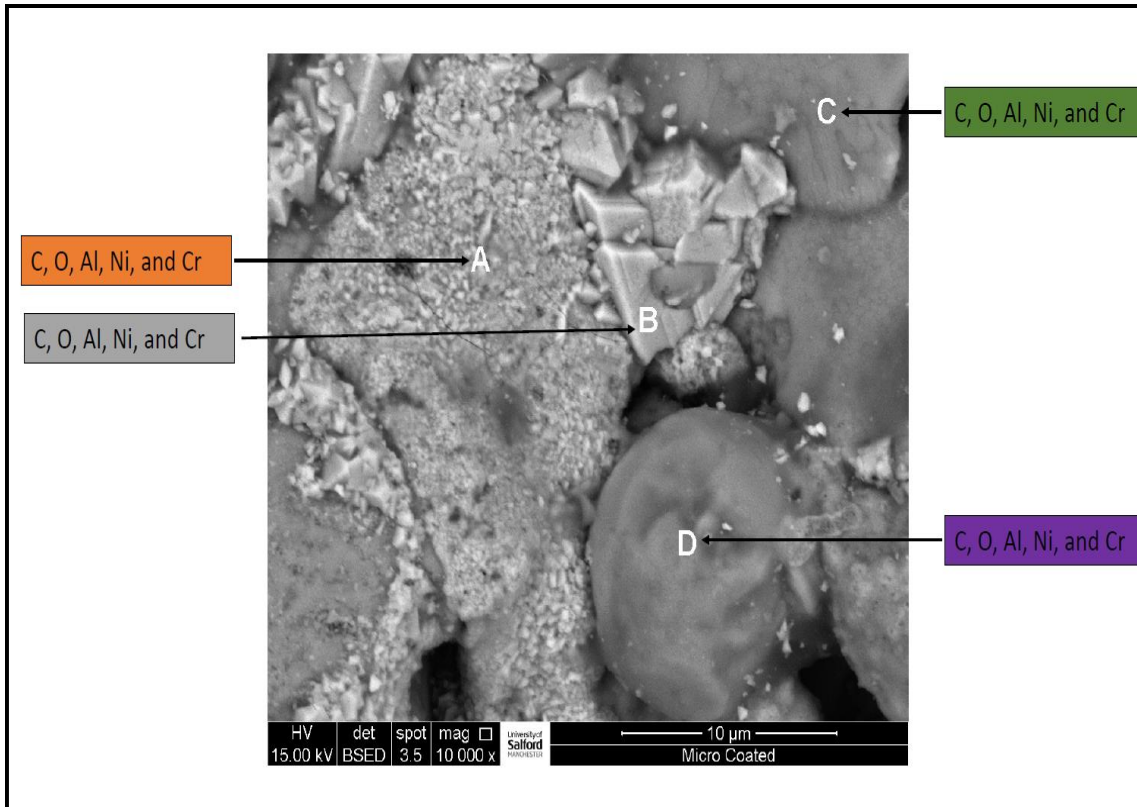
Figure 5.17: SEM micrograph of the cross section with magnification factor 10000x after 50 hours oxidation up to $1000\,^{0}$C.
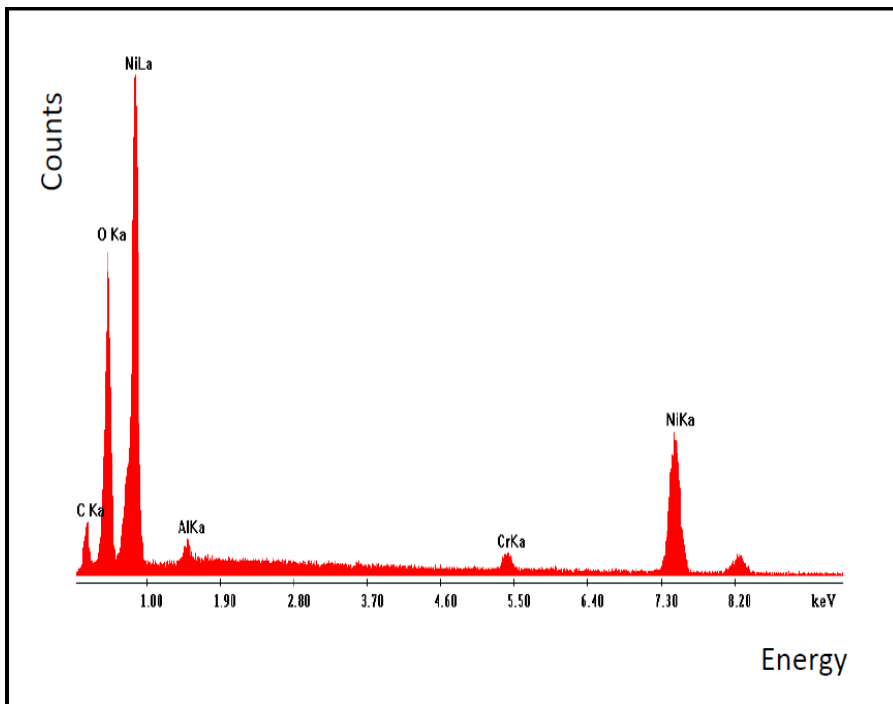
Element	Wt%	At%
C	10.29	25.18
O	21.62	39.7
Al	1.5	1.63
Cr	2.74	1.55
Ni	63.85	31.95
Total	100	100

Figure 5.18: EDXA Spectra at point A.
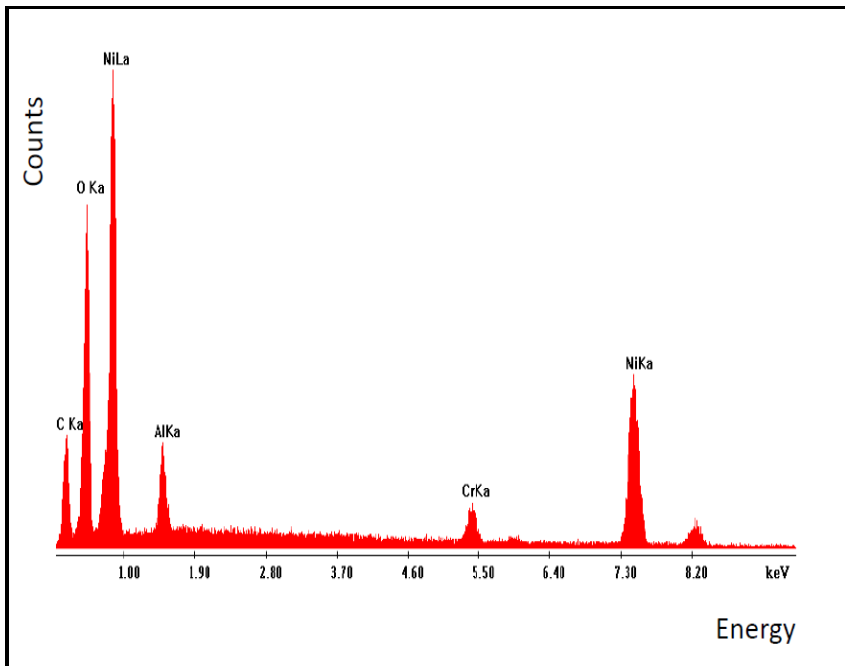
Element	Wt%	At%
C	16.51	36.85
O	18.44	30.89
Al	4.34	4.31
Cr	4.08	2.1
Ni	56.63	25.85
Total	100	100

Figure 5.19: EDXA Spectra at point B.
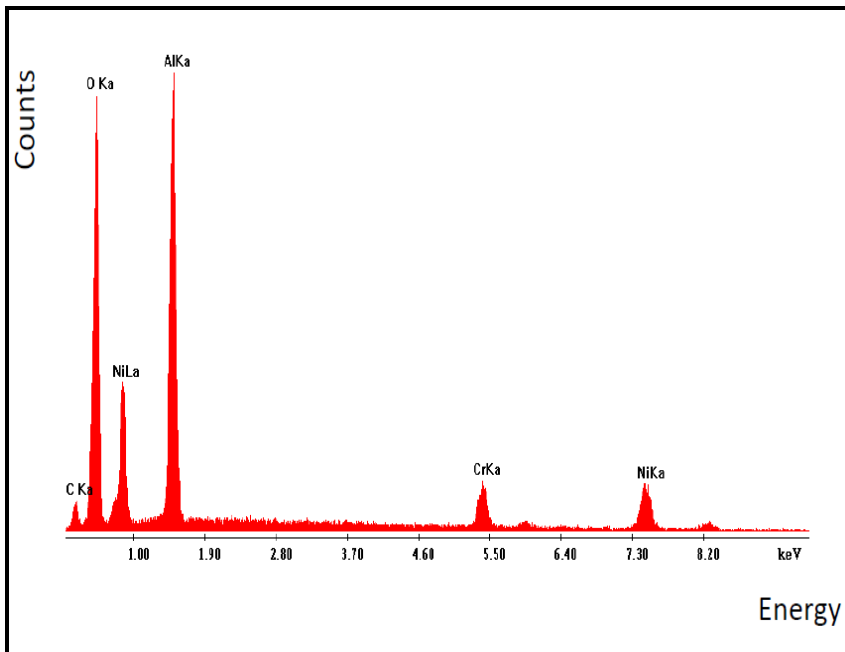
Element	Wt %	At%
C	7.54	14.86
O	31.69	46.89
Al	28.06	24.62
Cr	8.36	3.81
Ni	24.35	9.82
Total	100	100

Figure 5.20: EDXA Spectra at point C.

129
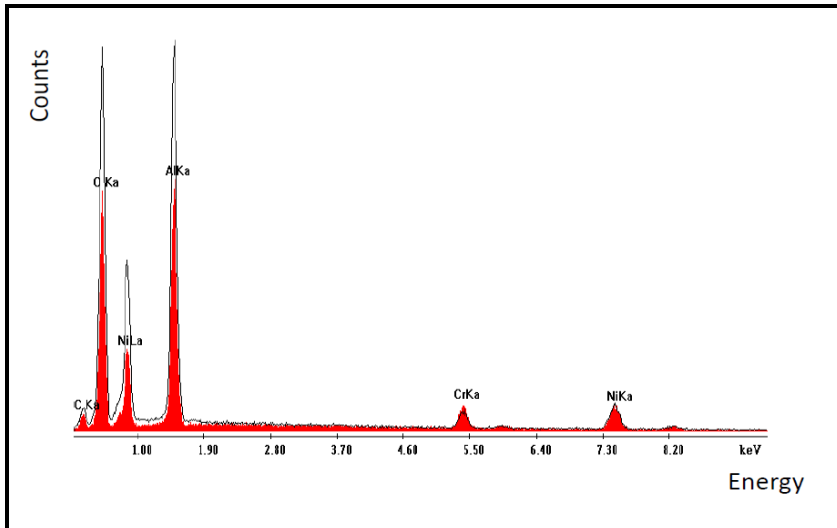
Element	Wt %	At%
C	7.42	13.54
O	38.16	52.25
Al	31.21	25.34
Cr	4.65	1.96
Ni	18.55	6.92
Total	100	100

Figure 5.21: EDXA Spectra at point D.

5.3-2 *60: 40* Aluminium oxide-Titanium oxide nano-coating results from SEM and EDS

5.3-2.1 SEM and EDS (EDXA) results

Only a single set of results was possible for the nano-coating at SEM magnification factor of 10, 000x as shown in **Figure 5.22**. This shows the SEM micrograph results for points A, B and C and their element contents. This was then analysed using EDS (EDXA) in the same way as the micro-coatings (section 5.3-1).
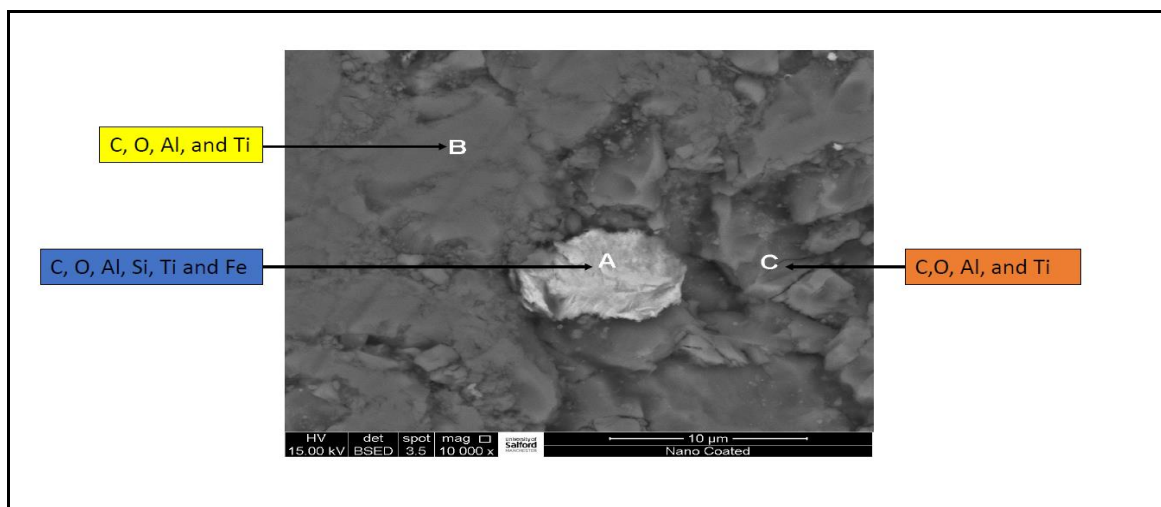
Figure 5.22: SEM micrograph of the cross section of 60: 40 aluminium oxide-titanium oxide *nanocoating* with magnification factor 10000x (BSE).

Elements	Wt%	At%
C	12.18	35.74
O	4.4	9.69
Al	0.31	0.41
Si	2.4	3.02
Ti	1.99	1.47
Fe	78.72	49.69
Total	100	100
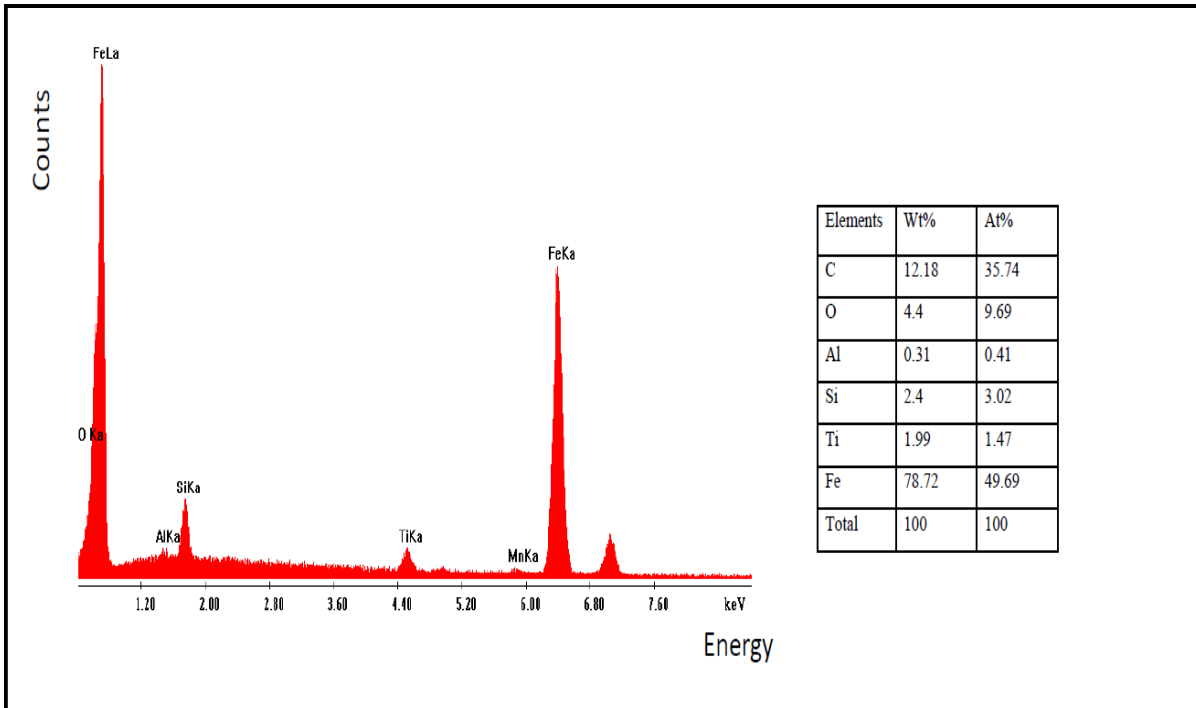
Figure 5.23: EDXA Spectra at point A.

Figure 5.23 shows that the main components through oxidation at point A are Carbon (12.18 Wt% and 35.74 At%), Oxygen (4.4 Wt% and 9.69 At%), Aluminium (0.3 Wt% and 0.41 At%), Silicon (2.4 Wt% and 3.02 At%), Titanium (1.99 Wt% and 1.47 At%) and Iron (78.72 Wt% and 49.69 At%). The Iron level is the highest at this point in terms of Wt% and At% followed by the carbon level. The lowest component element is Aluminium.

Elements	Wt%	At%
C	7.43	12.96
O	39.47	51.67
Al	35.84	27.82
Ti	17.26	7.55
Total	100	100
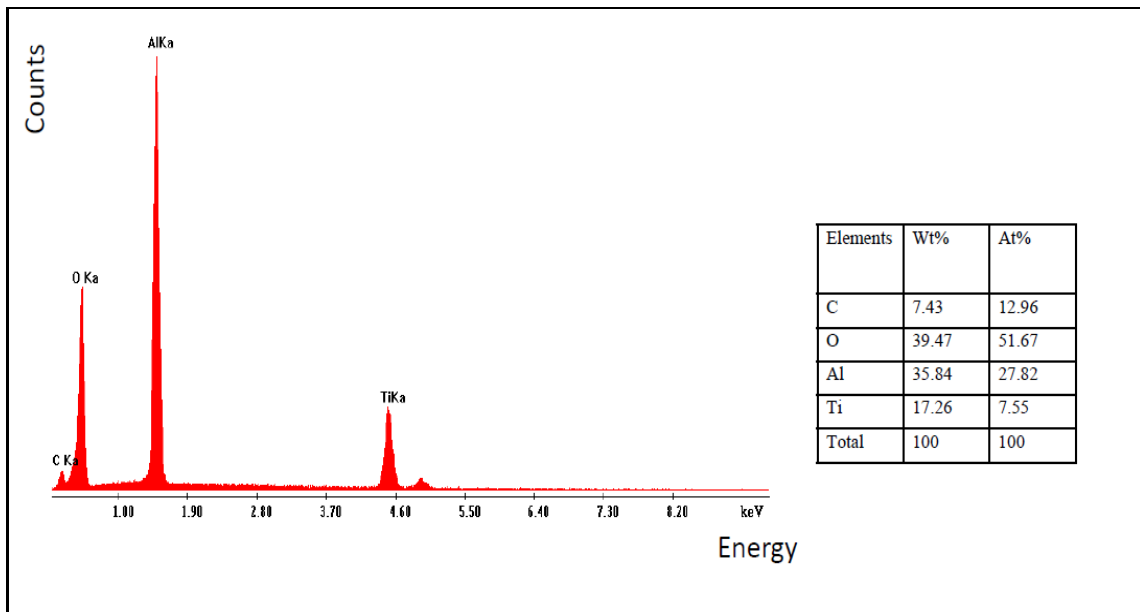
Figure 5.24: EDXA Spectra at point B.

131

In **Figure 5.24** the Oxygen level has the highest value in Wt% and At% and the Aluminium is second. Carbon values are the lowest.

Elements	Wt%	At%
C	5.75	10.18
O	39.75	52.83
Al	37.18	29.3
Ti	17.32	7.69
Total	100	100
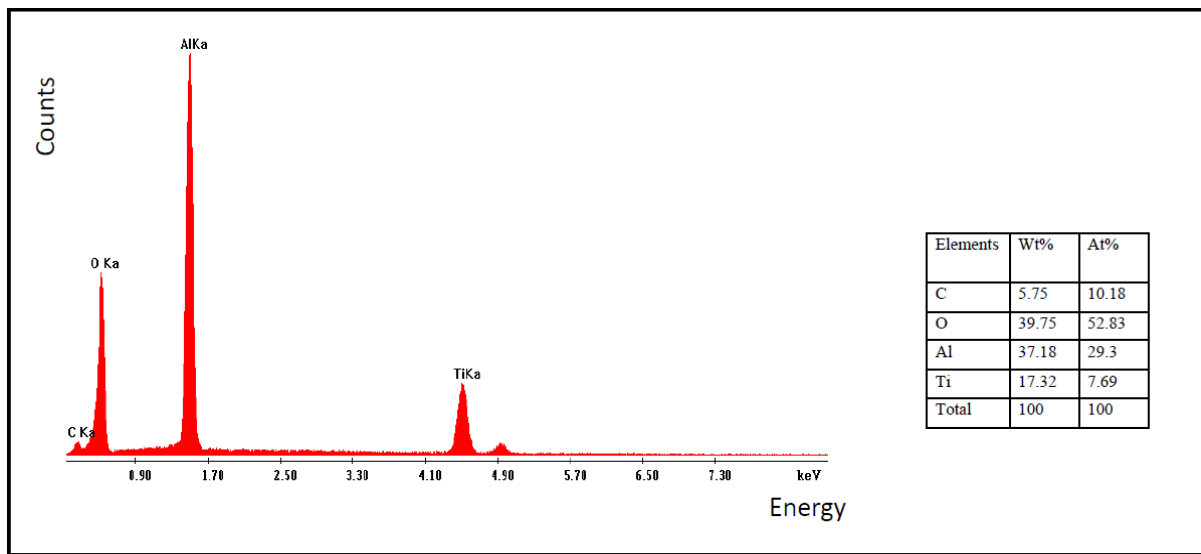
Figure 5.25: EDXA Spectra at point C.

In **Figure 5.25**, again the Oxygen and Aluminium levels are higher and a slight reduction in the Carbon content is observed. Titanium content is almost the same as point B. The SEM and EDXA results for the nano-coating indicate that the oxidation level is high which gives good protection to the sample from corrosion. Additional protection will be supplied by the Aluminium content and finally the Titanium prevents the wear on the coated sample against any frictional contact.

5.3-3 Uncoated sample results from SEM and EDS

In addition to the micro-coated and nano-coated samples which were tested in TGA (Section 5.2), an uncoated AISI 304 substrate sample was also tested in an oven at 900 ^{0}C. The SEM and EDS (EDXA) results for the elemental values of Wt% and At% were also produced for this uncoated sample. Again, as with the nano-coating, only a *single set of results* was produced. **Figure 5.26** shows the SEM micrograph for the uncoated sample at points *A, B, C, and D*.
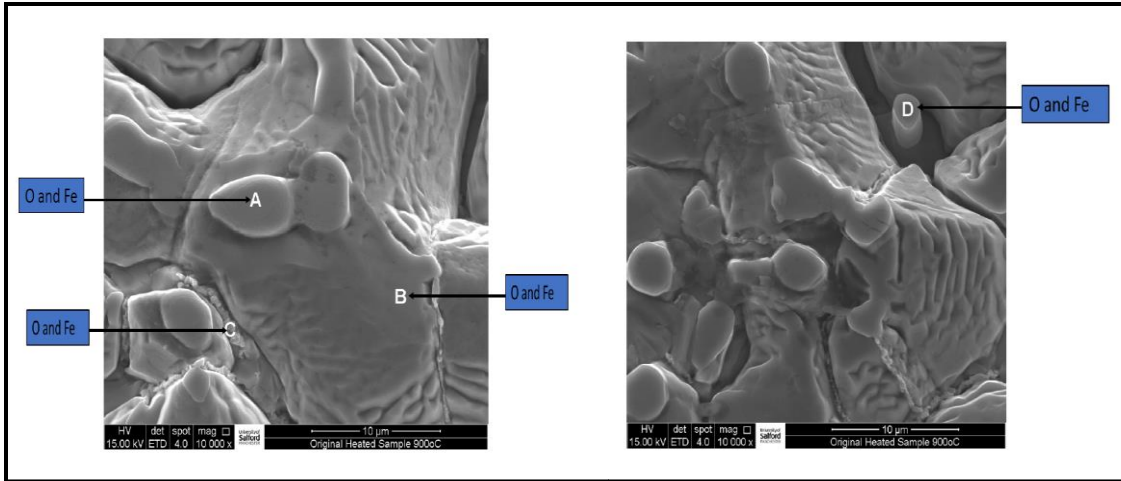
Figure 5.26: SEM micrograph of the cross section with magnification factor 10,000x.

Elements	Wt%	At%
O	33.41	63.65
Fe	66.59	36.35
Total	100	100
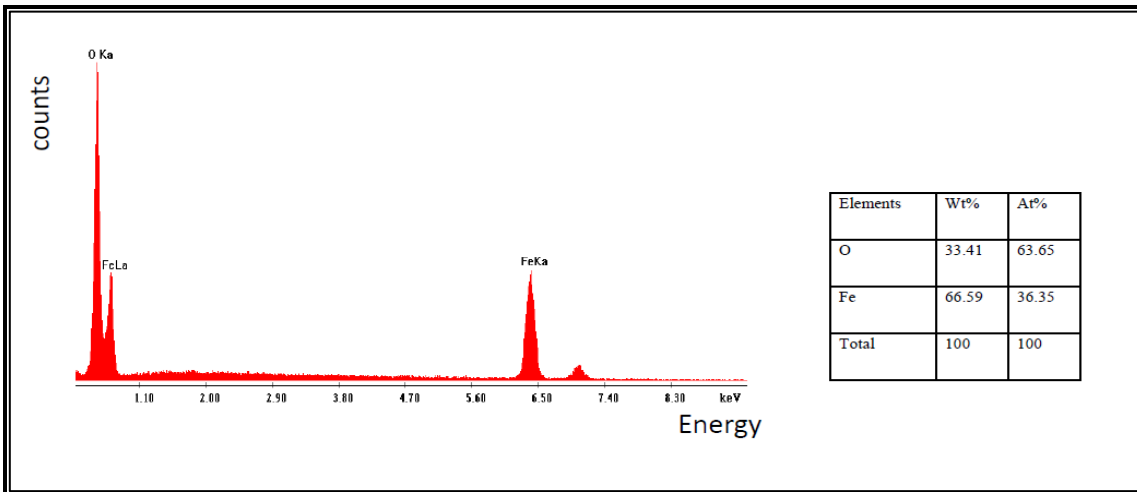
Figure 5.27: EDXA Spectra at point A.

Elements	Wt%	At%
O	34.8	65.05
Fe	65.2	34.93
Total	100	100
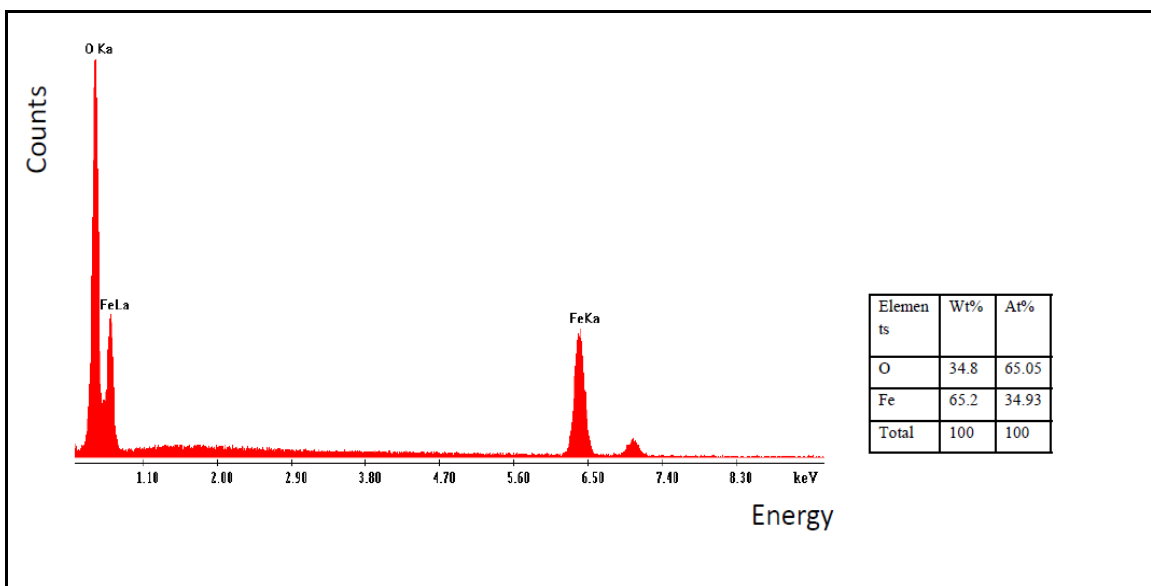
Figure 5.28: EDXA Spectra at point B.

133
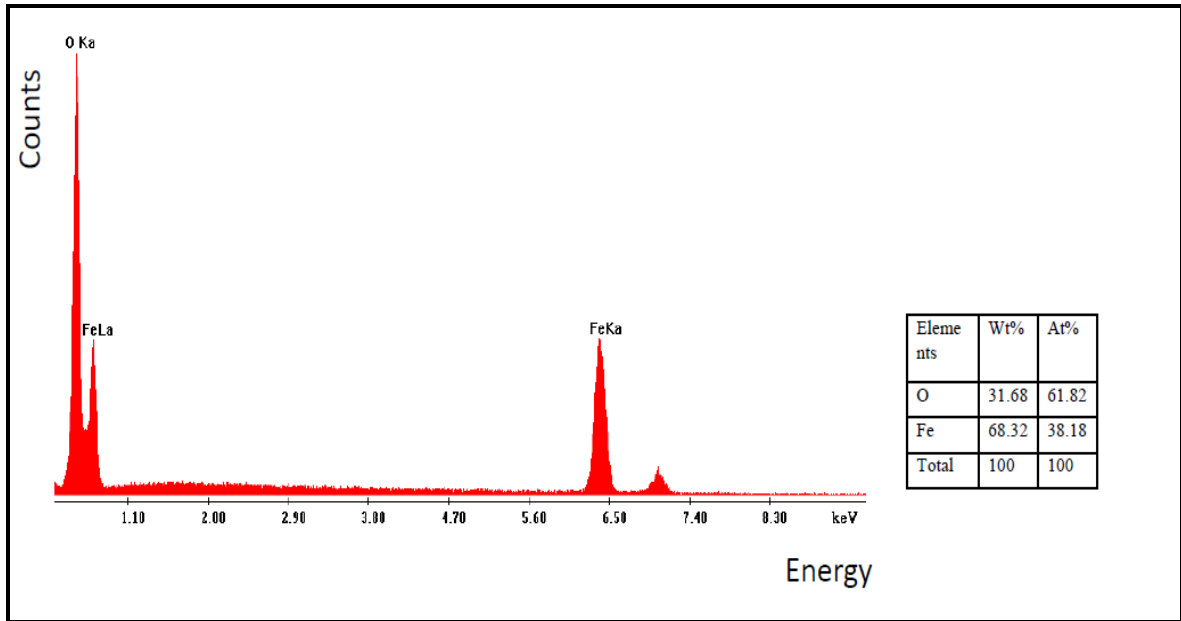
Figure 5.29: EDXA Spectra at point C.
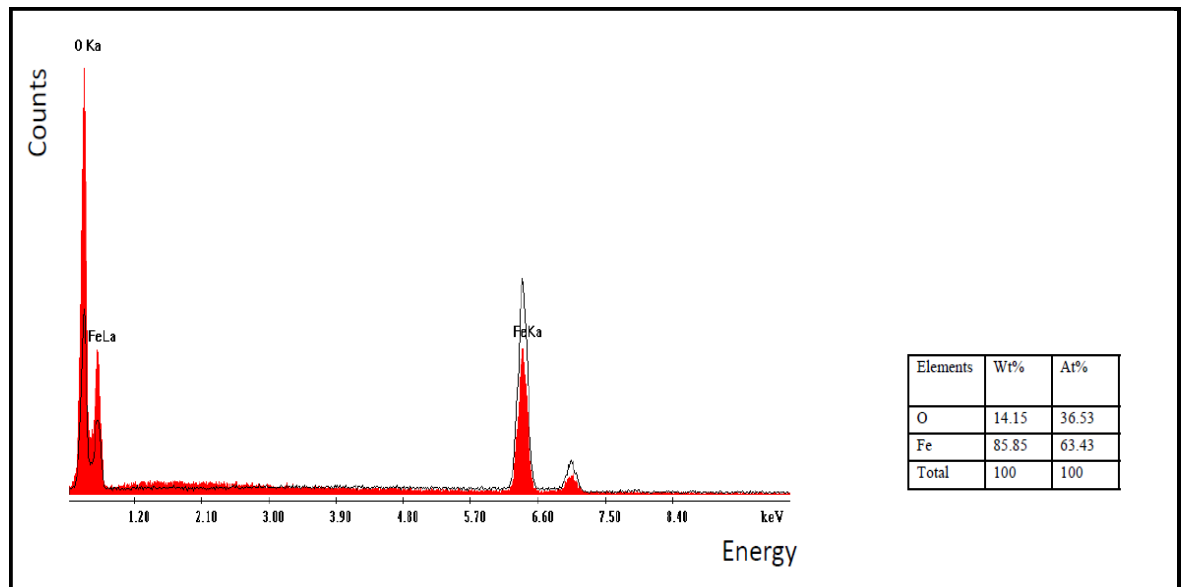
Figure 5.30: EDXA Spectra at point D.

EDXA spectra results in **Figure 5.27** at point A, **Figure 5.28** at point B and **Figure 5.29** at point C shows high values of Wt% and At% of Oxygen and Iron levels whereas at point D in **Figure 5.30**, the Iron level is higher than Oxygen at Wt% and At%. This leads to the conclusion that the substrate in general *without coating material* experiences a relatively high levels of corrosion.

5.3-4 Comparison of SEM/EDS results for micro-coated, nano-coated sample and unprotected AISI 304 substrate sample

Close inspection of the EDS plots has revealed that while the micro-coating produces a maximum Oxygen content Wt% of *38.16* (set 2, point D), this is lower than that produced for the nano-coating which shows a maximum oxygen content Wt% of *39.75* (at point C). Both micro-coated and nano-coated samples achieve *higher oxygen content* than the unprotected sample which shows a maximum of *33.41* at point *A*. Metals and alloys are usually protected from sulphidation attack due to the oxide scale presence. Reducing the oxygen content increases the sulphidation and induces more damage as noted in [5, 6]. Higher oxygen content is conducive to better oxidation layer protection, indicating that nano-coatings operate the best under high temperature, although micro-coatings do perform quite well also. No iron content is detected in the micro-coated sample but the maximum Wt% value for the *nano-coated* sample is 78.72 and again this is considerably lower than the maximum of 85.85 for the *unprotected sample*, indicating that there is much more propensity for corrosion (iron reacts excessively) in the uncoated sample and therefore a much higher corrosion rate is produced as testified to by the *Kp* values from the TGA tests. However, it is likely that the high iron content value is due to a spot being missed on the nano-coating (during the coating process with the thermal flame spray gun), as seen in the light grey central zone in **Figure. 5.22**. The mechanical behaviour of the nano-coated samples is superior to the micro-coating. Also, there is probably a porosity percentage decrease in the nano-coated sample compared to the micro-coated sample. In addition, higher hardness is probably achieved in the nano-coating compared to the micro-coating which contributes to greater thermal protection. Effectively therefore the SEM/EDS results confirm that *nano-coatings* produce the best overall protection to high temperature corrosion effects, based on the elemental composition.

5.4 Conclusions

In this chapter extensive details of the TGA, SEM and EDS experiments on novel titanium-silicon carbide micro-coated, 60:40 aluminium oxide-titanium oxide nano-coated *and* unprotected (AISI 304 steel alloy) samples have been presented. The main findings are summarized below:

i) Based on TGA testing, the correct *parabolic behaviour* is demonstrated for the corrosion rate in both micro- and nano-coatings with an increase in temperature (and time) and also the "breakdown" state after 2 hours of oxidation (up to which the corrosion rate plot is *linear*). The oxidation rate increases beyond the breakdown limit and the oxidation behaviour changes from *linear to parabolic* after 2 hours. This agrees with the benchmark experimental study of Damra [1].

ii) The TGA results also show that titanium-silicon carbide micro-coating achieves a massive reduction in corrosion rate (*Kp*) value relative to the *unprotected (uncoated) blade specimen*. The unprotected substrate [1] showed a *Kp* value of $8.437 \times 10^{-8} \left(\frac{g^2}{cm^4 s} \right)$ whereas the micro-coating showed a much lower value of $0.036655 \times 10^{-8} \left(\frac{g^2}{cm^4 s} \right)$. There is therefore a 99. 57% decrease in corrosion rate. However, the nano-coating produced the lowest corrosion rate *Kp* value of $0.02001 \times 10^{-8} \left(\frac{g^2}{cm^4 s} \right)$. Hence, nano-coating reduces the corrosion rate *even further compared with the micro-coating*. There is a 45.4% decrease in corrosion rate achieved with the 60:40 aluminium oxide-titanium oxide nano-coated sample compared with the micro-coated sample. *This is a very significant finding which has not been reported before in the scientific literature*. It demonstrates that a *single layer of nano-coating* achieved enhanced thermal corrosion protection compared with a *double layer* (metallic-ceramic) micro-coating. This strongly endorses the adoption of metallic oxide single layer nano-coatings in practical

gas turbine blade protection from high temperature corrosion and shows that they perform better than metallic/ceramic combinations which are conventionally used in industry.

iii) The SEM morphology and EDS elemental composition results show that while the titanium-silicon carbide micro-coating significantly improves the protection of the AISI 304 substrate at high temperature, it is not as effective as the 60: 40 aluminium oxide-titanium oxide nano-coating which shows the *highest oxygen content* and therefore offers the best protection against sulphidation. Furthermore, iron content in the nano-coating is lower than the unprotected sample and again this will provide better protection against corrosion attack at high temperatures.

iv) Significant reduction in surfacial damage is achieved with the nano-coating and the flaking and cracking encountered with micro-coating is eliminated, largely since the cracks generated are of the micro scale and are inhibited with nanoscale engineering particles in the nanocoating. This again confirms that mechanically much better protection is attained with the nano-coating.

These findings provide a good insight into the high temperature corrosion material response for subsequent computational modelling (finite element analysis and computational fluid dynamics analysis), which is elaborated in *Chapter 6 for both micro-coated and nano-coated specimens*. It is noteworthy that the *mineralogy of the oxidation products* could not be determined using SEM/EDS. This requires XRD techniques which may be explored in the future.

CHAPTER 6: COMPUTATIONAL SIMULATIONS OF MICRO-COATED AND NANO-COATED GAS TURBINE BLADE SPECIMENS

6.1   Introduction

In the previous chapter detailed TGA and SEM/EDS (EDXA) experiments on micro-coated and nano-coated samples were described. These tests identified important characteristics of the behaviour of titanium-silicon carbide micro-coating and 60: 40 aluminium oxide-titanium oxide nano-coating at high temperature, in particular the excellent reduction in corrosion rates achieved, decrease in surface degradation and elimination in surface material flaking for the nano-coated specimens.

To provide a deeper insight into the mechanics of this behaviour, aimed at explaining the thermal protection achieved with micro-coating and the even better protection attained with nano-coating, in this chapter, computational simulations are described. The 3-D models are based on a small representative rectangular sample from an actual gas turbine blade.

CFD is included for the *micro-coated* specimens to enable consideration of the flaking effects i.e. removal of material from the micro-coated blade specimens. Since no such flaking was detected in the TGA testing of the nano-coated samples, CFD is not considered for the nano-coating.

It is important to note in the experimentally tested micro- and nano-coated specimens corrosion rates were measured in the TGA under *transient* conditions. However, in the computational simulations, the maximum temperature achieved is imposed as a thermal condition and steady-state finite element stress analysis is conducted. Owing to mesh density restrictions transient analysis was not conducted. The finite element simulations are performed to provide an insight into the *worse case scenario* i.e. highest temperature that would be experienced in real gas turbine specimens and therefore a single high temperature condition is imposed (1000 Celsius). Three sections on computational modelling are included:

(i) 3-dimensional finite element *elastic stress* and *thermal stress* simulation and also *CFD erosion modelling* for the titanium-silicon carbide ceramic micro-coated AISI 304 substrate (3-layer model), titanium micro-coated AISI 304 substrate (2-layer model) and the unprotected substrate (single layer model).

(ii) 3-dimensional finite element *elastic stress* modelling of multiple combinations of aluminium oxide-titanium oxide nano-powder coating (2-layer model) *without thermal effects*. This is a stepping-stone which enables identification of the best possible mix for subsequent *thermoelastic stress analysis*.

(iii) 3-dimensional *thermoelastic finite element stress analysis* of a 60:40 aluminium oxide-nano-powder coating (2-layer model).

Extensive visualization of *equivalent elastic strain, total deformation, equivalent stress and strain energy* is included for the *finite element stress and thermal stress* computations. *Erosion rate only* is included for the micro-coated specimen *CFD turbulent erosion* simulations. The coating layers are modelled as a *composite* i.e. superposed layers are built on top of each other for the micro-coating and a single layer on top of the substrate for the nano-coating. Chemical corrosion effects could not be simulated as they are not possible in ANSYS software. In all *thermal modelling* cases 1000 Celsius is imposed as the thermal condition to investigate the micro-coated and nano-coated specimen response under the highest temperature achieved in any of the experiments in *chapter 5* and this provides a realistic estimate of actual gas turbine operational temperatures. The simulations confirm that while micro-coatings do provide very good protection, *erosion does occur at the surface* of the specimen (substrate) and while the metallic/ceramic combination does reduce surface deformation, high thermal stress zones are still captured in the core area of the face of the specimen. These *high thermal stress core zones are eliminated* with the nano-coated specimen. For the nano-coated specimen, generally the

60: 40 aluminium oxide-titanium oxide mix produces the best thermal protection although good structural (non-thermal elastic) performance is achieved with 50: 50 and 40: 60 mix designs.

6.2 Computational analysis of titanium-silicon carbide micro-coated specimens

All finite element stress (structural) and computational fluid dynamics simulations for the micro-coated specimens have been executed in **ANSYS Workbench version 16.2** [1, 2]. These analyses are described next.

6.2-1 Finite element stress analysis of titanium-silicon carbide micro-coated specimens

The general methodology is summarized in **Figure 6.1**. A three-dimensional model was created using the ANSYS static structural geometry modeller to represent as accurately as possible the specimen deployed for testing in chapter 5. The dimensions of the full 3-D model therefore exactly matched the micro-coated specimen before TGA testing and are shown below, in **Figure 6.2,** for the *three-layer micro-coated system* (titanium plus silicon carbide plus AISI 304 substrate) the exact dimensions of the actual micro-coated sample tested in TGA, were re-created i.e. *20.76mm x 10.98mm x 1.86mm* (see chapter 5).
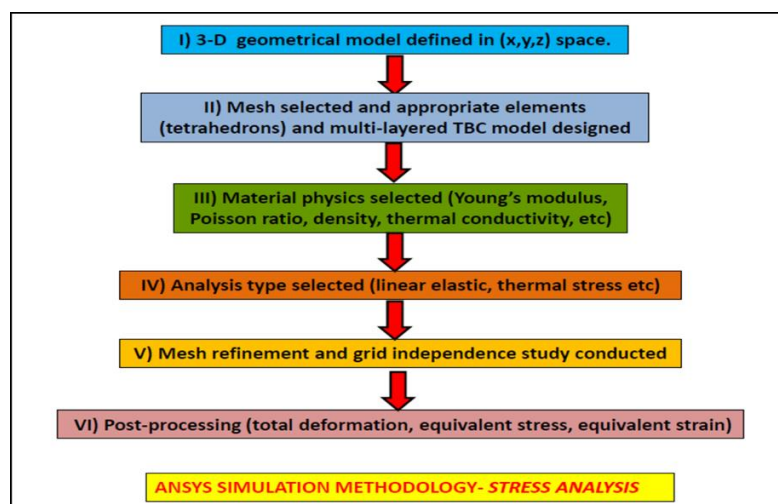
Figure 6.1: ANSYS finite element stress analysis procedure.

For the *two-layer system* (titanium plus AISI 304 substrate) the coating thickness was half of the combined titanium-silicon carbide thickness. For example, on the upper and lower faces, the titanium layer coating thickness is half of 0.18mm i.e. *0.09mm*.

A three-layered domain in (*x, y, z*) space was created with each layer representing the three main materials of interest, namely a core steel layer *(AISI 304 substrate alloy)*, an intermediate Titanium layer and an outer ceramic (Silicon Carbide SiC) layer. The core steel layer is shown in **Figures 6.3**. The inner Titanium (metallic) layer domain is depicted in **Figure 6.4.**
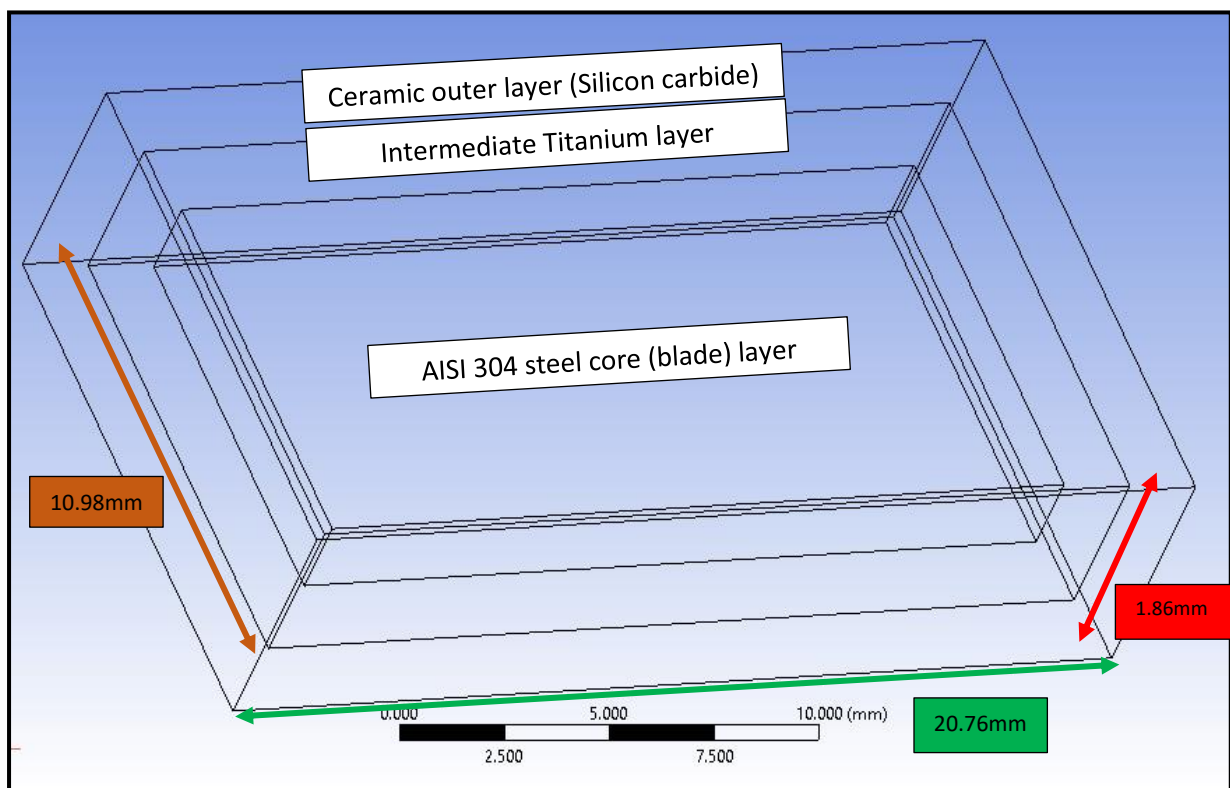
Figure 6.2: Dimensions of the final micro-coated sample i.e. sample substrate plus titanium intermediate coating plus ceramic Silicon Carbide outer coating (identical to experimental specimen *before TGA testing).*

All material parameters (Young modulus, Poisson ratio, coefficient of thermal expansion, density etc) are selected from the engineering data library present in the ANSYS code. Isotropic, homogenous elastic behaviour is assumed. The three-dimensional elasticity equations (equilibrium, constitutive and compatibility) and thermal conduction model have

also been presented in *Chapter 3* and therefore are not repeated here. Due to the relatively simple geometry of the blade sample model, a body-sizing meshing approach, compromising mainly of tetrahedral (3-D pyramidal) cells, was used to produce efficient meshing which guarantees high accuracy and low computational times. Refinements were concentrated at the connection points between the layers to displace the focus towards the static effects dissipated between them.
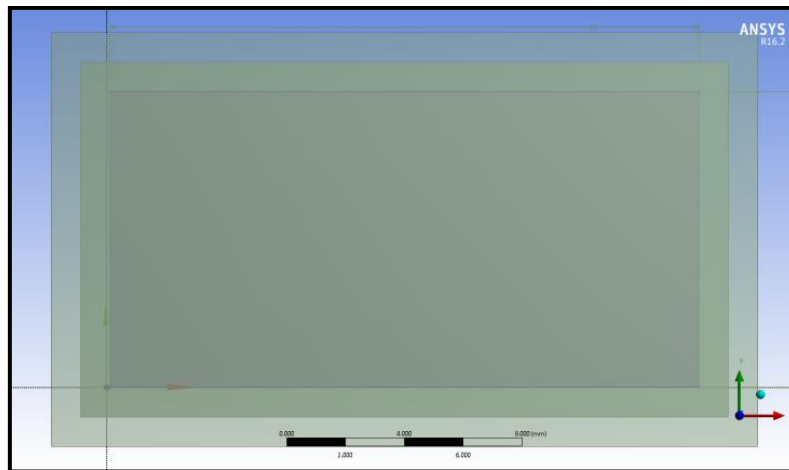
Figure 6.3: AISI 304 steel core layer (bare substrate) at centre with dimensions *20mm x 10mm x 1.5mm.*
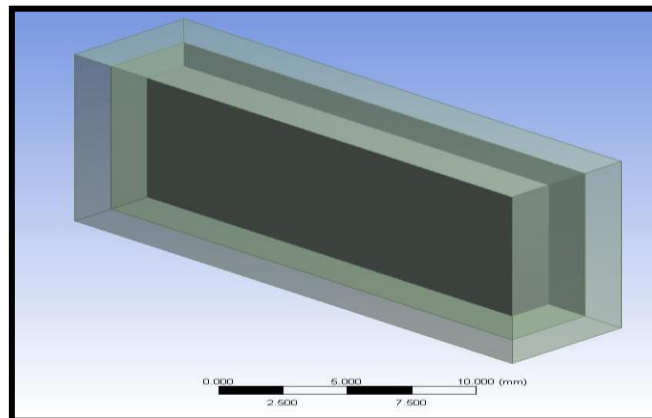
Figure 6.4: Intermediate Titanium layer (between the substrate and outer ceramic layer) with coating thickness dimensions of 0.09mm on the top and lower faces, 0.19mm on the long edges and 0.245mm on the shorter edges.

The cell distribution around the model is shown in **Figures 6.5 and 6.6**. To verify the accuracy of the meshing, a grid-independence study was also conducted. The results are crystallized in **Table 6.1** and **Figure 6.7**. The grid independency study results indicated that reducing the mesh size by half saved a massive amount of computing time while maintaining the accuracy of the results. **Table 6.2** gives all the material properties used in the stress analysis.
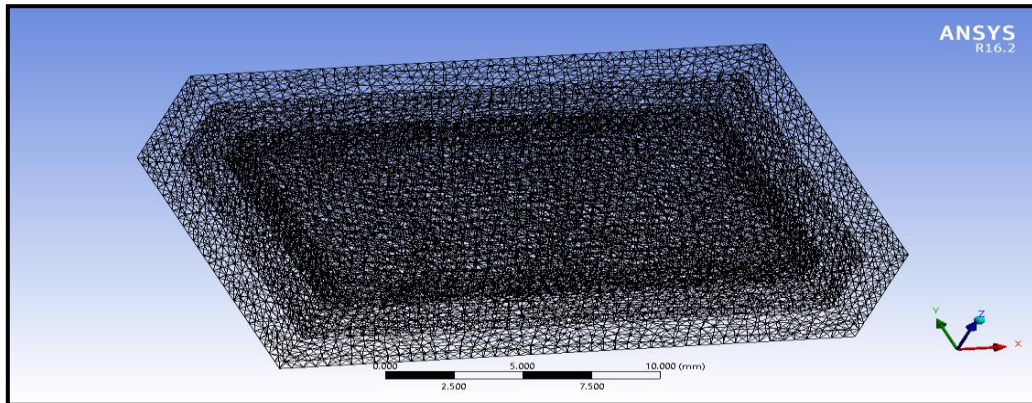
Figure 6.5: Representing a wireframe of the geometrical model seen above.
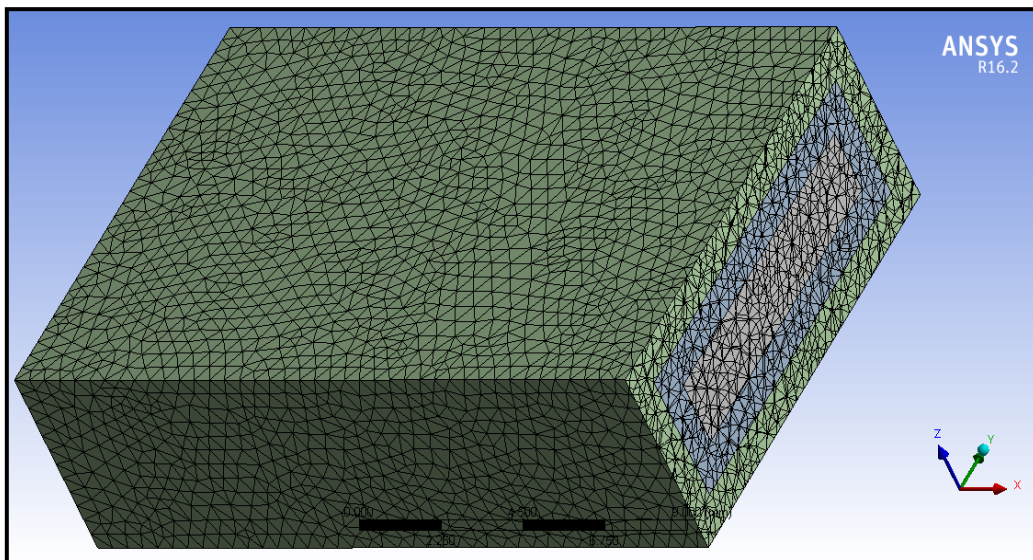
Figure 6.6: Showing a section plane from the mesh produced outlining the refinement between the layers.

Mesh	Total no. of cells	Total Deformation (mm)	Computational time (minutes)
Double refinement	1543818	0.24521	90
Original mesh	362018	0.24493	20
Half element sizing	148167	0.24406	5
Quarter element sizing	68256	0.22564	2

Table 6.1: Representation of the effect of mesh density on the simulation values.

Property	Steel	Titanium	Silicon Carbide Ceramic
Young Modulus	200GPa	100GPa	450GPa
Poisson Ratio	0.28	0.3	0.19
Density	$7850kg/m^3$	$4500kg/m^3$	$3200kg/m^3$
Thermal conductivity	50W/mK	20W/mK	175W/mK

Table 6.2: Material properties.

Following the successful meshing of the models and the prescription of the material properties, static and thermal stress simulations are conducted. Static loading of 10 bars is applied on the top face of the model.

For the *static analysis*, the default solver is set to control the simulation on all six faces which are fixed. The software automatically computes the *equivalent elastic strain, total deformation, equivalent stress and strain energy*.

The same process is repeated for the thermal study with the exception of the inclusion of a thermal condition of 1000 degrees Celsius, while keeping the same outputs.

First the *statical analysis* results are shown and then the *thermal stress analysis* results are given. The results will be compared for each of the three models, viz the *double coated sample* (Titanium and SiC ceramic) i. e. "three layer model", *single coated sample* (Titanium) sample i.e. two-layer model and finally the *unprotected steel blade sample* i.e. single layer model.

Figures 6.7- 6.18 present extensive results for all *static stress analysis.* **Figures 6.19-6.27** present all the results for *thermal stress analysis*. In both sets of simulations, each of the coating models are considered in turn i.e. three-layer model (steel + Titanium + Silicon Carbide (SiC) ceramic), two-layer model (steel + Titanium) and the uncoated (steel) model. *Four elastic characteristics* are considered- *total deformation, equivalent elastic strain, equivalent stress and strain energy distribution.*

Figures 6.7 to 6.18 correspond to the *static non-thermal* scenario and are considered first.

Figs. 6.7- 6.9 show the *total deformation* in all three coating cases. Inspection of the two-dimensional face deformation contour surface plots indicates there is a significant variation in deformation with the three different combinations. Substantially higher deformations are computed in the *three-layer model* (dual Titanium and Silicon Carbide (SiC) ceramic coatings) as shown in **Figure 6.7**. The large red (high deformation) zone covers most of the steel model surface. The maximum deformation arises in the lower left quadrant towards the left edge. The minimal deformation is in the opposite quadrant closer to the right edge. The titanium coating results in the high deformation zone being eliminated in the major central area of the face. However small red zones re-emerge at the corners of the coated plate structure. The maximum deformation is observed in the lower quadrant corner vicinity and the minimum deformation is located in close proximity further upwards near the right edge. Concentric bands of progressively lower deformation (orange, yellow, light green, dark green, light blue) are

145

witnessed as we move for the periphery to the central zone. Generally, a deformation gradient is achieved i.e. smoother deformation transition from the edges to the core, which is absent in the single layer steel model (where very narrow bands are confined to the outermost periphery of the structure). With the *purely steel case* (uncoated) (**Figure 6.9**) there is an even more significant departure from the purely steel case. Much larger high deformation zones are computed at the corners and there is also a slightly higher deformation zone in the core region compared with the two-layer model (**Figure 6.8**). The presence of a titanium coating therefore clearly suppresses deformation for the vast majority of the area of the loaded gas turbine surface. The great resilience of Titanium is therefore shown here. However only with the *addition of the ceramic (Silicon carbide) coating* are the *peak deformation zones* reduced at the edges (**Figure 6.7**) which are discontinuities and potential zones for failure. In **Figure 6.7** (three-layer model) it is also noteworthy that the minimum deformation migrates deep into the upper right quadrant edge as opposed to the two-layer model (**Figure 6.8**) where it is (as discussed earlier) appears at the lower right quadrant edge. The maximum deformation location is also distinctly different between **Figure 6.7** (three-layer model) and **Figure 6.8** (two-layer model) as it is now computed at the upper right quadrant corner. The presence of ceramic in addition to Titanium coating layers (**Figure 6.7**) therefore provides additional resistance to deformation of the surface of the structure as whole, although only Titanium in the two-layer model (**Figure 6.8**) significantly suppresses high deformation in the central zone. An important achievement with the three-layer model (**Figure 6.7**) is that maximum deformation is further from any edge indicating that the potential for failure is lowered. However, the high deformation in the core zone indicates that potentially the ceramic can absorb the major damage.

Figures 6.10-6.12 depict the *equivalent elastic strain plots* for the three models studied. It is evident that the *maximum elastic strain* is only computed in the core zone (far from the edge

discontinuities) for the *three-layered* model (**Figure 6.10**) and the *minimum elastic strain* is located near the uppermost edge of the surface. However elastic strain values are quite high in the core area. For the two-layered model (**Figure 6.11**) the maximum strain location is pushed to the upper edge (right corner) and again for the single layer model i.e. unprotected steel (**Figure 6.12**) it arises near the upper edge although it is displaced towards the left top corner. The *dual (titanium coating) and single layer (unprotected steel) models* therefore do not achieve the desired effect i.e. they localize the maximum strains in the edge zones where failure is most likely to occur. The combination of titanium and silicon carbide *ceramic i.e. the double layer micro-coating* is successful in avoiding this by restricting maximum elastic strain to the central zone which is the strongest and least likely to fail under loading.

Figures 6.13-6.15 illustrate the *equivalent elastic stress* computational plots for the three models. The three-layered model (**Figure 6.13**) produces a *maximum stress* in the core zone (central area) whereas this is displaced towards the upper and lower edges, respectively, for the two-layer model (**Figure 6.14**) and single layer (uncoated) model (**Figure 6.15**) with a strong orientation towards the right vertical edge (the minimum stress locations are always in the core area for these models whereas minimum stress is pushed into the upper edge corner zone for the three-layer model. This is undesirable again since the probability of failure is greatest at the edges. The amalgamation of a titanium coating layer and silicon carbide layer (Figure 6.13) i.e. the three-layer model therefore produces more beneficial stress distributions and reduces the likelihood of structural degradation and failure at the edges.

Figures 6.16-6.18 illustrate the contour plots for *strain energy distributions* for the three model cases. Maximum strain energy is further into the surface area for the three-layer model (**Figure 6.16**) compared with the two-layer model (**Figures 6.17**) and single layer unprotected model (**Figure 6.18**) in which it is displaced progressively further towards the left vertical edge. A much more *homogenous* distribution of strain energy is noted in **Figure 6.16** for the three-layer

model. Some variation and heterogeneity is computed for the two-layer model (**Figure 6.17**); however there is a significantly different pattern for the single layer model (**Figure 6.18**) which exhibits an *outer peripheral band of low strain* and an *inner oblate edged rectangular zone* of minimum strain energy. The computations show good similarity with other single, two-and three-layered metal/ceramic coating finite element models, for example Tavaresa *et al.* [3] and Shekeri *et al.* [4].
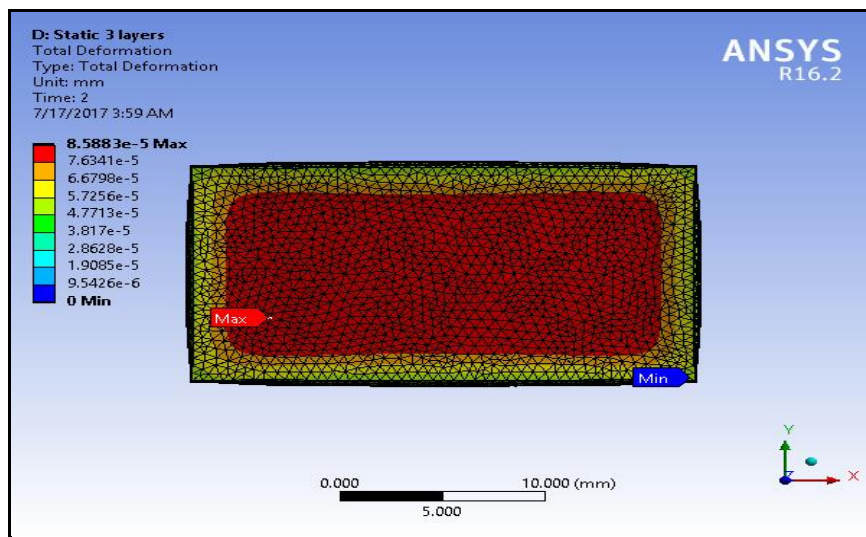
Figure 6.7: Total deformation results for three-layer model (steel + Titanium + SiC ceramic)- *static case.*
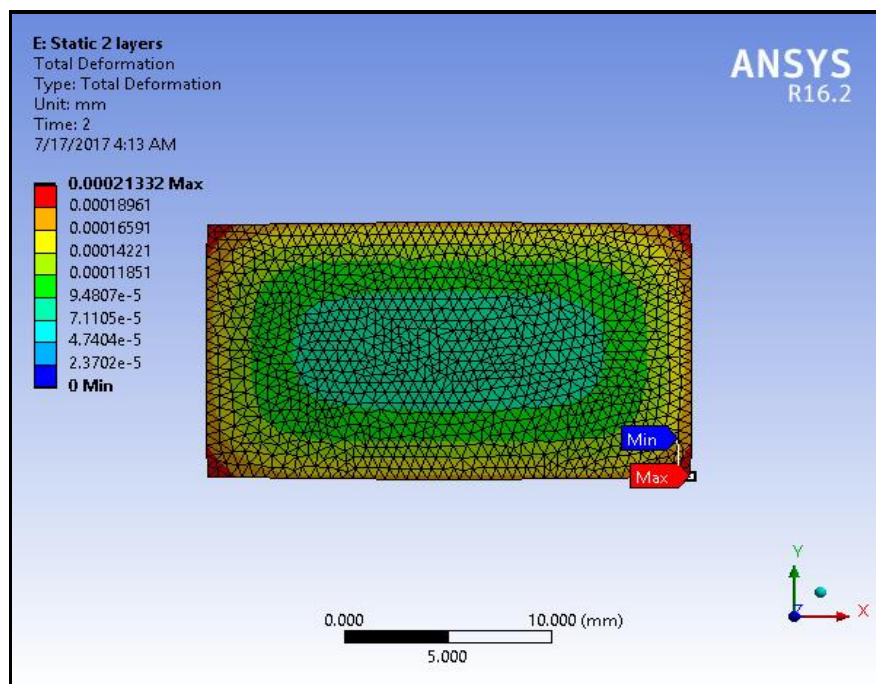
Figure 6.8: Total deformation results for two-layer model (steel + Titanium) - *static case.*
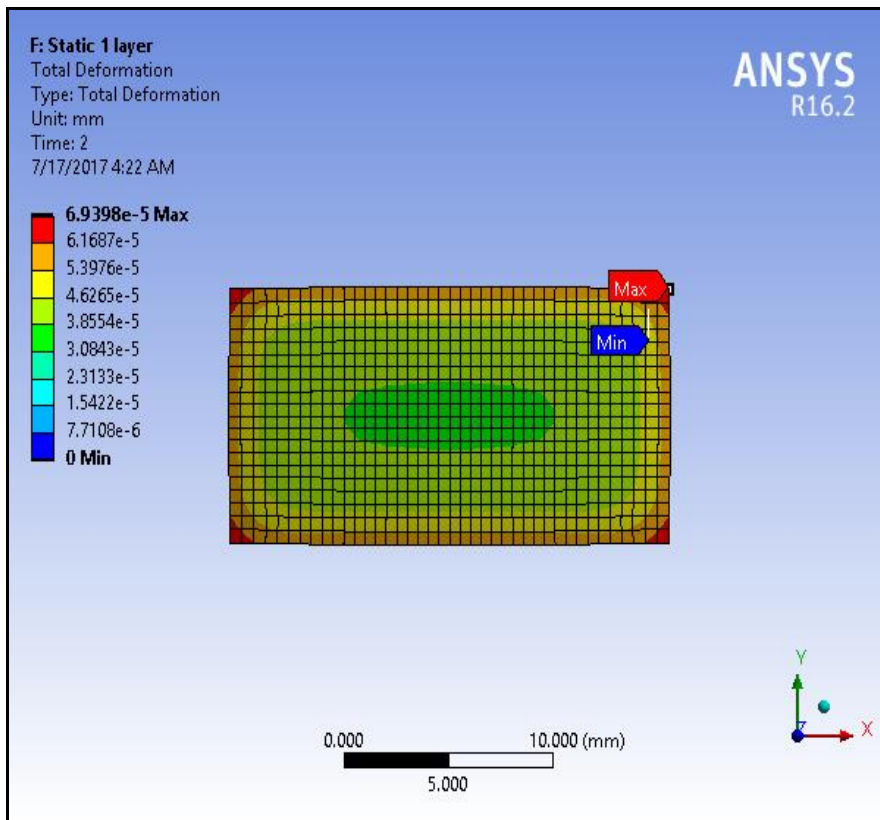
Figure 6.9: Total deformation results for one-layer model (bare unprotected steel) - *static case*.
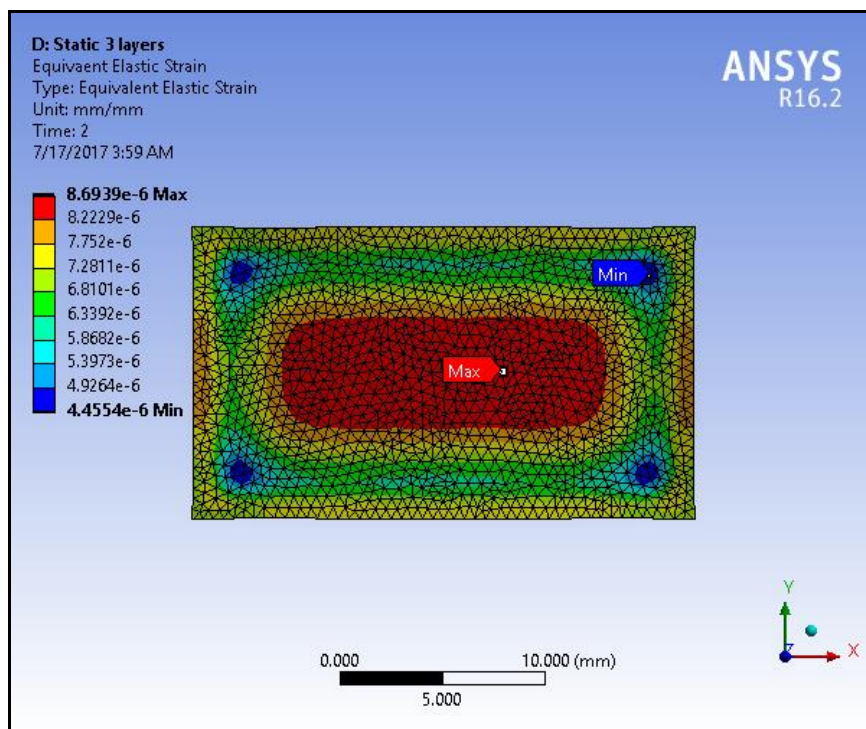
Figure 6.10: Equivalent elastic strain results for three-layer model (steel + Titanium + SiC ceramic) - *static case*

149
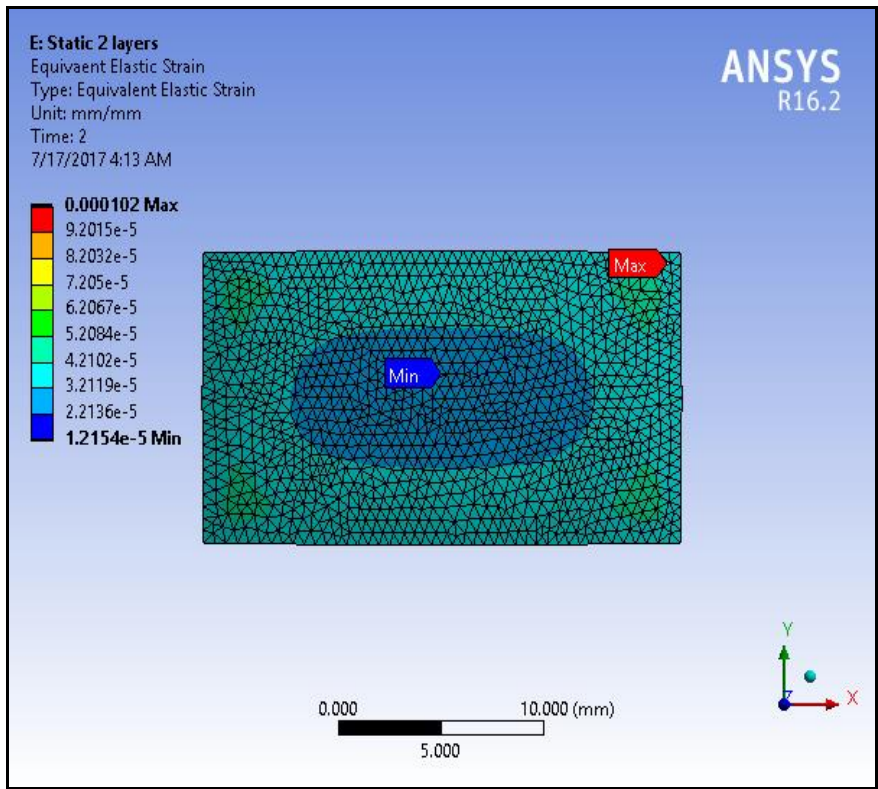
Figure 6.11: Equivalent elastic strain results for two-layer model (steel + Titanium) - *static case.*
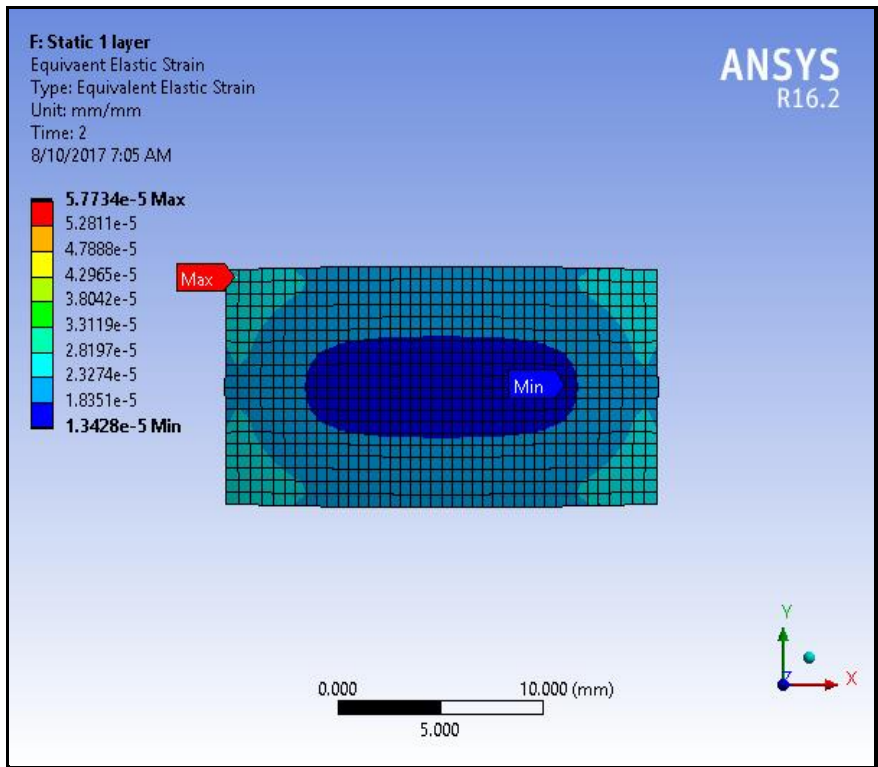
Figure 6.12: Equivalent elastic strain results for one-layer model (steel) - *static case.*
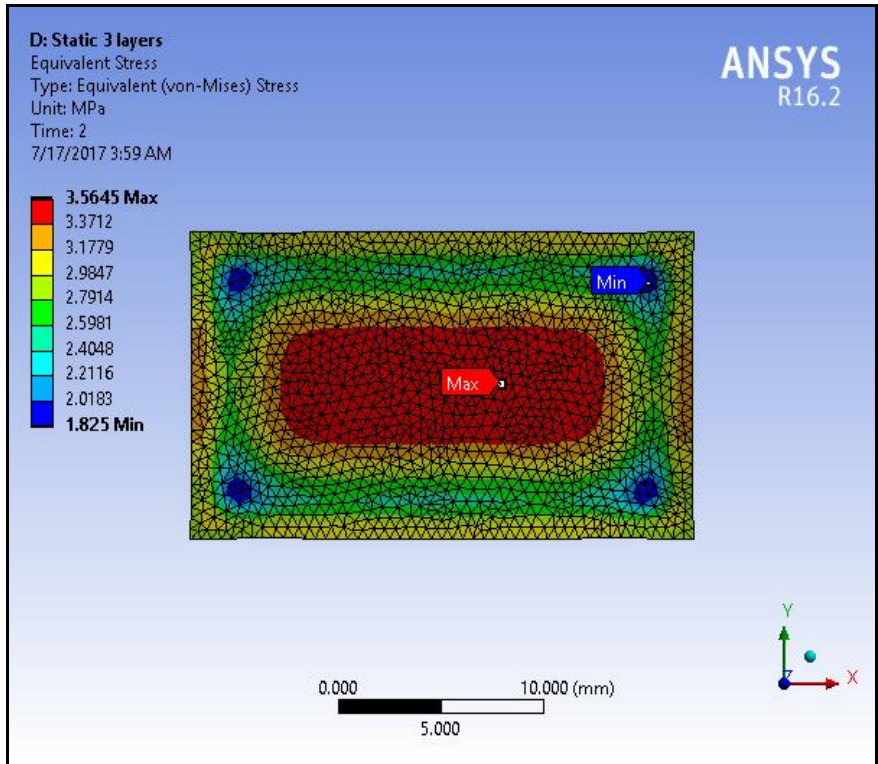
Figure 6.13: Equivalent stress plot for three-layer model (steel + Titanium + SiC ceramic)-
static case.
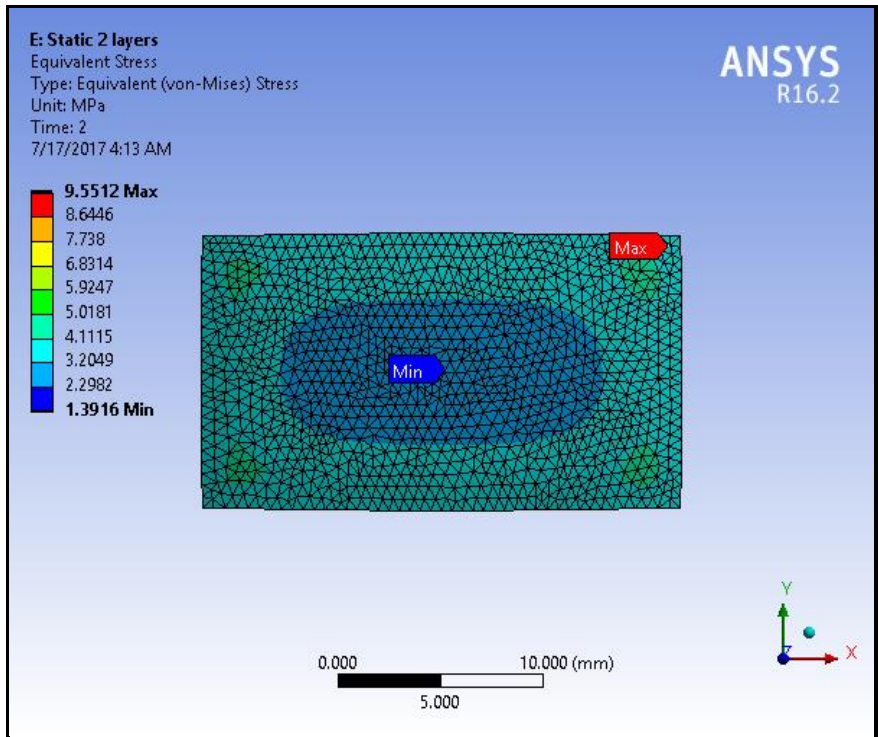
Figure 6.14: Equivalent stress plot for two-layer model (steel + Titanium) - *static case.*
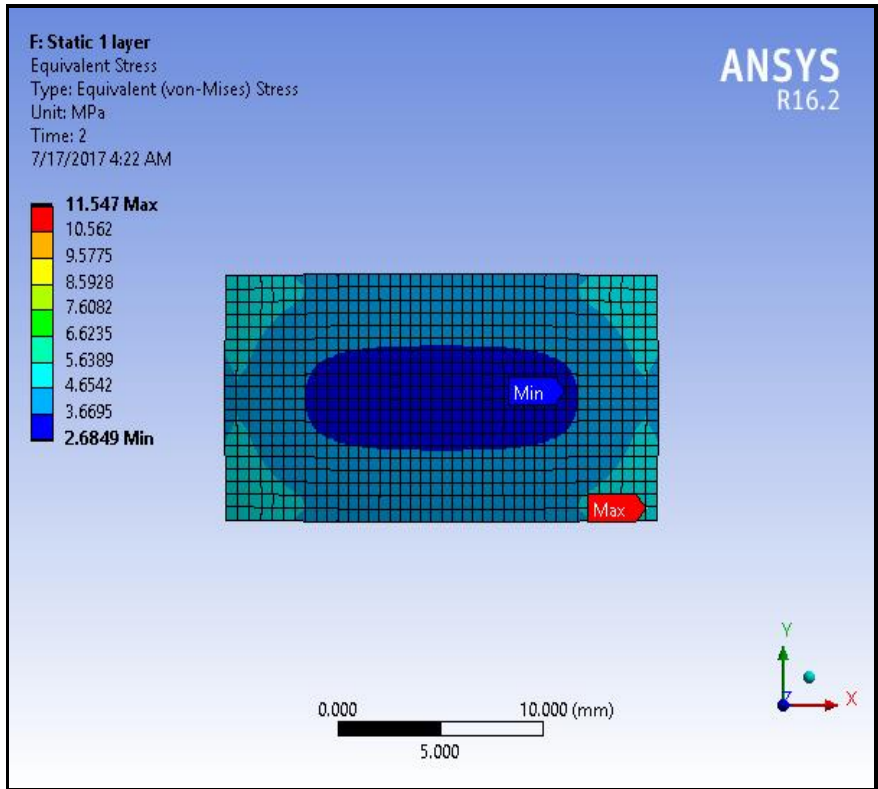
Figure 6.15: Equivalent stress plot for one-layer model (steel) - *static case.*
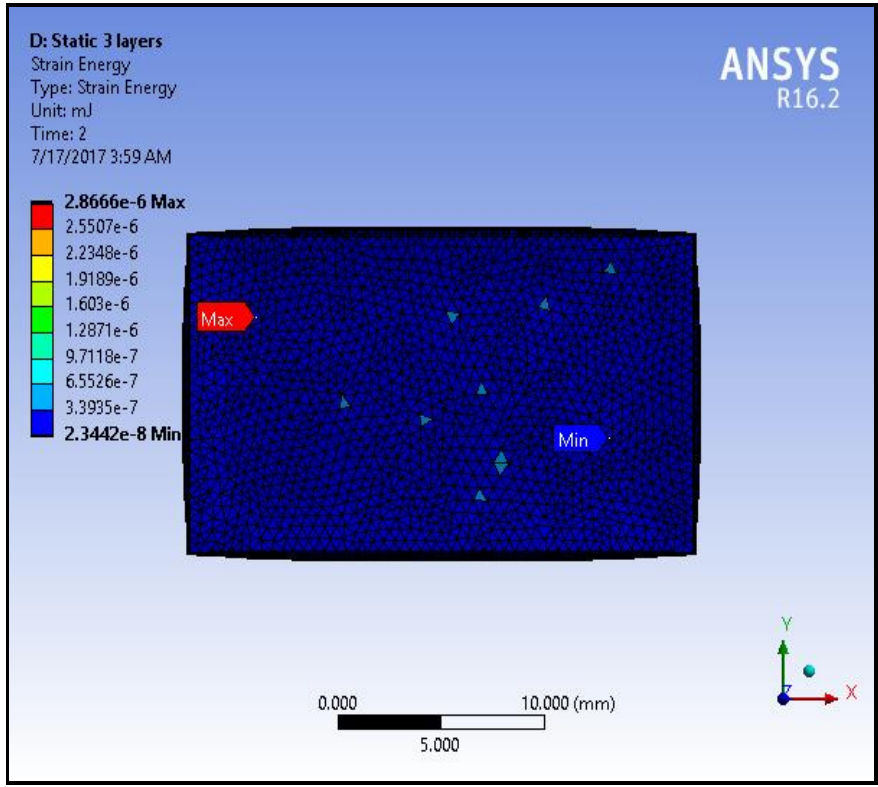
Figure 6.16: Strain energy distribution for three-layer model (steel + Titanium + SiC ceramic)-*static case.*
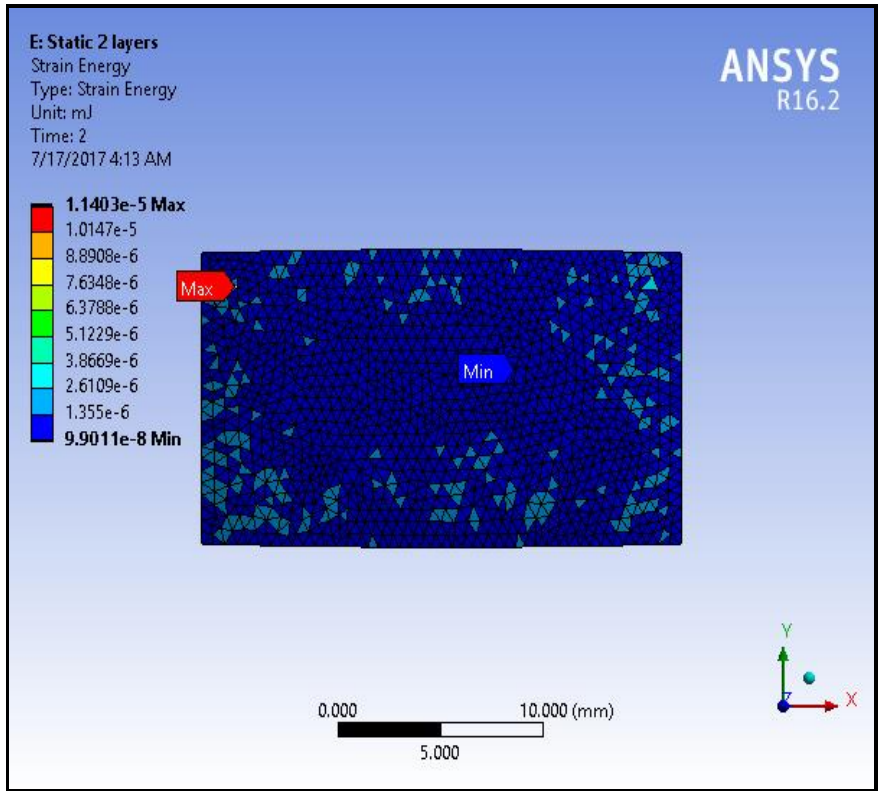
Figure 6.17: Strain energy distribution for two-layer model (steel + Titanium) - *static case.*
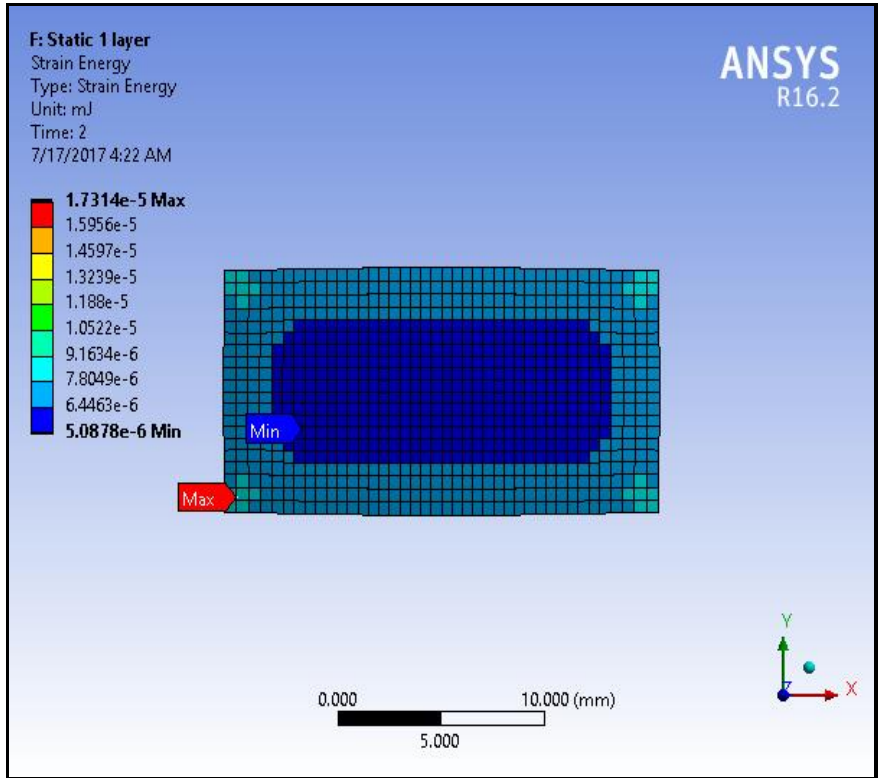
Figure 6.18: Strain energy distribution for one-layer model (steel) - *static case.*

Figures 6.19- 6.27 present computational contour visualizations for the *thermal elastic simulations* of the three-layer model (steel + Titanium + Silicon Carbide (SiC) ceramic), two-layer model (steel + Titanium) and the uncoated (steel) model. For these simulations the full body models (3-dimensional) are presented rather than just the top surface two-dimensional distribution plots (as in **Figures 6.7-6.18**). The *presence of heat significantly modifies the total deformation plots* i.e. **Figures 6.19-6.21**. Red (high deformation) zones are localized in all three cases at the left and right vertical cases; however, the zone of influence penetrates much deeper into the body for the single layer model (**Figure 6.21**), less deeper with double layer model i.e. *only titanium micro-coating* (**Figure 6.20**) and is minimized with the *three-layer model i.e. titanium plus silicon carbide micro-coating* (**Figure 6.19**). Much lower total deformation is also computed throughout the body of the structure in **Figure 6.19** indicating that the three-layer model achieves the best performance overall. As corroborated by Breitbach and Schubert [5] there is clearly a *non-uniform distribution of temperature* at different locations of the coated steel specimen (hypothetical blade surface), which directly impacts on the deformation field. Even though the analysis is thermally and elastically isotropic, there is still irregularity in the heat transferred via thermal conduction through the body of the material. *Maximum deformation* is observed at the bottom left corner of the upper surface in the three-layered model whereas it is confined to the bottom right corner for the two-layer and single layer models.

Figures 6.22-6.24 illustrate the evolution in *equivalent strain contour plots* for the three different micro-coating models examined. While lower strains are computed in **Figure 6.24** (single layer model) the maximum strain is located near the edge. Higher strains are computed for the two-layer model (**Figure 6.23**) – however again with only titanium coating present, the maximum stress is dangerously close to the lower edge. Only with the *three-layer titanium-silicon carbide ceramic coating model* (**Figure 6.22**) is the maximum equivalent strain *pushed*

deeper towards the core central area. Therefore, with the three-layer model the desired effect of restricting high stresses to the strongest region of the gas turbine blade model is achieved whereas in the other two models, *lower strains are produced* in the core central zones. Unlike other studies e. g. Breitbach and Schubert [5], in the current study *a more refined conjugate heat transfer analysis with fully coupled thermal-stress calculation* is conducted (i.e. the model is not decoupled as in [5] and many other studies). The thermal results indicate that strain state of the structural material adjacent to the coating interface is *the controlling mechanism* for the coating strains. Due to the non-uniform distribution of displacement, strain and stress in a real gas turbine blade, the regions located at the top and bottom sides tend to produce a maximum of displacement, with the occurrence of a bigger strain or stress, where *sub-critical cracks* preferentially form. The simulations confirm this trend and agree with the general findings in the literature including, for example, Cao *et al.* [6] and Fan *et al*. [7].

Figures 6.25-6.27 show the *equivalent elastic stress contour plots* for the three coating models. For the three-layer model (**Figure 6.25**) a similar distribution to the static case (**Figure 6.13**) is observed indicating that the heat has the least impact on stress distribution when both ceramic and titanium micro-coatings are combined. However significantly higher stresses are computed for the two-layer model (**Figure 6.26**) and especially the single layer model (**Figure 6.27**) compared with their *non-thermal* static analysis equivalent plots in **Figures 6.14, 6.15,** described earlier. Higher stresses are also computed at the edge zones for the thermal cases of single and two-layer models compared with the *static* cases. Overall, therefore the best protection is provided by the three-layer ceramic-titanium-steel model confirming the very good thermal protection barrier properties of both ceramics and titanium under high temperature loading scenarios. It is also noteworthy that the high deformations sustained in the three-layer model are taken largely by the ceramic outer layer and this explains why in the experiments there is surfacial damage (and flaking) observed in the titanium-silicon carbide

micro-coated specimen. The key objective of mitigating thermal damage on the steel substrate is achieved with the titanium-silicon carbide micro-coating.
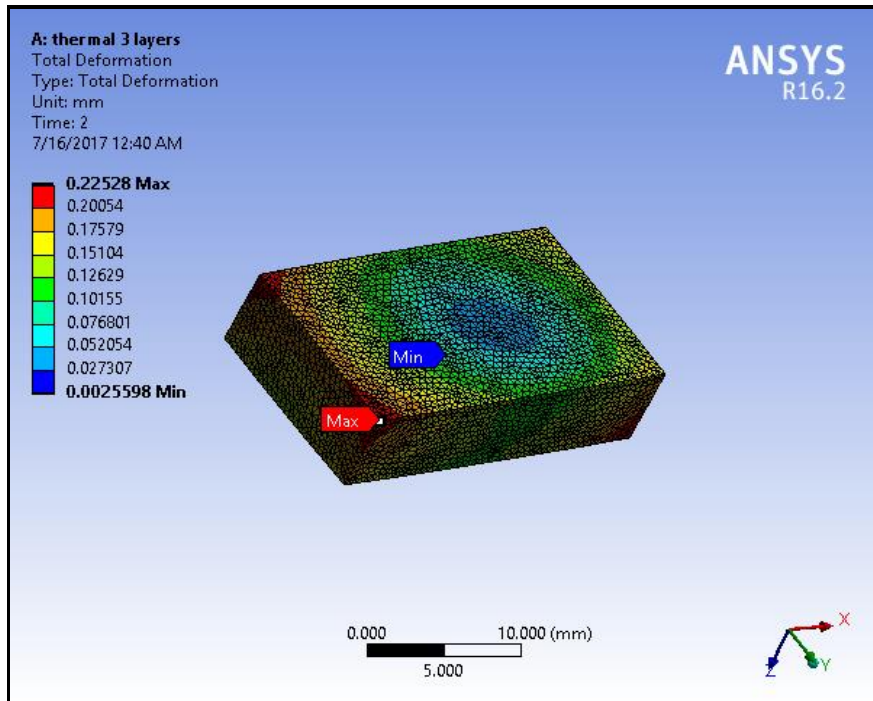
Figure 6.19: Total deformation for three-layer model (steel + Titanium + SiC ceramic) – *thermal case.*
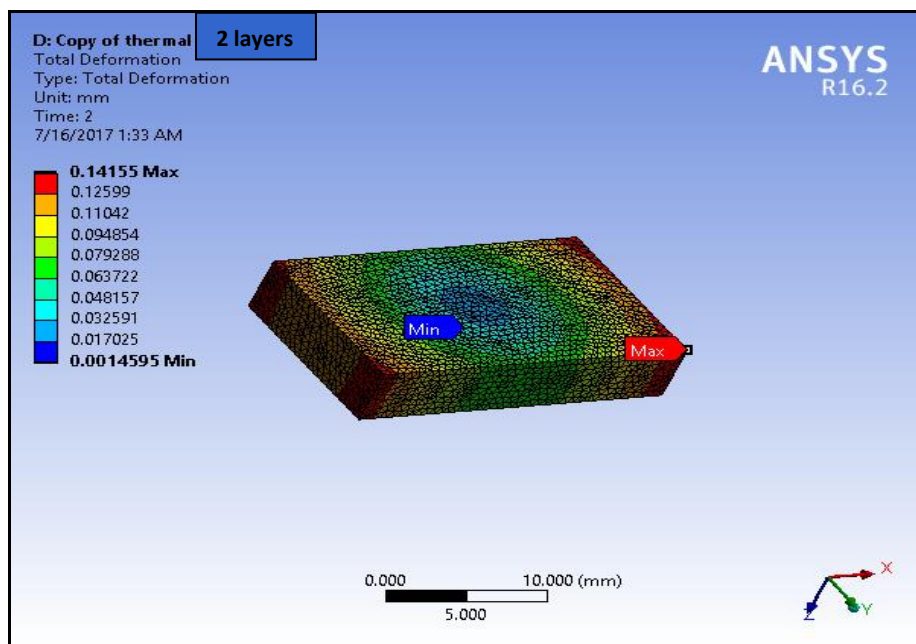
Figure 6.20: Total deformation for two-layer model (steel + Titanium) – *thermal case.*
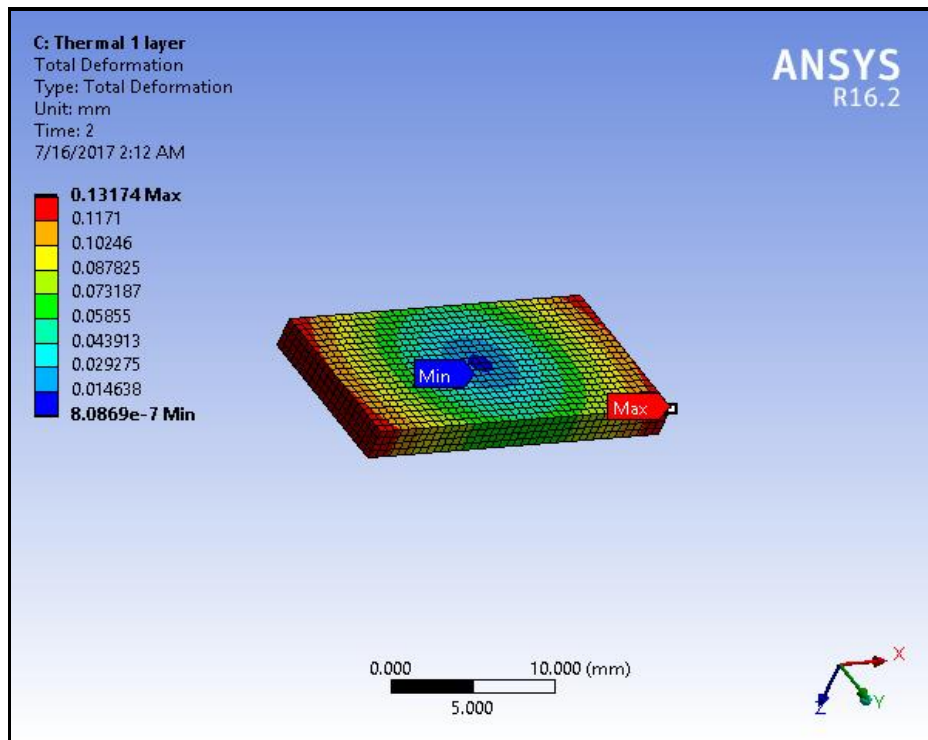
Figure 6.21: Total deformation for one-layer model (steel) – *thermal case.*
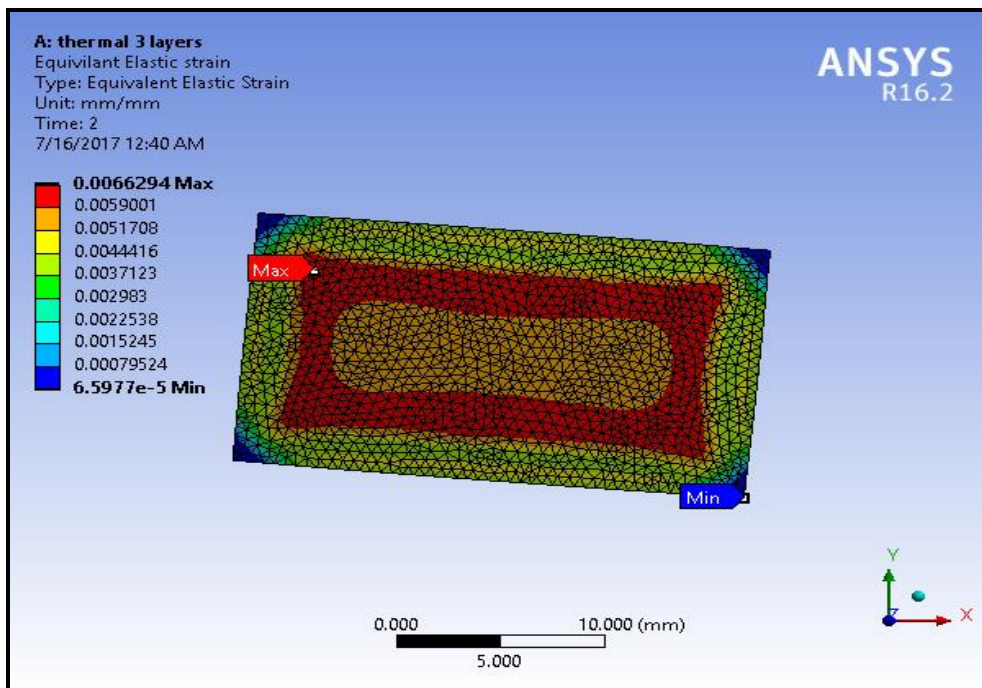
Figure 6.22: Equivalent elastic strain for three-layer model (steel + Titanium + SiC ceramic)
– *thermal case.*
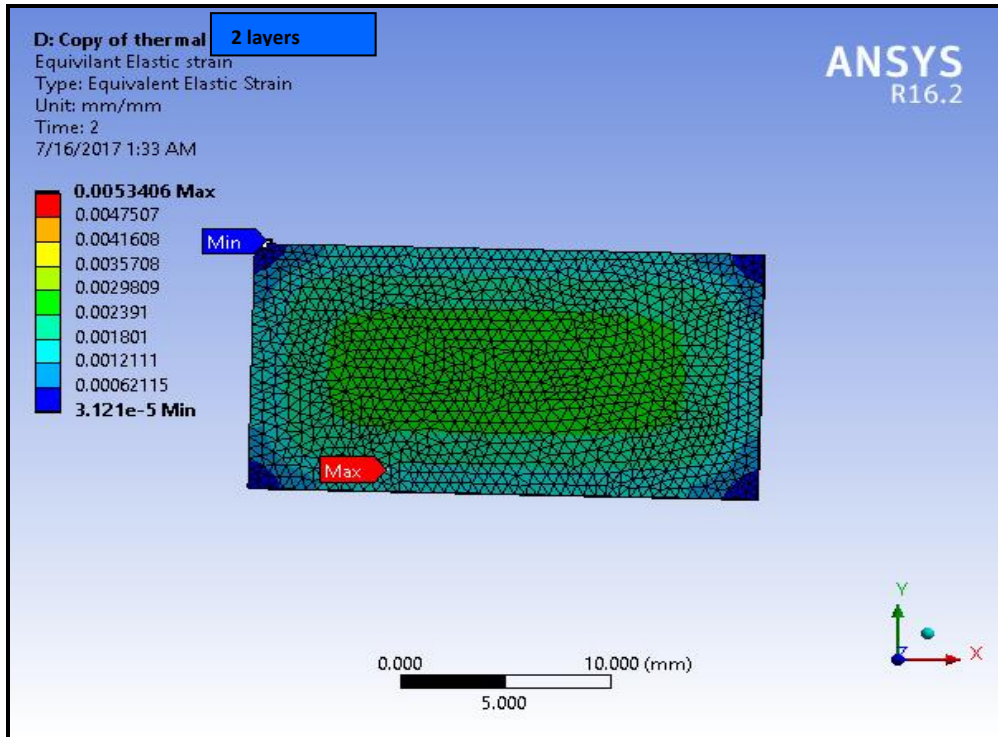
Figure 6.23: Equivalent elastic strain for two-layer model (steel + Titanium) – *thermal case.*
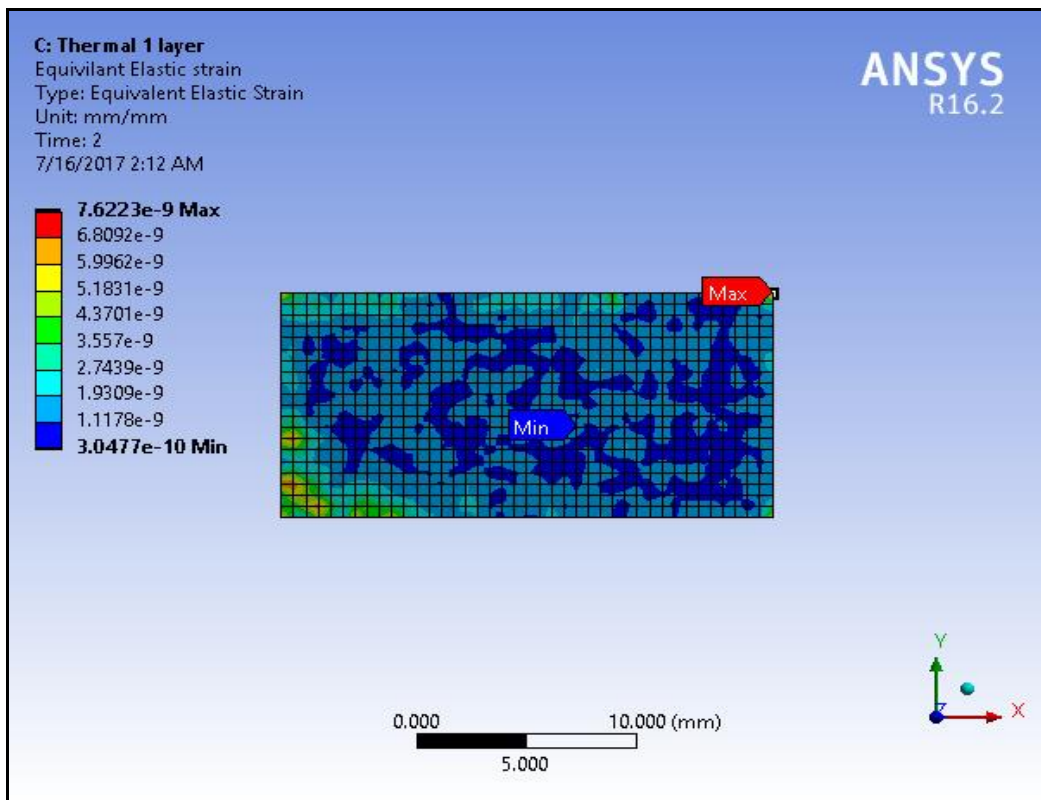
Figure 6.24: Equivalent elastic strain for one-layer model (steel) – *thermal case.*
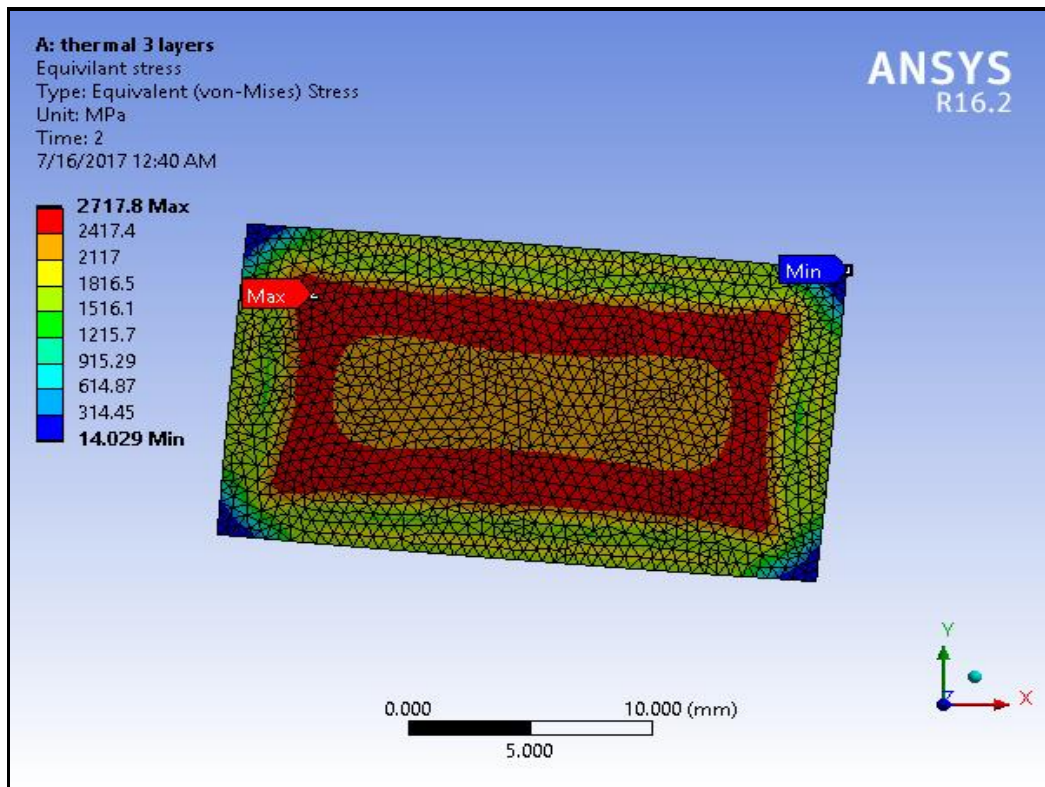
Figure 6.25: Equivalent elastic stress for three-layer model (steel + Titanium + SiC ceramic) – *thermal case.*
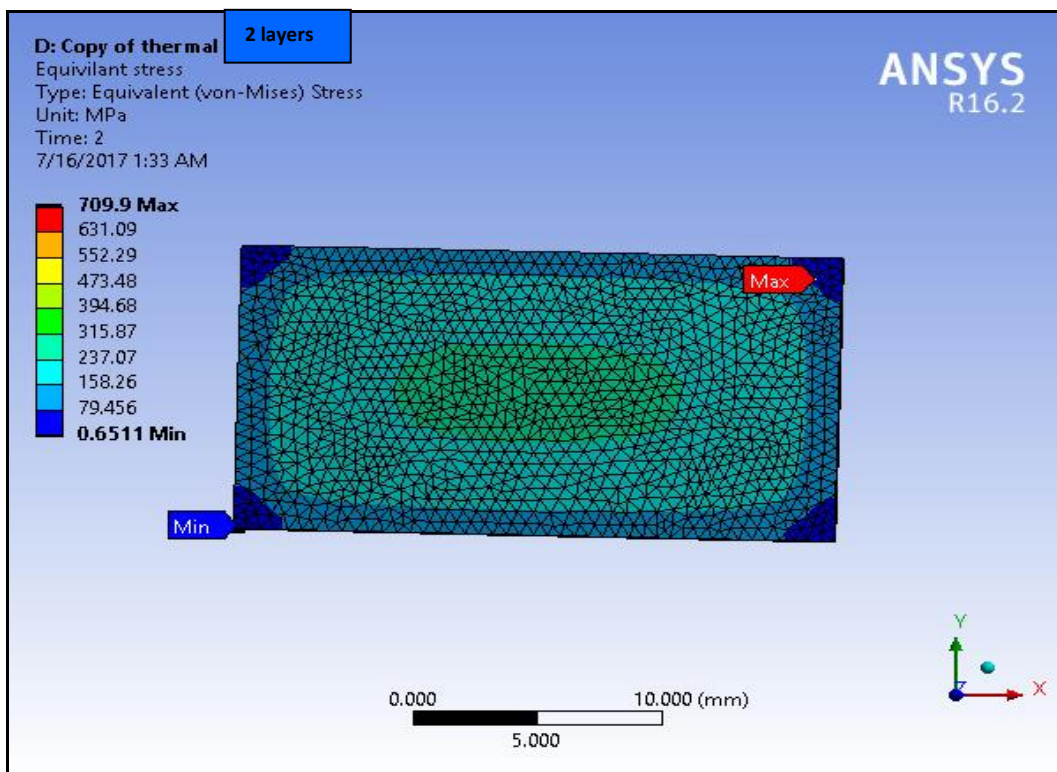
Figure 6.26: Equivalent elastic stress for two-layer model (steel + Titanium) – *thermal case.*
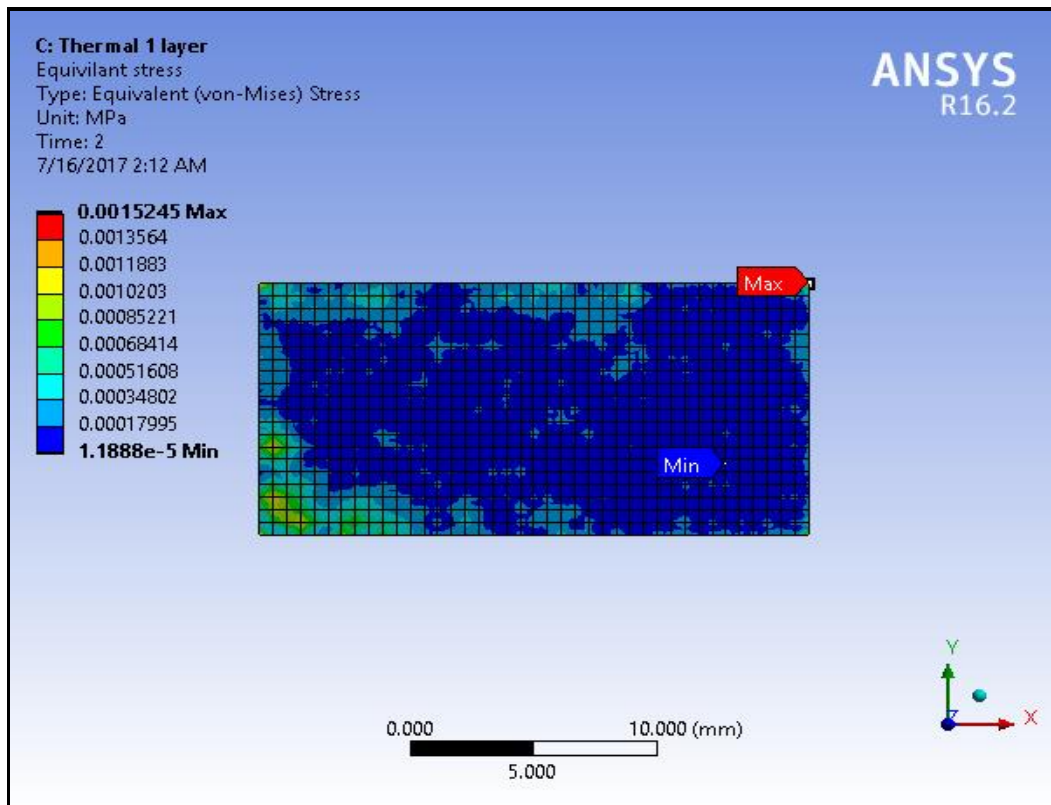
Figure 6.27: Equivalent elastic stress for one-layer model (steel) – *thermal case.*

6.2-2 CFD erosion analysis of titanium-silicon carbide micro-coated specimens

The meshed model described in **Section. 6.2-1** is imported into ANSYS FLUENT [2] to conduct the CFD erosion simulation on the micro-coated blade specimen. The CFD simulation is inevitably more demanding than the stress analysis. It requires some refinement of the mesh to accommodate for the size of the air particles (hot corrosive air stream at 1000 Celsius) leading to the erosion of the structural micro-coating. Chemical reaction effects are neglected. *The CFD analysis is however a supplementary consideration in this PhD and is only used to provide an estimate of erosion rate.* The CFD modelling generate a representative pressure and thermal field. This grid refinement is conducted in the solver phase of the simulation to avoid altering the main mesh of the structure and avoiding errors. The solver is set to include the double precision option to allow a higher accuracy and the parallel processing option is enabled to utilize the power of the multi-core system and the double GPU feature. The effects of gravity

160

are also taken into consideration with $g=-9.81$ m/s^2 along the z-axis. The standard *K-epsilon* turbulence model has been used in this simulation to provide enough refinement in the velocity field and simultaneously avoid excessive compilation times required with alternate turbulence models (e. g. RNG - renormalizable group, k-omega or Large Eddy Simulations (LES)). As a first approximation the *K-epsilon* (*k* turbulence energy - *epsilon* dissipation rate) turbulence model is known to provide satisfactory results [8]. Since air is considered, the model constants in the "material physics" option in ANSYS FLUENT are left unaltered. Viscous heating is however switched on to achieve more elegant simulation of the interfacial heat transfer between the layers of the model i. e. at the steel core-Titanium coating and Titanium coating-silicon carbide ceramic interfaces. The energy equation is activated to allow a 3-D heat transfer analysis to be included, based on the classical Fourier law (i. e. thermal relaxation effects are neglected). The Discrete Phase Model (DPM) option is also mobilized (see chapter 3) to simulate hot gas injection as a continuous stream of high temperature uniform air particles representing corrosive gas impingement on the blade sample onto the model. This provides a facility for computing the *erosion damage* induced by hot gas turbine environments. The particles were set at a speed of 5 m/s and a temperature of 1273.15 º Kelvin (1000 Celsius) and 30 bars pressure i.e. 3MPa (worse scenario case in an actual gas turbine) was prescribed. Boundary conditions were left unaltered with the exception of the inlet with a similar velocity condition to that of the injected particles. A simple scheme with *second order upwind* pressure and momentum was selected and the solution was left to converge for 1000 iterations. The solution converged after 427 iterations within a time frame of 180 minutes. All simulations were performed using a Lenovo Y510p laptop machine with 8 GB of RAM and an Intel® Core i7-4700MQ CPU @ 2.4 GHz processor with a NVidia® 755m gt SLI GPU running on a Windows 10 platform. The ANSYS FLUENT methodology has been given in chapter 3 and is not repeated here (see **Figure 3.12**). The **SIMPLE** (Semi-implicit pressure linked equation) is

161

deployed, as described also in chapter 3. The k-epsilon turbulence calculations are linked to this procedure and further details are given in Daud *et al.* [9]. A detailed grid independence study is conducted to confirm the accuracy of the selected mesh densities and shown in **Figure 6.28**. It is important to note that for the CFD erosion analysis, only the *three-layer* model (steel + Titanium + Silicon Carbide (SiC) ceramic) is considered. 800, 000 cells (volumes) were deployed in all simulations.
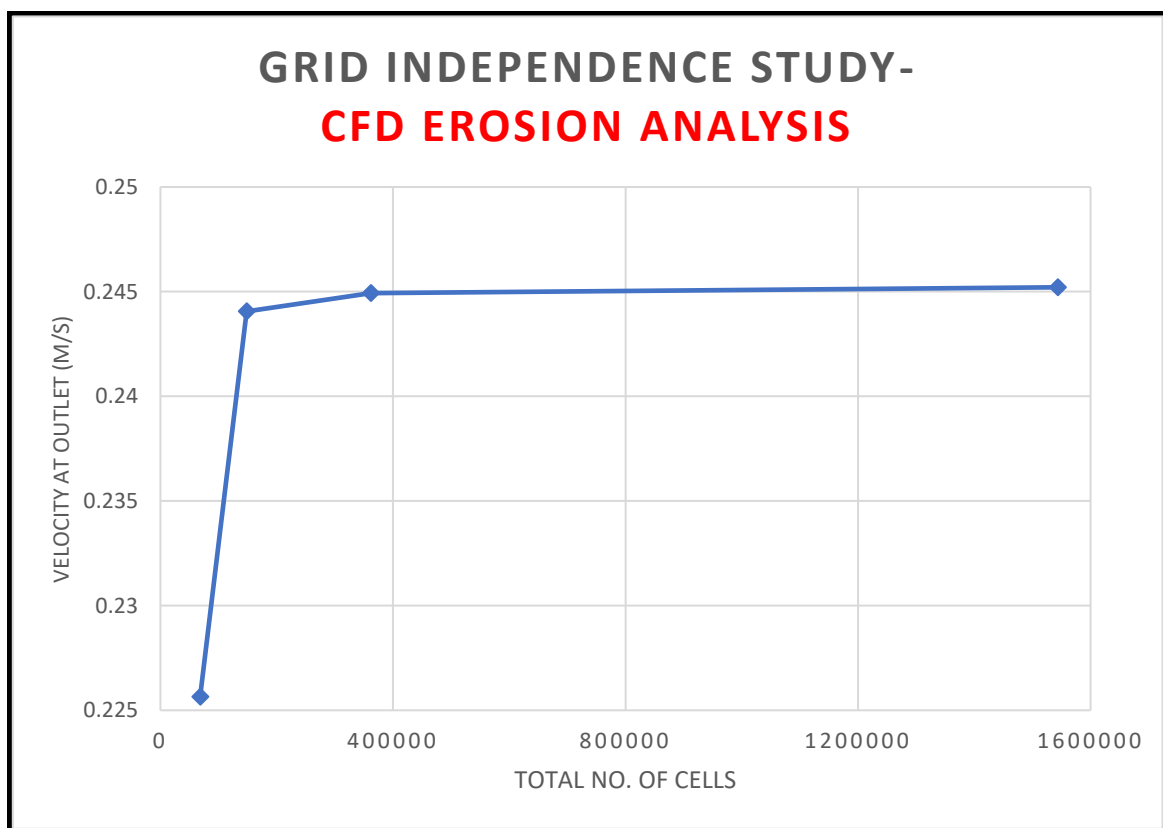
Figure 6.28: Grid independence study showing convergence.

Figure 6.29 shows the erosion rates induced in the three-layer model as obtained by ANSYS FLUENT in addition to pressure, vorticity, turbulence energy etc. Generally *maximum erosion rates* are confined to a local zone on the upper face of the three-layer system which is in fact the *sacrificial layer* (ceramic coating). The titanium is not de-bonded or damaged which is essential for creating a buffer to the actual blade surface. Even though the magnitudes are small for the erosion rates, they are still present and this correlates with the flaking characteristics (material removal) observed in the micro-coating TGA tests described earlier in chapter 5.
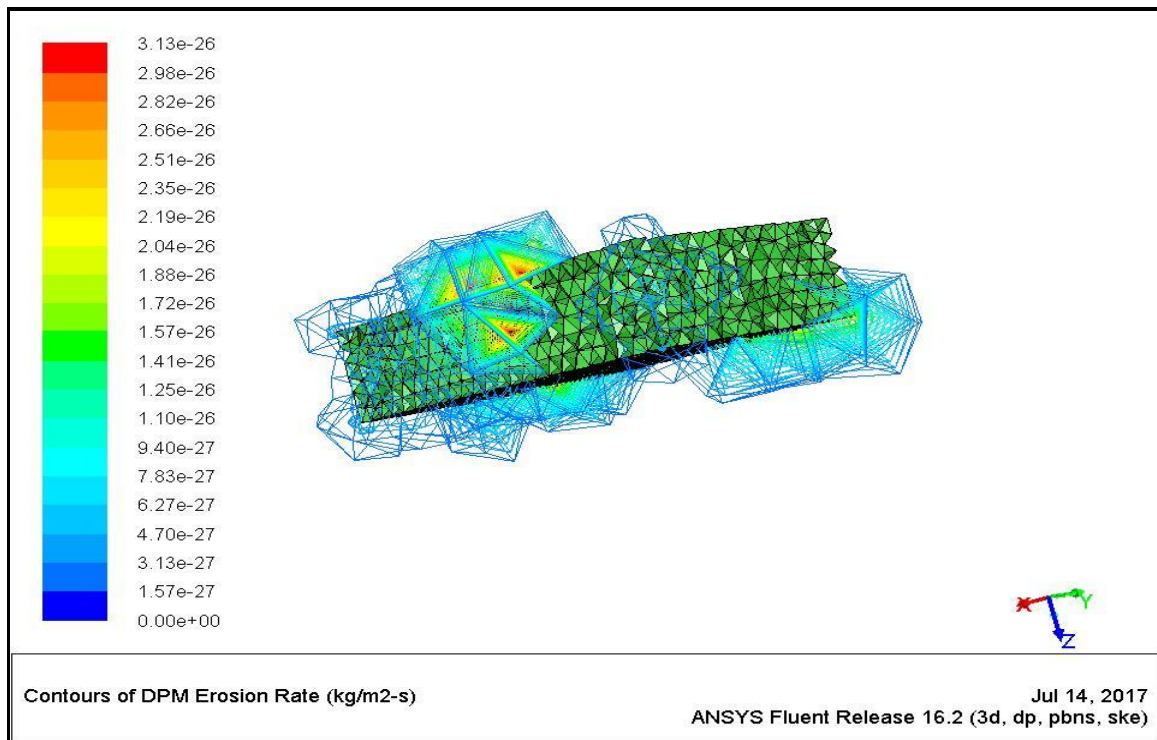
Figure 6.29: Erosion rates computed with DPM in ANSYS FLUENT.

Overall, the three-layer micro-coating is shown to perform very well and minimal erosion actually occurs. However, the *erosion observed in micro-coatings associated* with the ceramics (cracking, delamination, spalling) may be inhibited with improved nano-embedded coating particles and this has been confirmed experimentally in chapter 5 for the 60: 40 aluminium oxide-titanium oxide nanocoated sample. The CFD analysis of course may be refined to consider simultaneously chemical reaction effects and erosion (flaking of material off the blade surface); coupling of chemical kinetics in the erosion/corrosion model is extremely challenging and this requires interfacing the ANSYS model with a *chemical corrosion* model e.g. CAPLHAD [10], which may be investigated in the future. The current simulations have nevertheless provided a reasonable corroboration with the experimental findings of chapter 5 where surface material (ceramic outer layer) was shown to be removed after the TGA thermal testing on the micro-coated specimen.

6.3 Finite element (static) stress analysis of *60: 40* aluminium oxide-titanium oxide nano-coated specimens

In this section, detailed finite element stress/strain analysis of a nano-coated steel substrate with both single and multiple layers of nano-powder composite consisting of Titanium Oxide and Aluminium Oxide nanoparticles (in different percentages) is described to explore the most ideal combination of nano-powder components for subsequent thermal stress analysis.

ANSYS software is again deployed to simulate three-dimensional stress, strain, and deformation response. This section ignores heat transfer which is considered in the next section (6.4) for thermal stress simulations of an aluminium oxide-titanium oxide nano-coated substrate with *60: 40* percentage distribution. The geometry to be studied for the substrate was again the 20mm x 10 mm x 1.5 mm geometry (uncoated AISI 304 blade specimen). However, since thermal loading was not considered, *exact nanocoating dimensions used in the TGA testing (chapter 5) were not studied*, and these are addressed later in section 6.4 for the *thermal stress analysis*. The objective was to test the sensitivity of the different mixes of nano-coatings to elastic stresses. The coated specimen was subjected to high uniform static pressure (30 bars) which was done to subject the nano-coatings to the highest possible pressures encountered in real gas turbines.
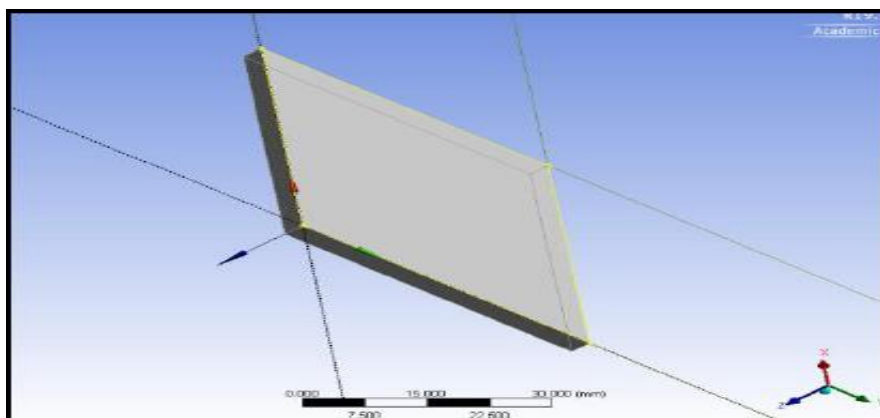
Figure 6.30: 3-dimensional AISI 304 steel plate substrate (uncoated gas turbine specimen) simulated in ANSYS workbench.

The same material properties are deployed for the substrate as in the micro-coated model (section 6.2-1) and summarized below in **Table 6.3**.

AISI 304 Structural Steel substrate properties				
Density, ρ (kg/m^3)	Young's Modulus, E (GPa)	Poisson's Ratio, ν	Bulk Modulus, K (Pa)	St. Venant (Shear) Modulus, G (Pa)
7850	200	0.28	1.6667E+11	7.6923E+10

Table 6.3: Material properties for structural steel AISI 304 substrate (uncoated blade specimen).

The unprotected (bare) steel substrate model is first created (**Model I**) and then composite models (**Models II**) designed using nano-material coatings. These three nano-coated plate models feature *three different variations (60: 40, 50: 50, 40: 60) of nano-powder coating layers* consisting of Aluminium Oxide (Al_2O_3) and Titanium Oxide (TiO_2) *deposited on the upper face and the lower face* of the AISI304 substrate i.e. the 4 edges are not coated. This is a first step in simulating the elastic behaviour of the nano-coated specimen to achieve confidence in the modelling. The *full 6-face coating is simulated only for the thermal stress analysis described later in section 6.4*. Each variation of the composite will have varying amounts of percentage content of Al_2O_3 and TiO_2. These amounts can be seen in **Table 6.4** below. **Tables 6.5 - 6.6** show the virgin properties for the metallic oxide nanoparticles and the resulting effective properties (volume averaged).

Nano-coating composite material	Percentage Content Aluminium Oxide (%)	Percentage Content Titanium Oxide (%)
1	60	40
2	50	50
3	40	60

Table 6.4: Variations in percentage composition of nano-coating composite material.

Properties	Young's Modulus (GPa)	Poisson's Ratio	Density (Kg/m³)
Aluminium Oxide	*413*	*0.33*	*3980*
Titanium Oxide	*288*	*0.29*	*4050*

Table 6.5: Material properties of Aluminium Oxide and Titanium Oxide nano-powder.

Nano-coating composite material	Young's Modulus (GPa)	Density (kg/m³)	Poisson's Ratio
Al_2O_3 (60%) & TiO_2 (40%)	363	4008	0.314
Al_2O_3 (50%) & TiO_2 (50%)	350.5	4015	0.281
Al_2O_3 (40%) & TiO_2 (60%)	338	4022	0.306

Table 6.6: Calculated material properties for the nano-powder coating mixes.

The associated calculations for the nano-powder composite properties are summarized below:

Al_2O_3 (60%) & TiO_2 (40%) Composite

$E_c = 413(0.6) + 288(0.4) = 363 \, GPa$

$\rho_c = 3980(0.6) + 4050(0.4) = 4008 \, kg/m^3$

$\nu_c = 0.33(0.6) + 0.29(0.4) = 0.314$

Al_2O_3 (50%) & TiO_2 (50%) Composite

$E_c = 413(0.5) + 288(0.5) = 350.5 \, GPa$

$\rho_c = 3980(0.5) + 4050(0.5) = 4015 \, kg/m^3$

$\nu_c = 0.33(0.5) + 0.29(0.5) = 0.281$

Al_2O_3 (40%) & TiO_2 (60%) Composite

$E_c = 413(0.4) + 288(0.6) = 338 \, GPa$

$\rho_c = 3980(0.4) + 4050(0.6) = 4022 \, kg/m^3$

$\nu_c = 0.33(0.4) + 0.29(0.6) = 0.306$

The nano-powder composite is superposed on the solid steel substrate (AISI 304) plate in ANSYS workbench and has the combined properties given in **Table 6.6**.

6.3- 1 Model type I – Structural Steel Substrate (unprotected)

This model is meshed with 3-D quadrilateral elements, as depicted in **Figure 6.31**. After extensive mesh independence tests, an *optimized mesh of 225 elements* and 1728 nodes is designed. Mesh densities were massively lower than for the micro-coated analysis (section 6.2-1) since thermal effects were ignored.
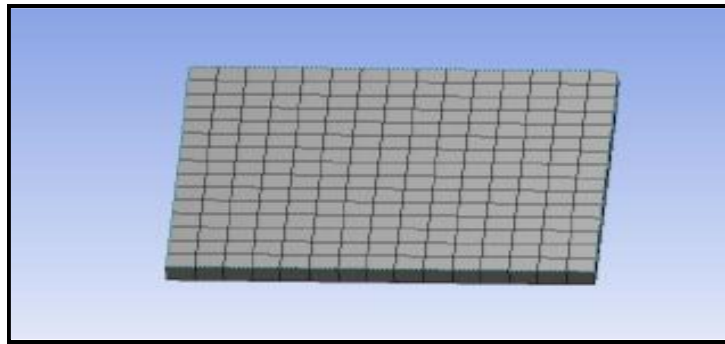
Figure 6.31: Structural AISI 304 steel substrate with optimized mesh.

The plate (substrate) is fixed at all edges (clamped) (**Figure 6.32**) and uniform surface pressure of 30 bars is applied on the upper and lower faces (**Figure 6.33**).
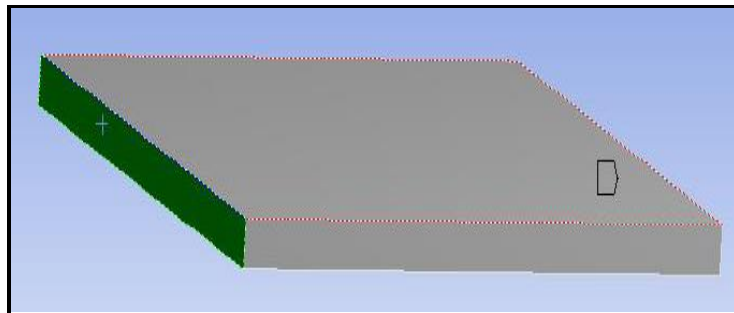
Figure 6.32: Example of selected face for fixing (unprotected steel substrate).
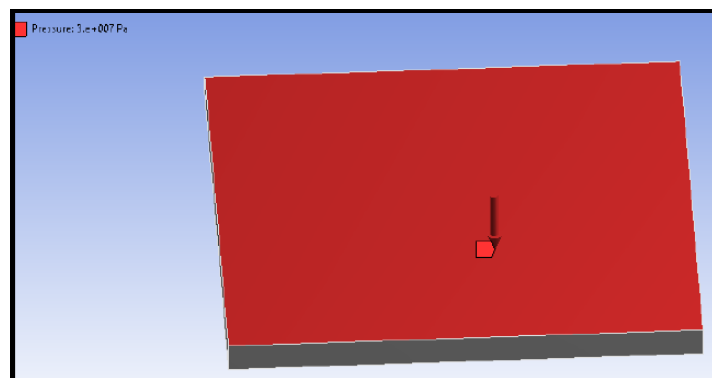
Figure 6.33: Example of selected face for pressure of 30 bars (unprotected steel substrate).

The solution options selected in ANSYS are contour plots of *total deformation, equivalent stress, and equivalent elastic strain, as with the micro-coating analysis described earlier.*

6.3-2   Model type II – Nano-coated Substrate

The second model type is the substrate (1.5mm thick as in the TGA tests) coated on the top and base face surfaces with 1mm nano-coating comprising different mixes of Aluminium Oxide (Al_2O_3) and Titanium Oxide (TiO_2). To create the second model type, different stages of the geometric modelling are required even for static stress analysis. Great care is needed, in particular for the double nano-coated layers (4-layer model) and as adhesive (bonding) aspects cannot be simulated, again a *composites layer model* is therefore adopted, as with the micro-coating. The optimized finite element mesh in this case has 64 elements and 81 nodes as seen in **Figure 6.34.**
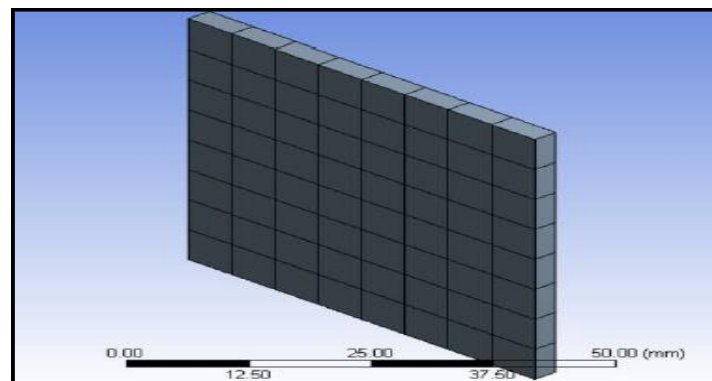
Figure 6.34: Selected face for 30 bars pressure (steel plate).

This generates the solid model with a central structural steel plate (AISI 304 substrate) of 1.5 mm thickness intercalated between a *1 mm thick layer* of the (Al_2O_3 (60%) & TiO_2 (40%) composite above and below the steel substrate (**Figure 6.35**). The high static pressure of 30 bars is imposed as in **Figure 6.36**.
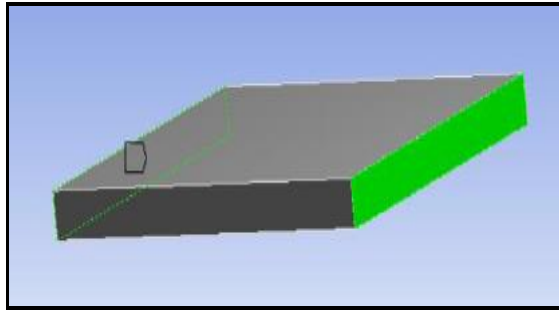
Figure 6.35: Selecting the faces of the nano-powder coated substrate for fixed-supports to be applied.
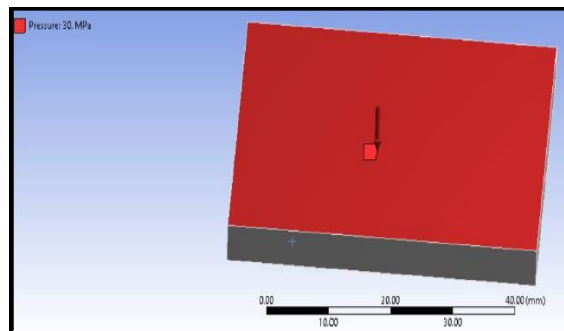
Figure 6.36: Face of the nano-powder coated substrate for the pressure application.

Once the basic model of the nano-powder coated substrate i.e. structural steel and $(Al_2O_3$ (60%) & TiO_2 (40%) composite is created, the model can be easily modified for multiple nano-composite coating layers. Overall, five different ANSYS nano-coated composite models are presented in the form of contour plots, tables, and performance is compared with bar charts. The results are then interpreted in detail and the findings are summarised.

6.3-3   Uncoated Structural Steel substrate results

Figures 6.37-6.39 show the *total deformation, equivalent stress, and equivalent strain contour plots* respectively and the corresponding results are extracted in **Table 6.7**. The steel plate shows zero deformation at the two fixed-ends of the uncoated steel plate, indicated by the blue contour bands in **Figure 6.37**. The plate deformation increases as the distance from the ends to the centre of the plate, decreases, and is the largest at the centre of the plate, with a maximum value of 3.76E-03 mm.

169
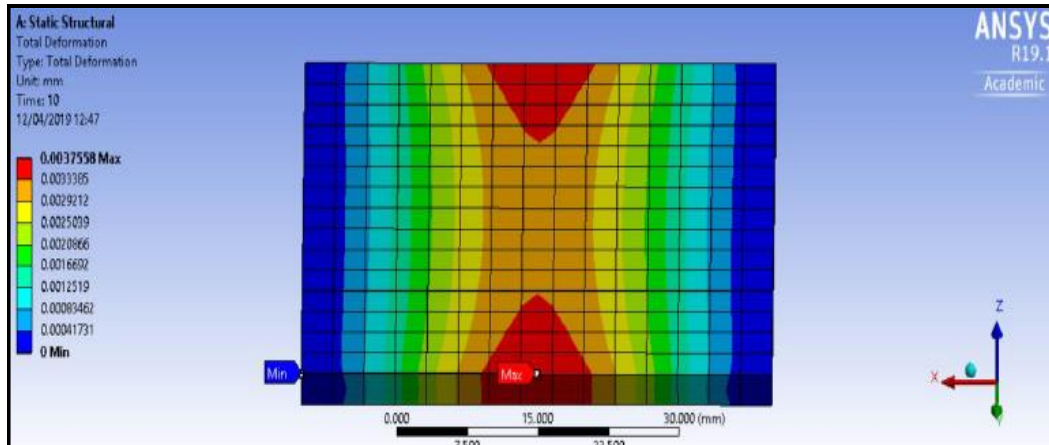
Figure 6.37: Total Deformation: unprotected structural steel plate.

For the equivalent stress (**Figure 6.38**) of the uncoated steel plate, the *highest stress* (10.478 MPa) is again seen at left and right fixed-ends, and the least stress (0.10205 MPa) is seen between the centre and the fixed-ends. Moderately high stress is observed at the centre of the plate. In some of the plots the lateral direction is stretched for enhanced visibility. The equivalent strain experienced by the plate shows a similar pattern to the stress, with high strains (52.7 E-06) and the lowest strains computed (5.3 E-06) at zones between the centre and the fixed ends of the plate as shown in **Figure 6.39**.
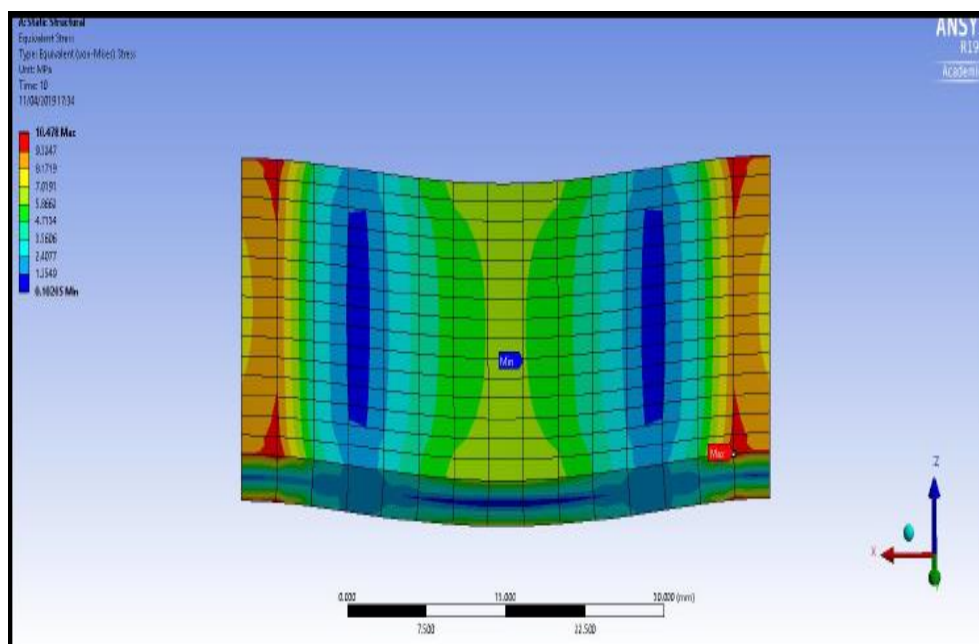
Figure 6.38: Equivalent Stress (von-Mises): unprotected structural steel plate.
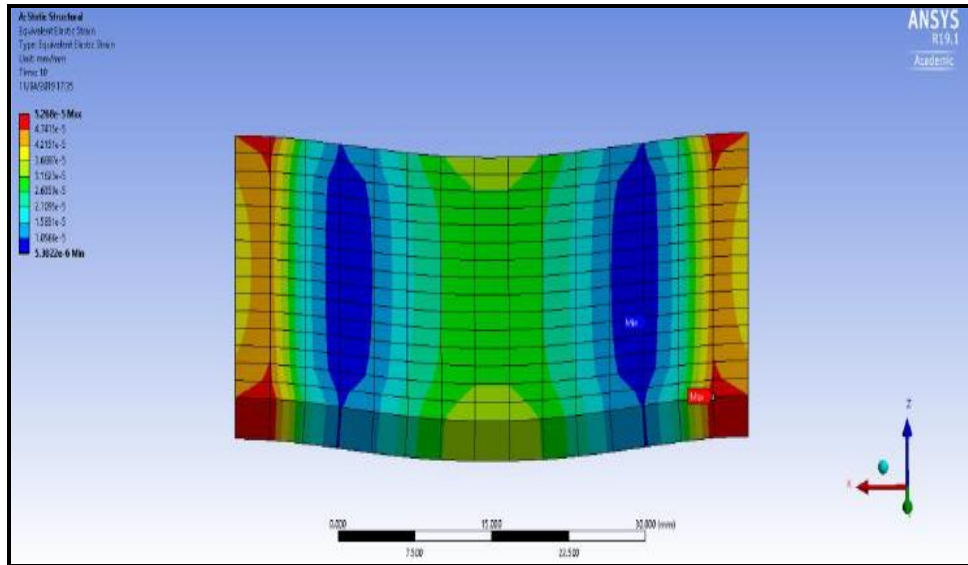
Figure 6.39: Equivalent Elastic Strain (von-Mises): unprotected structural steel plate.

Structural Steel Plate	
Weight (kg)	5.89E-02
Deformation (Min) (mm)	0
Deformation (Max) (mm)	3.76E-03
Equivalent Stress (Min) (MPa)	0.10205
Equivalent Stress (Max) (MPa)	10.478
Equivalent Strain (Min)	5.30E-06
Equivalent Strain (Max)	5.27E-05

Table 6.7: Unprotected structural steel AISI 304 substrate results- summary.

6.3-4   Structural Steel with Al_2O_3 (60%) & TiO_2 (40%) nano-coating - results

Model II -A *Two nano-coating (composite) Layers*

Figure 6.40 shows the finite element mesh for the structural substrate coated with two layers of (Al_2O_3 (60%) & TiO_2 (40%) nano-composite coating above and below the substrate. All the models for structural steel with two composite nano-coating layers are modified from the previous sub-section (Model I) for different material properties of the Aluminium Oxide and Titanium Oxide due to the differences in percentage composition of the constituent nano-powder coating materials.
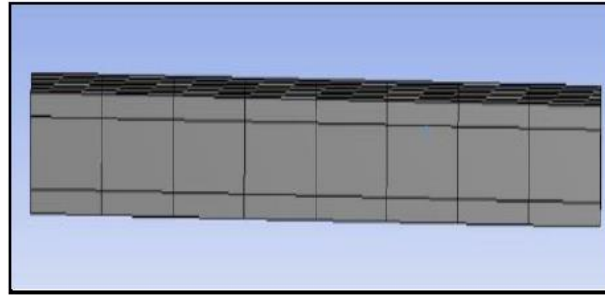
Figure 6.40: Structural steel AISI 304 substrate with two layers of nano-coating (on top and base faces)

Following imposition of the high pressure, to the nano-coated plate, the following contour plots (**Figures 6.41-6.43**) are produced in ANSYS, for *total deformation, equivalent stress, and equivalent strain respectively.* The total deformation for the structural steel plate with *2 layers* and 60%:40% nano-material composition (**Figure 6.41**) shows zero deformation at the fixed-ends and the maximum deformation of 5.24E-04 mm at the centre edges of the plate.
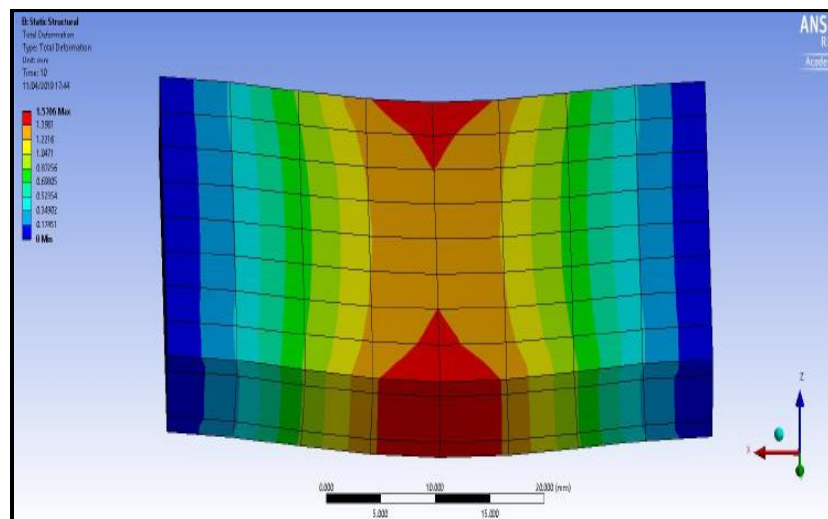
Figure 6.41: Total deformation: structural steel substrate with Al_2O_3 (60%) & TiO_2 (40%) with 2 composite layers.

With this composition, the highest magnitude of stress (2.6669 MPa) (**Figure 6.42**) is computed at the corners of the fixed-ends and the centre edges of the plate. The least stressed areas (0.42411 MPa) arise between the centre and the fixed end of the plate. For this model, most of the stress is absorbed by the top and bottom layer of the nano-composite and the centre

steel layer (substrate) experiences very low amounts of stress, indicated by the blue contour bands.
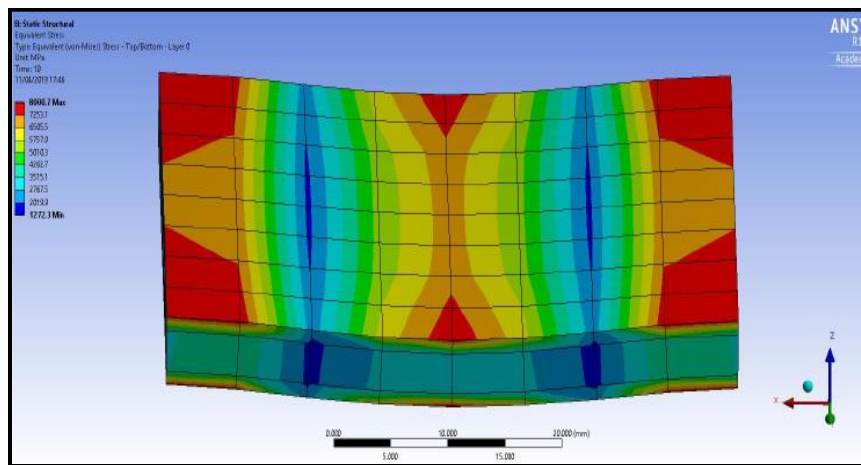
Figure 6.42: Equivalent Stress: structural steel substrate and Al_2O_3 (60%), TiO_2 (40%) - 2 nano-coating composite layers.

The strain experienced (**Figure 6.43**) by this model is similar to the stress contour plot, with the least strain being 1.85E-06, and the highest being 7.37E-06. Similarly, the strain is largely taken by the top and bottom nano-coatings with the centre steel layer experiencing intermediate strain between the two extreme values, indicated by the green contour bands.
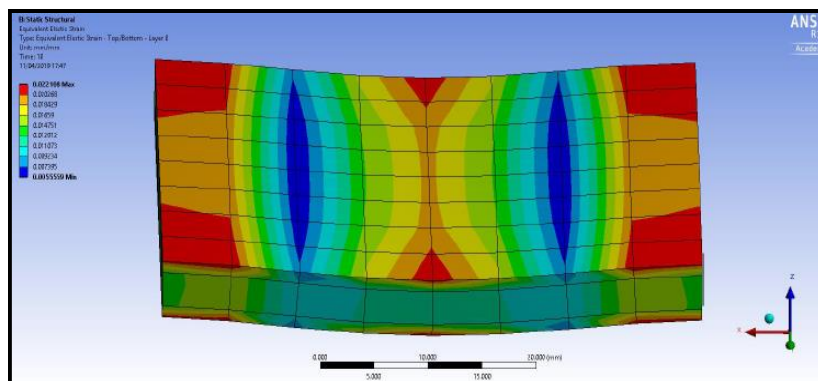
Figure 6.43: Equivalent Strain: Structural Steel substrate with Al_2O_3 (60%) & TiO_2 (40%) - 2 nano-coating composite layers.

6.3-5   Structural Steel with Al_2O_3 (60%) & TiO_2 (40%) nano-coating - results
Model II -B Four *nano-coating (composite) Layers*

Figures 6.44-6.46 show the contour plots for the total deformation, equivalent stress, and equivalent strain respectively, for the structural steel substrate with 4 layers of (Al_2O_3 (60%)

173

& TiO$_2$ (40%) nano-coating i.e. *two nanocoating composite layers above and two below the substrate*. The deformation contour plot (**Figure 6.44**) shows a similar pattern for the plate with four layers of composite material, as the plate with two layers of composite. The maximum deformation of the plate being 2.08E-04 mm and the least being zero.
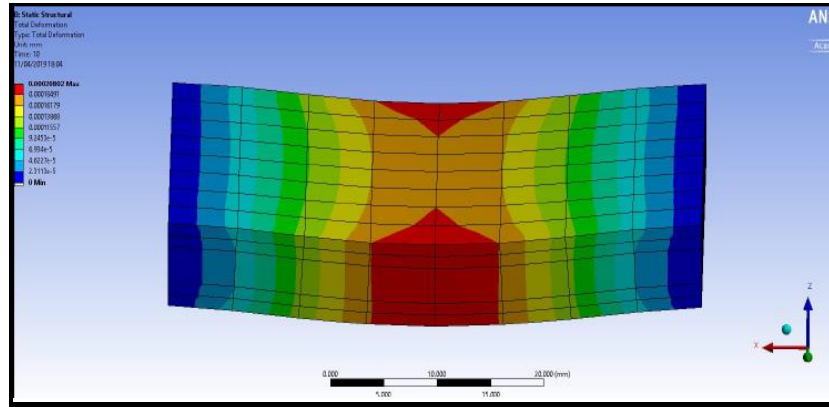
Figure 6.44: Total Deformation: structural steel substrate with Al_2O_3 (60%) & TiO_2 (40%) - 4 nano-coating composite layers.

Although the contour plot show a similar pattern for the plate with four layers of composite material (Model II-B), as with the plate with two layers of composite (Model II-A), the maxium stress area (**Figure 6.45**) is larger in the Model II-B and extends along the entire width of the substrate on the top and bottom layers of the nano-coating. The maximum stress computed in the plate was 1.305 MPa and the least being 0.24414 MPa.
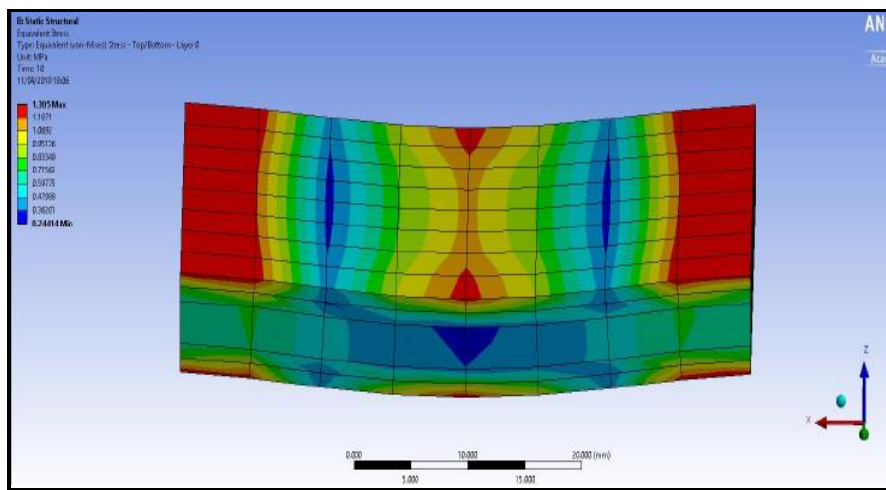
Figure 6.45: Equivalent Stress: structural steel with Al_2O_3 (60%) & TiO_2 (40%) - 4 composite layers.

For model II-B, i.e. the 4 layer nano-coating composite system, a higher maximum strain (**Figure 6.46**) area is larger and runs along width of the plate on the top and bottom layers of the composite. The maximum strain on the plate is 8.78E-07, and the minimum is 3.64E-06.
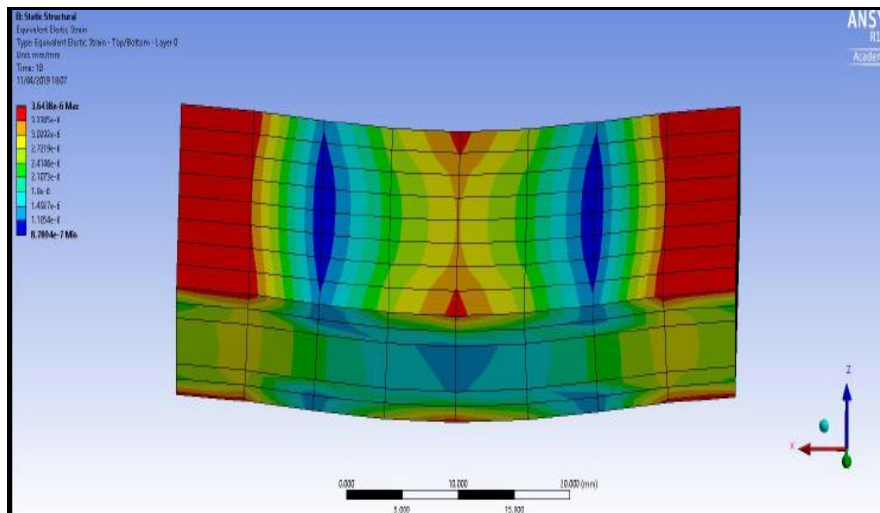
Figure 6.46: Equivalent Elastic Strain: structural steel with Al_2O_3 (60%) & TiO_2 (40%) - 4 composite layers.

The corresponding data and extracted solutions are given in **Table 6.8** for both 2-layer and 4-layer nanocoated models.

Structural Steel with Al_2O_3 (60%) & TiO_2 (40%) Composite Layers		
Quantities	**2 Layers**	**4 Layers**
Weight (kg)	7.90E-02	9.91E-02
Deformation (Min) (mm)	0	0
Deformation (Max) (mm)	5.24E-04	2.08E-04
Equivalent Stress (Min) (MPa)	0.42411	0.24414
Equivalent Stress (Max) (MPa)	2.6669	1.305
Equivalent Strain (Min)	1.85E-06	8.78E-07
Equivalent Strain (Max)	7.37E-06	3.64E-06

Table 6.8: Results for structural steel substrate coated with Al_2O_3 (60%) & TiO_2 (40%) – 2 and 4 nano-coating composite layers.

6.3-6   Structural Steel with Al_2O_3 (50%) & TiO_2 (50%) Composite Layers - results

Model II – C   Two *nano-coating (composite) layers*

Figures 6.47-6.49 show the ANSYS contour plots of the total deformation, equivalent stress, and equivalent strain respectively for structural steel plate coated with two layers of (Al_2O_3

(50%) & TiO$_2$ (50%) composite above and below. The total deformation contour plot (**Figure 6.47**) for 2 layers (50:50) exhibits a similar pattern for the earlier model II-B. The *maximum* deformation of the coated substrate is computed however as 5.45E-04 mm with the least being zero. **Figure 6.48** illustrates the equivalent stress contour plot for 2 layers (50:50), and it is evident that the red contour bands for the high stressed areas are distributed in curved manner near the fixed-ends, unlike in previous models. The maximum stress for the plate is 2.7581 MPa and the lowest is 0.42332 MPa. **Figure 6.49** shows that the at the edges of the substrate, curved high strain zones appear rather than the vertical bands seen in previous models.
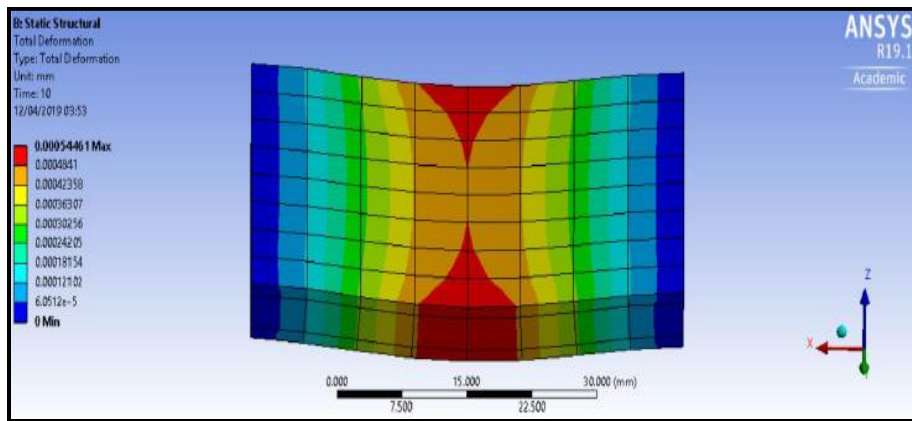
Figure 6.47: Total Deformation: structural steel substrate - Al_2O_3 (50%) & TiO_2 (50%), 2 layers.
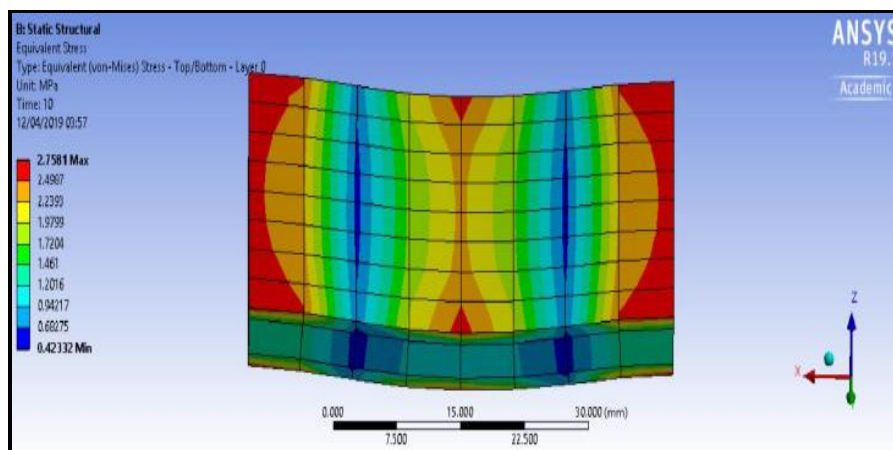
Figure 6.48: Equivalent Stress: structural steel substrate with Al_2O_3 (50%) & TiO_2 (50%) with 2 composite layers.
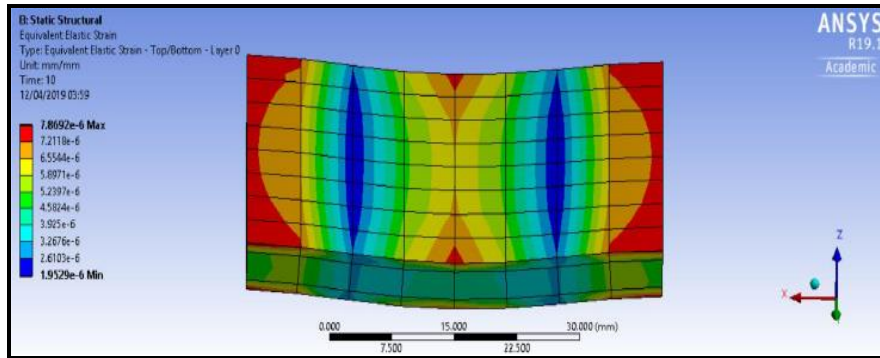
Figure 6.49: Equivalent Elastic Strain: structural steel substrate - Al_2O_3 (50%) & TiO_2 (50%) -2 layers.

6.3-7   Structural Steel with Al$_2$O$_3$ (50%) & TiO$_2$ (50%) Composite Layers - results Model II - D Four *nano-coating (composite) layers*

Figures 6.50-6.52 show the contour plots for the total deformation, equivalent stress, and equivalent strain respectively, for the structural steel plate with 4 layers of (Al$_2$O$_3$ (50%) & TiO$_2$ (50%) i.e. *two nano-coating layers at the top face of the steel substrate and two at the lower face.* The maximum deformation of the plate is found to be 2.16E-04 mm and the least zero (**Figure 6.50**).
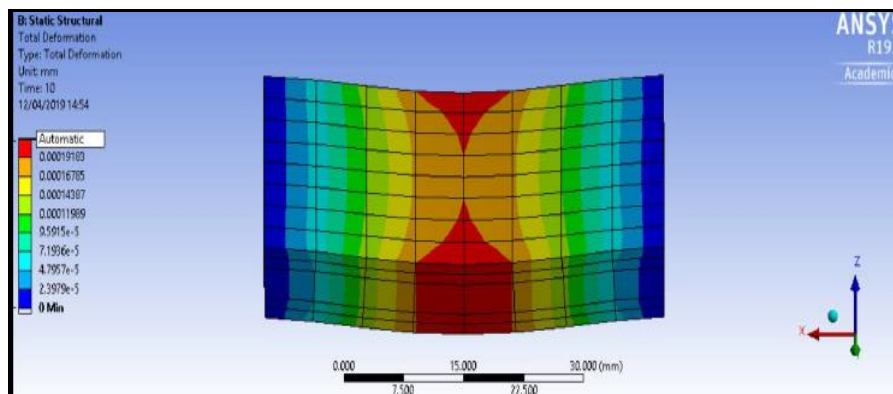
Figure 6.50: Total deformation: structural steel substrate with Al_2O_3 (50%) & TiO_2 (50%) - 4 layers.

The contour stress plot (**Figure 6.51**) shows that the red contour bands for the high stressed areas are distributed in curved manner near the fixed ends and in the mid-plane edge zones, the triangular high stress zones are eliminated. The minimum stress for this scenario is 0.24317 MPa and the maximum is 1.3992 MPa.
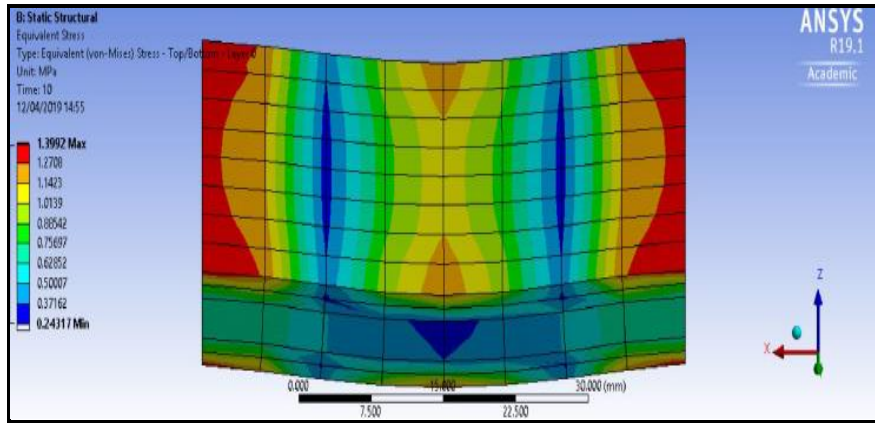
Figure 6.51: Equivalent Stress: structural steel substrate with Al_2O_3 (50%) & TiO_2 (50%) - 4 composite layers.

The contours on the equivalent strain plot (**Figure 6.52**) reveals the red high strain zones *shrink at the extreme ends* of the substrate surface and also the triangular red zones computed earlier in **Figure 6.49** for the 50: 50 two composite layer nanocoating, are replaced with lower strain orange zones at the mid-points of the horizontal edges on the face. The minimum strain for this case is 9.21E-07 whereas the maximum is 3.99E-06.
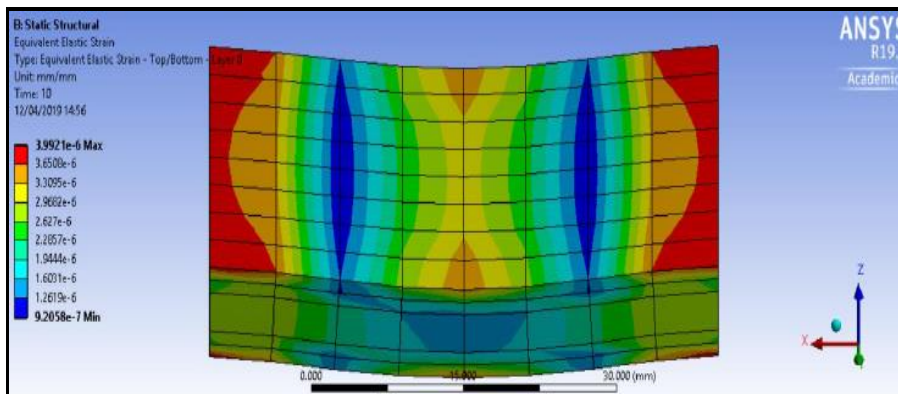
Figure 6.52: Equivalent elastic strain: structural steel substrate with Al_2O_3 (50%) & TiO_2 (50%) - 4 composite layers.

Extracted results are shown in **Table 6.9** for both 2 and 4 composite nano-coating layers.

Structural Steel with Al_2O_3 (50%) & TiO_2 (50%) Composite Layers		
Quantities	2 Layers	4 Layers
Weight (kg)	7.91E-02	9.93E-02
Deformation (Min) (mm)	0	0
Deformation (Max) (mm)	5.45E-04	2.16E-04
Equivalent Stress (Min) (MPa)	0.42332	0.24317
Equivalent Stress (Max) (MPa)	2.7581	1.3992
Equivalent Strain (Min)	1.95E-06	9.21E-07
Equivalent Strain (Max)	7.87E-06	3.99E-06

Table 6.9: Results for structural steel substrate with Al_2O_3 (50%) & TiO_2 (50%) - 2 and 4 composite layers.

6.3-8   Structural Steel with Al_2O_3 (40%) & TiO_2 (60%) Composite Layers- results Model II -E Two Composite Layers

Figures 6.53-6.55 show the contour plots of the total deformation, equivalent stress, and equivalent strain respectively for *2 (40: 60) nanocoating composite layers* i.e. one nano-coating on the upper face and one on the lower face of the steel AISI 304 substrate. **Figure 6.53** shows that maximum deformation of the plate for this case is 5.54E-04 mm and the least is zero. A similar behaviour is computed to the 60:40 case studied earlier (Model II-A, B). **Figure 6.54** reveals that a greater equivalent stress is generated at the substrate centre compared to the 50%: 50% `nano-coating composition case. Also, the high stress area at the fixed end is larger in extent and more curved in comparison to the 50%:50% composition. The minimum stress for the substrate was 0.42559 MPa and the lowest was 2.6434 MPa. **Figure 6.55** demonstrates that the equivalent elastic strain experienced at the substrate centre is greater when compared to the 50%:50% nanomaterial composition and the strain area at the fixed-end is more extensive and exhibits greater curvature in comparison to the 50%:50% composition. The minimum strain for the substrate is 1.98E-06 and the maximum is 7.84E-06.
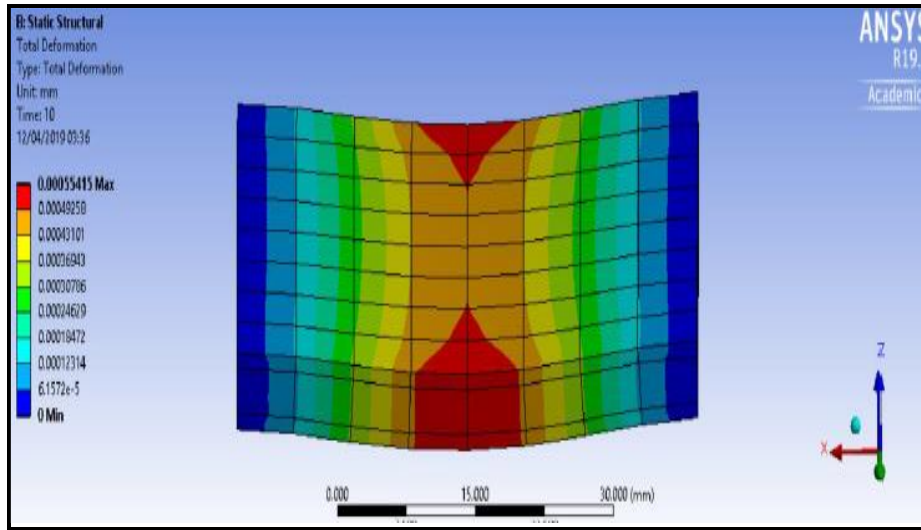
Figure 6.53: Total deformation: structural steel substrate with Al_2O_3 (40%) & TiO_2 (60%) with 2 nano-coating composite layers.
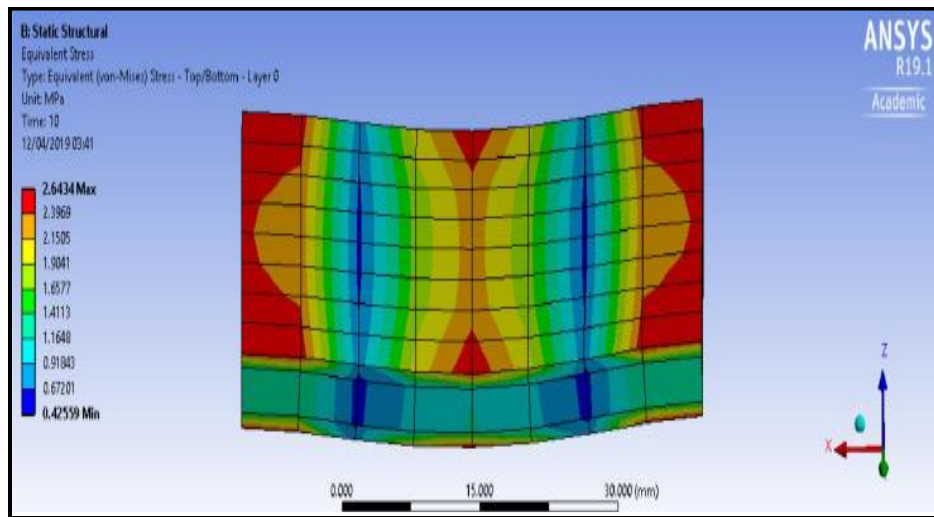
Figure 6.54: Equivalent stress: structural steel substrate with Al_2O_3 (40%) & TiO_2 (60%) with 2 nano-coating composite layers.
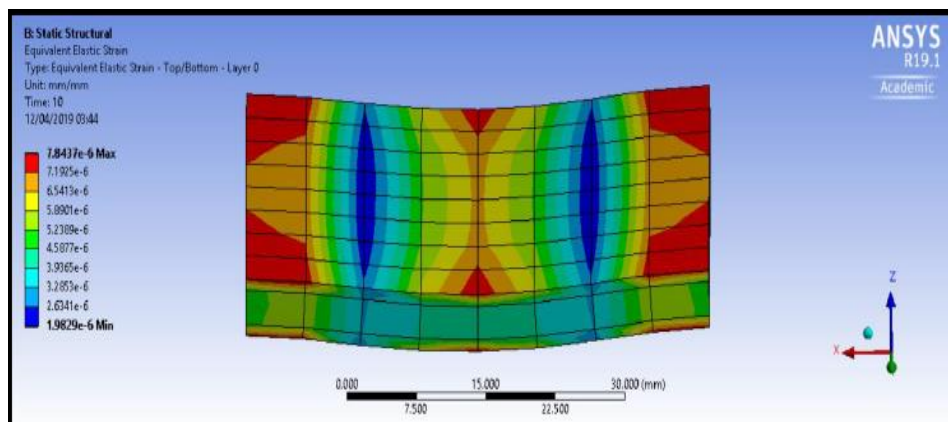
Figure 6.55: Equivalent strain: structural steel substrate with Al_2O_3 (40%) & TiO_2 (60%) with 2 nano-coating composite layers.

6.3-9   Structural Steel with Al_2O_3 (40%) & TiO_2 (60%) Composite Layers- results

Model II -F   Four Composite Layers

Figures 6.56-6.58 show the contour plots for the total deformation, equivalent stress and equivalent strain respectively, for the structural steel plate with 4 layers of (Al_2O_3 (40%) & TiO_2 (60%), two layers on the upper face and two layers on the lower face. The maximum deformation (**Figure 6.56**) for this case is found to be 2.20E-04 mm and the least is again zero. The contours follow the same general topology as the 50:50 nanocoating (shown earlier) although the high deformation zone areas are more protracted. **Figure 6.57** shows that although the high red equivalent stress zones are curved as in previous cases, they are *less crescent-shaped,* and this 40:60 nano-coating is less effective than the 50:50 nano-coating case.
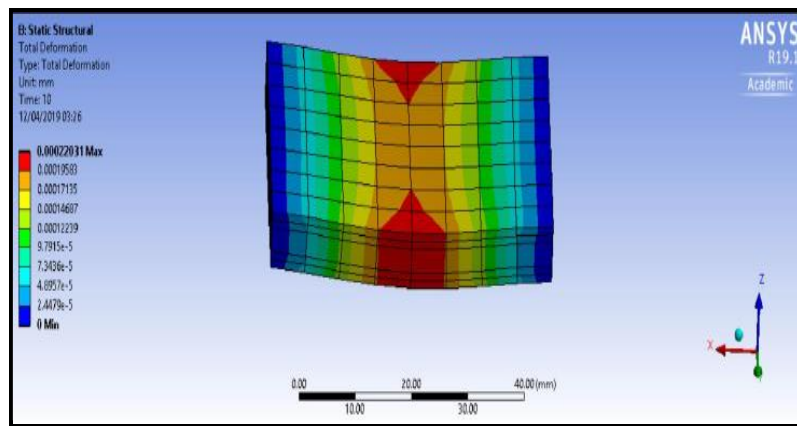
Figure 6.56: Total deformation: structural steel substrate with Al_2O_3 (40%) & TiO_2 (60%) with 4 nano-coating composite layers.
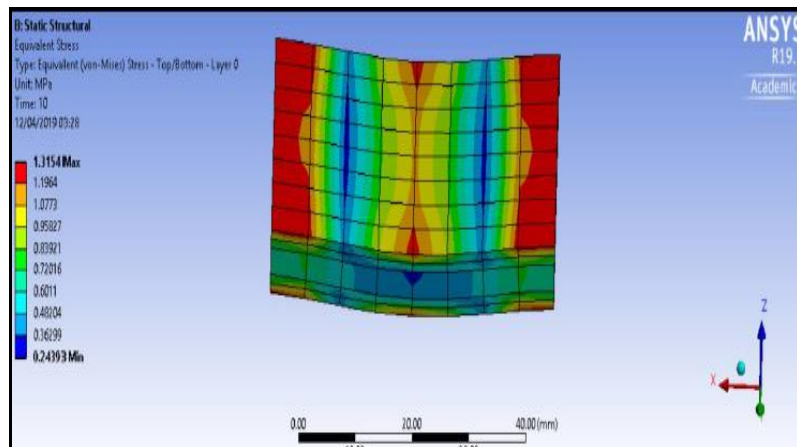
Figure 6.57: Equivalent stress: structural steel substrate with Al_2O_3 (40%) & TiO_2 (60%) with 4 nano-coating composite layers.

In **Figure 6.58**, a similar distribution of elastic strain is computed as for the 50%:50% nano-coating scenario shown earlier. However the red contour bands for the high strained areas are larger and have a small curved area near the fixed-ends when compared to the 50%:50% nano-coating case. The minimum strain for the substrate is observed to be 9.52E-07 and the maximum is 3.89E-06.
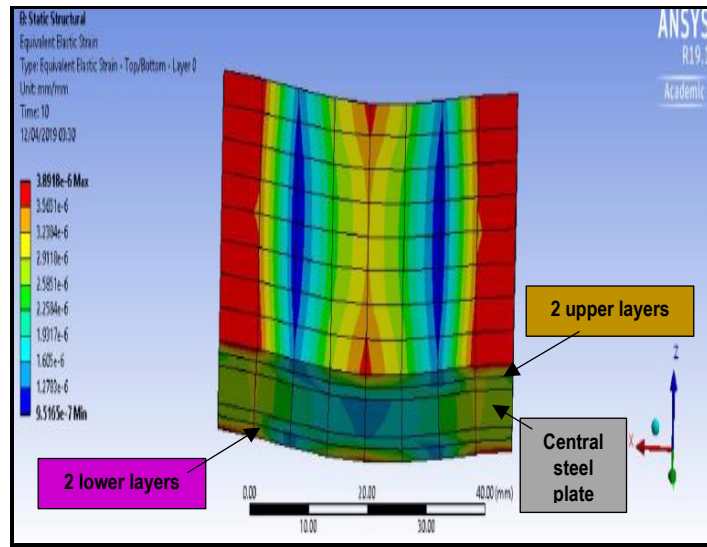
Figure 6.58: Equivalent elastic strain: structural steel substrate with Al_2O_3 (40%) & TiO_2 (60%) with 4 nano-coating composite layers.

Extracted data is shown in **Table 6.10** for both 2 and 4 nano-coating composite layers.

Structural Steel with Al_2O_3 (40%) & TiO_2 (60%) Composite Layers		
Quantities	2 Layers (one each on top and lower face)	4 Layers (two each on top and lower face)
Weight (kg)	7.92E-02	9.94E-02
Deformation (Min) (mm)	0	0
Deformation (Max) (mm)	5.54E-04	2.20E-04
Equivalent Stress (Min) (MPa)	0.42559	0.24393
Equivalent Stress (Max) (MPa)	2.6434	1.3154
Equivalent Strain (Min)	1.98E-06	9.52E-07
Equivalent Strain (Max)	7.84E-06	3.89E-06

Table 6.10: Results for structural steel substrate with Al_2O_3 (40%) & TiO_2 (60%) – 2 and 4 nano-coating composite layers.

The most promising results overall (for the largest surface areas on the substrate surface) have been computed for the nanocoating layers of Aluminium Oxide and Titanium Oxide, with 60%:40% composition. Another model was also designed in ANSYS again with a 1.5 mm steel substrate but sandwiched between *3 layers of the 60: 40 nanocoating*. Results were again compared to the unprotected steel plate (Model I), although for brevity they have been omitted here. Overall, **5 sets of models** have been studied for purely elastic stress analysis of nano-coatings and are compared next.

6.3-10 Comparison of different nano-coating mix models

The different quantities calculated by ANSYS for each of the 5 model sets (unprotected steel and 4 nano-composite model sets) were used to create graphs for comparison, shown in **Figures 6.59-6.62**. Considering the ***first nano-composite model set*** *i.e. structural steel plate with* $(Al_2O_3$ *(60%) &* TiO_2 *(40%) composite layers*, when compared to the results obtained for the unprotected structural steel substrate, an overall improvement in the mechanical performance is seen.
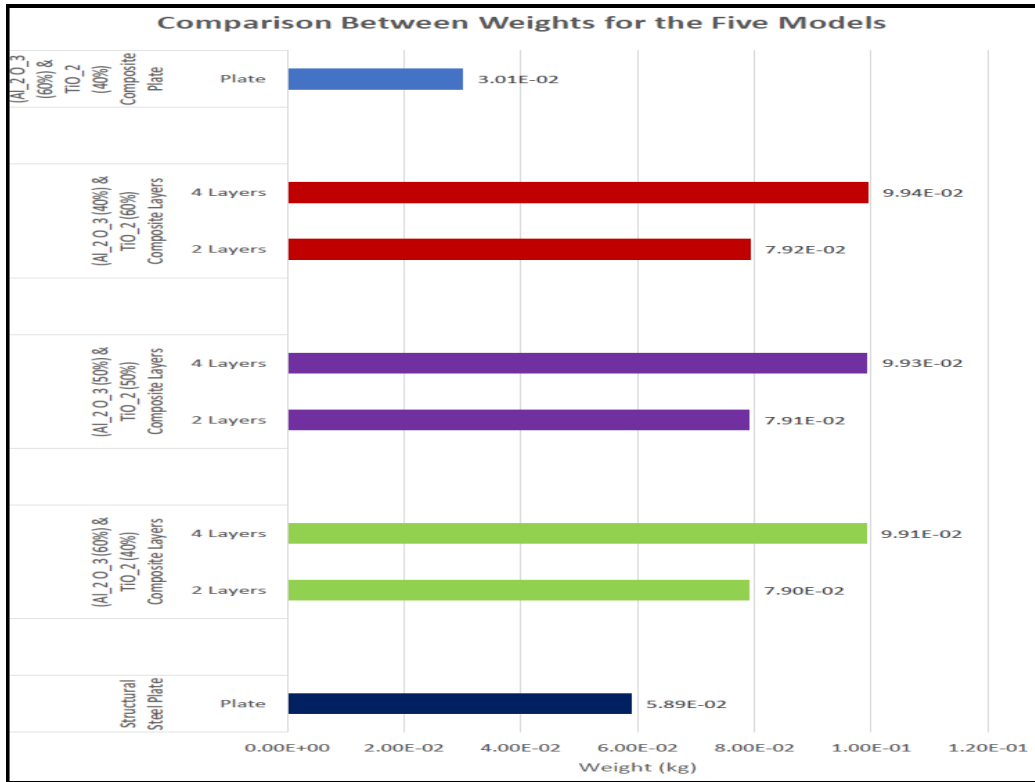
Figure 6.59: Comparison between *weights* for the five models.
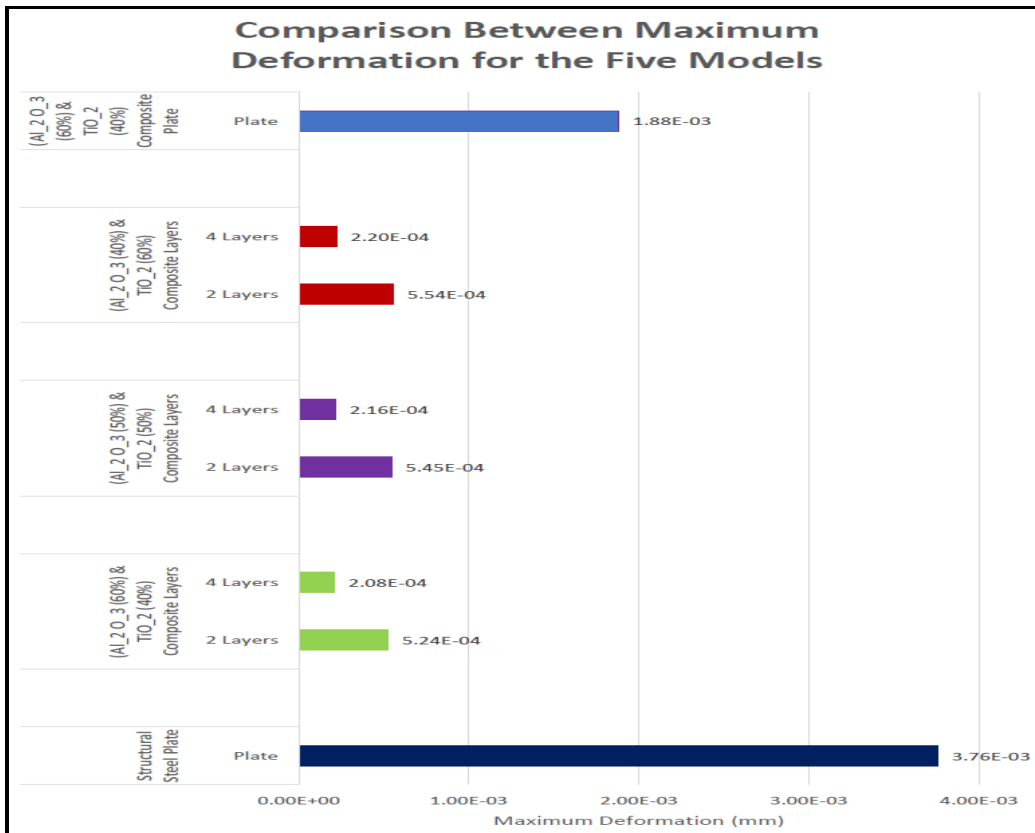
Figure 6.60: Comparison between *total deformation* for the five models.
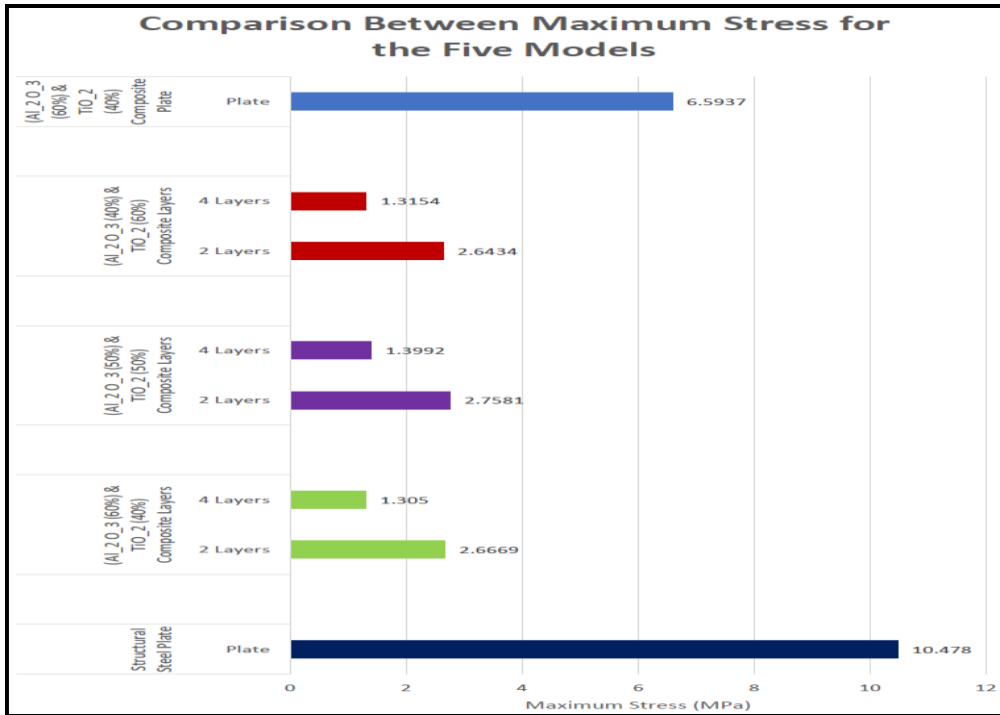
Figure 6.61: Comparison between maximum *stress* for the five models.
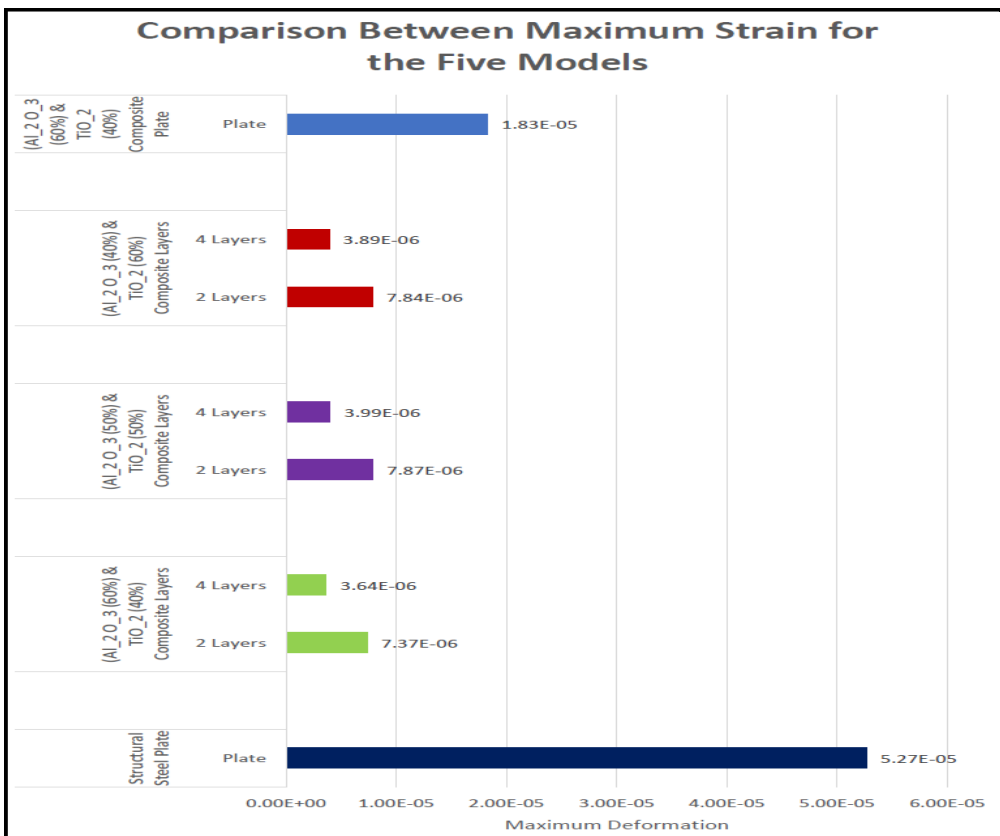
Figure 6.62: Comparison between maximum *strain* for the five models.

The stress and strain experienced by the nano-coated substrate were reduced compared to the uncoated steel substrate (plate), as the top and bottom layers of the plate hold the majority of the strain and stress, whilst the middle steel layer, experiences very little strain and stress. When *two layers* of the nano-composite material were applied to the steel substrate, the maximum equivalent stress experienced reduced by 74.54 % when compared to the uncoated steel substrate, from a value of 10.478 MPa to a value of 2.6669 MPa. Likewise, a decrease in the total deformation was seen, by 86.06% from 3.76E-03 mm to 5.24E-04 mm. The strain experienced also reduced, by -86.02 %, from 5.27E-05 to 1.85E-06. The only disadvantage of this model is the additional weight, which increases by 34.13%, from an initial weight of 5.89E-02 kg to 7.90E-02 kg. For the nano-coated substrate (plate) with *four* composite layers, a similar trend was seen, with the equivalent stress, equivalent stain, and total deformation were reduced by 87.54%, -93.09% and -94.47%, respectively. The weight of the substrate coated with 3 nano-coating layers (above and below the substrate) however increased by 68.25%.

For the ***second nano-composite model set*** *i.e. the structural steel plate with (Al_2O_3 (50%) & TiO_2 (50%) composite layers*, an overall improvement in the plate elasto-mechanical behaviour was also seen, apart from an increase in the weight by 34.3% for the substrate coated with two nano-coating composite layers, and by 68.59% for four nano-coating composite layers, similar to the weights for the 60%:40% cases. With two composite layers, the total deformation decreased by 85.05%, and 94.26% for the substrate coated with *four nano-coating composite layers*. The overall equivalent strain and stress were also reduced and again the majority of stress and strain were sustained by the top and bottom layers of the nano-coatings as seen with the first model, with the middle layer experiencing relatively minor stress and strain. Hence, the equivalent stress reduced by 73.68% and 86.64% for the composite plate with two and four layers, respectively, in comparison to the uncoated steel substrate. The equivalent strain reduced by 85.07% and 92.43% for the composite plate with two and four layers, respectively.

Finally, the total deformation experienced was reduced by 85.05% and 94.26% for the composite plate with two and four layers, respectively, when compared to the uncoated steel substrate case. An overall decline was seen in the performance when compared to the 60%:40% composition.

For the ***third nano-composite model set*** *i.e. structural steel plate with (Al_2O_3 (40%) & TiO_2 (60%) composite layers.* When compared to the uncoated substrate, an overall improvement was also seen. The total deformation was reduced by 85.27% and 94.15% for the composite nano-coated substrate with two and four layers, respectively, with the maximum equivalent stress being reduced by 74.77%, and 87.44% for the composite plate with two and four layers, respectively. An overall reduction in the maximum equivalent strain was also seen as with the other models, with a reduction of 85.12% and 92.62% for the nano-coated substrate with two and four layers, respectively. The major stresses and strains were concentrated at the top and bottom layers, as with the other models, with the middle layer being the least stressed and strained area. Finally, an increase of 34.47% and 68.25% was seen, for the weights of the nano-coated substrates with two and four composite layers, respectively with the 40%:60% composition. An *overall decline in performance* was computed for this model, in comparison to the results obtained for the 50%:50% nano-coating composition.

For the ***fourth nano-composite model set*** *i.e.* (contour plots not shown) a 1.5 mm thick model was formed by joining *three layers of the 1 mm thick, (Al_2O_3 (60%) & TiO_2 (40%) composite without the use of any structural steel material*. Although this is a hypothetical scenario and not practical for real coating (since the substrate is missing), it does allow *an examination of pure nanomaterial properties compared with pure structural steel*. When compared to the structural steel plate, an overall improvement in the properties of the plate were seen. The high stress and strain regions on the plate were located on the top and bottom layers in the corners in the fixed-ends of the plate. The centre layer, however, exhibited regions where the stress and

strain are the lowest, indicated by the blue contour bands. In comparison to *the uncoated steel substrate*, this model showed a reduction in weight by 48.9% from 5.89E-02 kg to 3.01E-02 kg whilst maintaining the same volume and surface area. A reduction in the maximum equivalent stress by 37.07% (6.5937 MPa) and a reduction in the maximum equivalent strain by 65.28% (1.83E-05), was also seen. Finally, the last improvement, which was observed, was a reduction of 50% in the total deformation of the *purely nano-composite 3-layer system. When compared to the models before it, the composite plate does not offer the same level of strength* as which have *a structural steel substrate* with composite material layers, however, this model does show a significant decrease in the weight by almost 50 in comparison to *uncoated structural steel substrate* with the same dimensions. Thus, type of composite material is ideal for industrial applications as it shows a high strength-to-weight ratio and showcases results which are expected of typical composite materials. However, it cannot be used as a coating design since a structural steel substrate must be used as this is the material being protected in real applications i.e. the gas turbine blade.

In summary, the most ideal model which showcased the most enhancements in mechanical performance was the ***first nano-composite model set*** *i.e. structural steel substrate with (Al_2O_3 (60%) & TiO_2 (40%) composite layers.* This composite plate reduced the total equivalent stress by almost 75%, and the total deformation by almost 86%. When 4 layers of the composite material were added, instead of two, a further improvement of around 17% was seen in the equivalent stress and, a further reduction in the total plate deformation of around 9% was seen. The only disadvantage of this model was the addition of extra weight by 34.13% and 68.25%, for 2 and 4 composite layers respectively. In terms of the model with the least improved properties, this was found to be the ***third nano-composite model set*** *i.e. structural steel substrate with (Al_2O_3 (40%) & TiO_2 (60%) composite layers* which achieves the *least enhanced properties*, although still showing an improvement over the *uncoated structural steel*

substrate. This design showed reduction in maximum stress by a little more than 37% and a reduction in total plate deformation by exactly 50%. In addition, it showed a surprising weight reduction by almost 50%, unlike the other models. The other three models also showed improvements, in comparison to the uncoated steel substrate, which lie in between these two extremes. A summary of the enhancement in properties of each composite plate model can be seen in **Table 6.11** below, which shows the nano-coated composite models ordered top to bottom, in terms of the most enhanced to the least enhanced properties. Here the negative symbol (-) in front of the values indicates a reduction in the quantity, when compared to the *uncoated structural steel substrate* (Model I).

Percentage Difference in Properties Between Composite Models and Structural Steel					
Composite coating Models		Weight (%)	Total Deformation (%)	Maximum Stress (%)	Maximum Strain (%)
Structural Steel Plate with Al_2O_3 (60%) & TiO_2 (40%) Composite coating layers	2 Layers	34.13	-86.06	-74.54	-86.02
	4 Layers	68.25	-94.47	-87.54	-93.09
Structural Steel Plate with Al_2O_3 (50%) & TiO_2 (50%) Composite coating layers	2 Layers	34.3	-85.05	-73.68	-85.07
	4 Layers	68.59	-94.26	-86.64	-92.43
Structural Steel Plate with Al_2O_3 (40%) & TiO_2 (60%) Composite coating layers	2 Layers	34.47	-85.27	-74.77	-85.12
	4 Layers	68.76	-94.15	-87.44	-92.62
Al_2O_3 (60%) & TiO_2 (40%) Composite coating layers	-	-48.9	-50	-37.07	-65.28

Table 6.11: Percentage difference in properties between nano-coated composite mix models and structural steel substrate.

6.4 Finite element thermal stress analysis of aluminium oxide-titanium oxide (60:40) nano-coated specimen

Having established from section 6.3 via elastic finite element analysis that the *60: 40 nano-coated steel substrate* performs best, in this final set of simulations *thermal stress analysis* was performed for this case to exactly match the experiments conducted in TGA in chapter 5 in which also a 60: 40 aluminium oxide-titanium oxide nano-coating was used. Therefore, the *final nano-coated substrate system* studied in the experiments (chapter 5) i.e. *20.35mm x 10.36mm x 2.807mm* (see **Figure 5.8**) was examined.

ANSYS workbench version 19.1 was deployed to simulate the thermal stress response of nano-coatings. A temperature of 850 Celsius was used initially (the maximum achieved in the TGA experiments in chapter 5) and then increased to a maximum of *1000 Celsius (to model the worse-case scenario representing actual gas turbine conditions) for the final simulations described here*. The sample has a piercing (hole) near the upper edge (which is required for securing in the TGA device in the experiments, see chapter 5). This hole was also included in the finite element model (with 3 mm diameter) to reproduce as accurately as possible the thermo-structural performance of the TGA tested sample. The total nano coating thickness achieved in the sample (chapter 5) is 2.807- 1.5mm i.e. 1.307mm for *both upper and lower surfaces of the substrate*. This equates to 1.307/2 = *0.6535mm* for each of the upper and lower nano-coating thickness and this is modelled exactly in ANSYS. The three-dimensional model was created again in the ANSYS static structural geometry modeller in (*x, y, z*) space to represent the *nano-coated specimen* in the TGA tests [*see chapter 5*] and is shown in **Figure 6.63**. As in all other simulations described in section 6.2 and 6.3, gas turbine blade substrate is modelled as AISI 304 super alloy (steel); however *distinct from the elastic nano-coating models* in section 6.3, all 6 faces are coated with 60: 40 Alumina-Titanium oxide nano-coating. Therefore, the nano-coating *completely engulfs* the substrate specimen as in the experimental

190

TGA testing. The fixture (cylindrical hole is also shown). All material parameters (Young modulus, Poisson ratio, coefficient of thermal expansion, density etc) are selected from the engineering data library present in the ANSYS theory Manual version 19.1 and for the substrate are identical as with other simulations described earlier. Again isotropic, homogenous elastic behaviour is assumed. **Table 6.12** shows the material properties for the coating nano-mixture and the substrate. The ANSYS procedure is exactly the same as with the *micro-coating* thermal stress analysis (see **Figure 6.1**).
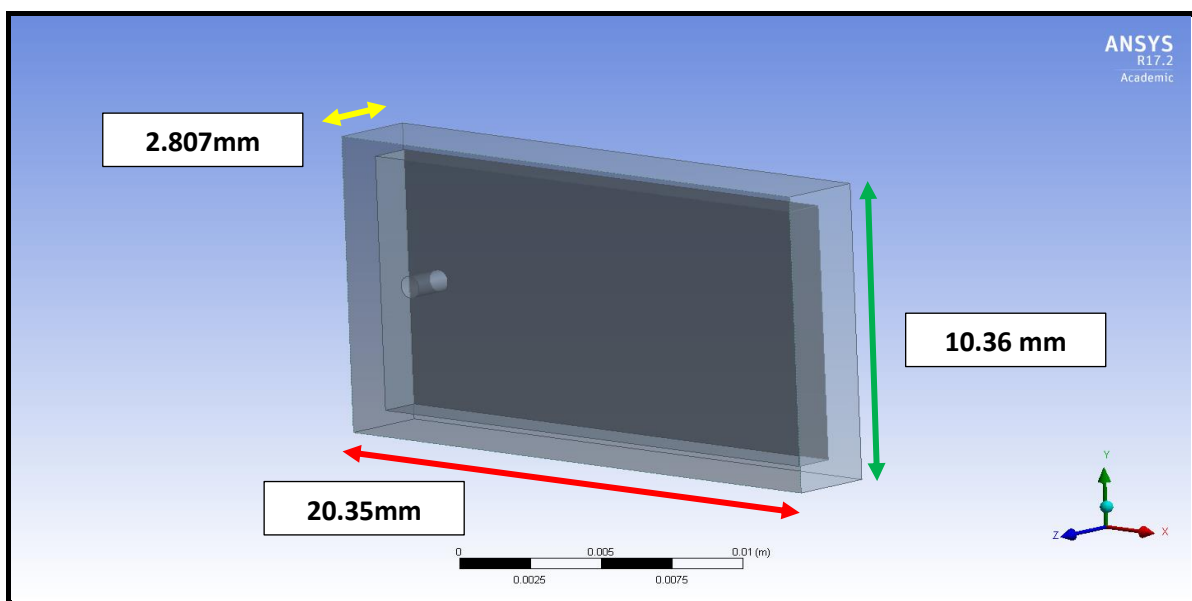
Figure 6.63: ANSYS geometric model for substrate with nano-coating engulfing layer (oblique view).

Property	Steel (AISI 304 Superalloy)	Titania (Titanium oxide nano-powder)	Alumina (Aluminum oxide nano-powder)	Nano-coating Alumina-Titanium Oxide 60:40 mix
Young Modulus (GPa)	200	100	310	226
Poisson Ratio	0.28	0.3	0.22	0.24
Density (kg/m^3)	7850	4500	3690	4,014
Thermal conductivity (W/mK)	50	20	24	22.4

Table 6.12: Material properties for nano-coating and steel substrate.

Figure 6.64 shows the front elevation rendition of the model (top face). The clamping is achieved via the hole which penetrates the entire substrate and is filled with nanomaterial during the coating process.
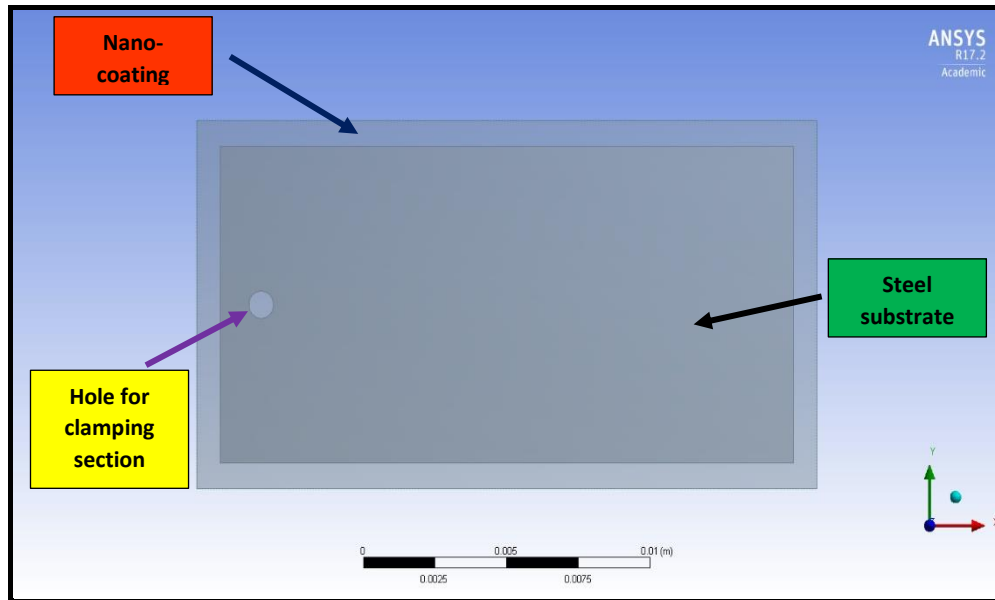
Figure 6.64: ANSYS geometric model for substrate with nano-coating engulfing layer (front view).

In the ANSYS simulation model, a thermal boundary conditions is imposed on all six faces of the coated model to represent hot gas at an average temperature of 1000 °C again with 30 bar pressure. A mesh independence study has been conducted, and 2000 triangular elements are employed in the final refined mesh. Selected simulations are visualized in **Figures 6.65-6.68**. Visualizations are considered for the largest surface of the sample only, for brevity. **Figure 6.65** shows the total deformation on the upper face of the nano-coated sample is constrained to the furthest extremity of the sample (right hand side). Weak deformation is generated generally throughout the sample, and there is a progressive wave of deformation growth from the hole end to the opposite end. Effectively the nano-coating performs well and is found to avoid the proliferation of high deformation zones (red bands) over the majority of the steel substrate which were computed for the micro-coating (section 6.2). The larger component of aluminium

oxide relative to titanium oxide is known to provide a better *oxide layer* which inhibits deformation effects on the coated sample, as noted by Gell [11]. While titanium oxide does provide thermal protection owing to the exceptionally high melting point of titanium, the primary benefit is with aluminium oxide for corrosion protection.
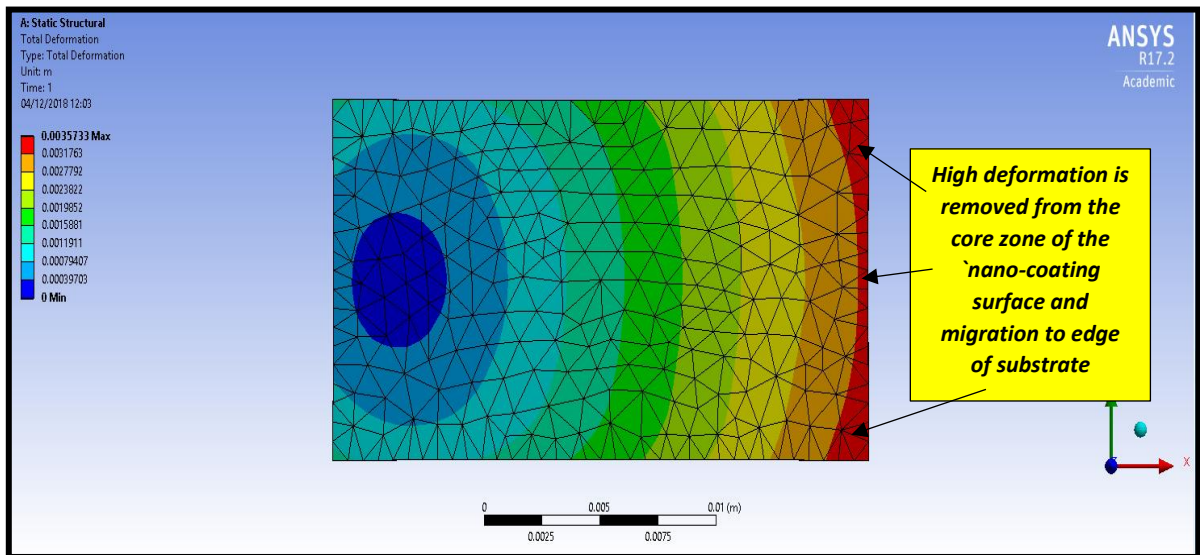
Figure 6.65: Total deformation plot for 60:40 Alumina-Titanium oxide nano-coating.
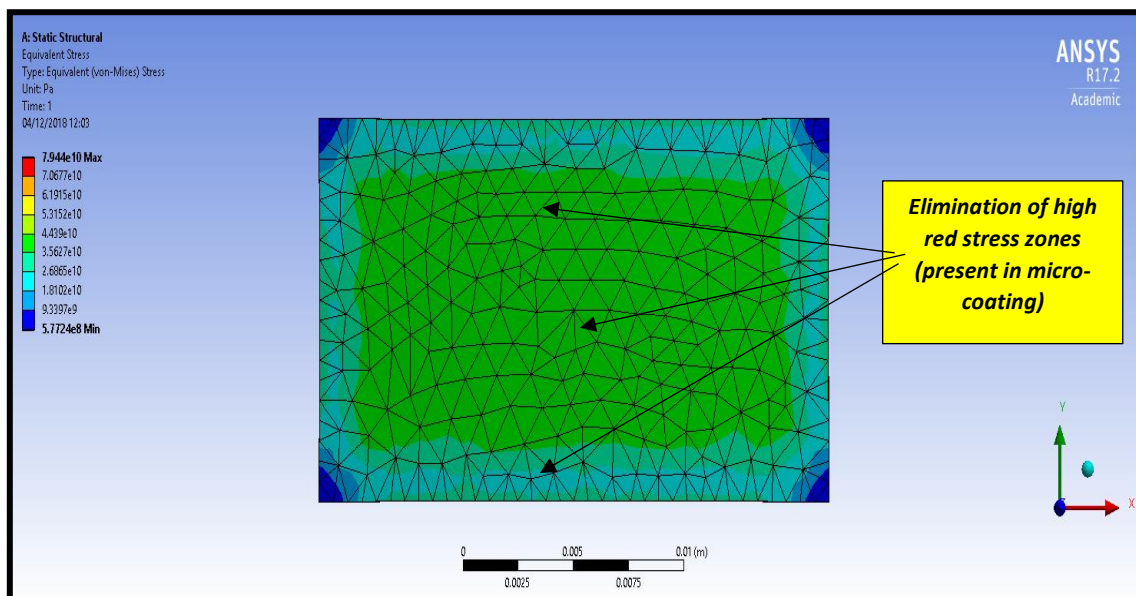
Figure 6.66: Equivalent stress plot for 60:40 Alumina-Titanium oxide nano-coating.

193
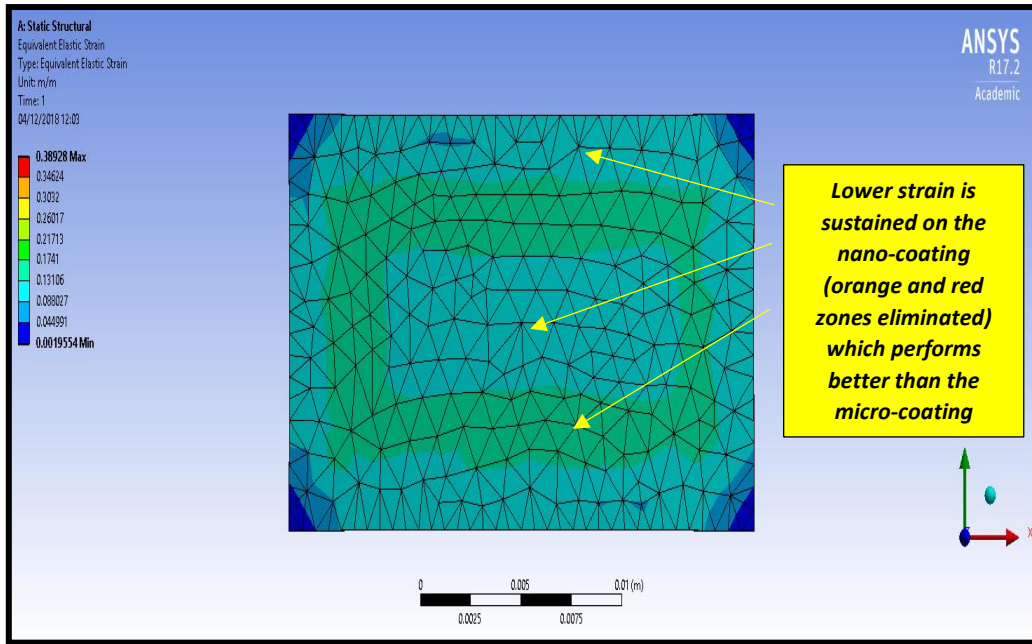
Figure 6.67: Equivalent strain plot for 60:40 Alumina-Titanium oxide nano-coating.

For this reason, also it was elected not to simulate the *40: 60 or 50: 50 aluminium oxide-titanium oxide nano-powder composite mixes*, since they contain a lower percentage of aluminium oxide. **Figure 6.66** shows the Von Mises (equivalent) stress distribution over the nano-coated sample. The nano-coating achieves the desired suppression in stress generated on the sample. There is a complete elimination of red zones (peak thermal stresses) which are known to arise in high temperature loading in gas turbine blades, as earlier computed for *micro-coated samples* by Zhu [12]. However, in the present thermoelastic simulations, a conjugate heat transfer analysis with fully coupled thermal-stress calculation is conducted (i.e. the model is not decoupled as in numerous other finite element simulation studies). **Figure 6.67** shows the elastic strain contour plot and it is evident that generally relatively low equivalent strains are produced over the surface of the sample (light green zones) and again there is no occurrence of dangerously high (red) strains induced, which are present in the micro-coatings simulated in section 6.2 under the same temperature load (1000 Celsius). The strain state of the structural material adjacent to the coating interface is *the controlling mechanism* for the coating strains.

194

Due to the *non-uniform* distribution of displacement, strain and stress on the nano-coated blade specimen (substrate), the regions located at the top and bottom sides tend to produce a maximum of displacement, with the occurrence of a bigger strain or stress, where *sub-critical cracks* preferentially form. In the ANSYS model a dominant rectangular zone of intermediate equivalent stress (green zone) is produced (**Figure 6.66**). The nanocoating therefore achieves the desired effect of circumventing *high stress localized zones* which would lead to surface degradation and enable hot gas penetration to the underlying steel substrate. This behaviour confirms the superior performance observed in the TGA tests described earlier in Chapter 5, where a much lower corrosion rate (*Kp*) value was computed for nano-coating compared with micro-coating, and surface material flaking was completely absent in the nano-coating whereas it was quite significant in the micro-coating (ceramic silicon carbide).

6.5 Summary of main outcomes from all simulations

Having performed extensive computational mechanics simulations in this chapter, the main outcomes can be summarized as follows:

(i) For the *thermal stress analysis* conducted at 1000 Celsius, substantially higher deformations are computed in the three-layer model (dual Titanium and Silicon Carbide (SiC) ceramic coatings) as observed in the large red (high deformation) zone which covers most of the steel model surface. These high deformation zones are successfully eliminated with the 60:40 *aluminium oxide-titanium oxide nano-powder composite mixes*. This confirms the experimental behaviour observed in the TGA tests (chapter 5) where significant surfacial degradation is observed in the micro-coating whereas it is *absent* in the nano-coated substrate.

(ii) For the micro-coating, only with the addition of ceramic coating are the *peak deformation zones* reduced at the edges which are discontinuities and potential

zones for failure. The combined titanium-silicon carbide ceramic micro-coating therefore performs significantly better than with only titanium micro-coating.

(iii)   For the *elastic finite element simulations* of *nano-powder composite mix, the (Al$_2$O$_3$ (60%) & TiO$_2$ (40%) composite layer* performs the best and achieves the lowest deformations, stresses and strains compared with all other nano-coating designs i.e. 50: 50, 40: 60 mixes, irrespective of the number of coating layers applied. There is a slight weight gain with this design, however the main advantage of better thermal protection is achieved.

(iv)   The *thermal stress analysis* confirms that 60: 40 *Al$_2$O$_3$ (60%) & TiO$_2$ (40%) nano-coating design* provides the best thermal protection (corroborating the TGA experiments in chapter 5). The larger component of aluminium oxide relative to titanium oxide is known to provide a better *oxide layer* which inhibits deformation effects on the coated sample. While titanium oxide does provide thermal protection owing to the exceptionally high melting point of titanium, the primary benefit is with aluminium oxide for high temperature corrosion protection.

(v)   For the *CFD turbulent gas flow erosion analysis*, which was only conducted on the micro-coating (since surface material removal was only observed in the TGA tests in chapter 5 for micro-coatings) generally *maximum erosion rates* are confined to a local zone on the upper face of the three-layer titanium-silicon carbide micro-coating. This upper layer is the *sacrificial layer* (ceramic coating). The titanium is not de-bonded or damaged which is essential for creating a buffer to the actual blade surface. Even though the magnitudes are small for the erosion rates, they are nevertheless present and this correlates with the flaking characteristics (material removal) observed in the micro-coating TGA tests described earlier in chapter 5. Overall, the three-layer titanium-silicon carbide substrate micro-coating is shown

to perform very well and does offer good protection (although it is not as effective as the aluminium-oxide-titanium oxide nano-coating).

(vi) Overall, the *best mitigation of high temperature corrosive damage* is achieved with the *nano-coating*. The substantial difference between micro and nano coating performance is strongly related to the size of the coating particles. Micro-coating particles are of the order of microns (microscale is 10^{-6}). Since cracks propagate at the micro-scale which leads to surface degradation, greater integrity of the coating is achieved with 60:40 aluminium oxide-titanium oxide nano-coating and lower susceptibility to corrosion gas penetration is obtained compared with micro-coatings. The elimination of cracks in the TGA experiments (chapter 5) for nano-coatings is therefore corroborated in the simulations.

(vii) A *single layer of aluminium oxide-titanium oxide nano-coating* performs better than a *double layered titanium-silicon carbide ceramic coating*. This is a very significant *novel finding of this PhD* and encourages strongly the use of nano-coatings in practical industrial gas turbine high corrosion thermal protection.

CHAPTER 7:   CONCLUSIONS AND FUTURE PATHWAYS

7.1   Introduction

In this PhD a number of methodologies have been explored to characterize and quantify the performance of both micro- and nano-coatings (thermal barrier coatings i. e. TBCs) on gas turbine blade specimens in high temperature corrosive environments encountered in aero-engine propulsion systems. High thermal stresses arise due to temperature gradient within the blade material and these effects can be reduced with proper deployment of coatings (micro- or nano).

Both experimental testing with TGA and SEM/EDS (EDXA) and computational simulations have been conducted on titanium-silicon carbide ceramic micro-coated substrates and aluminium oxide-titanium oxide nano-coated substrates with AISI 304 alloy steel used throughout as the gas turbine blade material. Additionally, SEM/EDS was conducted on an uncoated AISO304 substrate which had been heated in an oven. The performance of the micro-coating and nano-coating were compared with a benchmark TGA test [1] to establish the different corrosion rates.

The ANSYS computational simulations for *micro-coatings* included both elastic and thermal stress simulations and furthermore included a CFD ANSYS FLUENT turbulent erosion simulation with the discrete phase model (DPM).

The simulations for the *nano-coatings* included *elastic (static non-thermal) modelling* of different percentage mix nano-coatings (60:40, 50:50 and 40: 60) and *thermal stress analysis* of the best design i.e. 60: 40 aluminium oxide-titanium oxide.

The principal findings of this PhD can be summarized as follows based on the experiments and computational mechanics analysis are first summarized and then some future pathways highlighted for extending the research.

7.2 Key findings and novelties of the PhD research

7.2-1 Experimental findings and novelties

i) Based on TGA testing, the correct *parabolic behaviour* was demonstrated for the corrosion rate in both micro-coatings and nano-coatings with an increase in temperature (and time) and also the "breakdown" state after 2 hours of oxidation (up to which the corrosion rate plot is *linear*). The oxidation rate increased beyond the breakdown limit and the oxidation behaviour changed from *linear to parabolic* after 2 hours. This agrees with the benchmark experimental study of Damra [1].

ii) The TGA results also show that titanium-silicon carbide micro-coating achieves a massive reduction in corrosion rate (*Kp*) value relative to the *unprotected (uncoated) blade specimen*. The unprotected substrate [1] showed a *Kp* value of $8.437 \times 10^{-8} \left(\frac{g^2}{cm^4 s} \right)$ whereas the micro-coating showed a much lower value of $0.036655 \times 10^{-8} \left(\frac{g^2}{cm^4 s} \right)$. There is therefore a 99. 57% decrease in corrosion rate. However, the nano-coating produced the lowest corrosion rate *Kp* value of $0.02001 \times 10^{-8} \left(\frac{g^2}{cm^4 s} \right)$. Hence, nano-coating reduces the corrosion rate *even further compared with the micro-coating*. There is a 45.4% decrease in corrosion rate achieved with the 60:40 aluminium oxide-titanium oxide nano-coated sample compared with the micro-coated sample. *This is a very significant finding which has not been reported before in the scientific literature*. It demonstrates that a *single layer of nano-coating* achieved enhanced thermal corrosion protection compared with a *double layer* (metallic-ceramic) micro-coating. This novel result strongly endorses the adoption of metallic oxide single layer nano-coatings in practical gas turbine blade protection from high temperature corrosion and shows that they perform better than metallic/ceramic combinations which are conventionally used in industry.

iii) The SEM morphology and EDS elemental composition results show that while the *titanium-silicon carbide micro-coating* significantly improves the protection of the AISI 304 substrate at high temperature, it is not as effective as the *60: 40 aluminium oxide-titanium oxide nano-coating* which shows the *highest oxygen content* and therefore offers the best protection against sulphidation. Furthermore, iron content in the nano-coating *is lower than the unprotected sample* and again this will provide better protection against corrosion attack at high temperatures. The *novel titanium-silicon carbide micro-coating and 60: 40 aluminium oxide-titanium oxide nano-coating have been shown to offer excellent protection against high temperature corrosion, although the nano-coating has been shown to be superior in this respect. The traditional ceramic micro-coatings used in industry can therefore be replaced with nano-coatings.*

iv) Significant reduction in *surfacial damage* is achieved with the *nano-coating* and the flaking and cracking encountered with micro-coating is eliminated, largely since the cracks generated are of the micro scale and are inhibited with nanoscale engineering particles in the nanocoating. This again confirms that mechanically much better protection is attained with the nano-coating. *Again, this is a novel finding which has established experimentally that single nano-coating layer protection is more effective than the double-layer micro-coating (titanium-silicon carbide ceramic) for high temperature corrosion. This strongly endorses the adoption of nano-coatings in industrial gas turbine applications.*

7.2-2 Computational findings and novelties

(i) For the *finite element thermal stress analyses* conducted at 1000 Celsius, substantially higher deformations are computed in the three-layer model (dual Titanium-Silicon Carbide (SiC) ceramic coating design) as observed in the large red (high deformation) zone which covers most of the upper surface. These high deformation zones are successfully eliminated with the 60:40 *aluminium oxide-titanium oxide nano-powder composite mixes*. This confirms

the experimental behaviour observed in the TGA tests where significant surfacial degradation is observed in the micro-coating whereas it is *absent* in the nano-coated substrate.

(ii) For the *micro-coating thermal stress analysis*, only with the addition of ceramic coating are the *peak deformation zones* reduced at the edges which are discontinuities and potential zones for failure. The combined *titanium-silicon carbide ceramic* micro-coating (3-layer model) therefore performs significantly better than with *only* titanium micro-coating (2 layer-model).

(iii) For the *elastic finite element simulations* of *nano-powder composite mix, the (Al_2O_3 (60%) & TiO_2 (40%) composite nano-coating layer* performs the best and achieves the lowest deformations, stresses and strains compared with all other nano-coating designs i.e. *50: 50 and 40: 60* mixes, irrespective of the number of coating layers applied. There is a slight weight gain with this design, however the main advantage of better thermal protection is achieved with the 60:40 nano-coating. *This is again a novel result which has never been reported before in the literature.*

(iv) The *thermal stress analysis* confirms that 60: 40 Al_2O_3 (60%) & TiO_2 (40%) nano-coating design* provides the best thermal protection (corroborating the TGA experiments in chapter 5). The larger component of aluminium oxide relative to titanium oxide provides a better *oxide layer* which inhibits deformation effects on the coated sample. While titanium oxide does provide thermal protection owing to the exceptionally high melting point of titanium, the primary benefit is with *aluminium oxide* for high temperature corrosion protection.

(v) For the *CFD turbulent gas flow erosion analysis*, which was only conducted on the *micro-coating* (since surface material removal was only observed in the TGA tests in chapter 5 for micro-coatings and not in the nano-coatings), generally *maximum erosion rates* are confined to a local zone on the upper face of the three-layer titanium-silicon carbide micro-coating. This

upper layer is the *sacrificial layer* (ceramic coating). The titanium is not de-bonded or damaged which is essential for creating a buffer to the actual blade surface. Even though the magnitudes are small for the erosion rates, they are nevertheless present and this correlates with the flaking characteristics (material removal) observed in the micro-coating TGA tests as described earlier in chapter 5.

Overall, the titanium-silicon carbide substrate micro-coating is shown to perform very well and does offer good protection to the substrate (although it is not as effective as the 60: 40 aluminium-oxide-titanium oxide nano-coating).

vi) In general, the *best mitigation of high temperature corrosive damage* is achieved with the *nano-coating*. The substantial difference between micro-coating and nano-coating performance may be strongly related to the size of the coating particles. Micro-coatings are of the order of microns (microscale is 10^{-6}). Nano-coatings are of the order of 10^{-9}. Since cracks propagate at the micro-scale which leads to surface degradation, greater integrity of the coating is achieved with aluminium oxide-titanium oxide nano-coating (60:40) and lower susceptibility to corrosion gas penetration is obtained compared with micro-coatings.

(vii) A *single layer of aluminium oxide-titanium oxide nano-coating* performs better than a *double layered titanium-silicon carbide ceramic coating in the thermal stress simulations*. This is a *very significant novel finding* of this PhD, which concurs with the experimental findings from the TGA testing, and again encourages strongly the use of nano-coatings in practical industrial gas turbine high corrosion thermal protection.

7.3   Future Pathways

The present PhD has examined a number of aspects of gas turbine blade coating protection in high temperature corrosion. However as with any study not all phenomena could be examined.

Therefore, several possible new pathways for extending the work conducted are now briefly highlighted.

7.3-1 Extension to full 3-D skewed blade geometries in simulation

Actual gas turbine blades have very complex geometries. The TGA testing restricted consideration to only a very small coated specimen. The specimen samples studied in this PhD had to be very small for testing in order to fit into only TGA apparatus available. In the future however, with access to larger TGA testing apparatus (industrial), a complete micro-coated (or nano-coated) gas turbine blade geometry could be tested. This could then also be simulated with finite element analysis using more powerful computers (e.g. Silicon Graphics workstations). CFD erosion analysis could then also be done for the 3-D coated blade geometry. Some examples of simulations which could be achieved are shown in **Figure 7.1**.

The finite element mesh

a)
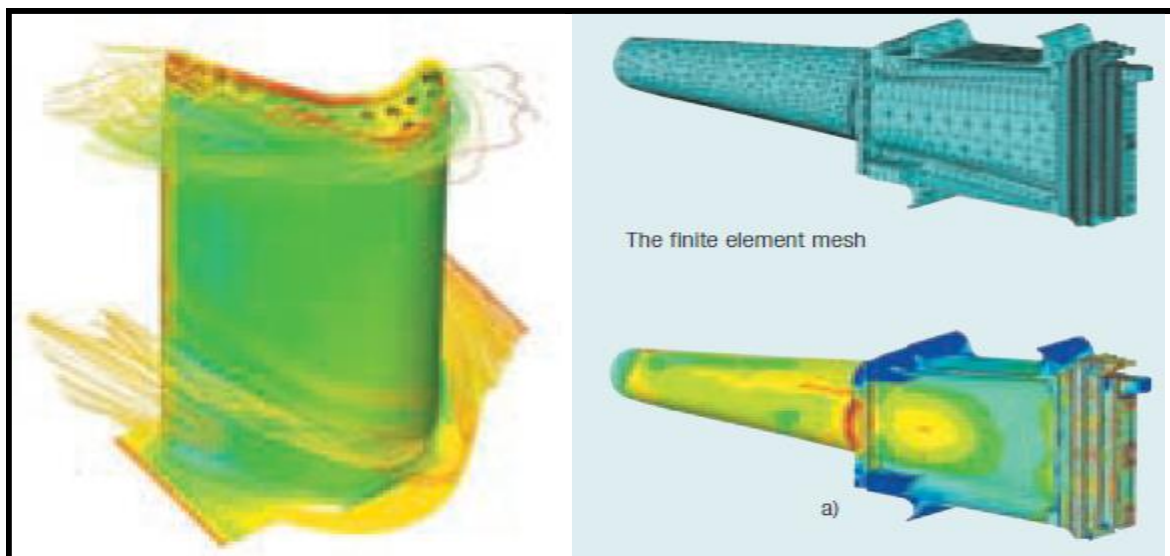
Figure 7.1: Extension to 3-d skewed blade geometries [2].

7.3-2 Extension to thermal-fluid-structure interaction in simulation

The thermal analysis and even CFD erosion simulations conducted in this PhD did not consider the *elastic flexibility of the specimen* i.e. thermal flow-structure interaction was not considered. This is significant in actual gas turbine blades under high temperature and pressure conditions. Therefore, with access to more powerful computers, in the future, much greater mesh densities

can be produced, and the interaction of thermal fluid flow and coated blade deformation can be studied.

7.3-3 Extension to include chemical kinetic corrosion effects in modelling

It is also noteworthy that the focus of this PhD is *coating performance* and therefore *chemo-thermo-mechanical flow-structure interaction* (which is actually the *total physical problem describing gas turbine blade behaviour in hot corrosive gas environments at high temperature*) was not considered. To properly analyze chemical corrosion effects simultaneously with fluid dynamic and thermal stress effects, a *chemo-thermo-fluid-structure interaction model* is needed. In the available computational software (ANSYS), chemical reactions i.e. corrosion chemistry cannot be coupled to the thermal-fluid structure interaction analysis. To do this would require interfacing with another chemical corrosion code such as CALPHAD [3]. This would then permit a full insight into the chemical reactions, oxidation, thermal, stress and flow effects to be analysed at the same time.

7.3-4 Extension to consider different substrate alloys in simulation and experiments

Additionally, simulations (and experimental tests) could be refined to consider a variety of different substrate alloys including Monel-400, Haste alloy X and Inconel 625 alloy. Actual aero-engine blades deploy many different substrates which have different thermal conductivity and structural properties. This influences their response to thermal loading and of course corrosion behaviour. In this PhD only AISI 304 steel alloy was studied. Future investigations could generalize this to consider e.g. Inconel-625 alloy.

7.3-5 Extension to alternative nano-powders, carbon nanotube (CNT) and graphene coatings for experiments and simulations

Since the general finding of this PhD is that *nano-coating is superior to micro-coating*, this area can be explored and exploited for practical gas turbine protection. Experiments and

simulations may both be refined by using alternative nanomaterials. In particular different nano-coating depths and constitution of different nano-powders can be explored. In this PhD only aluminium oxide-titanium oxide nano-powder was studied. Future work could study e. g. chromium nano-powder, aluminium oxide and chromium nano-powder mix etc. Future studies may also explore other types of nanomaterials e.g. *carbon nanotubes (CNTs) and graphene* which could be used to design the nano-coating in the experiments which may also be simulated with ANSYS finite element software. **Figure 7.2** shows a typical carbon nanotube system.
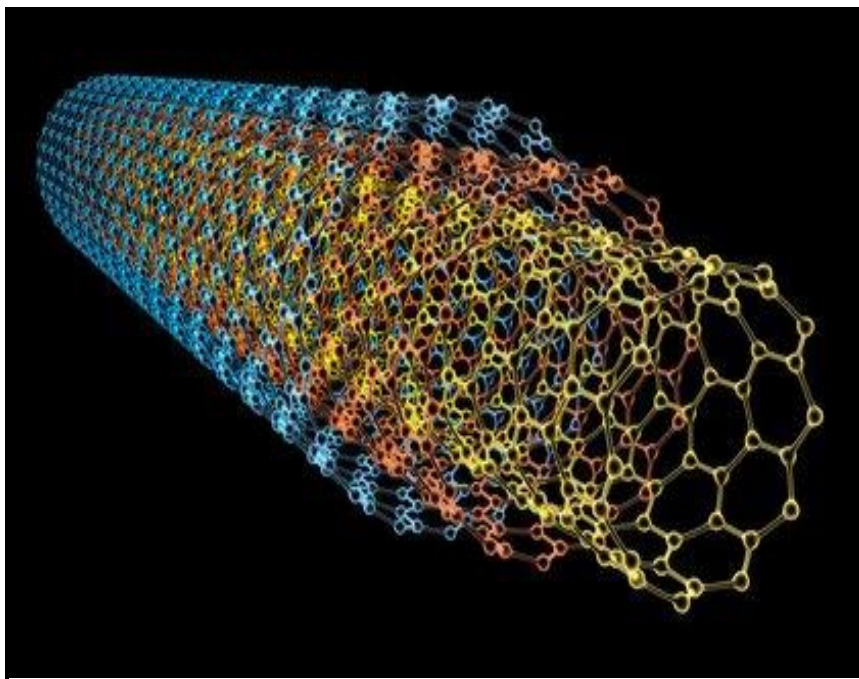
Figure 7.2: CNT for gas turbine blades and coatings - courtesy UCLA Nanoscience Institute.

Carbon nanotubes (CNTs) [4] are allotropes of carbon in which the length to diameter ratio exceeds 1,000,000 in order to produce very high tensile strength, unique electrical properties, and a very efficient conductor of heat. CNTs can also be deployed in multi-layered nano-powder coatings although again this would need an averaging of properties in ANSYS finite element simulations, since it would be difficult to analyse individual nanotube/shell structures without a molecular dynamics code.

7.3-6 Experimental extension to include XRD

X-ray diffraction [5] studies were not conducted in this PhD. This technique allows determination of *mineralogy of the oxidation products* and this would provide an excellent insight into the constitution of the actual corrosion products produced in the TGA testing of both micro-coatings and nano-coatings.

References

Chapter 1

[1] D. R. Coupland, I. R. McGill, C. W. Corti and G. L. Selman, *Spring Residential Conf. on the Environ. Degradation of High Temp. Mater., Isle of Man, 31 March–3 April* (1980).

[2] G.W. Meetham, D. Coutsouradis,, P. Felix,, H. Fischmeister,, L. Habraken,, V. Lindblom and M. O. Speidel, in *"High Temperature Alloys for Gas Turbines", Applied Science Publishers Ltd, London*, p. 837 (1978).

[3] Meherwan P. Boyce, *Gas Turbine Engineering Handbook*, Second Edition, Gulf Professional Publishing, Houston, Texas (1987).

[4] Bernstein H.L., Materials Issues for users of Gas Turbine, *Proceedings of the 27th Texas A&M Turbomachinery Symposium*, USA (1998).

[5] A S Khanna, *Introduction to High-Temperature Oxidation and Corrosion*, Materials Park, OH: ASM International (2002).

[6] G Y Lai, *High-Temperature Corrosion of Engineering Alloys*, Materials Park, OH: ASM International (1990).

[7] D F Bettridge, *Surface Engineering and Heat Treatment*, P H Morton, Institute of Metals, London, p43 (2000).

[8] M Schutze, *Protective Oxide Scales and their Breakdown*, Institute of Corrosion, Chichester and John Wiley, UK (1997).

[9] G W Meetham, M van de Voorde, *Materials for High-Temperature Engineering Applications*, Berlin, New York, Springer (2000).

Chapter 2

[1] N. P. Padture, M. Gell, and E. H. Jordan, Thermal barrier coatings for gas-turbine engine applications, *Science*, 296, 280–284 (2002).

[2] Echsler, H., Renusch, D., Schutze, M., Bond coat oxidation and its significance for life expectancy of thermal barrier coating systems, *Material Science and Technology*, 20, 307-318 (2004).

[3] P.C. Patnaik, J.E. Elder and R. Thamburaj, Degradation of aluminide coated directionally solidified superalloy turbine blades in an aero gas turbine engine, *Superalloys (Edited by S. Reichman, D.N. Duhl, G. Maurer, S. Antolovich and C. Lund),* The Metallurgical Society, USA (1988).

[4] R.Mévrel, State of the art on high-temperature corrosion-resistant coatings, *Materials Science and Engineering: A,* 120, 13-24 (1989).

[5] M. Yoshiba, Effect of hot corrosion on the mechanical performances of superalloys and coating systems, *Corros. Sci.*, 35, 1115–1124 (1993).

[6] G Y Lai, *High-Temperature Corrosion of Engineering Alloys*, Materials Park, OH: ASM International, 1990.

[7] D F Bettridge, *Surface Engineering and Heat Treatment*, P H Morton, Institute of Metals, London, p43 (2000).

[8] M Schutze, *Protective Oxide Scales and their Breakdown*, Institute of Corrosion, Chichester and John Wiley (1997).

[9] G W Meetham, M van de Voorde, *Materials for High-Temperature Engineering Applications*, Berlin, New York, Springer (2000)

[10] A J Sedriks, *Corrosion of Stainless Steels*, New York, Wiley (1996).

[11] T Flatley and C W Morris, *R and D of High-Temperature Materials for Industry*, E Bullock, Elsevier Applied Science, 129 (1989).

[12] César A. C. Sequeira, *High Temperature Corrosion: Fundamentals and Engineering*, 656 Pages, Wiley, USA (2019).

[13] M Schutze, *Protective Oxide Scales and their Breakdown*, Institute of Corrosion, Chichester and John Wiley (1997).

[14] P B Wallis, *The Nimonic Alloys*, Eds W Betteridge and J Heslop, Edward Arnold, London, 459 (1974).

[15] Echsler, H., Renusch, D., Schutze, M., Bond coat oxidation and its significance for life expectancy of thermal barrier coating systems, *Material Science and Technology*, 20, 307-318 (2004).

[16] P.C. Patnaik, J.E. Elder and R. Thamburaj, Degradation of aluminide coated directionally solidified superalloy turbine blades in an aero gas turbine engine, *Superalloys (Edited by S. Reichman, D.N. Duhl, G. Maurer, S. Antolovich and C. Lund),* The Metallurgical Society, USA (1988).

[17] R.Mévrel, State of the art on high-temperature corrosion-resistant coatings, *Materials Science and Engineering: A,* 120, 13-24 (1989).

[18] M. Yoshiba, Effect of hot corrosion on the mechanical performances of superalloys and coating systems, *Corros. Sci.*, 35, 1115–1124 (1993).

[19] M. Yoshiba *et al.,* High-temperature oxidation and hot corrosion behavior of two kinds of thermal barrier coating systems for advanced gas turbines, *Journal of Thermal Spray Technology*, 5, 259–268 (1996).

[20] C-Y. Bai *et al.,* Improvement of high temperature oxidation and corrosion resistance of superalloy IN-738LC by pack cementation, *Surface and Coatings Technology*, 183, 74–88 (2004).

[21] C-H. Koo *et al.,* The structure and high temperature corrosion behaviour of pack aluminized coatings on superalloy IN-738LC, *Materials Chemistry and Physics*, 86, 258–268 (2004).

[22] J. Sumner, A Encinas-Oropesa, N J Simms & J E Oakey, High temperature oxidation and corrosion of gas turbine materials in burner rig exposures, *Materials Science and Technology* 29(7):813-821 ·(2013).

[23] M. Oksa *et al.,* Optimizing NiCr and FeCr HVOF coating structures for high temperature corrosion protection applications, *Journal of Thermal Spray Technology,* 24, 436–453 (2015).

[24] M. A. Khan *et al.,* Oxidation and hot corrosion behavior of nickel-based superalloy for gas turbine applications, *Materials and Manufacturing Processes,* 29, 832-839 (2014).

[25] D. Vollath, *Nanomaterials: An Introduction to Synthesis, Properties and Applications*, 2nd Edition Wiley VCH, China (2013).

[26] M. Islam *et al.,* Influence of SiO_2 nanoparticles on hardness and corrosion resistance of electroless Ni–P coatings, *Surface and Coatings Technology*, 261, 141-148 (2015).

[27] N. Ghazali *et al.,* Super-amphiphobic coating system incorporating functionalized nano-Al_2O_3 in polyvinylidene fluoride (PVDF) with enhanced corrosion resistance, *Coatings*, 10(4), 387 (2020).

[28] H. Ahirwar *et al.,* Materials for orthopedic bioimplants: modulating degradation and surface modification using integrated nanomaterials, *Coatings,* 10(3), 264 (2020).

[29] S. Sana *et al.,* Effect of TiO_2-containing nano-coatings on the color protection of heat-treated jack pine, *J. Coatings Technology and Research*, 8, 183–190 (2011).

[30] H. Dastmalchian, Investigating the changes in electrochemical properties when nano-silica is incorporated into an acrylic-based polyurethane clearcoat, *J. Coatings Technology and Research*, 9, 195–201 (2012).

[31] A. Vereschaka *et al.,* Influence of thickness of multi-layered nano-structured coatings Ti-TiN-(TiCrAl) N and Zr-ZrN-(ZrCrNbAl)N on tool life of metal cutting tools at various cutting speeds, *Coatings, 8*(1), 44-50 (2018).

[32] J. Wang *et al.,* Torsional fretting wear properties of thermal oxidation treated (nano) Ti_3SiC_2 coatings, *Coatings, 8*(9), 324 (2018).

[33] H. Zhue *et al.,* Improvement of corrosion resistance of Hastelloy-N alloy in LiF-NaF-KF molten salt by laser cladding pure metallic coatings, *Coatings, 8*(9), 322 (2018).

[34] V. P. Swaminathan, R. Wei and D. W. Gandy, Nanotechnology Coatings for Erosion Protection of Turbine Components, *ASME J. Eng. Gas Turbines Power* 132(8), 082104 (2010).

[35] J. Sudagar *et al.,* Electroless nickel, alloy, composite and nano coatings – A critical review, *J. Alloys and Compounds*, 571, 83-204 (2013).

[36] S. Karthikeyan and B. Ramamoorthy, Effect of reducing agent and nano Al_2O_3 particles on the properties of electroless Ni–P coating, *Applied Surface Science*, 307, 654-660 (2014).

[37] L. Guo *et al.,* Preparation and hot corrosion behaviour of plasma sprayed nanostructured $Gd_2Zr_2O_7$-$LaPO_4$ thermal barrier coatings, *J. Alloys and Compounds*, 698, 13-19 (2017).

[38] M. Li *et al*., Preparation of nanostructured $Gd_2Zr_2O_7$-$LaPO_4$ thermal barrier coatings and their calcium-magnesium-alumina-silicate (CMAS) resistance, *J. Eur. Ceramic Soc*., 37, 3425-2434 (2017).

[39] R.S. Lima and B.R. Marple, Nanostructured YSZ thermal barrier coatings engineered to counteract sintering effects, *Materials Science and Engineering: A*, 485, 182-193 (2008).

[40] C.G. Zhou and Q.H. Yu, Nanostructured thermal barrier coatings, *Thermal Barrier Coatings*, Woodhead Publishing Series in Metals and Surface Engineering, 75-96 (2011).

[41] N.B. Dahotre and S. Nayak, Nanocoatings for engine application, *Surface and Coatings Technology*, 194, 58-67 (2005).

[42] M. Gell, Applying nanostructured materials to future gas turbine engines, *The Journal of The Minerals, Metals & Materials Society (TMS)*, 46, 30–34 (1994).

[43] Lukas H. L.; Fries Suzana G.; Sundman Bo, *Computational thermodynamics: the CALPHAD method*, Cambridge University Press, USA (2007).

[44] Stephan Petersen, The thermochemistry library ChemApp and its applications, *International Journal of Materials Research (formerly Zeitschrift fuer Metallkunde),* 98(10):935-945 (2007).

[45] J.A. Grogan *et al.* A physical corrosion model for bio-absorbable metal stents, *Acta Biomater.* 10, 2313–2322 (2014).

[46] R. Duddu *et al.,* An extended finite element method-based approach for modeling crevice and pitting corrosion. *J. Appl. Mech. Trans. ASME*, 83, 081005 (2016).

[47] W. Shang *et al.,* Corrosion resistance and molecular dynamics behavior of the MAO/SAM composite coatings on magnesium alloy. *Prot. Met. Phys. Chem. Surf.* 52, 847–853 (2016).

[48] Haris, N.I.N.; Sobri, S.; Yusof, Y.A.; Kassim, N.K. An overview of molecular dynamic simulation for corrosion inhibition of ferrous metals. *Metals*, 11, 46 (2021).

[49] M. Bäker, Finite element simulation of interface cracks in thermal barrier coatings, *Computational Materials Science*, 64, 79-83 (2012).

[50] X. Chen, Failure mechanisms of thermal barrier coatings at high temperature, *ASME 2003 International Mechanical Engineering Congress and Exposition, Washington, DC, USA, November 15–21 (*2003).

[51] L. Yang, Q.X. Liu, Y.C. Zhou, W.G. Mao, C. Lu, Finite element simulation on thermal fatigue of a turbine blade with thermal barrier coatings, *J. Materials Science & Technology*, 30, 371-380 (2014).

[52] H. Mohamed, Finite element analysis (FEA) implementation of thermal barrier coating (tbc) lifetime prediction methods, *Master of Science Dissertation, Swanson School of Engineering, University of Pittsburgh, USA* (2013).

[53] X. Fan, R. Xu, and T. J. Wang, Interfacial delamination of double-ceramic-layer thermal barrier coating system, *Ceramics International*, 40, 13793–13802 (2014).

[54] R. Xu, Interfacial fracture mechanism associated with mixed oxides growth in thermal barrier coating system, *Surface, and Coatings Technology*, 253, 139-147 (2014).

[55] M. Gupta *et al.,* Design of next generation thermal barrier coatings — Experiments and modelling, *Surface and Coatings Technology*, 220, 20-26 (2013).

[56] Busso, E.P., Lin J., Sakurai, S., Nakayama, M., A mechanistic study of oxidation-induced degradation in a plasma-sprayed thermal barrier coating system. part I: model formulation, *Acta Mater.,* 49:1515-1528 (2001).

[57] W. Zhu, Modeling and simulation of the temperature and stress fields in a 3D turbine blade coated with thermal barrier coatings, *Surface and Coatings Technology*, 315, 443-453 (2017).

[58] W. Z. Tang *et al.,* Numerical simulation of temperature distribution and thermal-stress field in a turbine blade with multilayer-structure TBCs by a fluid–solid coupling method, *Journal of Materials Science & Technology*, 32, 452-458 (2016).

[59] T. Sadowski and P.Golewski, Multidisciplinary analysis of the operational temperature increase of turbine blades in combustion engines by application of the ceramic thermal barrier coatings (TBC). *Computational Materials Science,* 50, 1326-1335 (2011).

[60] Zhu P, Lei ZX, Liew KM, Static and free vibration analyses of carbon nanotube-reinforced composite plates using finite element method with first order shear deformation plate theory. Compos Struct 94(4):1450–1460 (2012).

[61] Malekzadeh P. and Shojaee M. Buckling analysis of quadrilateral laminated plates with carbon nanotubes reinforced composite layers. *Thin Walled Struct*. 71:108–118 (2013).

[62] Lei ZX, Liew KM, Yu JL, Free vibration analysis of functionally graded carbon nanotube-reinforced composite plates using the element-free kp-Ritz method in thermal environment. *Compos Struct*, 106:128–138 (2013).

[63] Alibeigloo A, Liew KM. Thermoelastic analysis of functionally graded carbon nanotube reinforced composite plate using theory of elasticity. *Compos. Struct*. 106:873–881 (2013).

[64] Shen HS, Xiang Y., Nonlinear vibration of nanotube-reinforced composite cylindrical shells in thermal environments. *Comput. Methods Appl Mech Eng* 213–216:196–205 (2012).

[65] Kiran Ashok *et al*., Finite element analysis of thermal fatigue loading of nano materials coated turbine blade for critical applications, *IOP Conf. Ser.: Mater. Sci. Eng*. 1123 012017 (2021).

[66] Abbas, Guo H and Ramzan M, Comparative study on effect of oxide thickness on stress distribution of traditional and Nano structural zirconia coating systems, *Ceramics International,* 39, 475-481 (2018).

[67] J.R. Davis & Associates (Editors), *Handbook of Thermal Spray Technology*, ASM, New York, USA (2004).

[68] N. Espallargas, *Future Development of Thermal Spray Coatings: Types, Designs, Manufacture and Applications*, Elsevier, USA (2015).

[69] Fauchais, Pierre L., Heberlein, Joachim V.R., Boulos, Maher, *Thermal Spray Fundamentals: From Powder to Part*, Springer, New York (2014).

Chapter 3

[1] *ANSYS User Manual*, version 16.2, Swanson Analysis Systems, Pennsylvania, USA (2015).

[2] K.J. Bathe, *Finite Element Procedures*, Prentice-Hall, New Jersey, USA (1996).

[3] J. Holman, *Heat Transfer*, MacGraw Hill, USA (1993).

[4] F.M. White, *Viscous Flow*, MacGraw Hill, USA (1991).

[5] S. Chandrasekhar, *The Theory of Turbulence*, 1954 Lectures, Editors: Spiegel, Edward A. (Ed.), Springer (2011).

[6] Ferziger, J. H. and Peric, M. (2002). *Computational methods for fluid dynamics*. Springer-Verlag.

[7] Huebner, K.H.; Thornton, E.A.; and Byron, T.D. (1995). *The Finite Element Method for Engineers* (Third ed.). Wiley Interscience.

[8] Anderson, John D. (1995). *Computational Fluid Dynamics: The Basics with Applications*. Science/Engineering/Math. McGraw-Hill Science.

[9] Patankar, Suhas (1980). *Numerical Heat Transfer and Fluid Flow*. Hemisphere Series on Computational Methods in Mechanics and Thermal Science. Taylor & Francis.

[10] A. Sharma, *Introduction to Computational Fluid Dynamics: Development, Application and Analysis*, Wiley (2016).

[11] H. A. Daud, Q. Li, O. Anwar Bég and S.A. Ghani, CFD modeling of blowing ratio effects on 3-D skewed gas turbine film cooling, *11th Int. Conf. Advanced Computational Methods and Experimental Measurements in Heat Transfer, Tallinn, Estonia, 14-16 July* (2010).

[12] T.J. Barth and D.C. Jespersen, The design and application of upwind schemes on unstructured meshes, *AIAA, Aerospace Sciences Meeting, 27th, Reno, NV, Jan*. 9-12, (1989).

[13] *ANSYS FLUENT Theory Guide*, version 18.1, Swanson Analysis Systems, Pennsylvania, USA (2017).

[14] E. Mahdi, A. Rauf, S. Ghani, A. El-Noamany, and A. Pakari, Erosion-corrosion behavior and failure analysis of offshore steel tubular joint, *Int. J. Electrochem. Sci*., vol. 8, no. 5, pp. 7187–7210 (2013).

[15] M. Gupta *et al.,* Design of next generation thermal barrier coatings — Experiments and modelling, *Surface and Coatings Technology*, 220, 20-26 (2013).

[16] A. Hamed and W. Tabakoff, Erosion and deposition in turbomachinery. *AIAA Journal of Propulsion and Power*, Vol. 22, No. 2, pp. 350-360 (2006).

[17] I. Finnie, Erosion of surfaces by solid particles. *Wear*, Vol. 3, pp. 87-103 (1960).

[18] Y.I. Oka and T. Yoshida, Practical estimation of erosion damage caused by solid particle impact. part 2: mechanical properties of materials directly associated with erosion damage. *Wear,* Vol. 259, pp. 102-109 (2005).

[19] B. S. McLaury et al. Modeling erosion in chokes. *Proceeding of ASME Fluids Eng. Summer Meeting. San Diego, California, USA* (1996).

[20] B. Bozzini, M. E. Ricotti, M. Boniardi, and C. Mele, Evaluation of erosion-corrosion in multiphase flow via CFD and experimental analysis, *Wear*, vol. 255, no. 1–6, pp. 237–245 (2003).

[21] H. Arabnejad, A. Mansouri, S. A. Shirazi, and B. S. McLaury, Abrasion erosion modelling in particulate flow, *Wear*, vol. 376–377, pp. 1194–1199 (2017).

[22] Y. Zhang, B. S. McLaury, and S. A. Shirazi, Improvements of particle near-wall velocity and erosion predictions using a commercial CFD code, *ASME J. Fluids Eng.*, vol. 131, no. 3, p. 031303, (2009).

[23] L. Zeng, G. A. Zhang, and X. P. Guo, Erosion-corrosion at different locations of X65 carbon steel elbow, *Corros. Sci.*, vol. 85, pp. 318–330 (2014).

[24] M. M. Stack and S. M. Abdelrahman, A CFD model of particle concentration effects on erosion-corrosion of Fe in aqueous conditions, *Wear*, vol. 273, no. 1, pp. 38–42 (2011).

[25] F. Mohammadi and J. Luo, "Effects of particle angular velocity and friction force on erosion enhanced corrosion of 304 stainless steel, *Corros. Sci.*, vol. 52, no. 9, pp. 2994–3001, (2010).

[26] Harbi A. Daud, Qinling Li, O. Anwar Bég and S.A.A. AbdulGhani, Numerical investigations of wall-bounded turbulence, *Proc. Institution of Mechanical Engineers-Part C: Journal of Mechanical Engineering Science,* 225, 1163-1174 (2011).

[27] B.E. Launder and D.B. Spalding, The numerical computation of turbulent flows, *Computer Methods in Applied Mechanics and Engineering*, 3 (2) 269-289 (1974).

[28] Harbi A. Daud, Qinling Li, O. Anwar Bég and S A A Abdul Ghani, Numerical investigation of film cooling effectiveness and heat transfer along a flat plate, *Int. J. Applied Math. Mechanics,* 8(17): 17 – 33 (2012).

[29] O. Anwar Bég, B. Islam, MD. Shamshuddin and T. A. Bég, Computational fluid dynamics analysis of moisture ingress in aircraft structural composite materials, *Arabian J. Science Engineering* (2019). doi.org/10.1007/s13369-019-03917-4 *(23 pages)*

[30] Ali Kadir, O. Anwar Bég, M. E. El Gendy, Tasveer A. Bég and M. Shamshuddin, Computational fluid dynamic and thermal stress analysis of coatings for high-temperature corrosion protection of aerospace gas turbine blades, *Heat Transfer-Asian Research (2019).* doi: 10.1002/htj.21493 (*25 pages)*

[31] O. Anwar Bég, Armghan Zubair, Sireetorn Kuharat and Meisam Babaie, CFD simulation of turbulent convective heat transfer in rectangular mini-channels for rocket cooling applications, *ICHTFM 2018: 20th International Conference on Heat Transfer and Fluid Mechanics, WASET, Istanbul, Turkey, August 16 – 17* (2018).

[32] Ali Kadir, O. Anwar Bég, Walid S. Jouri, K. A. Habib, Tasveer A. Bég, M.D. Shamshuddin and Henry J. Leonard, Computational discrete phase model for turbulent erosion and experimental investigation of micro-coating protection performance of high-temperature gas turbine blades, *725th International Conference on Mechanical and Aerospace Engineering (ICMAE), Chennai, India, 23rd -24th July* (2020).

[33] O. Anwar Bég, Marvin Kitende, Sireetorn Kuharat, Tasveer A. Bég, Ali Kadir, M. El Gendy, B. Vasu, Ayesha Sohail, Henry J. Leonard and Walid S. Jouri, Aero-acoustic turbulent CFD simulation of a generic automotive body with multiple broadband source models, *ICMEAMT 2020: 14th International Conference on Mechanical Engineering, Applied Mechanics and Technology, Cairo, Egypt, December 14-15* (2020).

[34] A.B. Guess *et al*., Turbulent reacting flow analysis from gas turbine can-type combustor chamber using computational fluid dynamics code. *12TH Congrès de Mécanique, Casablanca, Morocco, 21-24 April* (2015).

[35] A. Kadir, *Internal Evaluation Report*, University of Salford, Stage II of PhD, August (2018).

[36] S.S. Rao, *The Finite Element Method in Engineering*, 4th edition, Elsevier, USA (1985).

[37] O. Anwar Bég, CFD in Aerospace Engineering, *MSc Engineering Computation Lecture Notes, version 4, University of Salford, Manchester, September* (2020).

Chapter 4

[1] Meherwan P. Boyce, *Gas Turbine Engineering Handbook*, Second Edition, Gulf Professional Publishing, Houston, Texas (1987).

[2] D F Bettridge, *Surface Engineering and Heat Treatment*, P H Morton, Institute of Metals, London, p43 (2000).

[3] J.R. Davis & Associates (Editors), *Handbook of Thermal Spray Technology*, ASM, New York, USA (2004).

[4] N. Espallargas, *Future Development of Thermal Spray Coatings: Types, Designs, Manufacture and Applications*, Elsevier, USA (2015).

[5] Fauchais, Pierre L., Heberlein, Joachim V.R., Boulos, Maher, *Thermal Spray Fundamentals: From Powder to Part*, Springer, New York (2014).

[6] A. A. Tracton, *Coatings Technology Handbook*, Taylor and Francis, New York (2015).

[7] M Schutze, *Protective Oxide Scales and their Breakdown*, Institute of Corrosion, Chichester and John Wiley, (1997).

[8] M. Wagner, *Thermal Analysis in Practice* (chapter 10, Thermogravimetric Analysis, p. 162-186, Carl Hanser Verlag, Munich (2018).

[9] L. Reimer, *Scanning Electron Microscopy: Physics of Image Formation and Microanalysis*, Springer, Switzerland (1998).

Chapter 5

[1] M. S. A. F. Damra, High temperature corrosion of stainless steels and NiCrAlY alloy coating deposited by oxyfuel thermal spraying technique, *PhD Thesis, Dept. Industrial Engineering, University Juame I, Castellón, Spain, May* (2009).

[2] A. S. Khana, *Introduction to High Temperature Oxidation and Corrosion*, Materials Park, Ohio, ASM International, USA (2002).

[3] N. P. Padture, M. Gell, and E. H. Jordan, Thermal barrier coatings for gas-turbine engine applications, *Science*, 296, 280–284 (2002).

[4] Echsler, H., Renusch, D., Schutze, M., Bond coat oxidation and its significance for life expectancy of thermal barrier coating systems, *Material Science and Technology*, 20, 307-318 (2004).

[5] Echsler, H., Renusch, D., Schutze, M., Bond coat oxidation and its significance for life expectancy of thermal barrier coating systems, *Material Science and Technology*, 20, 307-318 (2004).

[6] P.C. Patnaik, J.E. Elder and R. Thamburaj, Degradation of aluminide coated directionally solidified superalloy turbine blades in an aero gas turbine engine, *Superalloys (Edited by S. Reichman, D.N. Duhl, G. Maurer, S. Antolovich and C. Lund),* The Metallurgical Society, USA (1988).

Chapter 6

[1] *ANSYS User Manual*, version 16.2, Swanson Analysis Systems, Pennsylvania, USA (2015).

[2] *ANSYS FLUENT Theory Guide*, version 16.2, Swanson Analysis Systems, Pennsylvania, USA (2015).

[3] Tavaresa CJ, Reboutaa L, Andritschkya M, Ramos S., Mechanical characterization of TiN/ZrN multilayered coatings, *J Mat Procs Tech*, 92/93:177-183 (1999).

[4] Shakeri M, Sadough A, Ahmadi SR., Elastic stress analysis of bi-layered isotropic coatings and substrate subjected to line scratch indentation, *J Mat Process Tech*, 196:213–221 (2008).

[5] Breitbach G, Schubert F., A contribution to stress prediction in coatings for gas turbine blades, *Arch. Appl Mech*, 73(9/10):682–689 (2004).

[6] Cao XQ, Vassen R, Stoever D. Ceramic materials for thermal barrier coatings, *J. Euro Ceramic Soc,* 24:1– 10 (2004).

[7] Fan X, Jiang W, Li J, Suo T, Wang TJ, Xu R., Numerical study on interfacial delamination of thermal barrier coatings with multiple separations, *Surface and Coatings Tech*, 244:117–122 (2014).

[8] Jeyalaxmi PS, Kalivarathan G., CFD analysis of flow characteristics in a gas turbine- a viable approach to predict the turbulence, *Int J Mech Eng Tech*, 4(2):39-46 (2013).

[9] H. A. Daud, Q. Li, O. Anwar Bég and S.A. Ghani, CFD modeling of blowing ratio effects on 3-D skewed gas turbine film cooling, *11th Int. Conf. Advanced Computational Methods and Experimental Measurements in Heat Transfer, Tallinn, Estonia,* 14-16 July (2010).

[10] Lukas H. L.; Fries Suzana G.; Sundman Bo*, Computational thermodynamics: the CALPHAD method.* Cambridge: Cambridge University Press (2007).

[11] M. Gell, Applying nanostructured materials to future gas turbine engines, *The Journal of The Minerals, Metals & Materials Society (TMS)*, 46, 30–34 (1994).

[12] W. Zhu, Modeling and simulation of the temperature and stress fields in a 3D turbine blade coated with thermal barrier coatings, *Surface and Coatings Technology*, 315, 443-453 (2017).

Chapter 7

[1] M. S. A. F. Damra, High temperature corrosion of stainless steels and NiCrAlY alloy coating deposited by oxyfuel thermal spraying technique, *PhD Thesis, Dept. Industrial Engineering, University Juame I, Castellón, Spain,* May (2009).

[2] Candelario Bolaina, Julio Teloxa, Cesar Varela, Fernando Z. Sierra, Thermomechanical stress distributions in a gas turbine blade under the effect of cooling flow variations, *ASME J. Turbomach*. Nov 2013, 135(6): 064501 (9 pages).

[3] *Lukas H. L.; Fries Suzana G.; Sundman Bo, Computational Thermodynamics: the CALPHAD method. Cambridge:* Cambridge University Press (2007).

[4] M.S. Dresselhaus, G. Dresselhaus, P. Avouris, (Eds.), *Carbon Nanotubes: Synthesis, Structure, Properties, and Applications*, Springer (2001).

[5] S.K. Chatterjee, *X Ray Diffraction - Its Theory and Applications*, Prentice-Hall, India (2010).

THERMAL STRESS AND CFD ANALYSIS OF COATINGS FOR HIGH-TEMPERATURE CORROSION

Mr. Ali Kadir and Dr. O. Anwar Bég
Department of Mechanical and Aeronautical Engineering, Salford University, Manchester, UK.

Introduction

Modern gas turbine blades experience significant thermal loading during expected life cycles. Temperatures can attain in excess of 1000 Celsius. It is therefore necessary to coat the blades with thermal barrier coatings (TBCs) which also provide protection from oxidation, corrosion, debris impact and thereby mitigate possible failures. Additionally, there are high centrifugal stresses and shock loadings present. Many excellent studies have been conducted on the performance of TBCs in real systems. It has been established that temperature decay across TBCs is a function of material and geometrical properties of the TC layer, in particular the thickness of the layer and thermal conductivity. Ceramics have emerged as the most resilient to high temperature conditions, although cracking may occur and other discontinuities may appear under long duration exposure to corrosive gases.

In the current work we employ the ANSYS structural and FLUENT tools to perform computational stress analysis and high temperature flow analysis on bare (unprotected) and titanium or ceramic (SiC) coated gas turbine blade samples. A three dimensional model is produced in both cases. Body meshing is achieved with tetrahedron cells. A mesh independence study is included to verify the results, which provide a compliment to on-going experimental studies also being undertaken by the authors. The FEA methodology is shown in Fig 1 and the CFD methodology in Fig 2.
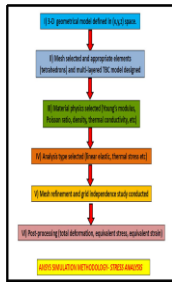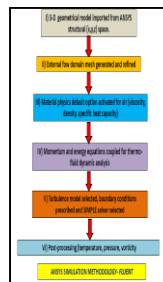

Fig 1   **Fig 2**

Methods and Materials

All finite element stress (structural) and fluid dynamics simulations have been executed in the ANSYS Workbench version 16.2 [1]. Here we first elaborate on the stress analysis and in the next section provide details on the ANSYS FLUENT CFD analysis [2]. A three-dimensional model was created using the ANSYS static structural geometry modeller to represent an exact replica of a sample deployed in HVOF high temperature corrosion bath experiments [3]. A three-layered domain in (x,y,z) space is created (Fig. 3) with each layer representing the three main materials of interest, namely a core steel layer, an intermediate Titanium layer and an outer ceramic (Silicon Carbide SiC) layer. The core and outer ceramic layers are plotted in Fig 3 below. The inner Titanium (metallic) domain measures 20 mm in width and 10 mm in height with the outer domains adding a millimetre depth to this core steel geometry section, respectively. All material parameters (Young modulus, Poisson ratio, coefficient of thermal expansion, density etc) are selected from the engineering data library present in the ANSYS code. Isotropic, homogenous elastic behaviour is assumed.
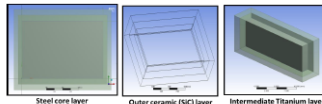

Steel core layer   Outer ceramic (SiC) layer   Intermediate Titanium layer

Fig 3

The cell distribution around the model is shown in Fig. 4. To verify the accuracy of the meshing, a grid-independence study was also conducted which is shown in Fig. 5.
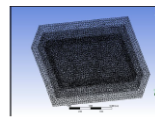

Fig 4   **Fig 5**

Following the successful meshing of the models, static and thermal stress simulations are conducted. Two temperatures are considered, 300 and 1000 degrees kelvin and static loading of up to 1000 Newtons. For the static analysis, the default solver is set the controls for the simulation with a fixed support prescribed at one edge face of the model while subjecting the opposite side to a force of 500 and 1000 Newtons. The software automatically computes the equivalent elastic strain, total deformation, equivalent stress and strain energy. The same process is repeated for the thermal study with the exception of the inclusion of a thermal condition of 300 and 1000 degrees Celsius, while keeping the same outputs. This was followed by duplicating each analysis twice to remove one of the layers each time. This allowed testing of the static and thermal effects on each of the coatings.

Results & Discussion

Thermal stress analysis and finally CFD erosion simulation results
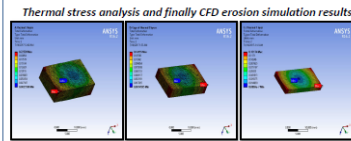

Fig 6 a-c

For the simulations above we have shown the full body models (3-dimensional), the presence of heat significantly modifies the total deformation plots. Red (high deformation) zones are localized in all three cases at the left and right vertical cases; however, the zone of influence penetrates much deeper into the body for the single layer model (fig.6c), less deeper with titanium coating (fig. 6b) and is minimized with the dual ceramic and titanium coating (fig. 6a). Much lower total deformation is also computed throughout the body of the structure in fig. 6a indicating that the dual coating achieves the best performance overall.
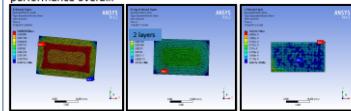

Fig 7a-c

Figs. 7a-c illustrate the evolution in equivalent strain contour plots for the three different coating models examined. While lower strains are computed in fig. 7c (single layer model) the maximum strain is located near the edge. Higher strains are computed for the two-layer model (fig. 7b) – however again with only titanium coating, the maximum stress is dangerously close to the lower edge. Only with the three-layer combined ceramic and titanium coating model (fig. 7a) is the maximum equivalent strain pushed deeper towards the core central area. Here the desired effect of restricting high stresses to the strongest region of the gas turbine blade model is achieved whereas in the other two models lower strains are produced in the core central zones. Unlike other studies e.g. Breitbach and Schubert [4], in the current study a conjugate heat transfer analysis with fully coupled thermal-stress calculation is conducted (i.e. the model is not decoupled as in many other studies). The thermal results indicate that strain state of the structural material adjacent to the coating interface is the controlling mechanism for the coating strains. Due to the non-uniform distribution of displacement, strain and stress in a real gas turbine blade, the regions located at the top and bottom sides tend to produce a maximum of displacement, with the occurrence of a bigger strain or stress, where sub-critical cracks preferentially form. The simulations confirm this trend and agree with the general findings in the literature of for example Cao et al. [5] and Fan et al. [6].
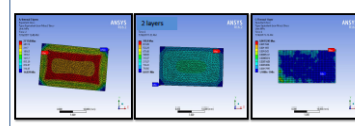

Fig 8 a-c

Figs. 8a-c show the equivalent elastic stress contour plots for the three coating models. For the three-layer model (fig. 8a) a similar distribution to the static case (non-thermal) is observed indicating that the heat has the least impact on stress distribution when both ceramic and titanium coatings are combined. However significantly higher stresses are computed for the two-layer model and especially single layer model in figs 8b, 8c compared with their non-thermal static analysis equivalent plots. Higher stresses are also computed at the edge zones for the thermal cases of single and two-layer models compared with the static cases. Overall therefore the required protection is best provided by the ceramic-titanium-steel model confirming the excellent thermal protection barrier properties of both ceramics and titanium under high temperature loading scenarios.
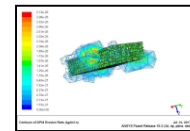

Fig 9

Finally, some preliminary results of CFD analysis are given in Fig. 9 for the erosion rates induced in the three-layer model as obtained by ANSYS FLUENT. Generally *maximum erosion rates* are confined to a local zone on the upper face of the three-layer system which is infact the sacrificial layer (ceramic coating). The titanium is not de-bonded or damaged which is essential for creating a buffer to the actual blade surface. However, the poor performance of ceramics (cracking, delamination, spalling) may be inhibited with improved nano-embedded coating particles and efforts in this direction are currently underway. A more detailed CFD analysis is currently being conducted also.

Conclusions

- Finally, some preliminary results of CFD analysis are given for the erosion rates induced in the three-layer model as obtained by ANSYS FLUENT.
- Generally maximum erosion rates are confined to a local zone on the upper face of the three-layer system which is infact the sacrificial layer (ceramic coating).
- The titanium is not debonded or damaged which is essential for creating a buffer to the actual blade surface.
- However, the poor performance of ceramics (cracking, delamination, spalling) may be inhibited with improved nano-embedded coating particles and efforts in this direction are currently underway.
- A more detailed CFD analysis is currently being conducted and will be reported imminently. The desk top PC I am using will probably require several graphics cards if more detailed CFD simulations are to be achieved in a realistic time scale.
- Furthermore the coupling of chemical kinetics in the erosion/corrosion model will be very challenging and requires multi-quad processor machines which I do not have access to. The current study has provided a good foundation for more refined computational analysis and central to this is the inclusion of an actual 3-dimensional skewed blade geometry. Furthermore, the ceramic may be enhanced in performance by embedding e.g. smart magnetic nano-particles [7,8] which create better bonding to the lower substrate (titanium) and mitigate delamination and crack penetration through the ceramic layer. Efforts to develop more sophisticated thermal barrier coating simulations in these directions (in addition to verification with experimental testing and considering other turbulence models).

Contact

Ali Kadir and Dr. O. Anwar Bég
University of Salford
Department of Aeronautical and Mechanical Engineering
Newton Building, Manchester, M5 4WT, UK.
Email: A.Kadir@salford.ac.uk & O.A.Beg@salford.ac.uk

References

[1] *ANSYS User Manual*, version 16.2, Swanson Analysis Systems, Pennsylvania, USA (2015).

[2] *ANSYS FLUENT Theory Guide*, version 16.2, Swanson Analysis Systems, Pennsylvania, USA (2015).

[3] A. **Kadir**, Corrosion testing of steel, titanium coated steel and titanium-silicon carbide coated steel samples in hot corrosive environments, *Technical Report, Aeronautical and Mechanical Engineering, University of Salford, July* (2017).

[4] G. Breitbach, F. Schubert, A contribution to stress prediction in coatings for gas turbine blades, *Archive of Applied Mechanics*, 73,9/10, 682–689 (2004).

[5] X. Q, Cao, R. Vassen, and D. Stoever, Ceramic materials for thermal barrier coatings, *Journal of the European Ceramic Society*, 24, 1–10 (2004).

[6] X. Fan, W. Jiang, J. Li, T. Suo, T. J. Wang, and R. Xu, Numerical study on interfacial delamination of thermal barrier coatings with multiple separations, *Surface and Coatings Technology*, 244, 117–122 (2014)

[7] O. Anwar **Bég**, A. Subba Rao, N. Nagendra, CH. Amanulla, M. Surya Narayana Reddy and A. Kadir, Numerical study of hydromagnetic non-Newtonian nanofluid transport phenomena from a horizontal cylinder with thermal slip: aerospace nanomaterial enrobing simulation, *J. Nanofluids*, Vol. 7, pp. 1–14 (2018).

[8] T. Thumma, O. Anwar **Bég** and A. Kadir, Numerical study of heat source/sink effects on dissipative magnetic nanofluid flow from a non-linear inclined stretching/shrinking sheet, *J. Molecular Liquids*, 232, 159–173 (2017).

FINITE ELEMENT THERMAL STRESS SIMULATION OF NANO-COATED GAS TURBINE BLADE SAMPLES UNDER HIGH TEMPERATURE

University of Salford MANCHESTER — 1967 · 2017 50 YEARS

Ali Kadir[1], O. Anwar Bég[1], Tasveer A. Bég[2] and Walid S. Jouri[1]

[1]Department of Mechanical/Aeronautical Engineering, Salford University, Manchester, M54WT, UK.

[2] Renewable Energy and Computational Multi-Physics, Israfil House, Dickenson Rd., Manchester, M13, UK.

Emails: A.Kadir@salford.ac.uk (Presenter); O.A.Beg@Salford.ac.uk; tasveerabeg@gmail.com; w.s.jouri@salford.ac.uk;

1.INTRODUCTION

Several studies have been communicated in recent years considering nano-coating protective layers for gas turbine environments. They have generally shown that improved protection is achieved compared with conventional thermal barrier coatings (TBCs) which are susceptible to various life limiting issues associated with their operating environment including erosion, corrosion, oxidation, sintering and foreign object damage (FOD) [1,2]. Nano-coatings engineered for high temperature applications have been investigated for surface roughness and topography, residual stress, adhesion, damage tolerance and resistance, tribological properties, lubrication, coefficient of friction and hot hardness. Motivated by these developments, in this presentation we describe recent finite element thermal stress simulations of nano-coated (Aluminium Oxide/Titanium Oxide metallic nano-particle mix). The simulations demonstrate that largely due to the higher thermal conductivity and smaller size of nano-particles, they achieve improved bonding in coatings and dissipate heat better than conventional micro-coatings. Greater integrity of the coating is achieved and lower susceptibility to corrosion gas penetration is obtained with nano-coatings compared with micro-coatings. ANSYS Workbench version 19.1 [3] has been employed to simulate the thermal stress response of nano-coatings. Extensive visualization of results is included. Important deductions on nano-coating performance are made. The study provides a useful compliment to experimental tests which are also being conducted.

2. NANO-COATING PROPERTIES

Since a continuum-based finite element approach is adopted, molecular variations in nano-particle dynamics in the coating cannot be simulated. Instead an *average value of materials properties* is adopted for a 60:40 % titanium oxide (TiO₂) : aluminium oxide (Al₂O₃) mix nano-coating (powder). The table below summarizes the key material properties (Young modulus, Poisson ratio, density and thermal conductivity) for the original nano–powders and the composite nano-coating:

3. ANSYS THERMAL STRESS FORMULATION

In ANSYS to simulate coupled thermal stress analysis, the stresses are related to the strains as follows [3]:

$$\{\sigma\} = [D]\{\varepsilon^{el}\}$$

- $\{\sigma\}$ = Stress Vector
- $[D]$ = Elastic or elasto-stiffness matrix
- $\{\varepsilon^{el}\}$ = Elastic strain vector
- $\{\varepsilon\}$ = Total strain vector
- $\{\varepsilon^{th}\}$ = Thermal strain vector

For the 3-dimensional analysis, thermal strain vector takes the form:

$$\{\varepsilon^{th}\} = \Delta T[\alpha_x \ \alpha_y \ \alpha_z \ 0 \ 0 \ 0]^T$$

- α_x = Thermal coefficient of expansion in the x direction (/C)
- $\Delta T = T - T_{ref}$ (C)
- T = current temperature (C)
- T_{ref} = reference strain - free temperature

The element integration point strains and stresses are computed by combining the following two equations:

$$\{\varepsilon^{el}\} = [B]\{u\} - \{\varepsilon^{th}\}$$

- $\{\varepsilon^{el}\}$ = Strain
- $[B]$ = Strain – displacement matrix at element of integration point
- $\{u\}$ = Nodal displacement vector
- $\{\varepsilon^{th}\}$ = Thermal strain vector

$$\{\sigma\} = [D]\{\varepsilon^{el}\}$$

- $\{\sigma\}$ = stress vector
- $[D]$ = Elasticity matrix

4. ANSYS MESH AND THERMAL STRESS ANALYSIS

A three-dimensional model was created using the ANSYS static structural geometry modeller to represent a steel sample under high temperature corrosion. A two-layered domain in (x,y,z) space is created with the base layer representing the gas turbine blade substrate (AISI 304 super alloy) and the upper layer simulating the Alumina-Titanium oxide nano-coating, as shown below. Note the nano-coating completely engulfs the substrate specimen. The fixture (cylindrical hole) is also shown in order to compare simulations with future HVOF experiments. Below shows the front (top) and 3-D rendition of the model. The clamping is achieved via the hole which penetrates the entire substrate and is filled with nano-material during the coating process. The nano coating thickness is 0.016 mm. The substrate sample dimensions are 10.98mm (depth), 20.76mm (length) and width (18.8mm). The boundary conditions imposed on all six faces of the coated model is a thermal one due to the hot gas at an average temperature of 1000 °C. The structural boundary condition is the fixing hole where the model is constrained.
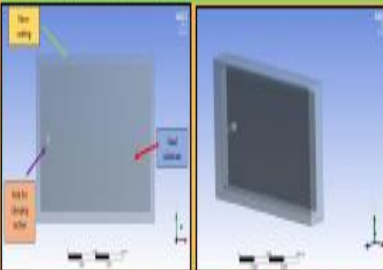
The von Mises or equivalent stress σ_e (output as SEQV) is computed as:

$$\sigma_e = MAX(|\sigma_1 - \sigma_2|, |\sigma_2 - \sigma_3|, |\sigma_1 - \sigma_3|)$$

The equivalent stress is related to the equivalent strain ε_e through:

$$\sigma_e = E\varepsilon_e$$
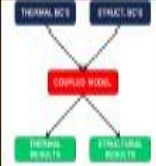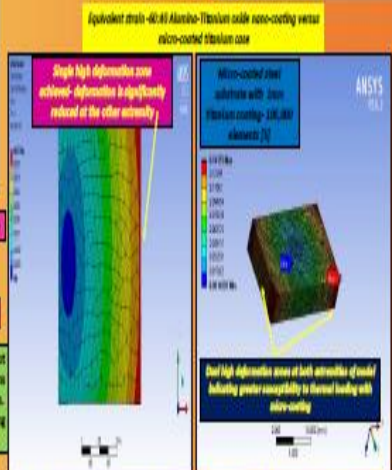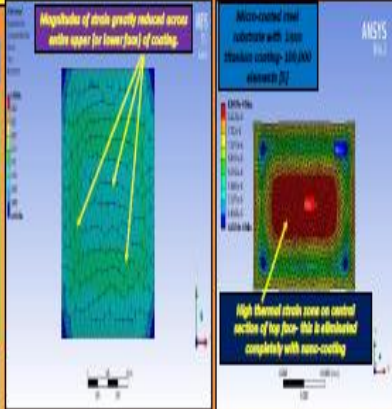
E= Young's modulus (used as EX or MP constant)

N.B. In ANSYS workbench, the data is usually supplied as a mean value and this data is correctly used by ANSYS, If T_{ref} is not only the definition temperature about which the data is supplied but also the reference temperature at which zero strains exist. Mesh independence was tested for. A default mesh of 140,000 elements was found to achieve grid independent results. The nano-coating simulations are compared with micro-coated steel samples using a single Titanium thermal barrier coating layer also engulfing the sample with 1mm depth, performed in an earlier study [4].

Equivalent strain -60:40 Alumina-Titanium oxide nano-coating versus micro-coated titanium case

Total deformation plot for 60:40 Alumina-Titanium oxide nano-coating versus micro-coated titanium case

Equivalent stress - 60:40 Alumina-Titanium oxide nano-coating versus micro-coated titanium case

5. CONCLUSIONS

In all cases the nano-coating is found to provide superior thermal protection to the steel substrate (AISI 304 super alloy). High stress zones are completely eliminated with nano-coating whereas they are prevalent with titanium micro-coating. Although titanium oxide has excellent thermal resistance properties, the alumina nano-powder when mixed with titania, produces an inert performance which is and resistant to inter-diffusion and this leads to stability during exposure to elevated temperatures for long periods of time, thus preserving the sharp interface and minimizing thermal stresses which are necessary for good thermal barrier performance. The alumina material tends to form an amorphous structure when it is deposited onto a substrate which is held at a relatively low temperature and in the alternative it tends to form a crystalline structure when applied via a vapor deposition to a substrate held at a relatively high temperature substrate. Either case will result in a very resilient nano-coating which achieves excellent bonding to the super alloy substrate and prevents the penetration of hot gas since at the nanoscale circles of micro-scale magnitude are mitigated. This is not possible in the micro-coating which flakes, permits heat penetration, has reduced integrity and eventually cracks. Alumina being integral to the coating layer and in contact with the substrate has the desirable characteristic that since the native oxide which forms on the substrate due to oxidation of the substrate will be alumina, therefore having a nano-structured alumina layer in the coating adjacent to a naturally occurring alumina layer will probably provide the best coating adherence as noted in [1]. Overall much lower stresses, strains and deformations are produced with nano-coatings compared with micro-coatings.

REFERENCES

[1] N.R. Dahotre and S. Nayak, Nanocoatings for engine application, Surface and Coatings Technology, 194, 58-67 (2005).

[2] C.A. Zhou and Q.H. Yu, Nanostructured thermal barrier coatings, Thermal Barrier Coatings, Woodhead Publishing Series in Metals and Surface Engineering, 75-96 (2011).

[3] ANSYS Theory Manual, ver 19.1, (Thermal stress analysis theory) Swanson Analysis Systems, Pittsburgh, USA (2018).

[4] Ali Kadir and O. Anwar Bég, Thermal stress and computational fluid dynamics analysis of coatings for high-temperature corrosion, ICHTMM 2018. 20th International Conference on Heat Transfer and Fluid Mechanics, Istanbul, Turkey, August 16 – 17 (2018).

ORIGINAL ARTICLE

WILEY

Computational fluid dynamic and thermal stress analysis of coatings for high-temperature corrosion protection of aerospace gas turbine blades

Ali Kadir[1] | Anwar O. Bég[1] | Mohammed El Gendy[2] |
Tasveer A. Bég[3] | MD. Shamshuddin[4] (iD)

[1]Department of Mechanical and Aeronautical Engineering, Salford University, Salford, UK

[2]Lufthansa Technik Malta (LTM), Luqa, Malta

[3]Department of Aerospace Engineering, Computational Mechanics and Renewable Energy Research, Manchester, UK

[4]Department of Mathematics, Vaagdevi College of Engineering, Warangal, Telangana, India

Correspondence
MD. Shamshuddin, Department of Mathematics, Vaagdevi College of Engineering, Warangal, Telangana 506005, India.
Email: shammaths@gmail.com and shamshuddin_md@vaagdevi.edu.in

Abstract

The current investigation presents detailed finite-element simulations of coating stress analysis for a three-dimensional, three-layered model of a test sample representing a typical gas turbine component. Structural steel, titanium alloy, and silicon carbide are selected for main inner, middle, and outermost layers respectively. ANSYS is used to conduct three types of analysis—static structural, thermal stress analysis, and also computational fluid dynamic erosion (via ANSYS FLUENT). The specified geometry, which corresponds to corrosion test samples exactly, is discretized using a body-sizing meshing approach, comprising mainly of tetrahedron cells. Refinements were concentrated at the connection points between the layers to shift the focus toward the static effects dissipated between them. A detailed grid independence study is conducted to confirm the accuracy of the selected mesh densities. The momentum and energy equations were solved, and the viscous heating option was applied to represent the improved thermal physics of heat transfer between the layers of the structures. A discrete phase model (DPM) in ANSYS FLUENT was used, which allows for the injection of continuous uniform air particles onto the model, thereby enabling an option for calculating the corrosion factor caused by hot air injection.

FINITE ELEMENT ANALYSIS OF NANOCOATED COMPOSITE GAS TURBINE BLADES USING METALLIC OXIDE NANO-POWDERS

Ali Kadir[1], O. Anwar Bég[1*], Walid S. Jouri[1]

[1]Multi-Physical Engineering Sciences Group, Mechanical Engineering Department, School of Science, Engineering and Environment (SEE), University of Salford, Manchester, M54WT, UK.

* Corresponding Author – Email:
O.A.Beg@salford.ac.uk ;

ABSTRACT

Nanomaterials are increasingly being deployed in engineering applications owing to their unique mechanical properties, including high strength-to-weight ratio, excellent electrical and thermal conductivity and high aspect ratios. Both carbon-based and metallic nanoparticles have been explored extensively. They provide enhanced protection in extreme loading situations including gas turbine blade coatings, aircraft wings, rail tracks etc. In the present study, motivated by studying the response of substrates of gas turbine blades, here, a detailed finite element stress/strain analysis of a square nano-coated steel plate with both single and multiple layers of nano-powder composite consisting of Titanium Oxide and Aluminium Oxide nano-particles (in different percentages). ANSYS software is deployed to simulate three-dimensional stress, strain and deformation response. Multiple composite layers are observed to enhance the resistance to deformation significantly and minimize peak stresses encountered with bare plates and single-layer nano-coatings. Maximum improvement in the mechanical properties of the plate are achieved with 60:40 ratio Titanium Oxide to Aluminium Oxide mixed nanocomposite layer coating.

KEYWORDS: *Nanocoatings; gas turbine blades; stress analysis; equivalent stress and strain; total deformation; titanium oxide and aluminium oxide nano-powder; finite element analysis.*

1.INTRODUCTION

Nanomaterials have emerged as a major development in modern mechanical and structural engineering. They include many different types of nanostructures, which are engineered at the nanoscale (1- 100nm). They include carbon nanotubes, metallic nanoparticles, nanowires, nano-shells and many other configurations which may be embedded within existing materials (metals, composites) or deposited as external coatings. Nano-engineered structures possess superior properties including enhanced thermal and electrical conductivity, superior tensile strength, enhanced resistance to corrosion and wear, self-sensing, self-healing properties, as well as high strength to weight ratios [1]. Nano-powders comprising various metallic oxides or silicates can be successfully deposited surfacially on structures using thermal spray technologies. This enables complete surface coating of structural elements. Several studies of the improved mechanical performance of coated structures with nanomaterials have been communicated in recent years. Islam *et al.* [2] used electrochemical impedance spectroscopy (EIS) to investigate the contribution of SiO_2 nanoparticles on hardness and corrosion resistance of electroless Ni–P coatings. They showed that although pure medium- and high-P coatings achieve a satisfactory corrosion protection, their performance attributes are greatly elevated through incorporation of silica (SiO_2) nanoparticles. Overall, the SiO_2 nanoparticles improve the deposit morphology via grain structure modification, decrease in the surface roughness and minimization of surface porosity in the nanocomposite coatings which produce greater micro hardness and wear resistance. Ghazali *et al.* [3] studied the corrosion inhibition behavior of super-amphiphobic coating using functionalized aluminium oxide nanoparticles. Arihwar *et al.* [4] have explored the reduction of degradation in biomaterial coating with titanium and zinc oxide nano-powders.